Measurement of the $t\bar{t}b\bar{b}$ production cross-section with 8 TeV ATLAS data

Dissertation
zur Erlangung des akademischen Grades
doctor rerum naturalium (Dr. rer. nat.)
im Fach Physik
eingereicht an der
Mathematisch-Naturwissenschaftlichen Fakultät der
Humboldt Universität zu Berlin
von

MSc Spyridon Argyropoulos

Präsident der Humboldt-Universität zu Berlin
Prof. Dr. Jan-Hendrik Olbertz

Dekan der Mathematisch-Naturwissenschaftlichen Fakultät
Prof. Dr. Elmar Kulke

Gutachter: 1. Prof. Dr. Klaus Mönig
2. Prof. Dr. Thomas Lohse
3. Prof. Dr. Christian Schwanenberger

Tag der mündlichen Prüfung: 15.12.2015

Erklärung

Ich versichere, dass ich die vorliegende Dissertation selbständig und nur unter Verwendung der in der Promotionsordnung angegebenen Hilfen und Hilfsmittel angefertigt habe.

Genf, 25. August 2015

Spyridon Argyropoulos

Στη μνήμη του Πέτρου.

Abstract

This thesis presents the measurement of the $t\bar{t}b\bar{b}$ production cross-section, using a dataset of 20.3 fb^{-1} of pp collisions collected with the ATLAS detector at $\sqrt{s} = 8$ TeV. The measurement is based on a cut-and-count method, using a sample of events with exactly four b-tagged jets, which is shown to have a high purity in signal events. The measurement exploits the most precise jet energy scale and b-tagging calibrations and is performed in a fiducial phase space that is designed to minimize the model dependence of the measurement.

The fiducial cross-section is measured to be

$$\sigma^{\text{fid}}_{t\bar{t}b\bar{b}} = 18.9 \pm 3.5\ (\text{stat})^{+5.6}_{-5.5}\ (\text{sys}) \pm 0.6\ (\text{Lumi})\ \text{fb} \tag{1}$$

or subtracting the contribution from $t\bar{t}H(b\bar{b})$ and $t\bar{t}Z(b\bar{b})$ final states,

$$\sigma^{\text{fid,QCD}}_{t\bar{t}b\bar{b}} = 17.8 \pm 3.5\ (\text{stat})^{+5.9}_{-5.7}\ (\text{sys}) \pm 0.6\ (\text{Lumi})\ \text{fb}. \tag{2}$$

The result is compared with a multitude of theoretical predictions, including different NLO calculations matched to a parton shower, which constitute the most precise predictions available to date, as well as with a series of models that differ in the description of the $g \to b\bar{b}$ splitting. It is shown that the most extreme $g \to b\bar{b}$ splitting model overestimates the observed rate of $t\bar{t}b\bar{b}$ production and that the measurement favors calculations performed with renormalization/factorization scales which are softer than the scales usually employed in similar calculations.

Zusammenfassung

Diese Dissertation beschreibt die Messung des Wirkungquerschnitts für die Produktion von $t\bar{t}b\bar{b}$ in Protonkollisionen mit einer Schwerpunktsenergie von $\sqrt{s} = 8$ TeV. Der verwendete Datensatz entspricht einer integrierten Luminosität von 20.3 fb^{-1}. Der Wirkungsquerschnitt wurde aus der Anzahl der Signalereignisse bestimmt, die durch harte Schnitte insbesondere auf genau 4 identifizierten b-jets, selektiert wurden, was zu einer hohen Reinheit des Signals führt. Bei der Messung wurden die präzisesten Kalibrierungen von der Jet-Energieskala und der b-jet Effizienz benutzt. Die Messung wurde in einem Referenzphasenraum (fiducial phase-space) durchgeführt, der daraufhin optimiert wurde, die Abhängigkeit von der Modellierung zu minimisieren.

Der gemessene Wirkungsquerschnitt beträgt

$$\sigma^{\text{fid}}_{t\bar{t}b\bar{b}} = 18.9 \pm 3.5\ (\text{stat})^{+5.6}_{-5.5}\ (\text{sys}) \pm 0.6\ (\text{Lumi})\ \text{fb} \tag{3}$$

oder, nachdem der Beitrag von $t\bar{t}H(b\bar{b})$ und $t\bar{t}Z(b\bar{b})$ abgezogen wurde:

$$\sigma^{\text{fid,QCD}}_{t\bar{t}b\bar{b}} = 17.8 \pm 3.5\ (\text{stat})^{+5.9}_{-5.7}\ (\text{sys}) \pm 0.6\ (\text{Lumi})\ \text{fb}. \tag{4}$$

Das Ergebnis wurde mit einer Vielzahl von theoretischen Vorhersagen verglichen, einschließlich NLO-Berechnungen mit Partonschauern und einer Reihe von Modellen die sich in der Beschreibung der $g \to b\bar{b}$-Spaltung unterscheiden. Es wurde gezeigt, dass das exstremste Model den Wirkungsquerschnitt überschätzt und dass die Messung die Vorhersagen bevorzugt, die mit einer niedrigen Renormierungs- und Faktorisierungsskala, berechnet wurden.

Contents

Preface

With the highest center-of-mass energy ever achieved in a collider experiment, the 8 TeV run of the LHC has enabled the measurement of rare processes involving the production of multiple heavy particles. Measurements of bottom quarks produced in association with vector bosons have been performed by both ATLAS [1, 2] and CMS [3, 4]. Being in tension with certain theoretical predictions, these measurements have stirred the interest of the theoretical community, both in terms of refining the higher-order QCD calculations for hadron collisions [5, 6], as well as understanding subtle aspects such as double parton scattering [7].

Among the processes involving the production of many heavy particles, $t\bar{t}H$ holds a prominent place. For a Higgs mass of 125 GeV, $H \to b\bar{b}$ is the dominant decay mode[1] in the $t\bar{t}H$ channel, thereby rendering $t\bar{t}H(b\bar{b})$ very promising for the measurement of both the top as well as the bottom Yukawa couplings. The $t\bar{t}b\bar{b}$ final state arises not only in the Standard Model Higgs production in association with top quarks, but also in the production of heavy charged Higgs bosons $pp \to tbH^{\pm} \to t\bar{t}b\bar{b}$ [8], as well as in the production of supersymmetric particles [9].

In this context, $pp \to t\bar{t}b\bar{b}$ plays an important role. With four particles in the final state and two mass scales involved, $t\bar{t}b\bar{b}$ poses several challenges for the theoretical predictions, which suffer from large uncertainties. Moreover, $t\bar{t}b\bar{b}$ constitutes the major irreducible background for several flagship searches in the ATLAS physics program, such as $t\bar{t}H(b\bar{b})$, as well as other searches for new physics. Finally, the $t\bar{t}b\bar{b}$ production is sensitive to the modeling of the $g \to b\bar{b}$ rate in parton shower generators, which is an important aspect of the modeling of processes with heavy quarks in the final state. Since the $g \to b\bar{b}$ rate is rather poorly constrained from LEP and SLC data [10–14], measuring the $t\bar{t}b\bar{b}$ production could potentially provide complementary information. An experimental determination of the $t\bar{t}b\bar{b}$ production cross-section has therefore become a necessity.

This thesis presents the first measurement of the absolute $t\bar{t}b\bar{b}$ production cross-section with four resolved b-jets, using a dataset of 20.3 fb^{-1} collected with the ATLAS detector at $\sqrt{s} = 8$ TeV. The measurement is based on a cut-and-count method, exploiting the most precise jet energy scale and b-tagging calibrations and is performed

[1] In what follows we will adopt the shorthand notation $X(ab)$ to denote the decay $X \to ab$.

in a fiducial phase space that is designed to minimize the model dependence of the measurement.

An estimate for the QCD production of $t\bar{t}b\bar{b}$ is obtained by subtracting the contributions of the irreducible backgrounds from the $t\bar{t}H$ and $t\bar{t}Z$ processes, and the resulting cross-section is compared with the latest available theoretical models. The measurement features an uncertainty which is competitive with the most precise theoretical predictions.

The measurement is found to disfavor the most extreme PYTHIA 8 model of $g \to b\bar{b}$ splitting and reveals certain systematic trends among the theory predictions. Most notably it is found that data favor calculations performed with renormalization/factorization scales which are softer than the scales usually employed in similar calculations.

The thesis is organized as follows. Part I contains an overview of the theoretical underpinnings of $t\bar{t}b\bar{b}$ production in the Standard Model and the different aspects involved in the simulation of $t\bar{t}b\bar{b}$ production in Monte-Carlo generators. Part II describes the LHC accelerator system and the ATLAS detector, with a particular emphasis on the detector performance aspects that affect the measurement. Finally, Part III contains a detailed description of the measurement methodology, as well as an interpretation of the result in terms of different theoretical models.

Part I

Theoretical Introduction

Chapter 1

Theoretical preliminaries

1.1 The Standard Model

Our current understanding of High Energy Physics can be summarized in the theory known as the Standard Model [15]. The Standard Model (SM) is a quantum field theory, which describes collectively the electromagnetic, weak and strong interactions between the fundamental constituents of matter, quarks and leptons.

The Standard Model is built upon the fundamental notion of symmetries. Global symmetries, i.e. transformations of the fundamental fields which are independent of the space-time coordinates, lead to conservation laws[1] which can be tested experimentally. While the space-time symmetries of the theory, such as space-time translations and rotations, are easily perceptible by the human senses, the Standard Model also possesses internal symmetries, whose effects manifest only at subatomic scales. These internal symmetries act on the quantum numbers of the subatomic particles, such as the charge, color, baryon number etc, and lead to the associated conservation laws that can be observed in particle physics experiments.

Interactions between fields/particles are introduced in the theory by the so-called gauging procedure, i.e. by demanding that global symmetries also hold locally, at every space-time point. In the Standard Model the symmetry that is gauged corresponds to the non-Abelian group $SU(3) \times SU(2)_L \times U(1)_Y$, where the subscript L denotes that the symmetry applies to left-handed fields only and $Y \equiv 2(Q - T_3)$ denotes the weak

[1] The fact that continuous global symmetries imply the existence of conservation laws is codified in the celebrated Noether's first theorem.

hypercharge[2]. The $SU(3)$ group is related to transformations which change the quark colors and is associated with the conservation of the color charge. The $SU(2)_L \times U(1)_Y$ group is related to transformations of the weak isospin and weak hypercharge of the quarks and leptons and is associated with the conservation of the corresponding quantities. The symmetries of the Standard Model and their implied conservation laws are summarized in Table 1.1. Moreover, the Standard Model Lagrangian exhibits a series of "accidental" global symmetries, such as the symmetries associated to the conservation of the lepton and baryon number, which are not fundamental but arise as a consequence of the renormalizable structure of the SM Lagrangian.

Symmetry	Symmetry group	Symmetry type	Conserved quantities
Gauge	$SU(3) \times SU(2)_L \times U(1)_Y$	Gauge (local)	Color charge, weak isospin weak hypercharge
Poincaré	$\mathbb{R}^{1,3} \times SO(1,3)$	Global	Energy, momentum angular momentum

Table 1.1: Symmetries satisfied by the SM Lagrangian by construction. $\mathbb{R}^{1,3}$ denotes the group of translations in $3+1$ dimensions.

While the Lagrangian of the Standard Model is invariant under the full gauge group $SU(3) \times SU(2)_L \times U(1)_Y$, the physical spectrum of the theory does not display traces of the $SU(3)$ color symmetry, due to the phenomenon of confinement and the $SU(2)_L \times U(1)_Y$ is reduced to the subgroup $U(1)_Q$, related to the conservation of the electric charge. This phenomenon is known as spontaneous symmetry breaking and is realized by the Higgs mechanism [16–20], as will be described later.

The last ingredient of the theory is its particle content. The gauge fields are related to the generators of the gauge group and are thus determined by the gauge symmetries, as will be described later in more detail. The fermion fields are introduced by hand as multiplets that transform under different representations of the gauge group, as shown in Table 1.2

[2]Here T_3 denotes the projection of the weak isospin along the z-axis and Q denotes the electric charge.

Particle	Spin	Color charge	Weak hypercharge	T_3	Electric charge	Representation
u_L, c_L, t_L	1/2	1	1/3	1/2	2/3	$\left(3, 2, \frac{1}{3}\right)$
d_L, s_L, b_L	1/2	1	1/3	-1/2	-1/3	$\left(3, 2, \frac{1}{3}\right)$
u_R, c_R, t_R	1/2	1	4/3	0	2/3	$\left(\bar{3}, 1, \frac{4}{3}\right)$
d_R, s_R, b_R	1/2	1	-2/3	0	-1/3	$\left(\bar{3}, 1, -\frac{2}{3}\right)$
e_L^-, μ_L^-, τ_L^-	1/2	0	-1	-1/2	-1	$(1, 2, -1)$
e_R^-, μ_R^-, τ_R^-	1/2	0	-2	0	-1	$(1, 1, -2)$
$\nu_{e,L}, \nu_{\mu,L}, \nu_{\tau,L}$	1/2	0	-1	1/2	0	$(1, 2, -1)$

Table 1.2: The Standard Model particle content. T_3 denotes the third component of the weak isospin. The subscripts L, R denote the left and right chiralities respectively.

The electroweak sector and spontaneous symmetry breaking

Symmetry breaking in the form of phase transitions is well known in classical physics and has been formalized by Landau [21, 22]. Considering for instance a ferromagnet, we know that, above the Curie temperature, the net magnetization is zero, the spins are randomly oriented and the system displays a symmetry under $SO(3)$ transformations (3-dimensional rotations). Below the Curie temperature, the system obtains a net magnetization with the spins pointing along a certain direction and the symmetry being reduced ("broken") from $SO(3)$ to $SO(2)$ (rotations about the external field direction). In this less symmetric phase, one needs additional degrees of freedom (the net magnetization for the case of the ferromagnet) in order to describe the system. These have been dubbed order parameters.

In an analogous way, Higgs, Brout, Englert, Guralnik, Hagen and Kibble proposed a way to apply these principles to systems of quantum fields [16–20]. Glashow, Weinberg and Salam then applied the idea of symmetry breaking into the description of the electromagnetic and weak interactions as a unified gauge field theory.

More specifically, in the electroweak theory [23–25], one starts from a symmetric phase which is invariant under the transformations of the gauge group $SU(2)_L \times U(1)_Y$. This symmetry has 4 generators, which correspond to 4 massless vector bosons: the W_1, W_2, W_3 bosons of $SU(2)_L$ that transform under the (1,3,0) representation of the SM gauge group and the B boson of $U(1)_Y$ that transforms under the (1,1,0) representation. Linear combinations of the W and B bosons are identified with the physical $W^{\pm}, Z^0$

and γ bosons as follows

$$W^{\pm,\mu} = \frac{1}{\sqrt{2}}(W_1^\mu \pm iW_2^\mu), \tag{1.1}$$

$$\gamma^\mu = \sin\theta_W W_3^\mu + \cos\theta_W B^\mu \tag{1.2}$$

$$Z^{0,\mu} = \cos\theta_W W_3^\mu - \sin\theta_W B^\mu, \tag{1.3}$$

where θ_W is known as the Weinberg angle and μ represent the Lorentz indices.

Along with the electroweak gauge bosons, the electroweak theory predicts the existence of a scalar field (dubbed the Higgs field), which plays the role of the order parameter of the theory. Below a certain energy scale, the Higgs field acquires a non-zero vacuum expectation value and the $SU(2)_L \times U(1)_Y$ symmetry is broken down to $U(1)_Q$, which is the gauge symmetry of electromagnetism. The Higgs field is a complex-valued field that transforms under the (1,2,1) representation of the SM gauge group, having therefore 4 degrees of freedom. After spontaneous symmetry breaking, 3 of these degrees of freedom are absorbed by the massless bosons $W^\pm$ and Z^0 bosons which consequently acquire a mass and the remaining degree of freedom constitutes the Higgs boson, i.e. a massive scalar particle with zero electric charge.

The electroweak theory has been consolidated by the discovery of the neutral current interactions and the W and Z bosons by the Gargamelle [26, 27], UA1 [28, 29] and UA2 [30, 31] experiments at CERN, while the Higgs boson was recently discovered by the ATLAS and CMS experiments [32, 33].

The strong sector (QCD)

The development of Quantum Chromodynamics (QCD) as the gauge theory of strong interactions began with the introduction of the quark model for the classification of hadron resonances [34, 35]. The color charge was introduced as a new degree of freedom in an attempt to solve the Δ^{++} puzzle, i.e. to allow for the existence of resonances with antisymmetric wave-functions comprised of three quarks with identical flavor and spin [36]. It was later realized by the seminal work of Gross, Wilczek [37] and Politzer [38] that non-Abelian gauge theories are asymptotically free, i.e. that the coupling between quarks and gluons vanishes in the limit of infinite energy,

and could thus explain Bjorken scaling[3] [39] which was observed by the SLAC-MIT deep inelastic scattering experiments [40].

The measurement of the cross-section ratio $\sigma(e^-e^+ \to \text{hadrons})/\sigma(e^-e^+ \to \mu^-\mu^+)$ at SLAC [41] provided evidence for the existence of three colors and the discovery of 3-jet events in e^-e^+ collisions by the TASSO experiment at DESY [42] established the existence of gluons thus proving that the strong interactions could be described as a gauge theory with a $SU(3)$ symmetry group, where 3 corresponds to the number of colors.

The QCD Lagrangian is comprised of two parts: the Yang-Mills part that describes the gauge bosons (gluons) [43] and the Dirac part [44, 45] that describes the fermions (quarks) which transform in a representation of the gauge group. One can schematically write[4]

$$\mathcal{L}^0_{QCD} = \mathcal{L}^0_{\text{YM}} + \mathcal{L}^0_{\text{Dirac}} = -\frac{1}{4}\text{Tr}\left[F^0_{\mu\nu}F^{0,\mu\nu}\right] + \sum_i \bar{\Psi}_i \left(i\not{\partial} - m_i\right)\Psi_i. \tag{1.4}$$

where $F^{0,\mu\nu}_a = \partial^\mu A^\nu_a - \partial^\nu A^\mu_a$ is the field strength and the indices a and i run over the color charges and the quark flavors respectively. This Lagrangian describes freely propagating gluons and quarks without interactions. Introducing a local infinitesimal $SU(3)$ transformation $\Psi'_i = \exp\left(ig\lambda^\alpha(x)[t_a]^j_i\right)\Psi_j$, where $\lambda^a(x)$ are small parameters and t_a are the generators of the $SU(3)$ group, we obtain

$$\begin{aligned}\delta\Psi_i = \Psi'_i - \Psi_i &= ig\lambda^a(x)[t_a]^j_i\Psi_j \\ &\equiv ig\Lambda\Psi.\end{aligned} \tag{1.5}$$

Then

$$\partial_\mu(\delta\Psi) = ig\Lambda\partial_\mu\Psi + ig(\partial_\mu\Lambda)\Psi, \tag{1.6}$$

[3] Bjorken scaling refers to the property of the nucleon structure functions being independent of the energy of the experiment or the four-momentum transfer and depending instead only on a dimensionless variable. Since energy independence implies the independence of the spatial resolution scale, Bjorken scaling suggested that nucleons were made of point-like constituents, which were later identified with the quarks.

[4] Upon attempting to quantize the QCD Lagrangian, one has to add an additional gauge fixing term, in order to eliminate unphysical degrees of freedom from the spectrum. This is not of crucial importance for the following discussion and will not be treated here.

with the second term spoiling the gauge invariance. In order to restore gauge invariance, the ordinary derivative ∂_μ has to be replaced by a new operator ∇_μ, which has to transform covariantly under the gauge transformation, i.e obey the same transformation as the field itself

$$\delta \nabla_\mu \Psi \equiv ig\Lambda \nabla_\mu \Psi. \tag{1.7}$$

Defining $\nabla_\mu \equiv \partial_\mu - igA_\mu$, where $A_\mu(x)$ is a vector field, we see that the property of covariance (equation (1.7)) determines the transformation of the field $A_\mu(x)$:

$$\begin{aligned} \delta A^a_\mu &= \partial_\mu \Lambda^a + ig\left[\Lambda, A_\mu\right] \\ &= \partial_\mu \Lambda^a + g C^a_{bc} \Lambda^c A^b_\mu \equiv \nabla_\mu \Lambda^a. \end{aligned} \tag{1.8}$$

Therefore, demanding that the Lagrangian be invariant under local $SU(3)$ transformations automatically introduces the gauge fields A_μ (gluons), which have to transform in the adjoint representation[5] of $SU(3)$. Furthermore, from equation (1.8) we observe that the requirement of gauge invariance completely determines the interaction between quarks and gluons. The interacting QCD Lagrangian becomes

$$\mathcal{L}_{QCD} = -\frac{1}{4}\mathrm{Tr}\left[F_{\mu\nu}F^{\mu\nu}\right] + \sum_i \bar{\Psi}_i \left(i\not{\nabla} - m_i\right)\Psi_i, \tag{1.9}$$

$$F_{\mu\nu} = \nabla_\mu A_\nu - \nabla_\nu A_\mu = \partial_\mu A_\nu - \partial_\nu A_\mu - ig\left[A_\mu, A_\nu\right]. \tag{1.10}$$

The constant g which appears in equations (1.9) and (1.10) is the gauge coupling parameter, which is related to the strong coupling constant by

$$\alpha_s \equiv \frac{g^2}{4\pi}. \tag{1.11}$$

Intuitively, one can picture the gauging procedure described above by drawing an analogy to general relativity. In order to compare vectors attached to different points on a curved surface, one has to introduce the notion of parallel transport. The effects of the parallel transport from point to point can then be described by the Christoffel symbols (affine connection). Also parallel transport along a closed contour provides a measure of the curvature of space-time and is described by the Riemann curvature tensor. An analogous picture for QCD is illustrated in Figure 1.1. The QCD fields take

[5] The adjoint representation is defined by $[t_a]^c_b \equiv iC^c_{ab}$, where C^c_{ab} are the structure constants of the gauge group.

values on a *base space*, which is the 4-dimensional Minkowski space-time of special relativity. At every space-time point there is a *fiber*, that is a copy of the gauge group $SU(3)$. When the $SU(3)$ symmetry is gauged, the quark fields can transform with different phases from point to point. Therefore, in order to compare quark fields at different space-time points, one has to introduce a *connection*, namely the gluon fields, that determines how the quark fields must be transported from one point to another. In this sense, the analogues of the Christoffel symbols are given by the gluon fields and the analogue of the curvature is given by the field strength $F_{\mu\nu}$.

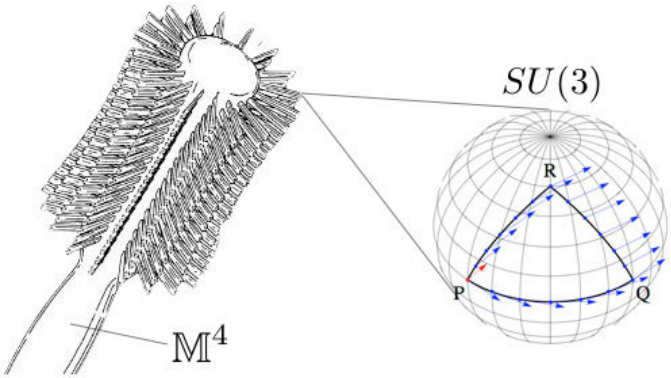

Figure 1.1: QCD as a hairbrush (*fiber bundle*). The handle (*base space*) is identified with the 4-dimensional Minkowski space-time and the bristles (*fibers*) are identified with the $SU(3)$ group. The gauge fields (*affine connection*) determine how quark fields are parallel-transported from point to point.

1.2 Matrix element calculations in perturbative QCD

The principal task of QCD calculations for collider experiments is to relate the incoming state to the outgoing state. This is accomplished by the scattering matrix, which relates asymptotic incoming $\Psi_{\text{in}}(\alpha)$ and outgoing states $\Psi_{\text{out}}(\beta)$, described by the set of quantum numbers α and β, through the relation

$$S_{\beta\alpha} \equiv \langle \Psi_{\text{out}}(\beta) | \Psi_{\text{in}}(\alpha) \rangle. \tag{1.12}$$

In QCD, Ψ_{in} and Ψ_{out} would in principle correspond to incoming and outgoing quarks and gluons, however complications arise due to the confining nature of the strong force. This complication is overcome via the factorization theorem that will be discussed in

Section 1.4. For the moment we can pretend that the fields appearing in equation (1.12) are the fundamental degrees of freedom of the theory, i.e. quarks and gluons.

The S matrix comprises of a trivial part (no interaction) and a non-trivial part

$$S_{\beta\alpha} = \delta_{\beta\alpha} + iT_{\beta\alpha} = \delta_{\beta\alpha} + (2\pi)^4 \delta^{(4)} \left(\sum_i p_i - \sum_f p_f \right) i\mathcal{M}_{\beta\alpha}. \tag{1.13}$$

The invariant matrix element $\mathcal{M}$ represents the non-trivial part of the scattering matrix, i.e. it encapsulates the dynamics of the interaction. The delta function in equation (1.13) imposes the conservation of the incoming 4-momenta p_i.

The matrix element can be calculated by perturbation theory using the QCD Feynman rules, which are derived from the QCD Lagrangian [46]. Cross-sections can then be calculated using the so-called Fermi's golden rule [47, 48], which states that the transition probabilities from one state to another are given by the amplitude of the matrix element describing the transition, multiplied by the density of final states. More specifically, for a process $p_1 p_2 \to k_1 \dots k_n$, the cross section is given by

$$d\sigma = \frac{1}{F} |\mathcal{M}|^2 d\Phi_n, \tag{1.14}$$

where F is the incoming particle flux and $d\Phi_n$ is the n-particle final state phase space.

1.3 Running of the strong coupling constant

In quantum field theory the physical space is thought of as being permeated by the fundamental fields (quark, gluon, photon, etc) and the vacuum is the state that corresponds to the lowest possible energy. While the vacuum state does not contain any real particles (particles satisfying the on-shell condition $E^2 = p^2 + m^2$), fluctuations in the energy of the fields can produce virtual particle-antiparticle pairs that annihilate after a time that is bounded by the Heisenberg uncertainty principle. These virtual particle pairs carry the quantum numbers of real particles, e.g. color, charge, therefore acting as dipoles. As a consequence of the presence of these dipoles, the vacuum acquires the properties of a polarizable material medium.

The so-called vacuum polarization processes, depicted in Figure 1.2, induces a dependence of the strong coupling constant α_s on the interaction energy. This

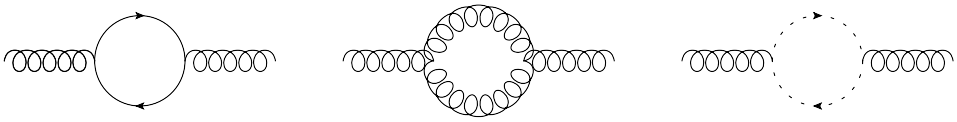

Figure 1.2: Vacuum polarization processes that induce the running of the strong coupling constant. Contributions arise due to fermion (left), gluon (middle) and ghost loops (right).

dependence[6] is governed by the QCD β function, which reads [49]

$$\beta\left(g(\mu)\right) \equiv \mu \frac{dg(\mu)}{d\mu} = -g\left[\frac{\alpha_s}{4\pi}\beta_1 + \left(\frac{\alpha_s}{4\pi}\right)^2 \beta_2 + \ldots\right] \approx -g\frac{\alpha_s}{4\pi}\left(11 - \frac{2N_f}{3}\right), \quad (1.15)$$

where β_i are the i-loop contributions to the beta function, μ is an energy scale which arises from the renormalization procedure, N_f is the number of flavors and the last approximation corresponds to retaining only the 1-loop contribution. Solving for α_s one obtains

$$\alpha_s(\mu^2) = \frac{\alpha_s(\mu_0^2)}{1 + \frac{\alpha_s(\mu_0^2)}{4\pi}\left(11 - \frac{2N_f}{3}\right)\ln\frac{\mu^2}{\mu_0^2}}. \quad (1.16)$$

From equation (1.16) we can see that α_s grows with decreasing energy. As shown in Figure 1.3, α_s is large for energies of the order of the proton mass. Therefore, at energies close to the hadronization scale ($\sim$1 GeV), perturbation theory, which is based on treating α_s as a small parameter, cannot be trusted.

1.4 The factorization theorem: PDFs and the DGLAP equations

In the previous sections, the theory was set-up using quarks and gluons. Nevertheless, only colorless hadrons are observed experimentally. Here we explain how we can use the parton level calculations to extract results for hadron observables.

It was first proposed by Feynman [51], that lepton-hadron scattering in the limit of large momentum transfer can be explained by the parton model, where the hadron is

[6] Ghost fields are fictitious fields that are introduced as one way to quantize a gauge invariant theory. Ghost fields violate the spin-statistics relation and appear only as virtual particles in loops.

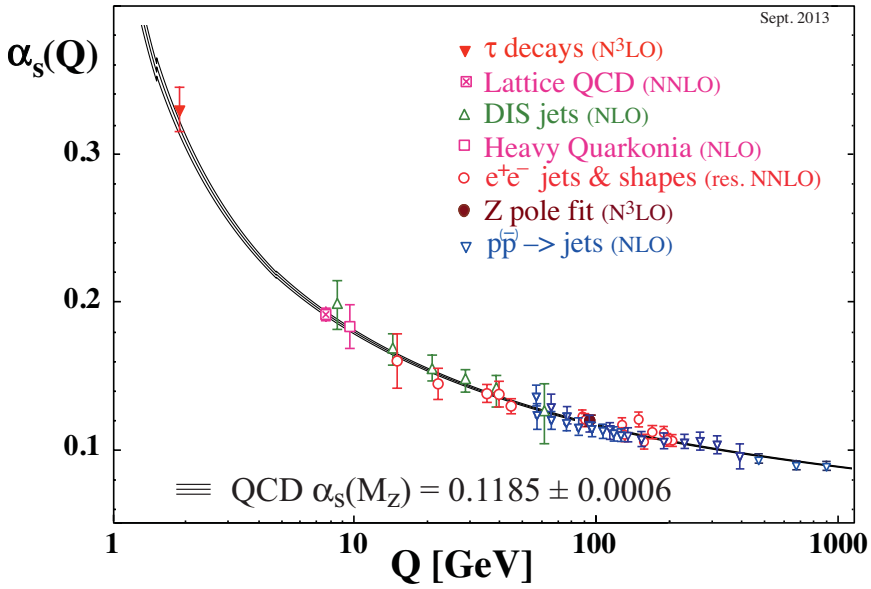

Figure 1.3: The QCD running coupling [50].

replaced by fundamental point-like constituents. These were later identified with the QCD quarks and gluons. As it was further elaborated by Bjorken and Paschos [52], the essential ingredient of the parton model is to consider a class of infinite momentum frames, in which a parton i will carry a fraction $0 < x_i < 1$ of the hadron's momentum. Lepton-hadron scattering can then be described by an incoherent sum[7] of all the possible lepton-parton scatterings. This idea was reversed by Drell and Yan [53] in the study of what is today known as the Drell-Yan process (i.e. lepton hadroproduction). There, it was postulated that the hadronic cross section $\sigma(H_1H_2 \to \mu^+\mu^- + X)$ could be obtained by convolving the cross-section for the hard-scattering subprocess $\hat{\sigma}(q\bar{q} \to \mu^+\mu^-)$ with the Parton Distribution Functions f_{i/H_1}

$$\sigma_{H_1H_2} = \sum_{i,j} \int dx_1 dx_2 f_{i/H_1}(x_1) f_{j/H_2}(x_2) \hat{\sigma}(ij \to \mu^+\mu^-). \tag{1.17}$$

The PDFs $f_{i/H}(x)$ express the probability of finding a parton i inside the hadron H, carrying a momentum fraction x. The domain of validity of equation (1.17) is the asymptotic scaling limit: $s = Q^2 \to \infty, x$ fixed. Measurements at lower values of x first made at SLAC [54] and later extended by several other experiments at CERN (BCDMS, NMC), Fermilab (E665) and HERA (H1, ZEUS) observed that the cross-sections in hadron scattering do not scale according to equation (1.17), but instead

[7] Incoherent sum is a sum which does not include interference terms.

display a logarithmic dependence on the annihilation energy. The appearance of these logarithms was attributed to the emission of gluons that were collinear to the incoming beam and it was shown that such contributions could be factored into the the PDFs, with equation (1.17) becoming

$$\begin{aligned}\sigma_{H_1H_2} &= \sum_{i,j}\int dx_1 dx_2 f_{i/H_1}(x_1,\mu_F^2) f_{j/H_2}(x_2,\mu_F^2)\hat{\sigma}(ij\to\mu^+\mu^-)\\ &= f_{i/H_1}\otimes f_{j/H_2}\otimes\hat{\sigma}(ij\to\mu^+\mu^-),\end{aligned} \tag{1.18}$$

where μ_F is an energy scale which characterizes the hard subprocess, known as the factorization scale. Equation (1.18) is an example of theorems called factorization theorems [55] which essentially express the fact that in certain kinematic regimes the non-perturbative dynamics (encapsulated in $f_{i/H_1}, f_{j/H_2}$) can be separated from the perturbative dynamics (encapsulated in $\hat{sigma}$).

From equation (1.18), we can see that hadronic observables $\mathcal{O}$ will be given by a convolution of the parton distribution functions with the parton-level observable $\hat{\mathcal{O}}$, i.e. $\mathcal{O} = f_i \otimes f_j \otimes \hat{\mathcal{O}}$. The fact that physical observables must be independent of unphysical scale is expressed via the so-called renormalization group equation (RGE)

$$\frac{\partial\mathcal{O}(x,Q^2)}{\partial\mu_F^2} = 0. \tag{1.19}$$

In analogy with the beta function for the QCD running coupling, the RGE leads to the evolution equations for the PDFs [49], which are known as the DGLAP equations [56–59]

$$\begin{aligned}\frac{\partial}{\partial\ln\mu_F^2}\begin{pmatrix} f_{q_i}(x,\mu_F,^2)\\ f_g(x,\mu_F^2)\end{pmatrix} &= \frac{\alpha_s}{2\pi}\sum_j\int_x^1\frac{d\xi}{\xi}\begin{pmatrix} P_{q_iq_j}\left(\frac{x}{\xi},\alpha_s(\mu_F^2)\right) & P_{q_ig}\left(\frac{x}{\xi},\alpha_s(\mu_F^2)\right)\\ P_{gq_j}\left(\frac{x}{\xi},\alpha_s(\mu_F^2)\right) & P_{gg}\left(\frac{x}{\xi},\alpha_s(\mu_F^2)\right)\end{pmatrix}\\ &\times\begin{pmatrix} f_{q_j}(x,\mu_F^2)\\ f_g(x,\mu_F^2)\end{pmatrix}.\end{aligned} \tag{1.20}$$

The DGLAP equations express the fact that a quark or gluon with momentum fraction x can come from a quark or gluon with a larger momentum fraction x/ξ with a probability proportional to $\alpha_s \cdot P_{ij}$. Here, P_{ij} are the so-called splitting kernels, which are calculable in perturbation theory, with the LO contributions shown in Figure 1.4. Physically, this corresponds to the fact that as the momentum scale of the interaction

is increased, the sea of quark-antiquark pairs and gluons that surround the original parton are resolved. We note that although the DGLAP equations determine the evolution of the PDFs with the energy transfer, the x-dependence can only be determined by data.

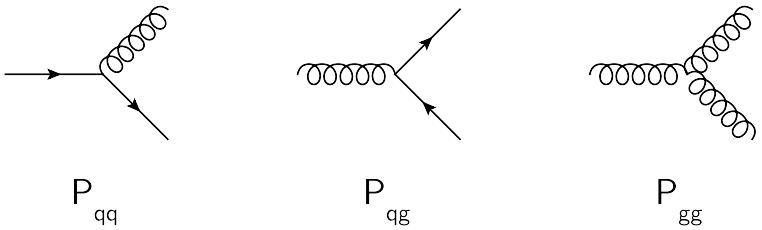

Figure 1.4: LO contributions to the DGLAP splitting kernels.

1.5 Higher order QCD calculations

The matrix element in equation (1.14) has a perturbative expansion in α_s. Going beyond the lowest order contributing to a given process corresponds to the emission or emission and re-absorption of gluons, as shown in Figure 1.5. In the usual nomenclature, the tree-level contributions (containing no loops) are referred to as the Born contributions. Real emission diagrams at N^{k}LO correspond to the emission of k gluons, while virtual diagrams correspond to the inclusion of k loops.

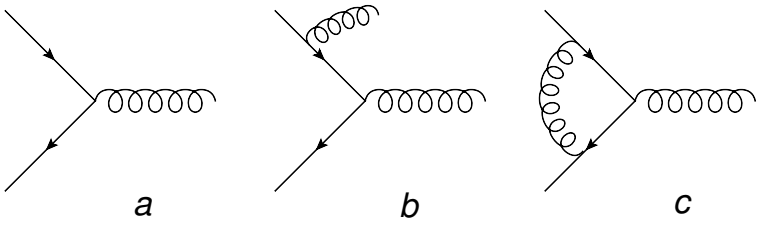

Figure 1.5: Example of Born (a), Real (b) and Virtual (c) Feynman diagrams.

One can symbolically write the parton-level cross-section at NLO accuracy as

$$\hat{\sigma}^{NLO} = \int_n d\hat{\sigma}^B + \int_{n+1} d\hat{\sigma}^R + \int_n d\hat{\sigma}^V, \tag{1.21}$$

with $d\hat{\sigma}^B, d\hat{\sigma}^R, d\hat{\sigma}^V$ representing the LO (Born), real and virtual contributions respectively and the integration subscripts representing the number of partons in the final state. It is evident from Figure 1.5 that the virtual diagrams are physically indistinguishable from the Born ones and thus the corresponding contribution to the cross section will be given by the interference of the two terms

$$d\hat{\sigma}^V = d\Phi_n \sum 2\mathrm{Re}\left(\mathcal{M}_1^V \mathcal{M}_0^*\right), \tag{1.22}$$

where the sum runs over all possible 1-loop contributions and the subscripts 1 and 0 refer to the NLO and LO matrix elements respectively., while $d\Phi_n$ denotes the n-particle final state phase-space. The corresponding contributions from the real emissions read

$$d\hat{\sigma}^R = d\Phi_{n+1} \sum \left|\mathcal{M}_1^R\right|^2. \tag{1.23}$$

The NLO contributions involve three types of divergences: *ultraviolet divergences* from the $p \to \infty$ limit of the loop integrals in the virtual contributions[8], *infrared divergences* from the $p \to 0$ limit of loop diagrams and the emission of soft gluons in the real contributions and *collinear divergences* coming from real emission diagrams which involve branchings between three massless partons. These divergences are not physical but signal the breakdown of perturbation theory. It has been formally established by the Bloch-Nordsieck and Kinoshita-Lee-Nauenberg theorems [60–62], that sufficiently inclusive quantities are finite in the massless limit. Ultraviolet divergences are regularized and absorbed in the running of the coupling constant. Infrared divergences cancel exactly between the real, collinear and virtual contributions in the final state[9]. Collinear singularities in the initial state do not cancel after summing the different contributions and have thus to be absorbed in the PDFs by virtue of the factorization theorem.

In order to deal with these divergences within perturbation theory, we need to introduce non-physical scales (cf. equation (1.15), equation (1.20)). If one retains all the orders of the perturbative expansion these scale dependencies cancel out, since physical observables do not depend on non-physical scales. However, truncating the perturbative expansion at a certain order introduces a dependence on these scales, which becomes smaller as the accuracy of the matrix element calculation increases.

[8] Here p is a 4-momentum and the limit is to be understood component-wise.
[9] For technical details see e.g. [49].

In order understand this statement, consider a dimensionless physical observable $\mathcal{O}$, which after renormalization acquires a dependence on Q^2/μ^2, where Q is a large energy scale and $\alpha_s(\mu^2)$ is the renormalized strong coupling constant. The perturbative expansion of $\mathcal{O}$ reads

$$\mathcal{O}\left(\frac{Q^2}{\mu^2}=1,\alpha_s(Q^2)\right)=\mathcal{O}_1\alpha_s(Q^2)+\mathcal{O}_2\alpha_s^2(Q^2)+\dots. \tag{1.24}$$

From (1.16) we have

$$\alpha_s(Q^2)=\alpha_s(\mu^2)-b_1\ln\frac{Q^2}{\mu^2}\alpha_s^2(\mu^2)+\dots, \tag{1.25}$$

where $b_1=\frac{1}{4\pi}\left(11-\frac{2N_f}{3}\right)$. Thus (1.24) becomes

$$\mathcal{O}\left(1,\alpha_s(Q^2)\right)=\mathcal{O}_1\alpha_s(\mu^2)+\left(\mathcal{O}_2-\mathcal{O}_1b_1\ln\frac{Q^2}{\mu^2}\right)\alpha_s^2(\mu^2)+\dots. \tag{1.26}$$

We see thus that the LO expansion $\mathcal{O}\left(1,\alpha_s(Q^2)\right)=\mathcal{O}_1\alpha_s(\mu^2)$ gives no information on the absolute normalization, since $\alpha_s(\mu)$ can take any value by changing the value of μ. Beginning at NLO, the μ dependence of $\ln\frac{Q^2}{\mu^2}$ starts to compensate the μ dependence of α_s and we can thus obtain information about the absolute normalization while also reducing the scale dependence of $\mathcal{O}$. Moreover, at NLO, new channels that are inaccessible at LO can open up leading to non-trivial distributions for observables that are trivial at LO.

1.6 The Parton Shower approach

Parton showers are an integral part of the simulation of a high energy particle collisions and are based on the description of independent subsequent parton branchings that occur as the partons' energies evolve from the collision scale down to the hadronization scale. Radioactive decay provides a familiar context for understanding the physics of the parton showers. In radioactive decays, the probability for a decay to happen at time t is proportional to the number of radioactive particles N, which obeys the

differential equation

$$\frac{dN(t)}{dt} = -\Gamma(t)N(t), \tag{1.27}$$

with Γ known as the decay width (in particle physics) or the decay constant in nuclear physics. The probability of having no decay in the time interval $[t_1, t_2]$ is given by

$$P_{\text{no-decay}}(t_1, t_2) = \exp\left[-\int_{t_1}^{t_2} dt\, \Gamma(t)\right] \equiv \Delta(t_1, t_2). \tag{1.28}$$

The function $\Delta(t_1, t_2)$ is known as the Sudakov form factor. In a parton shower, one encounters the same underlying process, with radioactive decays at times t being replaced by gluon emissions at energy scales t. The emission probability in a parton shower is proportional to the DGLAP splitting kernels, so extending equation (1.28) to the case of the parton shower, we obtain [49]

$$P_{\text{no-emission}}(t_1, t_2) = \exp\left\{-\sum_j \int_{t_1}^{t_2} \frac{dt}{t}\frac{\alpha_s(t)}{2\pi}\int dz P_{ij}(z)\right\} \equiv \Delta(t_1, t_2). \tag{1.29}$$

This obeys the evolution equation

$$t\frac{\partial}{\partial t}\left(\frac{f}{\Delta}\right) = \frac{1}{\Delta}\int \frac{dz}{z}\frac{\alpha_s}{2\pi}P(z) f\left(\frac{x}{z}, t\right), \tag{1.30}$$

which is nothing other but the DGLAP equation (1.20) with the substitution $f \to f/\Delta$. Integrating (1.30) and expanding the solution we obtain

$$\begin{aligned} f(x,t) &= \Delta(t) f(x, t_0) + \int_{t_0}^{t} \frac{dt'}{t'}\frac{\Delta(t)}{\Delta(t')}\int \frac{dz}{z}\frac{\alpha_s}{2\pi}\hat{P}(z) f\left(\frac{x}{z}, t'\right) \\ &= \Delta(t) f(x, t_0) + \int_{t_0}^{t} \frac{dt'}{t'}\frac{\Delta(t)}{\Delta(t')}\int \frac{dz}{z}\frac{\alpha_s}{2\pi}\hat{P}(z) \\ &\times \left[\Delta(t') f\left(\frac{x}{z}, t_0\right) + \int_{t_0}^{t'} \frac{dt''}{t''}\frac{\Delta(t')}{\Delta(t'')}\int \frac{dz}{z}\frac{\alpha_s}{2\pi}\hat{P}(z) f\left(\frac{x}{zz'}, t''\right)\right] \\ &+ \ldots \end{aligned} \tag{1.31}$$

with the integrals giving rise to logarithmic terms $\ln \frac{t}{t_0}$. Equation (1.31) is an exponential expansion containing an infinity of terms of order $\left(\frac{\alpha_s}{2\pi}\ln\frac{t}{t_0}\right)^n$. The parton shower corresponds therefore to an all-order calculation. We stress that the above equations are strictly only valid in the limit of small-angle gluon emission. As a consequence,

although the Sudakov region is correctly described by the parton shower, hard/wide-angle emissions will not be correctly described and one would have to resort to an exact matrix element calculation for those.

1.7 Matching and merging ME and PS calculations

From the previous discussion it should be clear that there are two different approaches for the calculation of observables in hadron collisions: the matrix element approach which relies on perturbative calculations performed at a given fixed order and the parton shower approach which includes all-order contributions in the collinear limit. The two approaches are complementary in the sense that in the soft/collinear region, where the parton shower approach is valid, the matrix-element calculation breaks down due to the appearance of large logarithms, while in the hard/wide-angle emission region, where the matrix-element calculation provides a good description, the approximations involved in the parton shower approach become invalid.

Combining the ME with the PS calculations offers the advantages of both approaches, extending the validity of the perturbative calculations to the whole of the phase space, as well as allowing to make the ME predictions exclusive and interface them to hadronization generators. While combining LO matrix elements with parton showers poses no difficulty, from NLO onwards, ambiguities start to arise due to the multiple counting of certain configurations, as illustrated in Figure 1.6. For instance a $(N+1)$-jet event can be obtained both from a NLO correction to a N-jet event and from extra emissions added by the parton shower to the N-jet event. The same problem arises also when attempting to merge LO+PS calculations of different final state particle multiplicities.

Several schemes have been constructed that allow for the matching of NLO calculations with parton showers and for the merging of LO+PS calculations with different final state particle multiplicities, avoiding the double counting problem, as explained in the following.

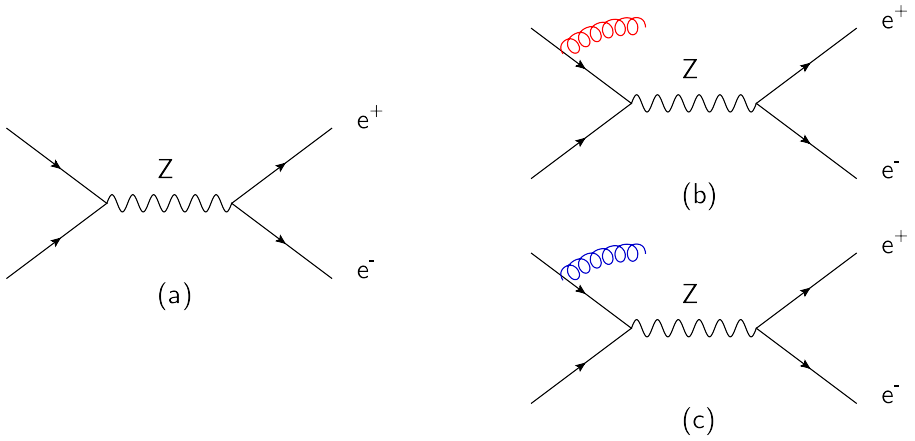

Figure 1.6: Schematic illustration of the double counting problem in the matching and merging of ME and PS calculations. Figure (a) illustrates a LO Feynman diagram of a $pp \to e^+e^-$ process. Figure (b) represents a possible configuration that may result from propagating the event in Figure (a) through a parton shower algorithm. Figure (c) represents a real emission (NLO) correction to the diagram in Figure (a) and corresponds to the same configuration as the one obtained from the parton shower (Figure b). Therefore naïvely matching NLO computations to parton showers results in a double counting of configurations. Alternatively Figure (c) can be thought of as the LO contribution to the $pp \to e^+e^-$+1 jet process, therefore merging LO+PS calculations with different final state particle multiplicities also results in the double counting of certain configurations.

Merging LO+PS calculations with different final state particle multiplicities

There are three schemes for merging LO matrix-element calculations interfaced to parton showers: CKKW [63], CKKW-L [64] and MLM [65]. The fundamental concept of these merging schemes is the partitioning of the phase space into two regions with the use of a transition scale y_{ini} defined by a given jet measure y. If y_{cut} is the resolution variable of a given jet algorithm, then for $y_{\text{cut}} > y_{\text{ini}}$ the observables are taken from matrix elements modified by Sudakov form factors, while for $y_{\text{cut}} < y_{\text{ini}}$ the observables are taken from the parton showers subjected to a veto procedure. In more detail, the different merging schemes follow the same basic procedure

1. definition of a jet measure y and calculation of the cross sections for the processes $pp \to X + n-$jets with $n = 0, 1, \ldots, n_{\text{max}}$. Typical examples include the jet radius used in the Alpgen implementation of the MLM matching and the k_T distance used in CKKW matching.

2. generation of hard partons with a probability proportional to the total cross section and a kinematic configuration given by the matrix element
3. acceptance or rejection of the configuration with a probability that includes Sudakov and running coupling effects
4. parton showering with a 'veto' that rejects events with extra jets

The differences between the merging schemes lie in

- the definition of the jet measure
- the way the acceptance/rejection of step (2) above is carried out
- the initial conditions for the parton shower algorithms and the application of the 'veto'.

A comparative study of the aforementioned merging algorithms was performed in [66].

Matching NLO calculations with parton showers

There are two methods for matching NLO matrix elements with parton showers, dubbed MC@NLO [67] and POWHEG [67, 68]. In both of these methods, the emission with the highest p_T is taken from the NLO matrix element (with the shower approximation subtracted) and the following emissions are taken from the parton shower and are thus only reliable in the collinear limit.

An observable calculated with NLO+PS accuracy can be schematically written as

$$\begin{aligned}\langle \mathcal{O} \rangle_{NLOPS} &= \int d\Phi_n \bar{B}(\Phi_n) \left\{ \mathcal{O}(\Phi_n)\Delta_{t_0} + \int d\Phi_r \mathcal{O}(\Phi_n, \Phi_r)\Delta_t \frac{R(\Phi_n, \Phi_r)}{B(\Phi_n)} \right\} \\ &+ \int d\Phi_{n+1} \mathcal{O}(\Phi_{n+1}) \left[R(\Phi_{n+1}) - R^s(\Phi_{n+1}) \right], \end{aligned} \tag{1.32}$$

with

$$\begin{aligned}\bar{B}(\Phi_n) &= B(\Phi_n) + V(\Phi_n) + \int d\Phi_r \left[R(\Phi_n, \Phi_r) - C(\Phi_n, \Phi_r) \right], \\ \Delta_t &= \exp\left[- \int d\Phi'_r \frac{R(\Phi_n, \Phi'_r)}{B(\Phi_n)} \theta(t' - t) \right]. \end{aligned} \tag{1.33}$$

In the above equations, B, V, R are the Born, virtual and real emission matrix elements multiplied by the PDFs, R^s is the the real emission contribution in the soft and collinear

limit and Φ_n, Φ_r parametrize the phase space which has n final state particles in the case of the Born and virtual contributions and $n+1$ particles in the case of the real emission contributions. The last term in (1.32) is the so-called *matrix element correction*, which provides the hard, large-angle contribution to the hardest emission calculated from the NLO matrix element.

Some comments are in order with respect to the specific implementation of the NLOPS formalism in the POWHEG and MC@NLO approaches. The first term of (1.32) $\bar{B}(\Phi_n)d\Phi_B$ is what is called a $\mathbb{S}$ event (for Standard MC evolution) and the last term $[R(\Phi_{n+1}) - R^s(\Phi_{n+1})]d\Phi_{n+1}$ is called a $\mathbb{H}$ event (for Hard MC evolution). In MC@NLO the difference $R(\Phi_{n+1}) - R^s(\Phi_{n+1})$ can become negative, thus leading to the appearance of events with a negative weight. In POWHEG on the other hand, one has a freedom to choose a parametrization $R^s(\Phi_{n+1}) = R(\Phi_{n+1})F(\Phi_{n+1})$ with $0 \leq F(\Phi_{n+1}) \leq 1$ and $F(\Phi_{n+1}) \to 1$ in the soft and collinear limit. Thus $R(\Phi_{n+1}) - R^s(\Phi_{n+1}) = R(\Phi_{n+1})[1 - F(\Phi_{n+1})] \geq 0$. Another difference with MC@NLO is that the part within the curly braces in (1.32), which corresponds to the hardest emission, is generated within POWHEG and is thus independent of the showering generator. Finally, we note that although the two approaches are equivalent at NLO, differences may arise at NNLO.

1.8 The Monte-Carlo method for event generation

Hadron collisions typically involve the production of multi-particle final states, therefore the computation of observables for hadron collider experiments involves multi-dimensional integrations over the final-state phase space. These integrals are almost always impossible to compute analytically and one has to resort to numerical methods. One of the most popular methods is the Monte-Carlo technique. The Monte-Carlo technique is based on the approximation of an integral as follows

$$I = \int_{x_1}^{x_2} f(x)dx = (x_2 - x_1)\,\langle f(x)\rangle \approx (x_2 - x_1)\frac{1}{N}\sum_{i=1}^{N} f(x_i). \tag{1.34}$$

The approximate equality becomes exact in the limit $N \to \infty$. Using this approximation for the cross-section one gets

$$\sigma = \int_0^1 dx \frac{d\sigma}{dx} \approx \frac{1}{N} \sum_{i=1}^{N} \left. \frac{d\sigma}{dx} \right|_i , \tag{1.35}$$

where x is an arbitrary parametrization of the phase space chosen so that the boundaries lie at $x = 0, 1$. The differential cross section $\left. \frac{d\sigma}{dx} \right|_i$ is called the *weight* of the event parametrized by x_i. After calculating the cross section for a process, one wants to go one step further and simulate physical events as they occur in nature, i.e. generate a set of 4-momenta distributed according to the dynamical laws governing the process under study. This step is called *event generation*. In a mathematical language the event generation amounts to choosing a value $x \in [x_{\min}, x_{\max}]$ distributed according to $f(x)$ or equivalently to selecting uniformly (x, y) in $x_{\min} < x < x_{\max}, 0 < y < f(x)$. In the case where the primitive F of f is known, the problem can be solved analytically by noting that

$$\int_{x_{\min}}^{x} f(x')dx' = R \int_{x_{\min}}^{x_{\max}} f(x')dx'. \tag{1.36}$$

Then

$$x = F^{-1} \left[F(x_{\min}) + R A_{tot} \right], \tag{1.37}$$

where $A_{tot} = \int_{x_{\min}}^{x_{\max}} f(x)dx$. In most of the cases, F is unknown and the problem is tackled using the *hit-and-miss* technique. The hit-and-miss algorithm proceeds as follows

1. generate two random numbers R, R' uniformly[10] distributed in $(0, 1)$
2. calculate $x = x_{\min} + R(x_{\max} - x_{\min})$ and $y = R' f_{\max}$
3. if $y < f(x)$ accept the event (hit), else go to (1)

One can write

$$I = \frac{\int_{x_{\min}}^{x_{\max}} f(x)dx}{f_{\max}(x_{\max} - x_{\min})} \Omega = \frac{N_{hit}}{N_{try}} \Omega, \tag{1.38}$$

[10] Many recent integration algorithms do not use uniform sampling.

where $\Omega = f_{\max}(x_{\max} - x_{\min})$ and N_{hit}, N_{try} is the number of hits and number of total tries respectively. Then the integral of a function can be computed by

$$\int_{x_{\min}}^{x_{\max}} f(x)dx = f_{\max}(x_{\max} - x_{\min})\frac{N_{hit}}{N_{try}}. \tag{1.39}$$

Thus the probability of a hit is proportional to $f/f_{\max}$. Performing the hit-and-miss technique on a sample of events generated with a uniform sampling over the phase space (*weighted events*) gives a final sample of events which occur with the same probability as in nature (*unweighted events*). The probability for an event to be accepted by the hit-and-miss technique is $\frac{(d\sigma/dx)_i}{(d\sigma/dx)_{\max}}$ while the unweighting efficiency is given by $\frac{(d\sigma/dx)_{ave}}{(d\sigma/dx)_{\max}}$.
This procedure has been automated by codes that are collectively called Monte-Carlo generators. These are separated into two categories: *cross-section integrators*, which calculate cross sections for specific processes, and *event generators*, which generate weighted and unweighted events and can thus be used for simulating physical processes, as described in the following section.

1.9 Structure of a simulated pp collision

The simulation of a pp collision in Monte-Carlo event generators is a multistep process, as depicted in Figure 1.7. The simulation starts from the calculation of the matrix element for the process of interest, referred to as the "hard scattering" (e.g. $pp \to t\bar{t}$), based on the perturbative QFT machinery that was described in Section 1.2[11].

The incoming and outgoing partons involved in the hard scattering process are produced with energies which are usually much higher than the hadronization scale $Q_{\text{had}} \simeq 1$ GeV. After the simulation of the hard scattering process, the phase-space from the scale of the hard scattering down to a cut-off scale $Q_0 \simeq Q_{\text{had}}$ is filled with partons mostly from soft and collinear parton branchings, simulated by the initial and final state parton shower algorithms, as discussed in Section 1.6.

An important aspect in the simulations of hadronic collisions is the description of multiple parton interactions (MPI), i.e. the scattering of multiple pairs of partons from the same pair of protons that take part in the hard scattering event. The necessity

[11] More efficient methods than the traditional Feynman diagram approach are being actively developed [69] and used in event generators such as SHERPA [70] and ALPGEN [71].

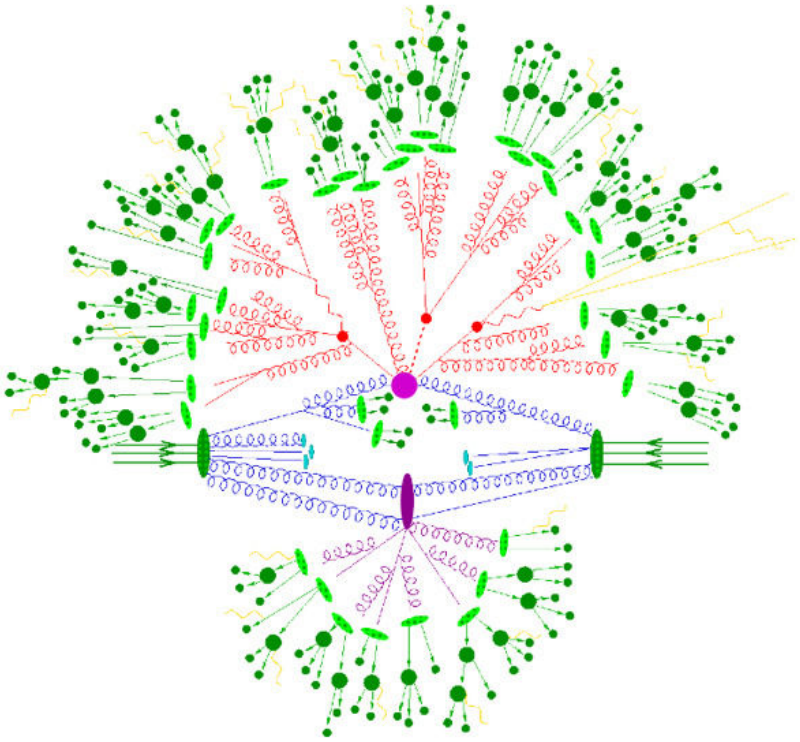

Figure 1.7: Typical structure of a hadron collision event with different steps in the event generation chain. The big magenta circle represents the hard scattering. Initial and final state parton showers are representaed with blue and red respectively. The light green blobs correspond to the hadronization stage, where colorless combinations of partons are formed and subsequent hadron decays are depicted in dark green. The purple ellipse depicts additional MPIs and the teal blue blobs represent the hadronization of the beam remnants. [72]

for the introduction of MPIs in event generators arises from the observation that the parton-level cross-section for a $2 \to 2$ QCD scattering behaves like [73]

$$\sigma_{\text{hard}}(p_{T,\text{min}}) \propto \frac{1}{p_{T,\text{min}}^2} \overset{p_{T,\text{min}} \longrightarrow 0}{\longrightarrow} \infty, \tag{1.40}$$

therefore $\sigma_{\text{hard}}(p_{T,\text{min}})$ becomes bigger than the total inelastic pp cross-section $\sigma_{\text{inel}}^{pp}$ at a certain energy scale. The paradox is resolved by postulating that more than one $2 \to 2$ scatterings take place in the single event, with the average number given by

$$\langle n \rangle (p_{T,\text{min}}) = \frac{\sigma_{\text{hard}}(p_{T,\text{min}})}{\sigma_{\text{inel}}^{pp}}. \tag{1.41}$$

The existence of multiple parton scatterings was first established experimentally by the AFS collaboration at CERN, which measured 4-jet events, in which the sum of the p_T of the jets would sum up to 0 for each of the two pairs of jets [74]. Additionally the forward-backward correlations in the charged particle multiplicities observed by the UA5 [75] and E735 [76] collaborations provided strong evidence for the existence of MPI. The simulation of MPI has thus become an integral part of the modern event generators. Different implementations exist, with the most widely used being the one in PYTHIA and the one in HERWIG. The PYTHIA MPI model is based mostly on perturbative $2 \to 2$ QCD scatterings, with the most recent implementation allowing for a wider array of processes to be included in the MPI [77]. The partons from the MPI are handled by the showering and hadronization machinery in the same way as the partons from the hard scattering. The HERWIG MPI model[12] is based on an eikonal model, which assumes that at fixed impact parameter b, the different MPI are independent, following a Poisson distribution with variance $A(b)\sigma_a$, where σ_a is the parton-parton cross-section and $A(b)$ is a function which describes the distribution of partons in the impact-parameter space. Both the PYTHIA and HERWIG models are thus based on a mixture of first-principle calculations and phenomenological models which are tuned to data via a set of tunable parameters.

After the parton showers have evolved the partons from the hard scattering process and the MPIs down to the cut-off scale, the strong coupling constant becomes so large (cf. Figure 1.3) that perturbation theory is no longer valid and the subsequent step of the confinement of the partons into colorless hadrons must be based on phenomenological models. The hadronization process is modeled in two distinct ways in the general-purpose Monte-Carlo generators: the cluster model employed by HERWIG and SHERPA and the string model used in PYTHIA. In the cluster model [79], the final state quarks and anti-quarks[13] are assigned to colorless combinations, called clusters. The clusters are then decayed isotropically into two hadron final states. In the string model [80] the force between $q\bar{q}$ pairs is described by the dynamics of a massless relativistic string. Quarks and antiquarks form the endpoints of a string, while gluons are described as string kinks. In analogy with the electron-positron pair creation in the presence of a strong electric field (Schwinger effect), the strong color force field of the string allows for virtual quark-antiquark pairs to tunnel out of the vacuum, breaking the string into segments, with the invariant mass of the string segments corresponding to the masses of the known hadron spectrum. The cluster model uses

[12] In the older HERWIG versions, the modeling of MPI was provided via JIMMY [78].
[13] Any gluons remaining after the parton shower step are split into quark-anti-quark pairs.

less free parameters than the string model, however it has problems in dealing with the decays of heavy clusters and suppressing baryon and heavy hadron production. The string model, on the other hand, offers a better description of the heavy particle and baryon production, at the cost of the introduction of additional free parameters, that have to be tuned to data.

General-purpose event generators such as the PYTHIA [81, 82] and HERWIG [83, 84] families as well as SHERPA [72] simulate all of the aforementioned stages. Specialized event generators, dedicated to the simulation of only a certain part of a pp collision, are also used, particularly when a higher accuracy than the one provided by the general-purpose generators is needed. Typically the matrix elements for the hard subprocess are calculated with specialized generators with a higher accuracy than what is achievable with the general-purpose generators and are the latter are used for the simulation of the subsequent steps.

1.10 Jets and Jet Algorithms

The parton shower evolution induces sequential parton branchings which are forced to self-collimate with the parent partons, as a consequence of color coherence. After hadronization, this will produce a collimated bunch of hadrons, which is called a jet. There are different ways in which one can define a jet, which are known as jet algorithms. These have to obey to a minimal set of rules [85].

Jet algorithms can be classified into two broad categories: *cone algorithms* and *sequential recombination algorithms*. Cone algorithms use conical structures to cluster particles within a certain angular distance, so that the sum of the clustered particle momenta coincides with the cone axis. Sequential recombination algorithms start by identifying the closest particles according to some distance measure, recombine them and iterate the procedure until a stopping criterion is reached. Here we will only describe a certain class of sequential recombination algorithms that are used for the studies reported here.

A very important property that a jet algorithm must satisfy is the *Infrared and Collinear* (IRC) *Safety*, which states that the set of hard jets in an event should be insensitive to a collinear splitting or a soft emission. As we have already seen, collinear and soft gluons lead to divergences in perturbation theory, whose cancellation depends

on the correct summation of the real and virtual contributions of the corresponding process. The situation might change in the case of IRC unsafe algorithms as illustrated in Figure 1.8: IRC unsafe algorithms can lead to different classes of events for real and virtual contributions, thus spoiling the cancellation of their divergences. The use of IRC safe algorithms also leads to a reduced sensitivity to hadronization effects. The

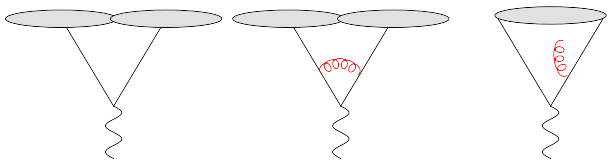

Figure 1.8: Illustration of IRC unsafety. The addition of a soft gluon changes the number of hard jets, spoiling the cancellation between real and virtual contributions.

Cambridge/Aachen, k_t and anti-k_t algorithms are based on the generalized distance measures [86]

$$\begin{aligned} d_{ij} &= \min\left(k_{ti}^{2p}, k_{tj}^{2p}\right)\frac{\Delta R_{ij}^2}{R^2} \\ d_{iB} &= k_{ti}^{2p} \\ \Delta R_{ij}^2 &= (y_i - y_j)^2 + (\phi_i - \phi_j)^2, \end{aligned} \tag{1.42}$$

where k_{t_i}, y_i, ϕ_i are the transverse momentum, rapidity and azimuth of particle i, d_{ij} and d_{iB} are the distances between the entities i and j and the distance between entity i and the beam respectively. The parameter R, also known as the radius parameter of the jet can be freely chosen and is usually taken to be in the range $0.4 \lesssim R \gtrsim 1$ [87]. The parameter p takes the values

$$p = \begin{cases} 1 & k_t \\ 0 & \text{Cambridge/Aachen} \\ -1 & \text{anti-}k_t \end{cases} \tag{1.43}$$

The clustering algorithm starts by identifying the smallest of the distances d_{ij}, d_{iB} and recombining i and j if d_{ij} is the smallest distance or defining i as a jet and removing it from the list of entities if d_{iB} is the smallest distance. This procedure is iterated until no entities are left. It is evident that soft and collinear emissions will be clustered right at the beginning of the clustering procedure and thus the k_t family of jet algorithms is IRC safe. It has been shown [86] that the choice $p = -1$ favors clustering around

hard particles, as opposed to the k_t algorithm which favors soft-particle clusterings or the Cambridge/Aachen algorithm which favors energy-independent clusterings. As a result anti-k_t gives circular hard jets (as opposed to irregularly shaped jets obtained with k_t and Cambridge/Aachen - cf. Figure 1.9) which is an appealing property for experimental jet reconstruction.

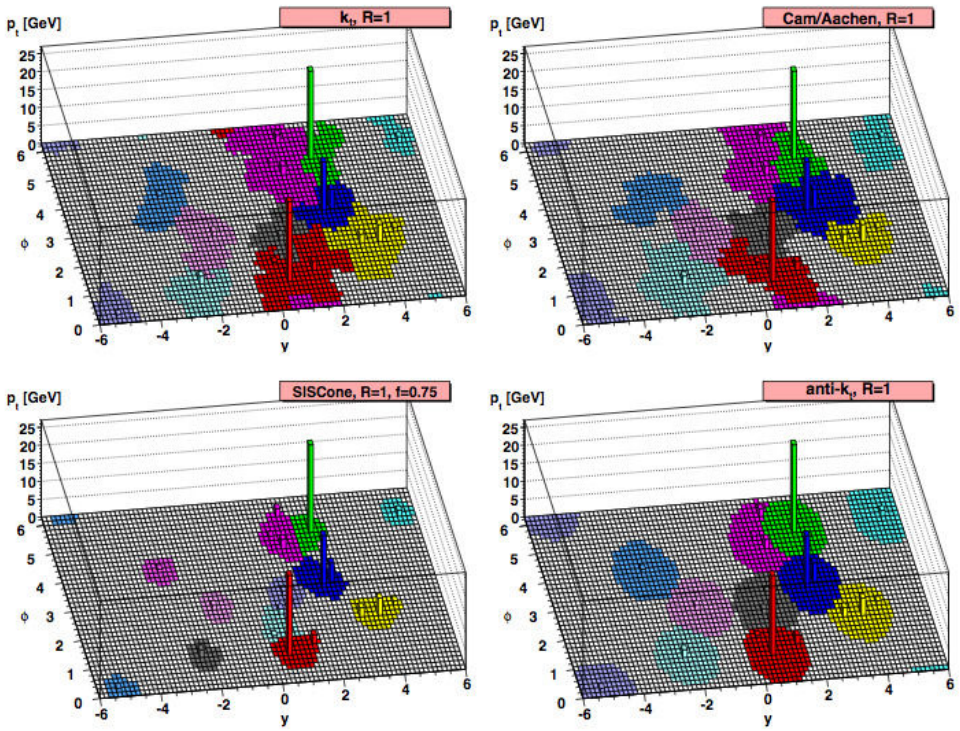

Figure 1.9: Parton-level jets with soft "ghosts" reconstructed with different jet algorithms [86].

Jet algorithms play a fundamental role in facilitating comparisons between theoretical calculations and experimental measurements. At LHC energies, the pp collisions produce hundreds of final state hadrons, which leave electronic signals in the detectors. Jet algorithms allow to cluster the electronic signals in the detectors and the final state hadrons in Monte-Carlo simulations, thereby reducing the complexity of the final state and enabling direct comparisons between experiment and theory.

Chapter 2

$t\bar{t}b\bar{b}$ production in the Standard Model

In the dilepton channel, the experimental signature for $t\bar{t}b\bar{b}$ consists of four b-jets, two leptons and missing transverse energy:

$$pp \to t\bar{t}b\bar{b} \to W^+bW^-\bar{b}b\bar{b} \to b\bar{b}b\bar{b}l^+\nu_l l^-\bar{\nu}_l. \tag{2.1}$$

From (2.1) we observe that $t\bar{t}b\bar{b}$ poses several challenges:

- $t\bar{t}b\bar{b}$ **is a process of extreme complexity**; the presence of 8 particles in the final state implies the existence of many partonic channels (Figure 2.1), which renders the calculation of the full process intractable for most Monte-Carlo generators. Therefore, although the experimental measurement is sensitive to all of these channels, as well as their interference, Monte-Carlo generators are usually only able to compute the double resonant diagrams (diagrams that contain two top quark propagators that can become resonant[1]) at $\mathcal{O}(\alpha_s^4)$, whereby the top is considered stable and interference effects are ignored.

- $t\bar{t}b\bar{b}$ **is very sensitive to the scale choice**; the lowest order contributions to the cross-section are

$$\sigma^{\text{LO}}_{t\bar{t}b\bar{b}} = \mathcal{O}(\alpha_s^{8-2k}\alpha^{2k}), \tag{2.2}$$

  where α is the electroweak coupling constant and $2 \leq k \leq 4$. Ignoring the top decay, and considering only the pure QCD terms (i.e. taking $k = 2$ in equation (2.2)), we can see that the LO contributions are proportional to α_s^4. A

[1] A top quark propagator becomes resonant when the 4-momentum of the top quark tends to the top quark mass, i.e. the top quark goes on-shell.

change of the scale at which α_s is calculated, yields according to equation (1.16):

$$\frac{\sigma^{\text{pure QCD,LO}}_{t\bar{t}b\bar{b}}(\alpha_s(Q^2))}{\sigma^{\text{pure QCD,LO}}_{t\bar{t}b\bar{b}}(\alpha_s(\mu^2))} = \left[\frac{\alpha_s(Q^2)}{\alpha_s(\mu^2)}\right]^4 = \left[\frac{1}{1+b_1\alpha_s(\mu^2)\ln\frac{Q^2}{\mu^2}}\right]^4. \tag{2.3}$$

At higher orders, the scale-dependence of the cross-section is lessened, however NLO calculations still exhibit a scale uncertainty of the order of 30% [88–90].

- $t\bar{t}b\bar{b}$ **contains multiple scales, thus being prone to perturbative instabilities**; the final state contains two explicit scales, the top and the bottom quark masses, with $\Lambda_{\text{QCD}} \ll m_b \ll m_{\text{top}}$. The presence of multiple scales introduces logarithms $\ln\frac{Q^2}{m_b^2}$, which can spoil the convergence of the perturbative expansion [5].

Monte-Carlo generators employ different approximations and calculation schemes, in order to overcome the above complications. This is discussed in the following sections.

2.1 Calculation of $t\bar{t}b\bar{b}$ in Monte-Carlo generators

The state-of-the-art Monte-Carlo generators can handle processes containing up to 5-6 partons at LO, however at NLO, 4-parton final states are at the border of what can be technically achieved. For the study of complicated processes, such as $t\bar{t}b\bar{b}$, one usually makes several approximations that reduce the complexity of the calculation, although at the cost of restricting the domain of validity of the results.

One approach is to calculate the matrix elements only for the $pp \to t\bar{t}$ process and let the parton shower simulate the additional b-quarks. NLO precision in the matrix element calculation is easily attainable with the current generators and spin correlations in the top decays can also be added with approximate methods [91]. The most important drawback of this approach is that the extra b-quark kinematics are calculated correctly only in the soft/collinear limit. Since we expect the additional b-quarks to be produced mostly in this region, this approach is well-motivated, however better approximations exist.

An improvement with respect to the previous approach is to calculate the matrix elements for the full $pp \to t\bar{t}b\bar{b}$ process, matching the calculation to a parton shower. LO matrix elements can easily be calculated with the current generators. Furthermore,

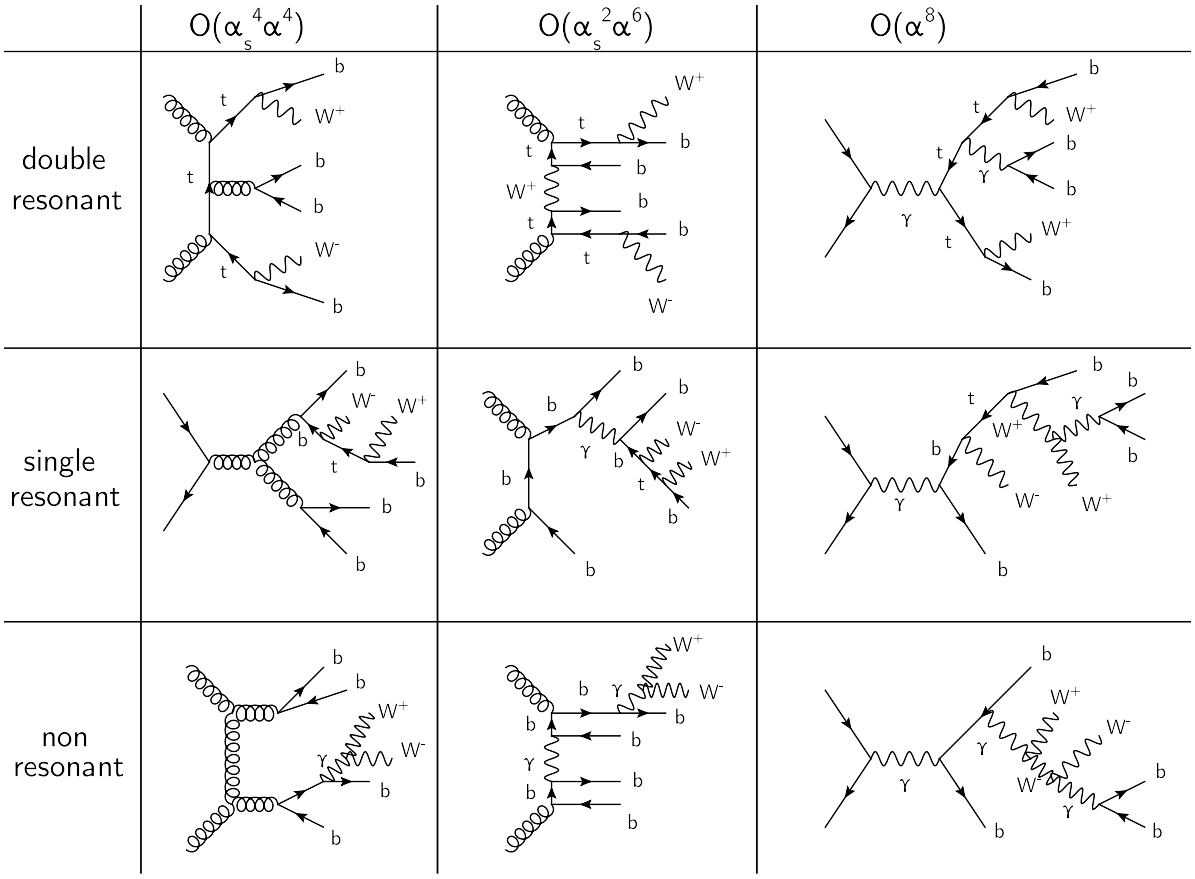

Figure 2.1: Leading order diagrams for $pp \to b\bar{b}b\bar{b}W^+W^-$ in the Standard Model. The decays of the W's are not shown, however both W's are implicitly assumed to decay leptonically. The three columns show contributions to the cross-section at different orders in the strong and electroweak coupling and the three rows display diagrams with two, one or no top propagators which can become resonant. Only the double resonant $\mathcal{O}(\alpha_s^4\alpha^4)$ contributions are usually generated by Monte-Carlo generators, with the top and W decays performed by the parton shower.

different LO samples corresponding to $t\bar{t} + N$ jets, with $N \leq 3$ can be merged, increasing the accuracy of the calculation. NLO matrix elements for $pp \to t\bar{t}b\bar{b}$ have been computed in [90, 92, 93] and implementations matched to parton showers [94–96] have become available in dedicated generators, such as POWHEL [94] or in automated ones such as MADGRAPH5_AMC@NLO [97]. These offer the most accurate predictions for the $t\bar{t}b\bar{b}$ process that is attainable with the current generators.

Even in the context of $t\bar{t}b\bar{b}$ matrix element calculations, there are several approximations that are involved. The most common one is to assume that only the pure QCD double resonant diagrams (see Figure 2.1) contribute to the cross-section and

neglect the rest of the contributions and their interference. This approximation is used in all of the Monte Carlo samples under consideration in this thesis.

The full calculation with 4 b-jets and the W decay products in the final state has been performed in [98] for semi-leptonic top decays. This calculation includes all of the contributions displayed in Figure 2.1 as well as their interference. The calculation showed that the QCD production of $t\bar{t}b\bar{b}$ gives the dominant contribution to the full process, with the mixed QCD/EW terms being half as large and the pure EW terms being negligible. Moreover the interference between the different contribution leads approximately to a 5% reduction of the cross-section. It has to be noted that while these results were obtained for semi-leptonic top decays, it is expected that they hold qualitatively for the di-lepton channel as well. Quantitative differences may arise however, particularly for the non-resonant contributions.

Another approximation which is commonly used is to neglect the masses of the b-quarks in the matrix element calculation and in the parton shower. The following sections deal with this approximation and its effect on the predicted cross-section.

2.2 4 and 5-flavor calculations

Calculations involving bottom quarks are typically performed in two schemes, differing by the treatment of the bottom quark mass. The first scheme is referred to as "massive" or 4-flavor scheme (4FS). In this scheme it is assumed that the bottom mass is significantly bigger than the proton mass and therefore the bottom quark can only appear in the final state. In that case the proton PDF consists only of 4 flavors (u, d, s, c) with the bottom PDF set to zero. In this scheme, the b-quark enters neither in the evolution of the PDFs nor in the evolution of the coupling constant.

The second scheme is referred to as the "massless" or 5-flavor scheme (5FS). In this scheme, one assumes that $m_b = 0$, an approximation which is valid in the case where the bottom mass is significantly smaller than the other scales of the interaction. In this case the proton PDFs contain 5 flavors (u, d, s, c, b) and the bottom parton density enters both in the PDF evolution equations as well as in the evolution of the coupling constant.

The above schemes are complementary, in the sense that they have advantages and shortcomings depending on the observable under study. More specifically, in the

5FS, the number of external legs and the number of the scales involved is reduced, compared to the 4FS, as shown in Figure 2.2. This allows higher order calculations to be performed more easily in the 5FS than in the 4FS. Additionally, in the 5FS, logarithms of the type $\ln \frac{Q^2}{m_b^2}$ are resummed by the evolution of the b-PDF, thereby leading to a more accurate prediction of the overall interaction rate and an improved stability of the calculation with respect to scale variations. The drawback of the 5FS is that it gives a less precise description of the b-quark kinematics than the 4FS at any given order. Consequently, while the 5FS is better suited for inclusive cross-section calculations, it performs worse in the description of more exclusive final states, particularly when cuts on b-jet kinematics are imposed. Moreover since the amplitude for $g \to b\bar{b}$ diverges as $p_T(b) \to 0$ [2] and as $\Delta R(b\bar{b}) \to 0$, when the b-quarks are massless, the 5F scheme cannot describe the phase space region where two b-quarks are merged in a single jet or when the b-quarks become very soft.

The 4FS is more reliable in describing the b-quark kinematics, since it explicitly takes into account the mass of the b-quark. It is therefore better suited for the description of more exclusive final states, particularly when cuts on b-jets are involved. The $g \to b\bar{b}$ splittings in the initial state, are associated with the appearance of collinear logarithms in the calculation, as can be seen in Figure 2.2: integrating over the b-quark propagator we get

$$\int_{t_{\min}}^{t_{\max}} \frac{dt}{t - m_b^2} = \ln \frac{t_{\max} - m_b^2}{t_{\min} - m_b^2} = \ln \frac{Q^2}{m_b^2}, \tag{2.4}$$

where Q^2 is a characteristic scale of the process [5]. Contrary to the 5FS, in the 4FS these logarithms are not resummed, therefore the 4FS may underestimate the total inclusive rate and typically displays a higher sensitivity to the scale choice than the 5FS.

In order to make manifest the differences in the two schemes, it is instructive to consider the evolution of the b-PDF in the 5FS:

$$\frac{db_{5\mathrm{F}}(x,\mu^2)}{d\ln\mu^2} = \frac{\alpha_s(\mu^2)}{2\pi} \int_x^1 \frac{dy}{y} \left[\mathcal{P}_{bg}\left(\frac{x}{y}\right) g(y,\mu^2) + \mathcal{P}_{bb}\left(\frac{x}{y}\right) b(y,\mu^2) \right], \tag{2.5}$$

[2] Here and in the following we define ΔR as the euclidean distance in the $\eta - \phi$ plane: $\Delta R_{ij} \equiv \sqrt{(\eta_i - \eta_j)^2 + [\min(|\phi_1 - \phi_2|, |2\pi - \phi_1 + \phi_2|)]^2}$.

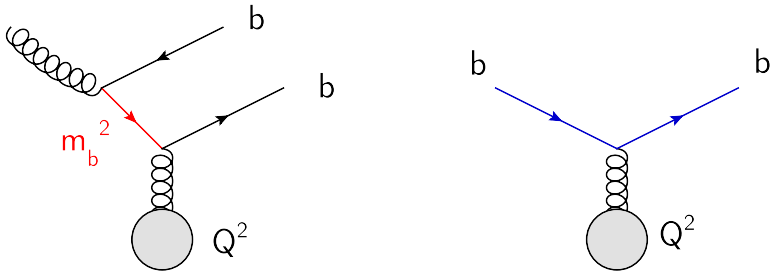

Figure 2.2: Illustration of a 4FS calculation (left) and a 5FS calculation (right). The blobs represent all possible diagram insertions. The 4FS calculation involves an additional external leg, compared to the 5FS calculation. In addition, in the 4FS, the calculation involves an integration over the b-quark propagator (shown in red), which is proportional to $(t - m_b^2)^{-1}$. Therefore while the 5FS calculation involves only the scale Q^2 of the interaction, the 4FS depends both on Q^2 and on m_b^2.

where $\mathcal{P}_{bg}, \mathcal{P}_{bb}$ are the DGLAP splitting kernels that correspond to the processes shown in Figure 2.3. In the approximation where $m_b = 0$, the latter are given by [49]

$$\mathcal{P}_{bb} = \frac{4}{3}\frac{1+z^2}{1-z} \quad , \quad \mathcal{P}_{bb} = \frac{5}{2}\left[z^2 + (1-z)^2\right]. \tag{2.6}$$

Introducing the Mellin transform of the b-PDF

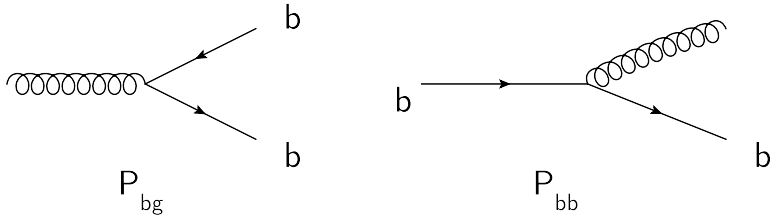

Figure 2.3: Illustration of the two processes that contribute to the b-PDF evolution (equation (2.5)).

$$\widetilde{b}(N, \mu^2) \equiv \int_0^1 dz\, z^{N-1} b(x, \mu^2), \tag{2.7}$$

and taking the flavor non-singlet combination $b^{\mathrm{NS}} = b - \bar{b}$, in order to decouple the gluon density, we have

$$\begin{aligned}\frac{d\widetilde{b}^{\mathrm{NS}}_{5\mathrm{F}}}{d\ln\mu^2} &= \frac{\alpha_s(\mu^2)}{2\pi}\int_0^1 dx\, x^{N-1}\int_x^1 \frac{dy}{y}\mathcal{P}_{bb}\left(\frac{x}{y}\right) b^{\mathrm{NS}}_{5\mathrm{F}}(y,\mu^2)\\ &= \frac{\alpha_s(\mu^2)}{2\pi}\int_0^1 dx\, x^{N-1}\int_0^1 dy\int_0^1 dz\,\mathcal{P}_{bb}(z) b^{\mathrm{NS}}_{5\mathrm{FS}}(y,\mu^2)\delta(x-zy)\\ &= \frac{\alpha_s(\mu^2)}{2\pi}\widetilde{b}^{\mathrm{NS}}_{5\mathrm{F}}(N,\mu^2)\gamma_{bb}(N,\mu^2),\end{aligned} \tag{2.8}$$

where γ_{bb} is the Mellin transform of the $\mathcal{P}_{bb}$ splitting kernel, also known as "anomalous dimension". Making use of the 1-loop running coupling (equation (1.16))

$$\alpha_s(Q^2) = \frac{1}{b\ln\frac{Q^2}{\Lambda^2}} \Longrightarrow \frac{d\alpha_s}{d\ln\mu^2} = -b\alpha_s^2, \tag{2.9}$$

equation (2.8) becomes

$$\frac{d\widetilde{b}^{\mathrm{NS}}_{5\mathrm{F}}(N,\mu^2)}{d\alpha_s(\mu^2)} = -\frac{\gamma_{bb}(N,\mu^2)}{2\pi b}\frac{1}{\alpha_s(\mu^2)}\widetilde{b}^{\mathrm{NS}}_{5\mathrm{F}}(N,\mu^2), \tag{2.10}$$

with the solution

$$\widetilde{b}^{\mathrm{NS}}_{5\mathrm{F}}(N,\mu^2) = \widetilde{b}^{\mathrm{NS}}_{5\mathrm{F}}(N,\mu_0^2)\left[\frac{\alpha_s(\mu_0^2)}{\alpha_s(\mu^2)}\right]^{\frac{\gamma_{bb}}{2\pi b}} = \widetilde{b}^{\mathrm{NS}}_{5\mathrm{F}}(N,\mu_0^2)\exp\left[\frac{\gamma_{bb}}{2\pi b}\ln\frac{\alpha_s(\mu_0^2)}{\alpha_s(\mu^2)}\right]. \tag{2.11}$$

Substituting the 1-loop expression for the running coupling

$$\alpha_s(\mu^2) = \frac{\alpha_s(\mu_0^2)}{1+\alpha_s(\mu_0^2)b\ln\frac{\mu^2}{\mu_0^2}}, \tag{2.12}$$

into equation (2.11), we obtain

$$\begin{aligned}\widetilde{b}^{\mathrm{NS}}_{5\mathrm{F}}(N,\mu^2) &= \widetilde{b}^{\mathrm{NS}}_{5\mathrm{F}}(N,\mu_0^2)\exp\left[\frac{\gamma_{bb}}{2\pi b}\left(1+\alpha_s(\mu_0^2)b\ln\frac{\mu^2}{\mu_0^2}\right)\right]\\ &= \widetilde{b}^{\mathrm{NS}}_{5\mathrm{F}}(N,\mu_0^2)\mathrm{e}^{\frac{\gamma_{bb}}{2\pi b}}\sum_{n=0}^{\infty}\frac{1}{n!}\left(\frac{\gamma_{bb}}{2\pi b}\right)^n\left[\alpha_s(\mu_0^2)\ln\frac{\mu^2}{\mu_0^2}\right]^n.\end{aligned} \tag{2.13}$$

Equation (2.13) shows that the evolution of the b-PDF induces a resummation of the terms $\alpha_s(m_b^2)\ln\frac{Q^2}{m_b^2}$.

In order to compare with the 4FS calculations, we note that in the 5FS the b-PDF is generated at scales $\mu > m_b$ by the evolution of the light quark and gluon densities, which has a perturbative expansion in α_s. As is pictorially represented in Figure 2.2, the 4FS matrix elements can be obtained from the 5FS matrix elements, with the $g \to b\bar{b}$ splitting in the initial state being described by the $\mathcal{P}_{bg}$ splitting kernel, truncated at LO. Doing so, we can derive an approximate expression for the b-PDF evolution [5]

$$\widetilde{b}_{4\mathrm{F}}^{\mathrm{approx.}}(x,\mu^2) = \frac{\alpha_s(\mu^2)}{2\pi}\gamma_{bg}(N)g_{4\mathrm{F}}(N,\mu^2)\ln\frac{\mu^2}{m_b^2}, \tag{2.14}$$

where we have added a subscript 4F, with a slight abuse of notation, in order to indicate that equation (2.14) provides an equivalent description of 4FS calculations.

Comparing equation (2.14) with equation (2.13), we observe that while the 4FS contains logarithmic terms of the kind $\ln\frac{Q^2}{m_b^2}$, the latter are not resummed, as in the 5FS.

The ratio $b_{4\mathrm{F}}^{\mathrm{approx.}}/b_{5\mathrm{F}}$, shown in Figure 2.4 provides an estimate of the difference between the two schemes. It is observed that the difference becomes significant

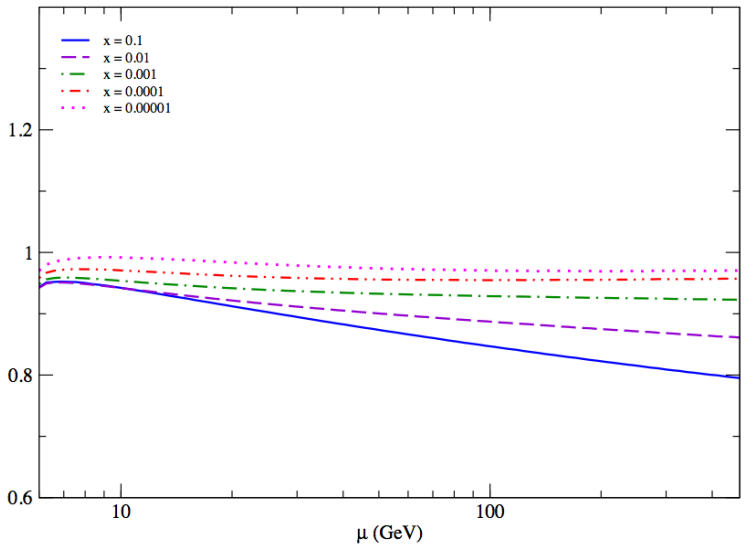

Figure 2.4: Ratio $b_{4\mathrm{F}}^{\mathrm{approx.}}/b_{5\mathrm{F}}$ of the b-PDF evaluated in the 4 and 5FS, using the MSTW2008 NLO PDF set [99] for different values of Bjorken-x. The discrepancy between the two PDFs is significant only at large x. Figure taken from [5].

only in the region of large Bjorken-x, nonetheless it is precisely this region that is probed by $t\bar{t}b\bar{b}$ production. The typical x values in $t\bar{t}b\bar{b}$ production can be estimated by considering that the final state quarks are produced at threshold. Then using the

expression $\hat{s} = x_1 x_2 s$ and making the approximation $x_1 \approx x_2 \approx x$, we obtain

$$x \approx \sqrt{\frac{\hat{s}}{s}} = \frac{2m_{\text{top}} + 2m_b}{\sqrt{s}} \approx 0.05. \tag{2.15}$$

Therefore, we expect that $t\bar{t}b\bar{b}$ production might be sensitive to the presence of large logarithms from collinear gluon splittings.

Finally, we note that even though fixed order 5FS calculations have b-quarks in the initial state, this is not the case for calculations which are matched to a parton shower. There, the shower replaces the incoming b-quark with a $g \to b\bar{b}$ splitting, when the scale approaches the b-mass during the backwards evolution, since $b(x, \mu^2) = 0$ for $\mu < m_b$. As a result, both in 4FS and 5FS calculations matched to a parton shower, b-quarks always appear in pairs in the final state[3].

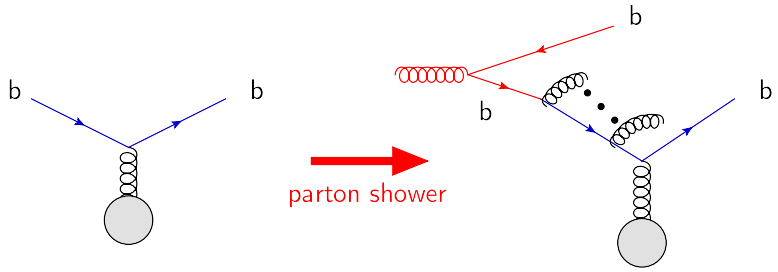

Figure 2.5: Illustration of the effect of the parton shower on a 5FS calculation. The parton shower performs the backward evolution from the scale of the hard process, down to the scale of the proton mass. When the evolution reaches a scale close to the bottom mass, the incoming b-quark is replaced by a $g \to b\bar{b}$ splitting. The $\bar{b}$ quark produced in the splitting will mostly be collinear to the beam pipe and will therefore not be detected.

2.3 Handling of $g \to b\bar{b}$ in the parton shower

The splitting of a gluon to a massless quark-antiquark pair is treated in parton showers using the massless DGLAP kernels

$$dP_{g\to q\bar{q}} = \frac{dt}{t}\frac{\alpha_s(t)}{2\pi}\frac{1}{2}\left[z^2 + (1-z)^2\right]dz. \tag{2.16}$$

[3]CKM suppressed transitions involving b-quarks can obviously violate this rule, however the corresponding diagrams are accompanied by a factor of $|V_{cb}|^2 \approx 0.0017$ or $|V_{ub}|^2 \approx 1.2 \cdot 10^{-5}$ and are therefore negligible.

The same expression was used in older implementations of parton showers to also generate gluon splittings to massive quarks. The kinematics of the massive $Q\overline{Q}$ pair were initially constructed assuming massless quarks and mass effects were introduced by rescaling the 3-momenta of the quarks in the $Q\overline{Q}$ rest frame according to the equations

$$\begin{aligned} p'_Q &= (1 - k_Q)p_Q + k_{\overline{Q}}p_{\overline{Q}} \\ p'_{\overline{Q}} &= (1 - k_{\overline{Q}})p_{\overline{Q}} + k_Q p_Q, \end{aligned} \tag{2.17}$$

where the unprimed quantities indicate the massless 4-momenta and the primed ones denote the 4-momenta after rescaling. The coefficients $k_Q, k_{\overline{Q}}$ are found by imposing the on-shell conditions on equations (2.17). Moreover, to account for the fact that the emission rate is damped for opening angles $\theta_0 < m_Q/E$, shower emissions were limited to the region $\theta > \theta_0$.

Later implementations use more sophisticated approaches, based on matrix element corrections (PYTHIA) [100] or generalizations of equation (2.16) for massive quarks (HERWIG++, SHERPA) [101]. Here we will content ourselves with describing only the recent modifications introduced into PYTHIA 8 for the description of $g \to Q\overline{Q}$.

The simplest option available in PYTHIA 8, which corresponds to setting `TimeShower:weightGluonToQuark=1`, is to use the massless splitting kernel in equation (2.16), multiplied by a phase-space suppression factor that is equal to the Lorentz β factor of the massive quark

$$\beta_Q = \frac{|\mathbf{p}_Q|}{E_Q} = \sqrt{1 - \frac{4m_Q^2}{m_{Q\overline{Q}}^2}}. \tag{2.18}$$

An improvement over this approximation, which corresponds to the setting `TimeShower:weightGluonToQuark=2`, is to retain the mass dependence in the splitting kernel, i.e.

$$dP^{\text{wgtq2}}_{g\to Q\overline{Q}} = \frac{dt}{t}\frac{\alpha_s(t)}{2\pi}\frac{\beta_Q}{2}\left[z^2 + (1-z)^2 + 8\frac{m_Q^2}{m_{Q\overline{Q}}^2}z(1-z)\right]dz, \tag{2.19}$$

A further option, corresponding to `TimeShower:weightGluonToQuark=3` is to use

$$dP^{\text{wgtq3}}_{g\to Q\overline{Q}} = \frac{dt}{t}\frac{\alpha_s(t)}{2\pi}\beta_Q\left[z^2+(1-z)^2+8\frac{m_Q^2}{m^2_{Q\overline{Q}}}z(1-z)\right]\frac{1+\frac{m^2_{Q\overline{Q}}}{m^2_{\text{dipole}}}}{1-\frac{m^2_{Q\overline{Q}}}{m^2_{\text{dipole}}}}dz. \tag{2.20}$$

This gives a high branching probability even for large masses and is therefore considered as an upper bound for the $g \to Q\overline{Q}$ rate. Finally in order to reproduce the matrix element behavior, where the branching probability is suppressed for high masses, option `TimeShower:weightGluonToQuark=4` can be used, which amounts to choosing a splitting kernel[4]

$$dP^{\text{wgtq4}}_{g\to Q\overline{Q}} = \frac{dt}{t}\frac{\alpha_s(t)}{2\pi}\beta_Q\left[z^2+(1-z)^2+8\frac{m_Q^2}{m^2_{Q\overline{Q}}}z(1-z)\right]\left(1+\frac{m^2_{Q\overline{Q}}}{m^2_{\text{dipole}}}\right) \times\left(1-\frac{m^2_{Q\overline{Q}}}{m^2_{\text{dipole}}}\right)^2 dz. \tag{2.21}$$

In the equations above, the argument of α_s is chosen by default to be the transverse momentum of the radiating dipole. An alternative choice is given by using the mass of the $Q\overline{Q}$ system instead. This can be accomplished by multiplying the splitting kernels above by a factor $\ln(p_T^2/\Lambda^2)/\ln(m^2_{Q\overline{Q}}/\Lambda^2)$ and corresponds to setting `TimeShower:weightGluonToQuark=n+4`, where $1 \leq n \leq 4$, are the 4 options outlined above. For the last set of options a further modification is possible, by scaling $m_{Q\overline{Q}}$ in the strong coupling by a factor $0.25 \leq k \leq 1$, thereby allowing for an increased $g \to b\bar{b}$ rate. This possibility is implemented in PYTHIA 8 via the setting `TimeShower:scaleGluonToQuark=k`.

2.4 Production of $t\bar{t}b\bar{b}$ from double parton scattering

The QCD production of a $t\bar{t}b\bar{b}$ final state can result either from a single parton-parton scattering or from two independent scatterings between partons coming from the same proton (double parton scattering - DPS), as illustrated in Figure 2.6. While the two cases are impossible to distinguish experimentally on an event-by-event basis and in fact both contribute to the measurement, the case where $t\bar{t}b\bar{b}$ is produced from DPS

[4]This corresponds to the default model in PYTHIA version 8.205 [102] that is used in this thesis.

should a priori be considered as background. However, we will prove below that this case constitutes a negligible fraction of the total number of $t\bar{t}b\bar{b}$ events.

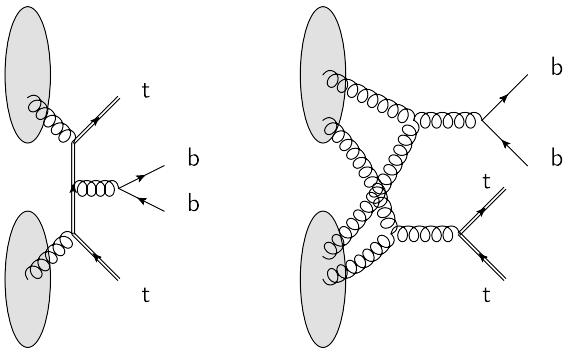

Figure 2.6: Illustration of the production of a $t\bar{t}b\bar{b}$ final state in a single (left) and in a double parton scattering (right). The blobs indicate the incoming protons in a pp collision.

The naïve expectation for the probability to have a $t\bar{t}b\bar{b}$ event from a single scattering $P(t\bar{t}b\bar{b})$ and the probability to have a $t\bar{t}$ event from a hard interaction and a $b\bar{b}$ event from an additional MPI $P(t\bar{t}+b\bar{b})$ is as follows

$$P(t\bar{t}b\bar{b}) = \frac{\sigma_{t\bar{t}b\bar{b}}}{\sigma_{\text{non-diffractive}}} \tag{2.22}$$

$$P(t\bar{t}+b\bar{b}) = \frac{\sigma_{t\bar{t}}\sigma_{b\bar{b}}}{\sigma^2_{\text{non-diffractive}}}. \tag{2.23}$$

Replacing the cross-sections with their LO estimates, obtained from PYTHIA 8 $\sigma_{t\bar{t}b\bar{b}} = 1.5$ pb, $\sigma_{t\bar{t}} = 150$ pb, $\sigma_{b\bar{b}} = 270$ μb, $\sigma_{\text{non-diffractive}} = 50$ mb, we get

$$\frac{P(t\bar{t}+b\bar{b})}{P(t\bar{t}b\bar{b})} = 0.52. \tag{2.24}$$

This is a naïve estimate for inclusive $t\bar{t}$ and $b\bar{b}$ production which doesn't take into account the impact-parameter dependence of the MPI. Generally the second interaction would produce very soft jets. Putting a cut on the p_T of the outgoing particles in the center-of-mass frame, $\hat{p}_T$, we obtain

$$\frac{P(t\bar{t}+b\bar{b})}{P(t\bar{t}b\bar{b})} = 0.05 \quad , \quad \text{for } \hat{p}_T > 10\,\text{GeV} \tag{2.25}$$

$$\frac{P(t\bar{t}+b\bar{b})}{P(t\bar{t}b\bar{b})} = 0.005 \quad , \quad \text{for } \hat{p}_T > 20\,\text{GeV}. \tag{2.26}$$

From this we can safely conclude that in the phase-space probed by the measurement, with $p_T^{\text{jet}} \geq 25$ GeV, the amount of $t\bar{t}b\bar{b}$ events coming from two MPIs should be negligible.

Part II

Experimental setup

Chapter 3

The LHC accelerator complex

3.1 Characteristics of the LHC accelerator chain

The Large Hadron Collider [103] is a synchrotron accelerator designed to accelerate protons up to a centre-of-mass energy of $\sqrt{s} = 14$ TeV and lead ions (Pb^{82+}) up to a center-of-mass energy of $\sqrt{s_{NN}} = 2.76$ TeV per nucleon pair. It consists of two rings of accelerating radio-frequency (RF) cavities, interleaved with bending and focusing magnets, where the beams are stored. The rings intersect at four points, where the LHC detectors are located. The LHC design parameters are presented in Table 3.1.

Parameter	Value
Circumference	26.7 km
Proton Energy per Beam	7 TeV
Lorentz γ factor	7461
Particles per bunch	$1.15 \cdot 10^{11}$
Bunches per beam	2808
Peak Luminosity	10^{34} cm^{-1}s^{-1}
Field of main bends	8.33 T
Revolution frequency	11.245 kHz
Collision rate	40 MHz
Stored Energy per beam	362 MJ
Bunch crossing interval	25 ns

Table 3.1: LHC design characteristics

The LHC is located underground at a depth ranging from 45 to 170 meters. After a startup period with the LHC working at $\sqrt{s} = 900$ GeV, from the beginning of 2010 the LHC has been operating at $\sqrt{s} = 2.36$ TeV, $\sqrt{s} = 7$ TeV and $\sqrt{s} = 8$ TeV. The gradual increase of the collision energy was not only necessary to ensure a safe operation of the superconducting magnets, but it was also useful for physics measurements, particularly for measuring the energy dependence of the underlying event [104] which is of crucial importance for tuning the MPI and ISR models in Monte-Carlo generators [105].

After a shutdown of one and a half years for consolidation works in the superconducting magnets, the LHC is scheduled to restart in the middle of 2015 at $\sqrt{s} = 13$ TeV, before ramping up to the design collision energy of 14 TeV. With a shorter training time required for the magnets, this intermediate step in collision energy will be adopted in order to expedite the delivery of collisions for physics research, thereby shortening the way to the discovery of new physics.

The proton acceleration sequence proceeds as follows. Before entering the LHC, the protons are grouped into bunches and accelerated to 450 GeV. This is achieved by the accelerator complex that precedes the LHC as illustrated in Fig. 3.1. Protons are extracted from Hydrogen gas, by applying an electric field. The protons are then accelerated up to 50 MeV by LINAC2. The beam is then injected into the Proton Booster reaching an energy of 1.4 GeV. In the next step the beam is transferred to the Proton Synchrotron, where it is accelerated to 26 GeV and circulated with the same frequency and bunch spacing as the LHC. The final step before entering the LHC is the Super Proton Synchrotron, which accelerates the beams to 450 GeV. Once the beams are inside the LHC accelerator, it takes approximately 20 minutes for them to be accelerated to the peak energy. Several processes contribute to reducing the number of protons in the beams, such as inelastic proton-proton collisions, inelastic collisions between the protons in the beam and residual gas left in the beam pipe and Coulomb scattering of protons in the same bunch. As a result the beam lifetime, i.e. the interval after which the beam intensity reaches $1/e$ of its initial value is limited to around 15 hours. At the end of its lifetime, or earlier if there are operating errors, the beam is dumped into a block of a 8-meter long cylinder of graphite.

The proton beams are not continuous but have a discrete structure, which is defined primarily by the characteristics of the LHC accelerating cavities (RF cavities). The RF system provides longitudinal focusing which constrains the longitudinal particle motion to a confined region called the RF bucket. Since a particle must always be

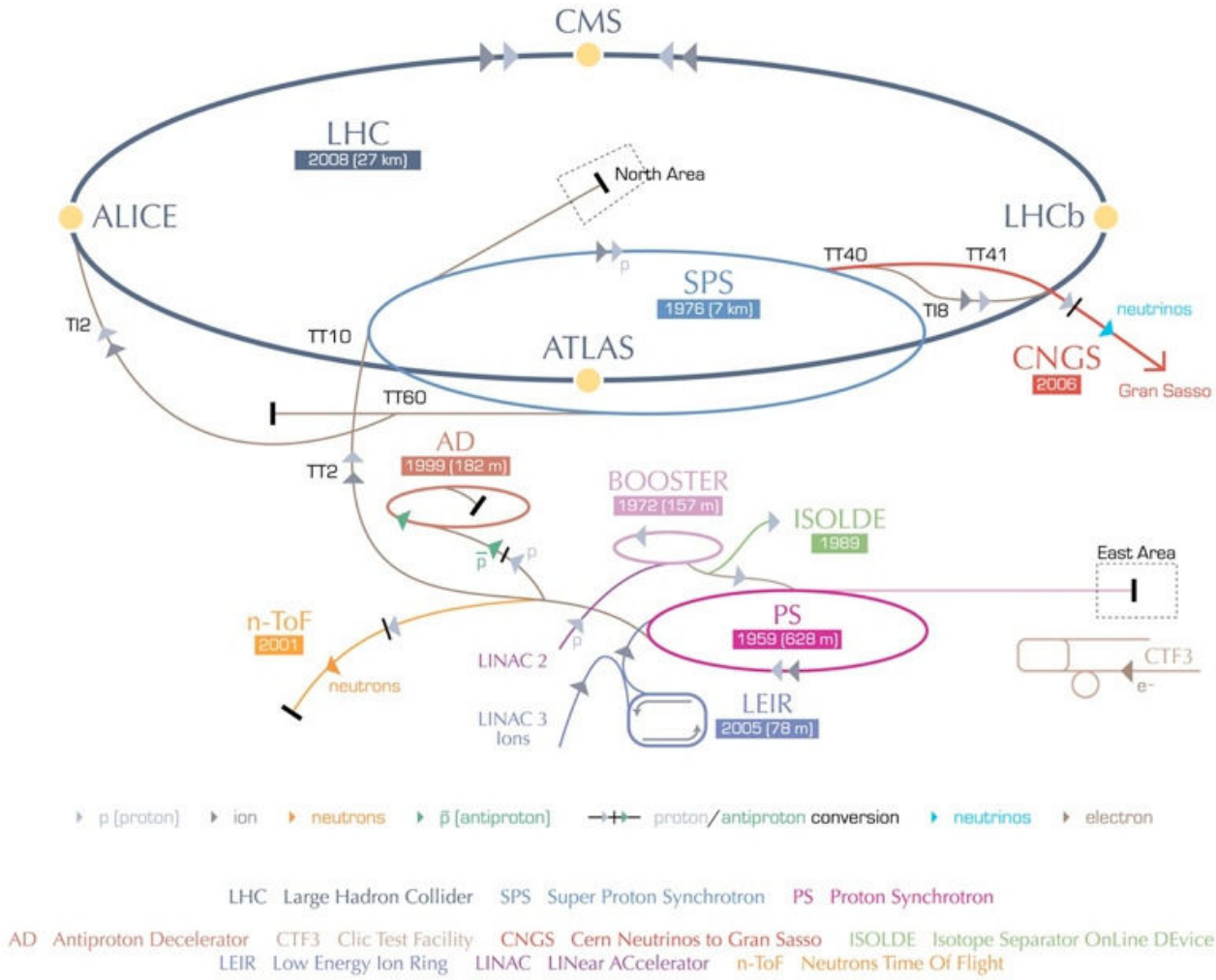

Figure 3.1: The CERN accelerator complex.

subjected to the same accelerating voltage at the same point, the RF frequency must be an integer multiple of the revolution frequency

$$f_{\mathrm{RF}} = h \cdot f_{\mathrm{rev}} = h \cdot \frac{\beta c}{2\pi R}, \tag{3.1}$$

where h is the so-called harmonic number, which is the number of RF buckets on the accelerator ring. For the LHC, $f_{\mathrm{RF}} = 400$ MHz, which gives $h = 35640$. Taking into consideration the requirements of the LHC experiments, the characteristics of the accelerator complex and beam stability issues, it was decided that a minimum distance of 10 buckets (25 ns) must be present between two proton bunches (RF buckets filled with protons). This limits the maximum number of proton bunches to 3564. Accounting for the finite rise time of the kicker magnets, which are used to inject or

dump the beam, further reduces the number of bunches to a maximum of 2808, at design luminosity.

Each bunch contains $1.15 \cdot 10^{11}$ protons at the beginning of the fill and the distance between two bunches under the Run I operating conditions was 15 m (or 50 ns), corresponding to a total of 1404 bunches per beam. This distance will be halved in Run 2, in order to attain the design instantaneous luminosity.

3.2 Luminosity

The instantaneous luminosity is one of the key accelerator characteristics, determining the rate for the production of particles per unit of area $L = \dot{N}_{\text{inel}}/\sigma_{\text{inel}}$, where $\dot{N}_{\text{inel}}$ is the rate of inelastic collisions and σ is the inelastic pp cross-section. For a storage ring operating at a revolution frequency f_r and with N_b bunch pairs colliding per revolution, the instantaneous luminosity can be expressed as

$$L = \frac{\langle\mu\rangle\, N_b\, f_r}{\sigma_{\text{inel}}} = \frac{\epsilon\langle\mu\rangle\, N_b\, f_r}{\epsilon\sigma_{\text{inel}}} = \frac{\langle\mu\rangle_{\text{vis}}\, N_b\, f_r}{\sigma_{\text{vis}}}, \tag{3.2}$$

where $\langle\mu\rangle$ is the average number of inelastic pp collisions per bunch crossing, ϵ is the efficiency for reconstructing an inelastic pp collision and $\langle\mu\rangle_{\text{vis}} \equiv \epsilon\langle\mu\rangle$, $\sigma_{\text{vis}} \equiv \epsilon\sigma_{\text{inel}}$.

ATLAS measures the delivered luminosity by measuring $\langle\mu\rangle_{\text{vis}}$ with a variety of detectors employing different algorithms [106]. The inner detector contributes to the luminosity measurement by the detection of primary vertices produced in inelastic pp interactions. The Beam Condition Monitor (BCM) is comprised of four diamond sensors arranged in a cross shape around the beam pipe at a distance of 184 cm from the interaction point. With the vertical and horizontal pair of sensors read out separately it provides two independent luminosity measurements. LUCID is a Cherenkov light detector dedicated to the online luminosity monitoring. Its main purpose is to detect inelastic pp scattering in the forward region, in order to measure the integrated luminosity and provide online monitoring for the instantaneous luminosity and beam conditions.

In order to use equation (3.2) for the determination of the instantaneous luminosity, σ_{vis} must be determined for each detector that provides a measurement of $\langle\mu\rangle_{\text{vis}}$. This is done primarily using beam separation scans, first proposed by van der Meer [107, 108],

whereby the instantaneous delivered luminosity is calculated from the measurable beam parameters

$$L_{\text{vdM}} = \frac{N_b \, f_r \, n_1 \, n_2}{2\pi \Sigma_x \Sigma_y} \tag{3.3}$$

where n_1, n_2 are the numbers of protons in beams 1 and 2, and Σ_x, Σ_y are the horizontal and vertical beam profile widths. Equating the luminosity measured in a van der Meer scan with equation (3.2) we obtain

$$\sigma_{\text{vis}} = \frac{2\pi \Sigma_x \Sigma_y \langle \mu \rangle_{\text{vis}}^{\text{max}}}{n_1 n_2}, \tag{3.4}$$

where $\langle \mu \rangle_{\text{vis}}^{\text{max}}$ is the number of inelastic pp interactions per bunch crossing observed at the peak of the scan curve. The number of protons in the two beams are determined by external measurements using current transformers. The precision of the luminosity measurements calibrated using the beam separation scans is at the level of 3% [106].

Alternative methods for determining σ_{vis} also exist. The visible cross-section can be estimated using Monte-Carlo generators by taking

$$\sigma_{\text{vis}} = \epsilon_{ND}\sigma_{ND} + \epsilon_{SD}\sigma_{SD} + \epsilon_{DD}\sigma_{DD}, \tag{3.5}$$

where ND, SD and DD refer to the non-diffractive, single diffractive and double diffractive processes and the ϵ_i to the different efficiencies for detecting the corresponding processes in the detector used for the luminosity measurement. The associated cross-sections suffer from quite large modeling uncertainties, which translate to an uncertainty of the order of 20% on the extracted instantaneous luminosity [109]. The ALFA detector [110] consists of scintillating fibers placed inside of Roman pots situated 237 m on either side of the ATLAS detector. ALFA will measure elastic pp scattering at small angles (of the order of μrad) with the aim of determining. For elastic scattering, the scattering angle θ is related to the four-momentum transfer t by $t = -2p^2(1 - \cos\theta)$, which for small angles becomes $t = -(p\theta)^2$, where p is the four-momentum of the protons. The luminosity can be determined by measuring the t distribution and fitting the spectrum dN/dt.

The design luminosity of the LHC is 10^{34} cm$^{-2}s^{-1}$. The peak instantaneous luminosity was $3.6 \cdot 10^{33}$ cm$^{-2}s^{-1}$ in the 7 TeV run of 2011 and reached a maximum of $7.7 \cdot 10^{33}$ cm$^{-2}s^{-1}$, around 25% below the design luminosity in the 2012 8 TeV run. The

integrated luminosity that was delivered and recorded by ATLAS during the 2011 and 2012 operations is shown in Figure 3.2.

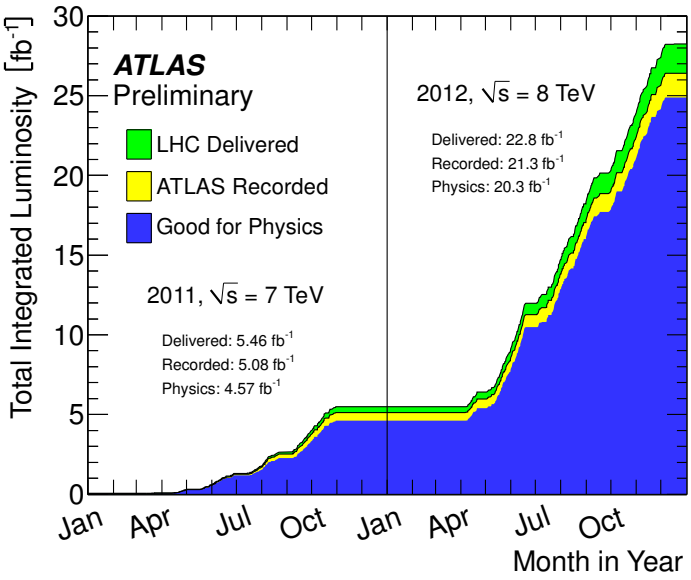

Figure 3.2: Integrated luminosity delivered to (green), recorded by ATLAS (yellow) and certified to be of good quality for physics analyses (blue).

The LHC is expected to reach its design luminosity in 2015 allowing to collect a total integrated luminosity of around 75-100 fb^{-1} until the beginning of 2018, according to present estimates. Future upgrades are scheduled in order to increase the design luminosity to $2 \cdot 10^{34}$ cm$^{-2}s^{-1}$ (Phase I upgrade in 2018) which would allow to collect an integrated luminosity of up to 300 fb^{-1} until the third planned long shutdown in 2022. A future upgrade, named High-Luminosity LHC is being considered, with the aim of increasing the peak luminosity to $5 \cdot 10^{34}$ cm$^{-2}s^{-1}$ (Phase II upgrade around 2022) and allowing for the collection of a total integrated luminosity of around 3 ab^{-1}.

3.3 Detectors installed on the LHC ring

There are in total seven experiments installed on the LHC ring:

- ATLAS - A Toroidal LHC ApparatuS [111]
- CMS - Compact Muon Solenoid [112]

- ALICE - A Large Ion Collider Experiment [113]
- LHCb - Large Hadron Collider beauty [114]
- LHCf - Large Hadron Collider forward [115]
- TOTEM - TOTtal Elastic and diffractive cross-section Measurement [116]
- MoEDAL - Monopole and Exotics Detector At the LHC [117]

ATLAS and CMS are general-purpose detectors designed to detect a wide range of signals in as wide a phase space as possible, with both experiments optimized for the detection of the Higgs boson. More specifically both ATLAS and CMS were designed to have very good electromagnetic calorimetry, optimized specifically for the search of the $H \to \gamma\gamma$ and $H \to ZZ^* \to 4\ell$ signatures. Both detectors also feature hadronic calorimeters which are big enough to contain very energetic jets that can arise from the decay of heavy resonances, have a high resolution so as to measure the jet energies with a high accuracy and a hermetic coverage, so that the missing energy can be accurately inferred. Good tracking capabilities are also an important ingredient in order to identify charged particles and measure their kinematics, as well as for the identification of b-hadrons, which arise in many of the flagship analyses of the ATLAS and CMS physics programs.

The ALICE experiment is designed to study the low-energy features of QCD, particularly the formation of quark-gluon plasma (QGP). The ALICE detector uses data from lead-lead and proton-lead collisions, which produce a vast amount of charged particles. Charged particle identification is the key element that drove the design of the ALICE detector. Different complementary techniques are used to measure the charge particles' momentum and charge, including ionization, time of flight, transition radiation and Cherenkov radiation. High resolution electromagnetic calorimetry is also necessary for the study of photons, which provide important information on the thermal properties of QGP. A high resolution muon spectrometry is also necessary for the detection and study of heavy quarkonium states, which constitute an important probe of the formation of QGP.

LHCb is a dedicated heavy flavor physics experiment, designed to study new physics in CP violation and rare decays of c and b-hadrons. Unlike ATLAS, CMS and ALICE the LHCb detector is highly asymmetric, covering only the forward region

within $1.8 \leq |\eta| < 4.9$.[1] This design was chosen due to limitations in the cavern space, taking advantage of the fact that $b\bar{b}$ pairs are produced with a large boost in the forward directions. High resolution tracking is a crucial component for the reconstruction of the displaced b-decay vertices. Particle identification is essential in order to separate the rare decays of interest from the background. In addition to the spectrometer system, composed of the tracking and magnet systems, complementary information is provided by two Ring Imaging Cherenkov detectors, the electromagnetic and hadronic calorimeters and muon chambers, which are essential for the searches of rare b-hadron decays to muons.

LHCf is a specialized detector located 140 m from Interaction Point 1, where ATLAS is installed. It uses two zero-degree calorimeters to measure neutral hadrons produced in the very forward region $\eta > 8.4$, with the aim of calibrating the hadronic interaction models that are used in the study of very high energy cosmic rays as well as elucidating the composition of cosmic ray showers, which cannot be determined by present experiments.

TOTEM is another specialized detector, located around Interaction Point 5, where the CMS detector is installed. It uses three types of detectors: roman pots equipped with silicon microstrip sensors to detect protons scattered elastically at small angles and gaseous ionization detectors (CSC and GEM) which are used to detect jets produced in the forward region $3.1 \leq |\eta| \leq 6.5$ due to the diffractive dissociation of protons. TOTEM aims at measuring the diffractive, elastic and total cross-sections at the different center-of-mass energies provided by the LHC, thereby testing non-perturbative models of soft QCD [118].

The MoEDAL experiment was designed to complement the searches of the ATLAS and CMS experiments for highly ionizing particles, in particular magnetic monopoles. The experiment consists of an array of passive track-etch detectors made of plastic, installed on the walls and ceiling of the VErtex LOcator detector of the LHCb experiment, which are sensitive enough to detect even a single magnetic monopole traversing the detector with masses up to several TeV and a magnetic charge of higher than 3 Dirac magnetic charges.

[1] Here and in the following η is the pseudorapidity which is defined by $\eta \equiv -\ln\left[\tan\frac{\theta}{2}\right]$, where θ is the polar angle relative to the beam axis. The direction perpendicular to the beam pipe has $\eta = 0$, while the direction parallel to the beam pipe has $\eta \to \pm\infty$. Positive (negative) η defines the forward (backward) direction.

Chapter 4

The ATLAS detector

ATLAS is a general purpose detector located at Interaction Point 1 on the LHC ring. It has cylindrical symmetry and a coverage of almost 4π steradians in solid angle, which is essential for reconstructing the energy flow in an event. The guiding principle in the construction of the ATLAS experiment was the maximization of the discovery potential of the searches for the Higgs boson and new physics. The major components of the ATLAS detector are illustrated in Figure 4.1.

4.1 Inner detector

The ATLAS tracking system covers the central region of the detector which spans up to $|\eta| = 2.5$. The inner detector (ID) is comprised of three sub-detectors, which surround the beryllium beam-pipe: the pixel detector, the semi-conductor tracker (SCT) and the transition radiation tracker (TRT). The sub-detectors are arranged in cylindrical layers in the central region of the ID (barrel) and in disk structures perpendicular to the beam pipe in the more forward regions (end-caps), as illustrated in Figure 4.2. The ID provides tracking information and measures the charge of particles. It is immersed into a 2T axial magnetic field provided by a superconducting solenoid.

The combined inner detector system can measure tracks efficiently down to $p_T = 500$ MeV, reaching as low as $p_T = 100$ MeV for minimum-bias measurements [119]. For the typical transverse momenta of the charged b-hadrons ($p_T = 5$ GeV), the transverse momentum resolution in the central region with $|\eta| < 0.3$ is around 75 MeV and the transverse impact parameter resolution is around 35 μm. Higher p_T tracks have a smaller curvature and therefore their momentum measurement is more

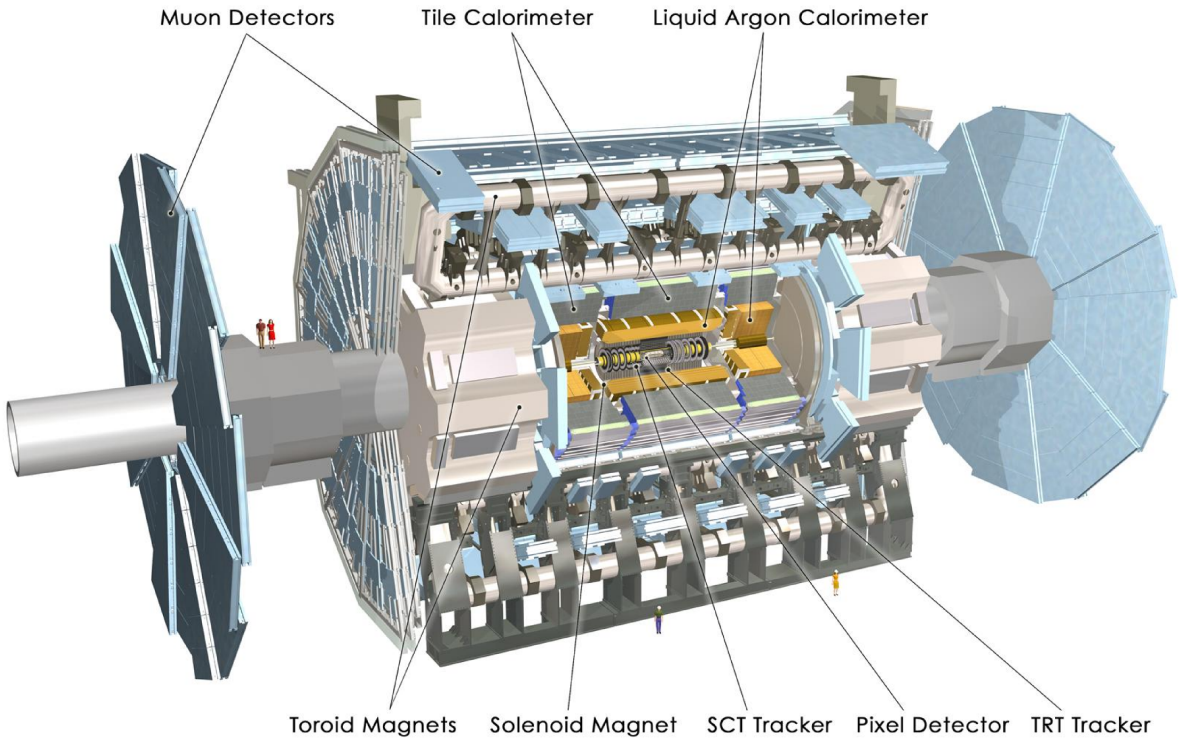

Figure 4.1: A computer generated image of the ATLAS detector [111].

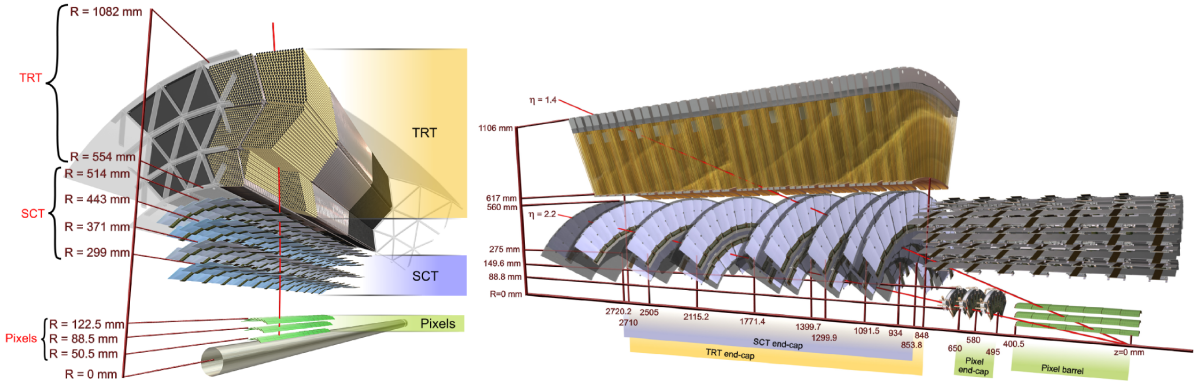

Figure 4.2: The barrel (left) and end-cap (right) regions of the ATLAS inner detector [111].

imprecise. The track momentum resolution decreases linearly with increasing track momentum. The track momentum resolution also decreases with increasing η, due to an increased material budget in the forward region, which increases the amount of multiple scattering for hadrons and Bremsstrahlung energy losses for electrons. The decrease in the number of expected hits per track with increasing $|\eta|$ is another factor that contributes to the deterioration of the track momentum resolution.

4.1.1 Pixel detector

The pixel detector constitutes the innermost part of the ATLAS tracking system. It is comprised of silicon sensors, that function as a solid-state ionization chamber. When a charged particle traverses the silicon layer it ionizes the molecules, creating a number of free electrons and holes, which is proportional to the energy loss of the incident particle. An electric field is applied to the sensors, causing the electrons and holes to drift towards the electrodes in opposite directions. The collected charges induce a signal in the pixel electrodes, allowing to determine the position of the particle passing through the detector.

The silicon sensors are arranged in three layers and are designed to provide the highest granularity around the interaction point. The innermost layer is located at a radius of 5 cm from the beam axis. A fourth pixel layer, called the insertable b-layer (IBL), was installed in the ID during the Phase-0 upgrade, after the end of Run I. This layer is located closer to the beam pipe, at a distance of 3.3 cm, and is expected to increase the precision of the measurement of the tracks' impact parameters. The pixel layers are segmented in $R - \phi$ providing in total 80 million readout channels.

The pixel detector, has an intrinsic measurement accuracy of around 10 μm in the transverse plane ($R - \phi$) and 115 μm along the beam axis (z). This subdetector contributes the most to the accuracy of the measurement of the locations of tracks and displaced vertices, the quintessential ingredients of b-tagging.

4.1.2 SCT

The pixel detector is surrounded by the SCT. The SCT is composed of silicon microstrips arranged in four barrel layers and nine end-cap discs on each side. The SCT modules consist of two single sided sensors glued back-to-back with a stereo angle crossing of 40 mrad, thus providing two dimensional tracking information on each layer. The SCT works in a similar way to the pixel detector, using the ionization of the silicon molecules for particle detection. The SCT has 6.3 million readout channels. The SCT detector contributes to the measurement of the momentum, impact parameter and vertex position. The intrinsic measurement accuracy of the SCT is 17 μm in the $R - \phi$ plane and 580 μm in the longitudinal plane.

4.1.3 TRT

The TRT constitutes the outer part of the ID. It consists of layers of straw tube elements interleaved with transition radiation material. The straws are parallel to the beam axis in the barrel region and arranged radially in wheels in the end-cap regions. Each straw is 4 mm in diameter, 144(37) cm long in the barrel (end-cap) region and filled with a gas mixture of 70% Xe, 27% CO_2 and 3% O_2. Thin gold plated tungsten wires, functioning as anodes, are located inside each straw. The inner part of the straws is covered with conducting material, and works as a cathode. The voltage difference between the anode and the cathode is a few kV. The space between the straws is filled with a material with widely varying indices of refraction, which causes charged particles to produce X-ray photons, known as transition radiation. The transition radiation photons interact with the molecules in the gas, freeing electrons, which move towards the anode, where the current is measured. The intensity (opening angle) of the transition radiation is proportional (inversely proportional) to the Lorentz γ factor of the incoming particle, therefore the radiation pattern can be used for particle identification, providing a separation of electrons from hadrons.

The TRT also functions as a drift chamber. When a charged particle traverses the straw tube, it ionizes the gas, producing electrons and positively charged ions which drift towards the anode and cathode respectively. The track hits are then reconstructed by measuring the time that it takes for the electrons to drift towards the anode. The intrinsic resolution of the TRT is 130 μm, which is lower compared to the silicon detectors. Nevertheless, the TRT contributes significantly to the determination of the particles' momentum due to the large number of expected hits per track.

4.2 Calorimeter system

The ATLAS calorimeter system comprises of a number of sampling detectors which offer full azimuthal coverage and are cylindrically symmetric around the beam axis. The calorimeter system consists of electromagnetic and hadronic calorimeters, which cover the region up to $|\eta| < 3.2$ and a system of Forward Calorimeters (FCal) which extend the η coverage to $3.1 < |\eta| < 4.9$. The calorimeter system is displayed in Figure 4.3

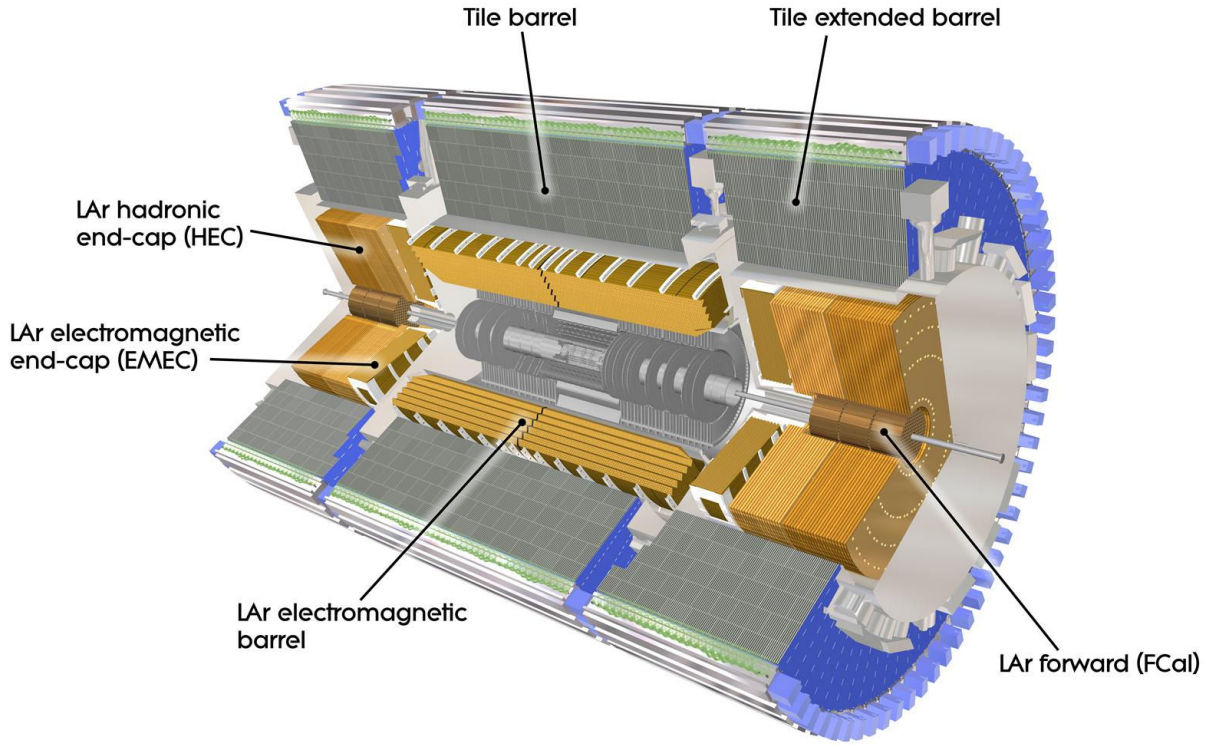

Figure 4.3: The ATLAS calorimeter system [111].

4.2.1 Electromagnetic calorimeters

Electromagnetic calorimetry is provided by the Liquid Argon (LAr) Electromagnetic Calorimeter (ECal) and the first module of the FCal. The ECal consists of two parts, the barrel (EMB) which covers the central region up to $|\eta| < 1.475$ and two end-caps (EMEC) which are divided into two coaxial wheels, the outer one covering the range $1.375 < |\eta| < 2.5$ and the inner one covering the range $2.5 < |\eta| < 3.2$.

The calorimeter features an accordion geometry, which provides a full azimuthal coverage with no cracks. The ECal modules consist of interleaved layers of lead/stainless steel plates, which act as the absorber and LAr, which acts as the active medium. The modules are segmented into 3 sections in depth (with a depth of 4.3, 16 and 2 X_0 respectively[1]) with a high granularity in the region $|\eta| < 2.5$ and two sections in depth with a coarser granularity in the more forward region. The first layer has the highest granularity and is used for separating single photons from π^0 particles. The second

[1]The radiation length X_0 is the distance at which an incident electron's energy is reduced to E/e.

layer takes up most of the ECal volume and is where the main energy deposition from the electromagnetic cascades takes place. The third layer is used for the separation of electromagnetic cascades from hadronic ones. In the region with $|\eta| < 1.8$ there is a thin LAr layer, known as the presampler, which is used to correct for upstream energy losses. The electromagnetic component of the FCal also uses LAr as the active medium but copper was chosen as the absorbing medium, due to its higher resolution and better heat removal capability. The layout of a barrel module of the ECal is shown in Figure 4.4.

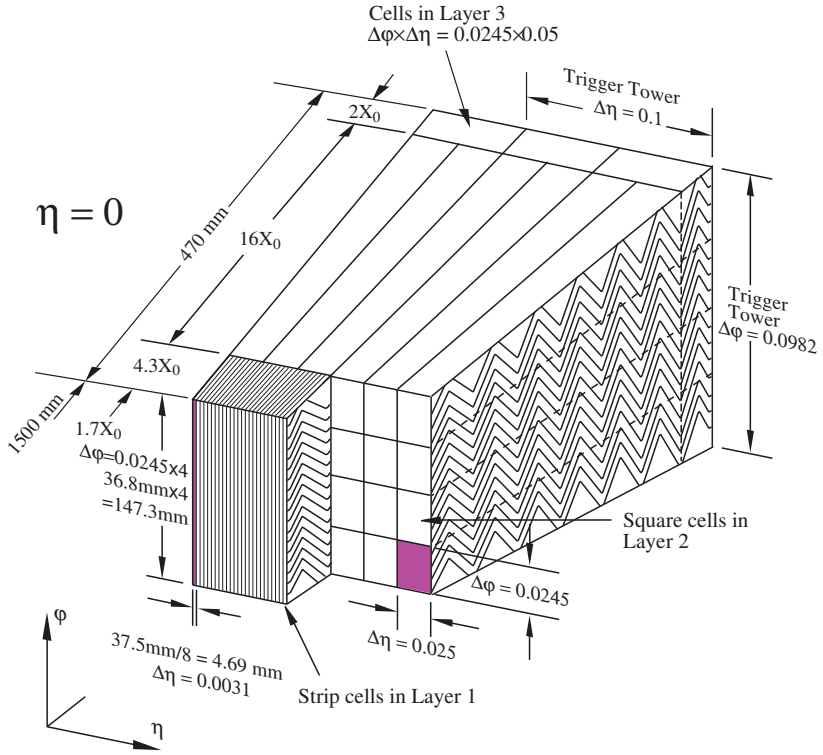

Figure 4.4: Sketch of a barrel module of the EM calorimeter, showing the different layers with their respective granularities in η and ϕ [111].

The principle of operation is based on the production of electromagnetic cascades as a result of the interaction of highly energetic particles with the absorber medium. The main processes at play are pair production ($\gamma \rightarrow e^+e^-$) and Bremsstrahlung ($e^\pm \rightarrow e^\pm\gamma$). The electromagnetic cascade continues as long as the energy of the radiated photons is higher than the threshold for e^+e^- production ($E_\gamma > 1.022$ MeV) and the energy of the radiated electrons/positrons is higher than the critical energy, at which the losses due to Bremsstrahlung become equal to the losses due to ionization. The particles produced in the cascade ionize the LAr producing an electrical signal.

The energy resolution σ of the calorimeter is parametrized as follows

$$\frac{\sigma}{E} = \frac{a}{E} \oplus \frac{b}{\sqrt{E}} \oplus c, \tag{4.1}$$

where a, b and c are known as the noise, sampling and constant terms respectively. The noise term is dominant at low energies and receives contributions from electronic noise and pile-up. For sampling calorimeters it is inversely proportional to the sampling fraction, i.e. the fraction of the incident particle's energy deposited in the active medium. The sampling term depends on the calorimeter characteristics, such as the absorber and active material properties and the thickness of the sampling layers. The constant term is dominant at high energies and depends on the calorimeter depth and other characteristics of the calorimeter layout, such as non-uniformities, cracks and the distribution of the dead material. Experimental measurements after noise subtraction give $b = 10\%\sqrt{\text{GeV}}$ and $c = 17\%$.

4.2.2 Hadronic calorimeters

The ATLAS Hadronic Calorimeter (HCal) system consists of the Tile calorimeter, which covers the region with $|\eta| < 1.7$, the Hadronic End-cap Calorimeter (HEC) which covers the region with $1.5 < |\eta| < 3.2$ and the second and third layers of the FCal.

The Tile calorimeter uses steel as the absorber and scintillating tiles as the active material and is segmented in depth in three layers. The tiles are connected to photo-multipliers by wavelength shifting fibers. For the HEC, LAr was chosen as the active medium for its robustness against high radiation fluxes which are expected in the forward region, while copper plates serve as absorbers. The second and third layer of the FCal, which are optimized for hadronic measurements, use LAr as active medium and tungsten as absorber. With its high atomic number, tungsten features a high nuclear interaction length which is necessary for containing the hadronic showers in the limited volume that is available to the FCal modules.

The principle of operation is similar to the ECal. Incoming hadrons induce hadronic cascades, which are composed of a hadronic component (consisting of hadrons and nuclear fragments) and an electromagnetic component (consisting of electromagnetically decaying π^0). Due to nuclear spallation and weak hadron decays, a fraction of the cascade's energy cannot be detected. As a result the calorimeter's response to electrons is

higher than its response to hadrons, a phenomenon known as non-compensation. The electromagnetic fraction of the hadronic cascade is highly dependent on the incoming particle's energy ranging from around 30% for energies of around 10 GeV to 50% for energies around 100 GeV.

The energy resolution of the hadronic calorimeter is parametrized by equation (4.1), with $b = 50\%\sqrt{\text{GeV}}$ for the sampling term and $c = 3\%$ for the constant term.

4.3 Muon system

The muon spectrometer forms the outer part of the ATLAS detector. The spectrometer subsystems are organized into three layers in the barrel region and three-wheels in the end-cap region extending up to $|\eta| < 2.7$. The spectrometer components are:

- the Monitored Drift Tube (MDT) chambers, which provide a precision measurement of the track coordinates and muon momenta. The MDT chambers are located on all barrel layers and on the two outer wheels. The drift chambers consist of aluminum tubes filled with a gas mixture of 93% Ar and 7% CO_2. At the center of the tubes lies a tungsten wire which functions as an anode. When a muon passes through the MDT chambers it ionizes the gas inside the tubes and causes the electrons to drift towards the anode wires. The drift time is used to measure the distance of the particle to the wire, thus allowing to determine the coordinates of the muon.

- the Cathode Strip Chambers (CSC), which are used for precise momentum measurements in the forward region. The CSC are placed in the innermost end-cap wheel and are designed to cope with the high particle rate in this region. The CSC are multi-wire proportional chambers with anode wires oriented in the radial direction and cathode strips segmented orthogonal to the wires. The chambers are filled with a 80% Ar, 20% CO_2 gas mixture. The volume of the gas is reduced relative to the MDT, allowing to minimize the drift time. The CSC determine the hit coordinates by interpolating the signals on adjacent strips.

- the Resistive plate chambers (RPC) are gaseous ionization detectors consisting of two parallel electrode plates. The gas used is a mixture of 94.7% $C_2H_2F_4$, 5% Iso-C_4H_10, 0.3% SF_6. The RPC provide a first-level muon trigger in the barrel region and measure the muon coordinates on the bending plane.

- the Thin Gap Chambers (TGC) are multi-wire proportional chambers providing two functions in the end-cap muon spectrometer: triggering and determination of the azimuthal coordinates of the muon tracks (the radial ones being provided by the MDT).

The η coverage of the RPC and TGC ($|\eta| < 2.4$) determines the region available for muon triggering. The muon spectrometer is immersed into a magnetic field generated by three toroid magnets. In the central region an air-core barrel magnet produces a 0.5 T field and in the forward regions, a 1 T field is generated by two air-core end-cap toroids.

4.4 Trigger system

Under the 2011 and 2012 operating conditions, the LHC was colliding proton bunches every 50 ns, which correponds to a collision rate of 20 MHz. The maximum rate with which data can be read out was limited however to 75 kHz. The Trigger/DAQ system of the ATLAS detector must therefore achieve rejection factors of the order of 400, while maintaining an excellent efficiency in recording rare processes.

The trigger consists of three levels of event selection: Level-1 (L1), Level-2 (L2) and the Event Filter (EF). The L1 trigger uses low granularity input from all calorimeter subsystems and the RPC and TGC sub-detectors of the muon system to search for high-p_T muons, electrons, photons, jets and hadronically decaying τ leptons. The L1 trigger reduces the accepted events rate to 75 kHz. The time taken from the bunch crossing until the L1 trigger decision is made is required to be less than 2.5 μs. Trigger information from the calorimeter and muon systems, consisting of multiplicities for electrons, photons, τ-leptons, jets, and muons, and of flags indicating which thresholds were passed for total and missing transverse energy, and for total jet transverse energy, is sent to the Central Trigger Processor (CTP). There, different trigger conditions are combined into trigger items and the CTP generates the L1 accept signal, which is defined as the logical OR of all trigger items. The L1 accept signal is propagated to the L2 trigger, along with an identifier of the bunch crossing of interest. The L1 trigger is purely hardware based, implemented with custom-built electronics.

The L2 trigger operates on Regions-of-Interest (RoI), which are regions where the L1 trigger has identified possible trigger objects. Using the ROI information, specific

information on coordinates, energy, and type of signatures is read from the Read Out System to perform the event selection. Since only a subset of the event data is used by L2, the network bandwidth as well as the processing time of the L2 trigger is considerably reduced. The accept rate is reduced by L2 to below 3.5 kHz with an average processing time of 40 ms per event. The EF then further reduces the accept rate to approximately 200 Hz with an average processing time of 4 s per event. The L2 trigger has access to the full detector granularity in the RoIs and the EF has access to the complete event data with the full detector granularity. Both the L2 and EF triggers are software based, using similar algorithms as the ones used in offline reconstruction, running on commodity computer farms.

For the upcoming Run 2, the trigger system underwent several modifications to cope with the higher expected instantaneous luminosity, which will lead to a doubling of the collision rate. More specifically, the L1 accept rate has been increased from 75 to 100 kHz. Apart from improvements in the calorimeter and muon triggers, a new topological trigger has been implemented, which offers the possibility of applying more complex cuts, such as the angular separation or invariant mass of trigger objects for the online selection of events. The CTP trigger items have been doubled, thus allowing for an increased triggering flexibility.

The L2 and EF triggers have been merged into a single High Level Trigger (HLT) capable of reaching an output rate of 500 Hz to 1 kHz. This merging eliminates the need for accessing the event data twice (from L2 and HLT), which was necessary with the Run 1 trigger architecture, while allowing for a higher flexibility in the order of selections.

Moreover, a new electronics system named Fast TracKer (FTK) [120], providing a fast track reconstruction for all events accepted by the L1 trigger will be commissioned in 2015. FTK is expected to improve the trigger performance in many areas, for instance extending the trigger sensitivity towards lower momentum b hadrons.

Chapter 5

Object reconstruction and detector performance

In this chapter we describe the reconstruction and identification of the individual final state objects that are used in the analysis.

5.1 Leptons

The lepton performance is quantified by the efficiency to reconstruct and identify a lepton from a set of lepton candidates, the efficiency to reject objects that can be mis-identified as electrons as well as the lepton energy scale and resolution.

Electrons

Electron reconstruction in the central detector region ($|\eta|$<2.47) is seeded from groups of EM calorimeter cells (clusters) with an energy deposit $E_T > 2.5$ GeV. The clusters have a fixed size of 3×5 in units of 0.025×0.025 in (η, ϕ) space. The clusters are matched to ID tracks with $p_T > 0.5$ GeV, by extrapolating the track to the middle layer of the calorimeter and calculating its distance from the cluster. A track is considered to be matched to the cluster if it falls within $|\Delta\eta| < 0.05$ and $|\Delta\phi| < 0.1(0.05)$ from the cluster barycenter. The looser requirement on $|\Delta\phi|$ is used in the direction of the bending of the electron candidate's track, in order to account for energy losses due to Bremsstrahlung, while the tighter cut is used for the opposite direction. Tracks matched to a cluster are refitted with a Gaussian Sum Filter algorithm [121], which

allows to account for large Bremsstrahlung energy losses, thereby improving the estimated track parameters particularly for low E_T electrons. In the last stage of electron reconstruction the clusters are enlarged to 3×7 units in the barrel and 5×5 units in the end-cap region of the calorimeter [122].

The reconstruction efficiency for electrons is defined as the ratio of the number of electrons reconstructed as a cluster matched to a track passing the track quality criteria to the number of clusters with or without a matching track. The electron reconstruction efficiency has been measured using the tag-and-probe method[1] with $Z \to e^+e^-$ events, as described in [123]. The reconstruction efficiency shows a mild dependence on the electron E_T, with values ranging from 97% for $E_T = 15$ GeV to 99% for $E_T \gtrsim 50$ GeV. The reconstruction efficiency is almost independent of the pseudorapidity in the barrel region and shows a mild dependence on η in the EMEC region.

A set of criteria is used to distinguish signal electrons from jets and electrons from photon conversions[2] that can fake electrons. The identification is based on the use of a set of track-based and calorimeter-based variables which can distinguish between electrons and photons and is performed either using independent cuts on the discriminating variables (cut-based identification) or a single cut on the ratio of the signal and background likelihood functions which take as input these discriminating variables (likelihood-based identification). The likelihood-based identification provides a higher rejection of fake electrons for the same identification efficiency compared to the cut-based approach. The cut-based identification was used in this thesis, since the likelihood-based one had not been fully validated. Three identification levels are defined, each with an increasing background rejection: Loose, Medium and Tight.

The Loose identification criteria use shower shape variables in the first and second layers of the EM calorimetar and the fraction of the energy deposited in the hadronic calorimeter, as well as information on the associated track quality and track-cluster matching. The Medium identification criteria, use in addition to the Loose selection, information from the third layer of the EM calorimeter, transverse impact parameter and TRT signals. Moreover, a measured hit in the innermost layer of the pixel

[1] The tag-and-probe method is a data-driven technique which exploits well known resonance, such as the Z boson, as a source for the production of electron-positron pairs. It selects events with a Z candidate, using tight identification requirements on the "tag" electron and looser requirements on the "probe" electron. The fraction of probe electrons which pass the selection under study gives an estimate of the corresponding efficiency.

[2] Photon conversions are processes in which a photon splits into an e^+e^- pair when interacting with the detector material.

detector is required to discriminate against electrons from photon conversions. The Tight identification criteria, use in addition to all variables included in the previous identification levels, a selection on the ratio between the candidate's cluster energy and its track momentum, stricter requirements on the discriminating variables and TRT information, and a veto on reconstructed photon conversion vertices associated to the cluster. The electron identification criteria are shown in Table 5.1.

Type	Description	Loose	Medium	Tight
Hadronic leakage	Ratio of the E_T in the first layer of the hadronic calorimeter to E_T of the EM cluster (for $\|\eta\| < 0.8$ and $\|\eta\| > 1.37$) or ratio of the E_T in the hadronic calorimeter to E_T of the EM cluster (for $\|\eta\| > 0.8$ and $\|\eta\| < 1.37$)	✓	✓	✓
Third layer of EM calorimeter	Ratio of the energy in the third layer to the total energy in the EM accordion calorimeter		✓	✓
Middle layer of EM calorimeter	Lateral shower width	✓	✓	✓
	Ratio of the energy in 3×7 cells over the energy in 7×7 cells centered at the electron cluster position	✓	✓	✓
Strip layer of EM calorimeter	Shower width	✓	✓	✓
	Ratio of the energy difference between the largest and second largest energy deposits in the cluster over the sum of these energies	✓	✓	✓
Track quality	Number of hits in the B-layer (discriminates against photon conversions)		✓	✓
	Number of hits in the pixel detector	✓	✓	✓
	Number of total hits in the pixel and SCT detectors	✓	✓	✓
	Transverse impact parameter		✓	✓
TRT	Total number of hits in the TRT		✓	✓
	Ratio of the number of high-threshold hits to the total number of hits in the TRT		✓	✓
Track-cluster matching	$\Delta\eta$ between the cluster position in the strip layer of the calorimeter and the extrapolated track	✓	✓	✓
	$\Delta\phi$ between the cluster position in the middle layer of the calorimeter and the extrapolated track			✓
	Ratio of the cluster energy to the track momentum			✓
Conversions	Veto electron candidates matched to reconstructed photon conversions			✓

Table 5.1: Shower shape and track information used for the identification of central electrons. The use of the variables for different identification levels in the cut-based approach is shown. (adapted from [123])

The identification efficiency is defined as the ratio of the number of electrons passing a certain identification selection to the total number of electron candidates defined as clusters with a matching track. It is measured in data using $Z \to e^+e^-$, $Z \to e^+e^-\gamma$ and $J/\psi \to e^+e^-$ events with the tag-and-probe technique. The combined reconstruction and identification efficiencies are shown in Figure 5.1.

The electron energy scale and resolution are measured by reconstructing the invariant mass of the J/ψ and Z resonances in $Z \to e^+e^-\gamma$ and $J/\psi \to e^+e^-$ events. The electron energy scale is known with 0.5-1% accuracy and the energy resolution is of

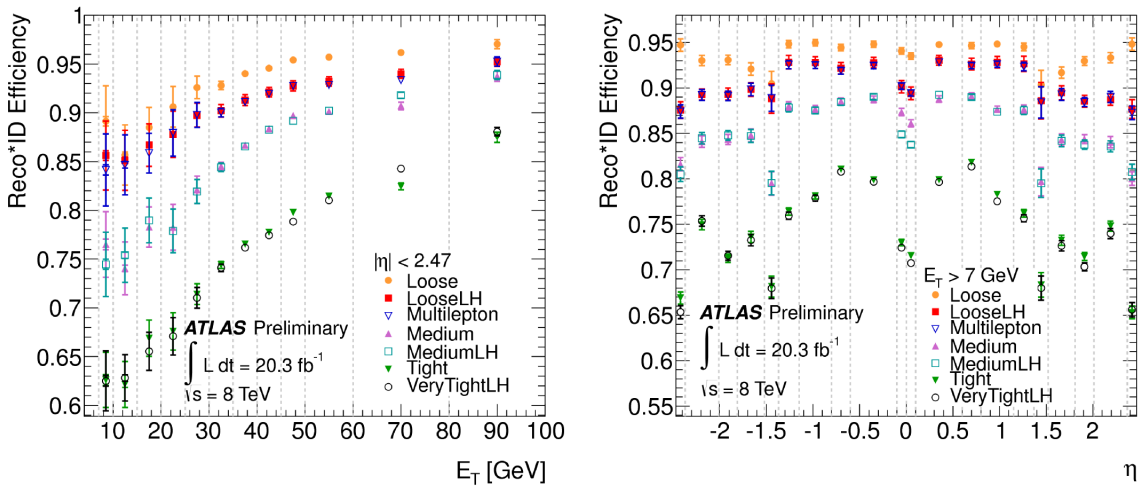

(a) (b)

Figure 5.1: Combined reconstruction and identification efficiency for electrons for the various cut-based and likelihood selections as a function of E_T (left) and η (right) [123].

the order of 2% for electrons with $E_T = 25$ GeV in the central region, as shown in Figure 5.2.

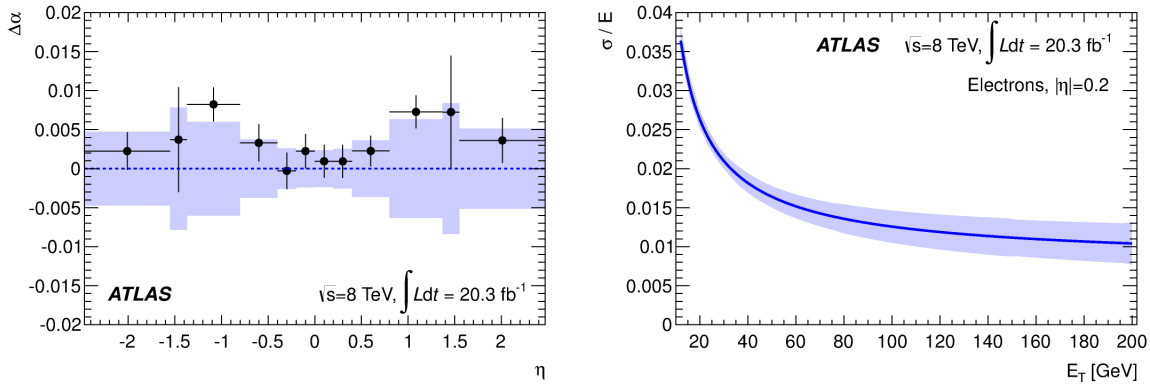

(a) (b)

Figure 5.2: Data to simulation ratio for the electron energy scale (left) and energy resolution (right) measured in $Z \to e^+e^-$ and $J/\psi \to e^+e^-$ events. The blue bands indicate the systematic uncertainty of the calibration [124].

Muons

Muons are reconstructed from tracks formed in either the Muon Spectrometer (MS) alone, or combining information from the MS with the ID. Different identification criteria define different muon "types", which are are reconstructed with different strategies, named "Chains" [125].

Further types of muons exist, such as standalone (SA) muons, segment-tagged (ST) muons and Calorimeter-tagged (CaloTag) muons. SA muons are muons reconstructed from a MS track. The muon has to traverse at least two layers of MS chambers to provide a track measurement. SA muons are mainly used to extend the acceptance to the range $2.5 < |\eta| < 2.7$ which is not covered by the ID. ST muons are muons reconstructed from an ID track, which once extrapolated to the MS, it is associated with at least one local track segment in the MDT or CSC chambers. ST muons can be used to increase the acceptance in cases in which the muon crossed only one layer of MS chambers, either because of its low transverse momentum or because it falls in regions with reduced MS acceptance. CaloTag muons are muons reconstructed from an ID track which can be associated to an energy deposit in the calorimeter, which is compatible with a minimum ionizing particle. In this thesis muons combined or segment-tagged (CB+ST), reconstructed reconstructed with the Muid algorithm (Chain 2) [125] are used. The algorithm uses tracks that are reconstructed independently in the ID and in the MS and performs a global refit, resulting in a combined track.

Similarly to the electron efficiency measurements, the muon efficiencies have been measured in data using $Z \to \mu^+\mu^-$, $J/\psi \to \mu^+\mu^-$ and $\Upsilon \to \mu^+\mu^-$ samples, as described in [125]. The reconstruction and identification efficiency for muons reconstructed from a combination of inner detector and muon spectrometer tracks is above 99% in the region $0.1 < |\eta| < 2.5$, as shown in Figure 5.3. In the region $|\eta| < 0.1$, the muon spectrometer is only partially equipped with muon chambers in order to provide space for the ID and calorimeter services, thereby leading to an acceptance and efficiency loss.

In the muon transverse momentum range of $6 < p_T < 100$ GeV, the muon momentum scale is known with 0.04% precision in the barrel region, decreasing to 0.2% in the region with $|\eta| > 2$.

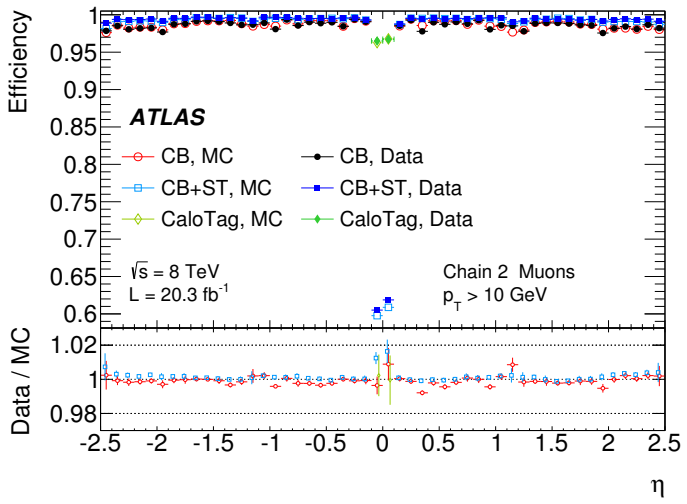

Figure 5.3: Reconstruction and identification efficiency for muons reconstructed with different algorithms: combined (CB), combined or segment-tagged (CB+ST) and Calorimeter-tagged (CaloTag). CaloTag muons are only shown in the region $|\eta| < 0.1$. The efficiencies are measured in $Z \to \mu^+\mu^-$, $J/\psi \to \mu^+\mu^-$ and $\Upsilon \to \mu^+\mu^-$ events [125].

5.2 Jets

Jets are reconstructed from 3-dimensional clusters of adjacent calorimeter cells. These "topological" clusters are seeded by calorimeter cells with a signal greater or equal to 4σ, where σ is the sum in quadrature of the standard deviations of the distributions of electronic and estimated pile-up noise. The cluster is built by adding iteratively the cells adjacent to the seed cells having a signal greater or equal to 2σ and a single layer of cells adjacent to the latter [126]. Jets are then reconstructed by clustering the topological clusters with a jet recombination algorithm.

The topological clusters are reconstructed at the so-called electromagnetic energy scale (EM), which corresponds to the energy deposited by particles in an electromagnetic shower in the calorimeter. The EM scale is established by calibrating the calorimeter electronic signals to the energies of electrons (for the EM calorimeters) or muons (for the hadronic calorimeters) using monochromatic test beams. A multi-step procedure is used to calibrate the jet energy scale (JES) as follows:

1. **pile-up correction**: due to the high number of protons in the LHC bunches, several inelastic pp interactions can occur simultaneously, contributing signals that are overlaid to the signals from the hard-scattering interaction in the calorimeter. Additional signals due to interactions happening in the same bunch crossing

as the hard-scattering interaction are known as in-time pile-up. In detectors with a slow response, such as the LAr calorimeters, signals due to interactions in preceding or subsequent bunch crossings can also interfere with the signals from the hard-scattering interaction, an effect which is known as out-of-time pile-up. Pile-up significantly affects the jet reconstruction by increasing the jet multiplicity, modifying the jet kinematics and substructure as well as degrading the jet energy resolution. The effects of pile-up on jets are mitigated by the jet-area based subtraction method [127], which corrects the jet's transverse momentum as follows

$$p_{T,\text{jet}}^{\text{corr}} = p_{T,\text{jet}} - \rho \cdot A_{\text{jet}} - \alpha(\eta_{\text{det}})(N_{\text{PV}} - 1) - \beta(\eta_{\text{det}})\langle\mu\rangle, \tag{5.1}$$

where ρ is the median p_T density per unit area $\rho \equiv \underset{\text{jet}}{\text{median}} \frac{p_T^{\text{jet}}}{A_{\text{jet}}}$ [128], A is the catchment area of the jet [129], N_{PV} is the number of primary vertices, $\langle\mu\rangle$ is the average number of inelastic pp collisions per bunch crossing, given by equation (3.2) and α, β are factors that parametrize a residual correction applied after the jet-area based correction. We note that N_{PV} is reconstructed using tracking information and is thus only sensitive to in-time pile-up, while $\langle\mu\rangle$ is calculated from the average instantaneous luminosity and is thus sensitive to both in-time and out-of-time pile-up. These factors depend on the pseudorapidity region in the detector in which the jet is reconstructed. The effect of the jet-area based and residual corrections on the jets' p_T is shown in Figure 5.4. The first two terms in equation (5.1) are evaluated on an event-by-event basis, therefore this method can account for event-to-event fluctuations in the amount of pile-up, thereby leading to an improved jet energy resolution and suppression of pile-up jets. Furthermore the first two terms, which are responsible for the bulk of the correction, do not need any input from simulation, therefore the method offers a reduced sensitivity to modeling.

2. **Monte-Carlo based JES correction**: after the pile-up subtraction, the reconstructed jet's energy is corrected to the energy of the simulated jet to which it matches[3]. The JES correction consists in restoring the jet response $\mathcal{R}_{\text{EM}} \equiv \frac{E_{\text{EM}}^{\text{jet}}}{E_{\text{truth}}^{\text{jet}}}$ to unity. The calibration procedure corrects for the calorimeter non-compensation,

[3] A reconstructed jet is considered to be matched to a simulated jet if their distance is $\Delta R < 0.3$. Both truth and reconstructed jets are considered to be isolated, i.e. have no jet with $p_T > 7$ GeV within $\Delta R \leq 2.5 \cdot R_{\text{jet}}$.

energy losses in crack regions in the calorimeters and in inactive material and energy losses due to the magnetic field in front of the calorimeter. The calibrated jet energy is defined as

$$E^{\text{jet}}_{\text{EM+JES}} = \frac{E^{\text{jet}}_{\text{EM}}}{\mathcal{F}_{\text{calib}}(E^{\text{jet}}_{\text{EM}}, \eta_{\text{det}})}, \tag{5.2}$$

where $\mathcal{F}_{\text{calib}}$ is obtained from a fit to the average jet response in bins of $E^{\text{jet}}_{\text{truth}}$ and η_{det}.

3. ***η*-intercalibration**: Due to the different calorimeter technology and the different amounts of dead material in the different calorimeter regions, the jet response depends on the pseudorapidity region in which the jet is reconstructed. Correction factors derived from Monte-Carlo simulations are applied in order to make the jet response uniform in η, a procedure known as η-intercalibration. The corrections are validated in-situ using dijet events. A reference jet in the region $|\eta| < 0.8$ is selected and the asymmetry between the reference jet's p_T and the second (probe) jet's p_T is calculated by

$$\mathcal{A} = 2\frac{p_T^{\text{probe}} - p_T^{\text{ref}}}{p_T^{\text{probe}} + p_T^{\text{ref}}}. \tag{5.3}$$

Calibration factors are then defined for each η bin by

$$c = \frac{2 - \langle \mathcal{A} \rangle}{2 + \langle \mathcal{A} \rangle}. \tag{5.4}$$

4. **In-situ determination of JES**: The jet response is measured in data using Z+jets, γ+jets and multi-jet events by exploiting the fact that the transverse momenta of the final state objects should sum up to 0. The ratio of the jet response in data to the jet response in simulation is shown in Figure 5.5.

Other calibration schemes use additional cluster-by-cluster and/or jet-by-jet information to reduce some of the sources of fluctuations in the jet energy response, thereby improving the jet energy resolution [130]. More precisely in the Local Cluster Weighting (LCW) calibration, cluster shape variables are used to separate the topological clusters into hadronic and electromagnetic ones. Correction factors are applied to hadronic clusters in order to correct for non-compensation effects. Further corrections

are applied to both type of clusters in order to correct for energy lost outside of the cluster as well as in dead material. In the Global Calorimeter cell Weighting (GCW) scheme, corrections are derived for each calorimeter cell within a jet, with the constraint that the jet energy resolution be minimized. Finally the Global Sequential (GS) calibration scheme, starts from jets calibrated with the EM+JES scheme and corrects for fluctuations in the jet particle content of the hadronic shower development, such that the mean jet energy is left unchanged. The jet reconstruction and calibration procedure is described in more detail in [130]. In this thesis only jets calibrated with the LCW+JES procedure are used.

The jet performance is quantified by the precision of the determination of the jet energy scale as well as the energy resolution. The JES is known with a precision of better than 3% for jets with $p_T > 50$ GeV, as shown in Figure 5.5, while the precision is worse for jets with lower p_T and jets in the forward region.

The jet energy resolution (JER) is measured in multi-jet events by probing the jet imbalance on the transverse plane, as described in [131]. The JER is of the order of 10% for jets with $p_T > 100$ GeV, growing to 20% for jets with $p_T \approx 30$ GeV.

The jet-area based pile-up subtraction has been found to eliminate most of the jets stemming from pile-up pp collisions. Pile-up jets that survive after the jet-area based pile-up subtraction have $p_T < 50$ GeV [127]. These remaining pile-up jets, can be removed by placing a cut on the jet vertex fraction (JVF) variable, which is defined for a given jet i with respect to a primary vertex j as

$$\mathrm{JVF}(\mathrm{jet}_i, \mathrm{PV}_j) = \frac{\sum_k p_{\mathrm{T}}(\mathrm{track}_k^{\mathrm{jet_i}}, \mathrm{PV}_j)}{\sum_n \sum_l p_{\mathrm{T}}(\mathrm{track}_l^{\mathrm{jet_i}}, \mathrm{PV}_n)}. \tag{5.5}$$

Jets without any associated tracks (typically jets with $|\eta| > 2.5$ where tracking is not available) are assigned a JVF value of -1. A cut on $\mathrm{JVF}(\mathrm{jet}, \mathrm{PV}_0) > 0.5$ is applied on jets with $p_T < 50$ GeV and $|\eta| < 2.4$ in order to suppress jets originating from pile-up interactions[4]. As Figure 5.4 indicates, the combination of the jet-area based pile-up subtraction with a cut on JVF eliminates pile-up jets for the pile-up conditions that were experienced in the 2012 run.

[4] PV_0 indicates the hard-scatter primary vertex which is defined as the primary vertex with the highest $\sum_{\mathrm{track}} p_{T,\mathrm{track}}^2$. We note that the specific values of the JVF cuts are analysis dependent [127].

5.3 b-tagging

Several algorithms used to identify jets containing the fragmentation products of b-quarks exist. These exploit the characteristic properties of b-hadron decays, such as

- the relatively long lifetime ($c\tau \approx 0.5$mm) which, for typical b-hadron energies expected at the LHC, lead to long decay lengths $\ell = \gamma\beta c\tau = \mathcal{O}(\text{mm})$. These can be reconstructed as displaced secondary vertices, which are used in secondary vertex (SV) b-taggers [132],
- the displaced decays of b hadrons (a consequence of the b hadrons' long lifetime), which produce tracks with high impact parameters with respect to the primary vertex. These are used as input to impact parameter (IP) b-taggers [133],
- the fact that b-hadrons will mostly decay to a charmed hadron, which will produce another displaced vertex along the flight path of the b-hadron. The topology of the b-hadron decay chain is exploited by the JetFitter algorithm [134].

These algorithms can be used independently to identify b-jets [135] but have also been combined into a neural network, known as the MV1 tagger [136], which is used in this analysis. A variant of this tagger, dubbed MV1c, trained for a higher rejection of c-jets is also available.

The efficiency of the MV1 algorithm for correctly identifying b-jets or for misidentifying charm (c) or light flavor (LF) jets as b-jets, has been measured in samples of $t\bar{t}$ [137], D^{*+} and dijet events [136] respectively. The corresponding efficiencies for the operating point corresponding to an inclusive b-jet efficiency of 70% together with the associated data-to-MC correction factors are shown in Figure 5.6. The correction factors are consistent with unity across the entire p_T and η range accessible to the calibration methods and are measured with a relative precision of around 2% in the range $60 \leq p_T < 140$ GeV. The precision is worse however for low p_T jets, rising to 3% for jets with $30 \leq p_T < 40$ GeV and 6% for jets with $20 \leq p_T < 30$ GeV, thereby constituting a significant uncertainty source for the $t\bar{t}b\bar{b}$ cross-section measurement.

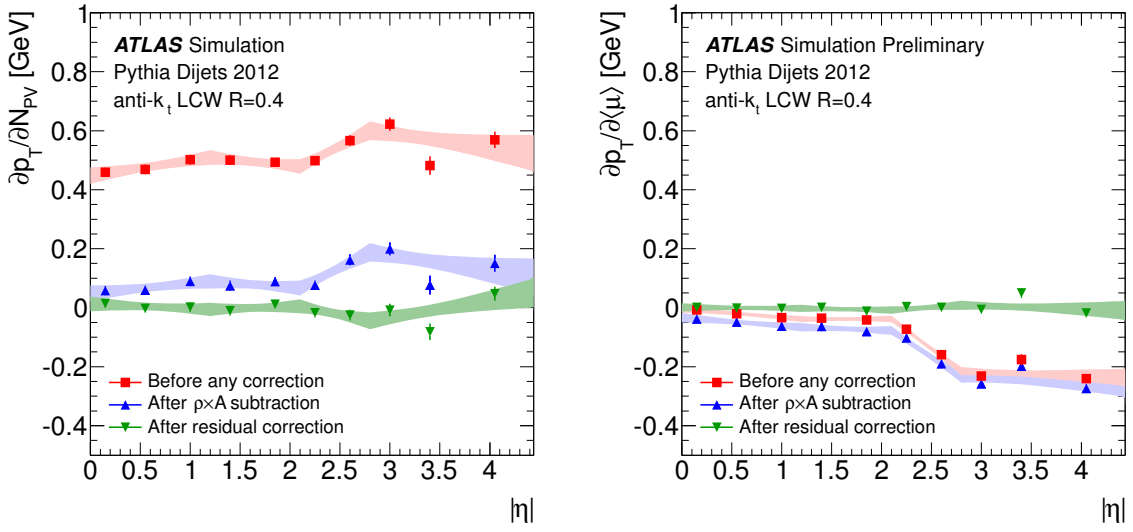

(a) (b)

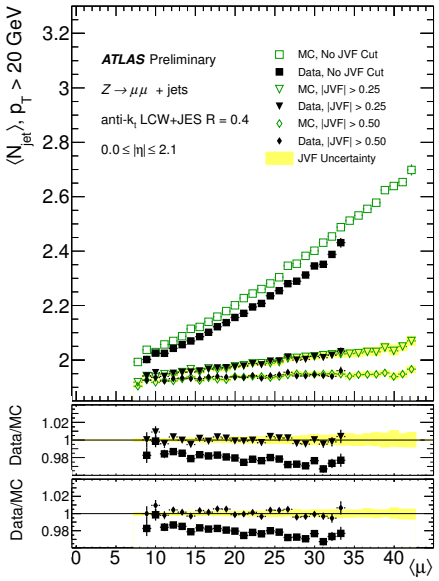

(c)

Figure 5.4: Dependence of the jet p_T on N_{PV} (a) and $\langle\mu\rangle$ as a function of the jet's pseudorapidity (b) and mean number of jets with $p_T > 20$ GeV as a function of $\langle\mu\rangle$ (c) [127]. It can be seen that the jet-area based pile-up correction almost eliminates the jet's sensitivity to in-time pile-up (a), while the residual correction is necessary to correct for the out-of-time pile-up effects (b). After cutting on the JVF variable, the mean number of jets is shown to be independent of the average number of interactions (c), thereby indicating the elimination of pile-up jets.

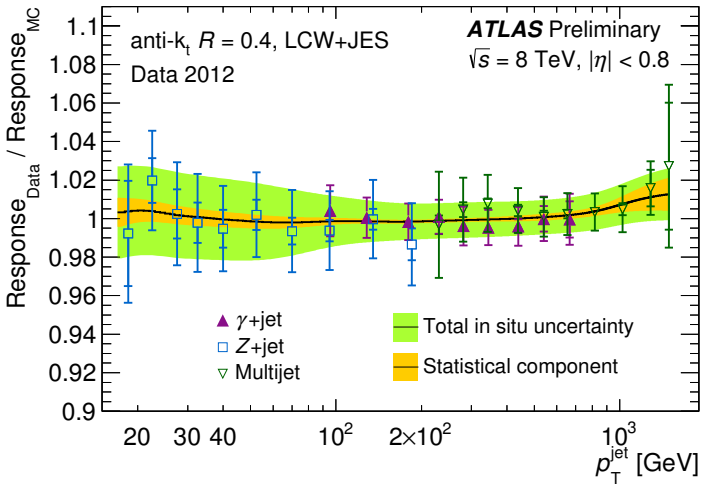

(a)

Figure 5.5: Ratio of the jet response determined in data to the jet response determined from simulation as a function of p_T for three in situ techniques combined to determine the in situ energy scale correction for anti-k_T jets with a radius parameter of $R = 0.4$ calibrated using the LCW+JES scheme.

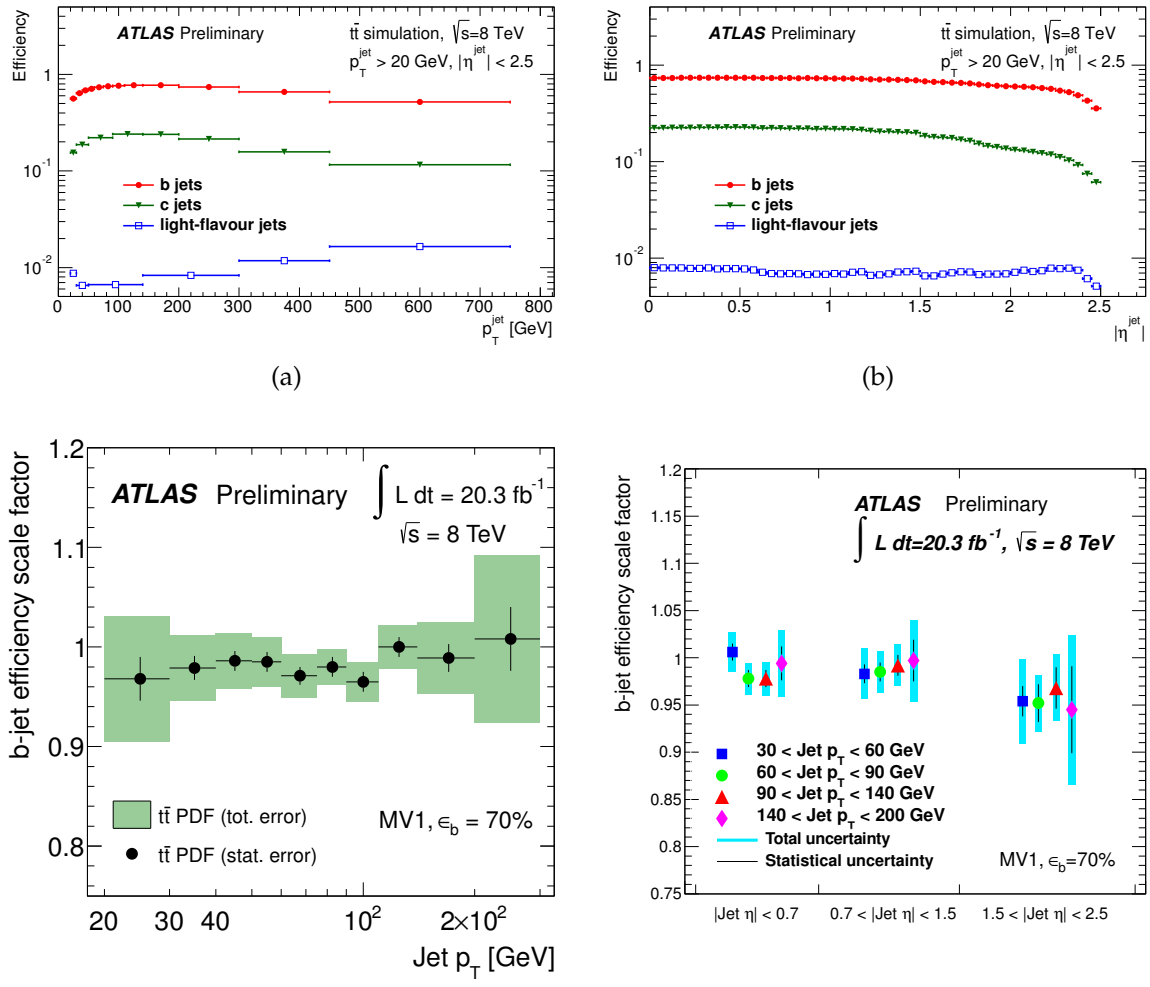

Figure 5.6: Efficiency of the MV1 tagger to select b, c, and light jets, as a function of jet p_T (a) and η (b) and data-to-MC correction factors for the b-tagging efficiency as a function of the jet p_T (c) and η (d) [137].

Part III

The measurement

Chapter 6

The measurement strategy

The choice of the analysis techniques and the definition of the phase space in which the $t\bar{t}b\bar{b}$ cross-section is measured are driven by the characteristics of the process as well as the capabilities of the detector. More specifically, the experimental determination of the $t\bar{t}b\bar{b}$ cross-section faces the following challenges:

- a **low production cross-section**, which implies low statistics and a high statistical uncertainty
- **backgrounds** which are not easy to separate from the signal. More specifically, the separation of the $t\bar{t}b\bar{b}$ signal from $t\bar{t}$+charm and $t\bar{t}$+LF jets, which are the dominant background processes relies on the use of b-tagging. With the b-tagging efficiency being inversely proportional to the c and LF-jet rejection, selecting a sample with low contamination from background events implies a further reduction in statistics
- both **signal and dominant background processes are hard to model**, with the available models being only poorly constrained by existing data. A robust determination of the cross-section should therefore aim at minimizing the modeling dependence.

It was found that increasing the purity of the signal region (or equivalently the signal-to-background ratio) provided the most straightforward way to address the aforementioned issues, without introducing further complications in the analysis. The analysis was optimized by studying different b-tagging operating points, corresponding to different efficiencies for identifying b-jets and rejecting c and LF jets and the optimal point was chosen as a compromise between reducing the statistical uncertainty and increasing the purity of the signal region. A low background contribution also

implies that the result is less sensitive to the background uncertainties. A further reduction of the background contributions was accomplished by performing the measurement in the dilepton decay channel. In spite of having the lowest branching ratio, the dilepton decay channel suffers from a lower background contamination, compared to the all-hadronic and semi-leptonic channels and is free of contributions from W decays into a cs pair, which have a high probability of being mis-tagged.

The analysis was based on a cutting and counting method, using rectangular cuts on a set of discriminating variables, such as the b-tagging weight, the jet and lepton kinematics etc, as will be described in more detail in Chapter 8. The cut-and-count method using rectangular cuts is the simplest and most intuitive analysis technique and is therefore well suited as the first approach to complicated measurements. While it usually provides a lower signal-to-background separation power than its more sophisticated counterparts it offers an increased robustness and is easier to interpret.

Finally, the measurement was performed in a region where the detector operates with a high efficiency, excluding regions in which the detector has little or no sensitivity. In order to compare the measurement with theoretical predictions, the measurement was extrapolated (unfolded) to a reference phase-space. This "fiducial" phase space was designed to be as close as possible to the region which is experimentally accessible, in order to minimize the extrapolation from the measurable phase space and the associated modeling dependence. More details on the definition of the fiducial phase space are given in Chapter 8.

6.1 Extraction of the cross-section

The cross-section for the production of a $t\bar{t}b\bar{b}$ final state is given by

$$\sigma^{\text{fid}}_{t\bar{t}b\bar{b}} = \frac{N_{\text{sig}}}{\mathcal{L} \cdot \epsilon_{\text{fid}}} = \frac{N^{\text{data}}_{4b} - N_{\text{bg}}}{\mathcal{L} \cdot \epsilon_{\text{fid}}}, \tag{6.1}$$

where N_{sig} denotes the number of signal $t\bar{t}b\bar{b}$ events, N^{data}_{4b} denotes the number of events measured in the signal region, N_{bg} the number of background events in the signal region, ϵ_{fid} the fiducial efficiency, i.e. the ratio of detected $t\bar{t}b\bar{b}$ events to the total number of produced $t\bar{t}b\bar{b}$ events and $\mathcal{L}$ the integrated luminosity of the data sample.

The number of signal events N_{sig} contains all events that lie in the fiducial volume, irrespective of their production mechanism. Processes like $t\bar{t}H(b\bar{b})$ and $t\bar{t}Z(b\bar{b})$ which lead to the same final state as the QCD production of $t\bar{t}b\bar{b}$ are considered to be part of the signal.

The background events N_{bg} in (6.1) can come from three sources. The first source corresponds to $t\bar{t}$ events produced in association with c or LF jets. These end up in the signal region if two jets are mis-tagged. This background will be referred to as $N_{t\bar{t}+\text{jets}}^{\text{mis-tagged}}$.

The second background source comes from $t\bar{t}b\bar{b}$ events that lie outside of the fiducial volume, but are reconstructed in the signal region due to detector effects. Since these events contain $t\bar{t}b\bar{b}$ in the final state at parton level, their contribution to the signal region must be scaled with the number of signal events. This background will be referred to as "non-fiducial" and the associated number of events will be denoted by $N_{t\bar{t}b\bar{b}}^{\text{non-fiducial}}$.

The final background source, denoted by $N_{\text{bg}}^{\text{non-}t\bar{t}+\text{jets}}$, contains non-$t\bar{t}$+jet events, i.e. events without a $t\bar{t}$ pair in the partonic final state, and includes contributions from single top, Z+jet and di-boson events. The Venn diagram in Figure 6.1 represents the classification of the events reconstructed in the signal region into signal and background.

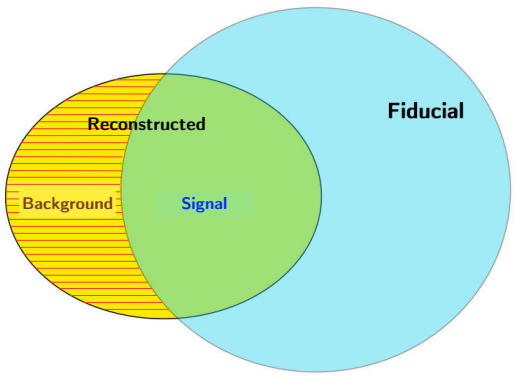

Figure 6.1: Venn diagram showing the reconstructed and fiducial regions. The hashed region, which corresponds to events reconstructed in the signal region but not satisfying the fiducial phase space requirements, represents the total background, comprising of non-fiducial $t\bar{t}b\bar{b}$ events, mis-tagged $t\bar{t}$+jets events and non-$t\bar{t}$+jet events.

The fiducial efficiency, ϵ_{fid}, expresses the probability to reconstruct an event that lies in the fiducial volume and is given by the product of the efficiencies for the reconstruction and identification of all final-state objects, as described in Chapter 12.

Equation (6.1) can be rewritten to make manifest the different background contributions, by noting that

$$N_{4b}^{\text{data}} = N_{\text{sig}} + N_{t\bar{t}b\bar{b}}^{\text{non-fiducial}} + N_{t\bar{t}+\text{jets}}^{\text{mis-tagged}} + N_{\text{bg}}^{\text{non-}t\bar{t}+\text{jets}} \tag{6.2}$$

The partonic processes that give rise to mis-tagged $t\bar{t}$+jets events and non-$t\bar{t}$+jets events are not the same as the ones that give rise to $t\bar{t}b\bar{b}$ events. As a result, $N_{t\bar{t}+\text{jets}}^{\text{mis-tagged}}$ and $N_{\text{bg}}^{\text{non-}t\bar{t}+\text{jets}}$ are expected to be independent of the amount of signal events. Their contribution to the signal region can therefore be estimated from simulation and subtracted from the number of events in the signal region.

In order to take into account the fact that non-fiducial $t\bar{t}b\bar{b}$ events come from the same underlying partonic process as the signal, $N_{t\bar{t}b\bar{b}}^{\text{non-fiducial}}$ should be scaled according to the number of signal events. To avoid relying on simulation for the prediction of the absolute cross-section of the non-fiducial background, one can instead make use of the weaker assumption that the simulation predicts correctly the fraction of signal events in the ensemble of signal and non-fiducial events.

Equation (6.2) can be rearranged to express the total number of events (both signal and non-fiducial) that are expected to be produced in a $t\bar{t}b\bar{b}$ process as

$$N_{\text{sig}} + N_{t\bar{t}b\bar{b}}^{\text{non-fiducial}} = N_{4b}^{\text{data}} - N_{t\bar{t}+\text{jets}}^{\text{mis-tagged}} - N_{\text{bg}}^{\text{non-}t\bar{t}+\text{jets}}. \tag{6.3}$$

In order to obtain the fiducial $t\bar{t}b\bar{b}$ cross-section, equation (6.3) should be scaled by the fraction of $t\bar{t}b\bar{b}$ events which are expected to lie in the fiducial volume, which can be estimated from simulation as

$$f_{\text{sig}} = \frac{N_{\text{sig}}}{N_{\text{sig}} + N_{t\bar{t}b\bar{b}}^{\text{non-fiducial}}}. \tag{6.4}$$

The formula for the $t\bar{t}b\bar{b}$ fiducial cross-section becomes

$$\sigma_{t\bar{t}b\bar{b}}^{\text{fid}} = \frac{\left(N_{4b}^{\text{data}} - N_{t\bar{t}+\text{jets}}^{\text{mis-tagged}} - N_{\text{bg}}^{\text{non-}t\bar{t}+\text{jets}}\right) \cdot f_{\text{sig}}}{\mathcal{L} \cdot \epsilon_{\text{fid}}}. \tag{6.5}$$

It has to be noted that equation (6.5) makes use of only the fraction of fiducial to total $t\bar{t}b\bar{b}$ events and there is no assumption involved on the total $t\bar{t}b\bar{b}$ cross-section.

6.2 The measurement ingredients

In order to calculate the fiducial $t\bar{t}b\bar{b}$ cross-section, we need to estimate the factors on the right hand-side of equation (6.5). This is done as follows:

- $\mathcal{L}$: corresponds to the integrated luminosity of the dataset that was used for this analysis, as described in Chapter 7.
- N_{4b}^{data}: is estimated by counting the number of events in data that fulfill the selection requirements. Chapter 8 presents the selection requirements that define the signal region and discusses the definition of the fiducial phase space. Potential systematic effects that may arise due to the specificities of the $t\bar{t}b\bar{b}$ event topology are discussed in Chapter 9.
- $N_{t\bar{t}+\text{jets}}^{\text{mis-tagged}}$, $N_{\text{bg}}^{\text{non}-t\bar{t}+\text{jets}}$, f_{sig}: are obtained from simulation, as described in Chapter 11.
- ϵ_{fid}: is obtained from simulation, as described in Chapter 12.

The uncertainties associated with the estimation of the aforementioned factors are described in Chapter 13. The final result is shown in Chapter 14.

Chapter 7

Data and simulation samples

7.1 Dataset selection

The analysis was performed using the 2012 dataset of pp collisions corresponding to $\sqrt{s} = 8$ TeV. Events were required to fulfill standard data quality requirements, corresponding to data-taking periods with stable beam collisions during which all detector subsystems were fully operational and no noise bursts or data integrity errors were observed in the LAr calorimeter.[1] The dataset that fulfills the data quality requirements corresponds to an integrated luminosity of

$$\mathcal{L} = 20.3 \pm 0.6 \text{ fb}^{-1}. \tag{7.1}$$

7.1.1 Triggers

Events were required to pass a single electron or single muon trigger chain. For electrons the logical OR of two unprescaled single electron triggers was used: one corresponding to a threshold of 24 GeV for the electron cluster E_T (`EF_e24vhi_medium1`) and the other corresponding to a threshold of 60 GeV (`EF_e60_medium1`).

For the low threshold trigger, an isolation requirement is applied, by requiring the sum of the transverse momenta of the tracks[2] that lie in a cone of radius $R = 0.2$

[1] This corresponds to the following "Good Run List":
`data12_8TeV.periodAllYear_DetStatus-v61-pro14-02_DQDefects-00-01-00_PHYS_StandardGRL_All_Good.xml`

[2] The tracks that are used by the HLT have to satisfy the following criteria: $p_T > 1$ GeV, $|d_0| < 1.5$ mm, $|z_0| < 1$ mm, at least 1 hit in the first layer of the pixel detector, at least 9 silicon hits and no pixel holes.

around the electron-candidate track (excluding the electron track) to be less than 10% of the trigger electron's transverse energy. This isolation cut is applied in order to reduce the high rate of electrons produced in hadron decays.

Since the isolation requirement which is applied on the primary trigger is absolute, it becomes inefficient in the region $E_T \gtrsim 60$ GeV, since high-p_T electrons have a higher probability of producing Bremsstrahlung photons (which further split into e^+e^- pairs) and therefore have a higher probability of failing the isolation cut. The logical OR with a second trigger, which has a higher E_T threshold and no isolation requirements, is used in order to increase the trigger efficiency for high-E_T electrons.

The triggered electron candidate is required to pass the "medium" electron identification criteria, defined in Table 5.1. These use the same variables and cut values as the ones employed by the offline electron identification.

For muons the OR of two unprescaled single muon triggers was used: one corresponding to a threshold of 24 GeV with isolation requirements (`EF_mu24i_tight`) and the other corresponding to a threshold of 36 GeV with no isolation requirements (`EF_mu36_tight`).

The muon isolation requirement at the trigger level is applied by requiring the sum of the tracks[3] in a cone of radius $R = 0.2$ around the muon candidate track (excluding the muon track itself) to be less than 12% of the muon track's p_T. The isolation criterion is applied using ID tracks.

The logical OR with the higher threshold trigger without an isolation cut is applied in order to increase the efficiency for high p_T muons. The trigger efficiencies for electrons and muons are shown in Figure 7.1.

7.2 Simulated samples

Simulated event samples obtained with Monte Carlo event generators were used to estimate the background contributions as well as to calculate the fiducial efficiency. For the modeling of the signal process, several generators were used, having different perturbative accuracy and covering a range of choices for the parton shower, hadronization, PDF and underlying event tune.

[3]The following cuts are applied on ID tracks: $p_T > 1$ GeV, $|z_0^{\text{muon}} - z_0^{\text{track}}| < 6$ mm

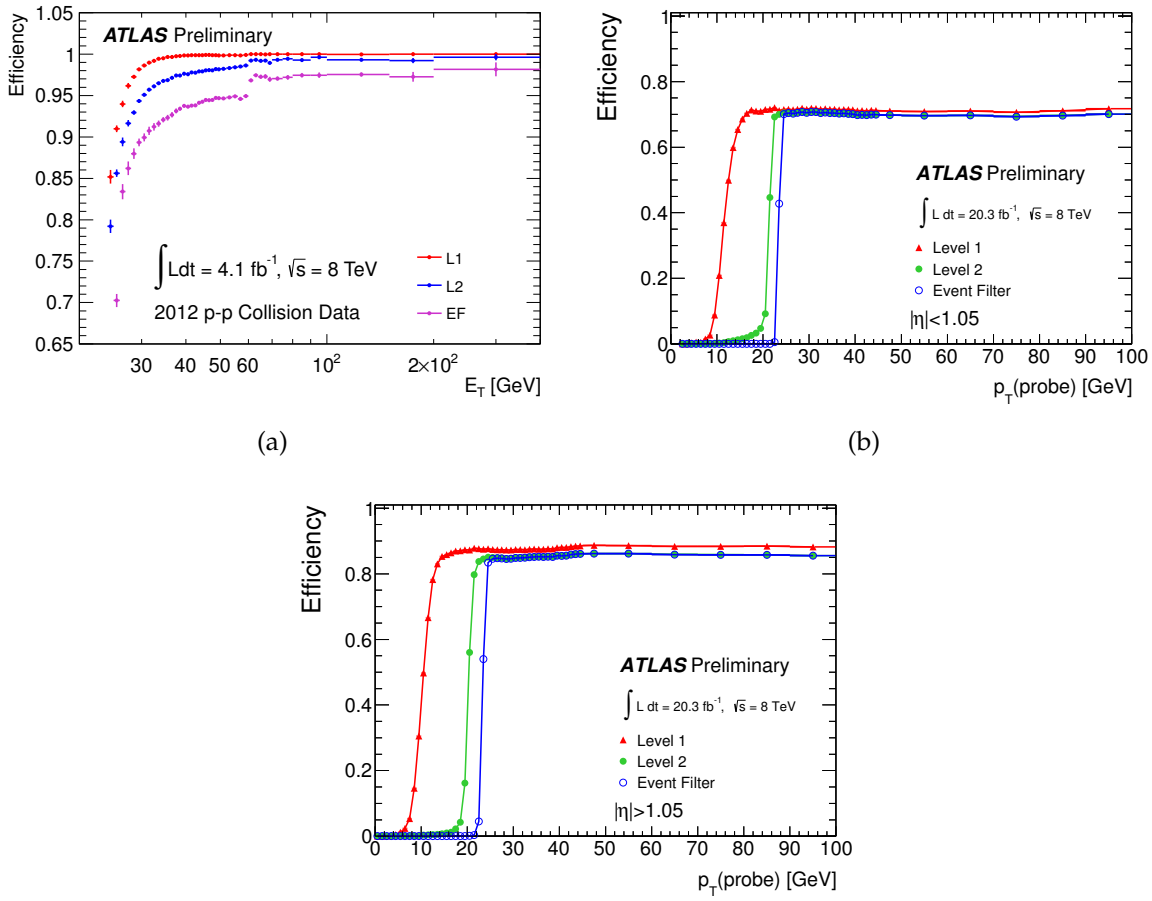

Figure 7.1: Efficiency for the OR of the two single electron triggers used in the analysis as a function of the electron E_T (upper left plot). The efficiency for the OR of the two single muon triggers used in the analysis is shown in the upper right and bottom plots for the barrel and end-cap regions respectively [138, 139].

The nominal signal sample was produced with the POWHEG-BOX, version 1, revision 2129 [67, 68, 140] interfaced to Pythia 6.427 [81]. It offers NLO matrix elements for the $pp \to t\bar{t}$ process [91]. The top decays are also simulated retaining approximate spin correlations according to the method presented in [141] but neglecting radiative corrections in the top decays. The calculation employs the 5 flavor scheme. Additional b-quarks are modeled from the parton shower with LL precision. The CT10 PDF set [142] was used for the calculation of the $pp \to t\bar{t}$ matrix elements, while the the Perugia 2011C tune [143], which employs the CTEQ6L1 PDF set [144] was used for the

parton shower. The renormalization and factorization scales were set equal to

$$\mu_R = \mu_F = \sqrt{m_{\text{top}}^2 + p_{T,\text{top}}^2}, \tag{7.2}$$

where $p_{T,\text{top}}$ is evaluated from the underlying Born configuration. Considering a LO process $pp \to ij$, the real NLO corrections correspond to parton branchings of the kind $i \to i_1 i_2$, so that the process becomes $pp \to i_1 i_2 j$. For such an event the underlying Born kinematics is defined by replacing the 4-momenta p_{i_1}, p_{i_2} by the 4-momentum before the branching p_i.

In the Powheg method, the real emission cross-section can be separated into two contributions: $R = R^s + R^f$, where R^s is singular at low p_T and R^f is finite. The divergence of R^s at low p_T is dampened by an all-order resummation of soft/collinear logarithms encoded in the Sudakov form factor that the parton shower provides. The splitting of the cross-section into a finite and a singular part is arbitrary, and can be achieved using a function $F(p_T^2)$ of the transverse momentum of the radiation, satisfying

$$0 \leq F(p_T^2) \leq 1 \quad , \quad \lim_{p_T^2 \to 0} F(p_T^2) = 1 \tag{7.3}$$

and defining [68]

$$R^s = RF(p_T^2), \tag{7.4}$$

$$R^f = R\left[1 - F(p_T^2)\right]. \tag{7.5}$$

A possible choice for $F(p_T^2)$ is given by [145]

$$R^s = \frac{h_{\text{damp}}^2}{h_{\text{damp}}^2 + p_T^2} R \quad , \quad R^f = \frac{p_T^2}{h_{\text{damp}}^2 + p_T^2} R, \tag{7.6}$$

where p_T is the transverse momentum of the radiated parton (which for a $t\bar{t}$ event is equal to the p_T of the $t\bar{t}$ system). The parameter h_{damp}, dampens the resummation effects in the region $p_T > h_{\text{damp}}$. The nominal MC sample was generated using $h_{\text{damp}} = m_{\text{top}}$, which has been shown to describe the multiplicity and transverse momentum spectra of the jets produced in association with a $t\bar{t}$ pair [146].

The aforementioned $t\bar{t}$ sample was also interfaced to HERWIG 6.520 [83], in order to probe the effect of modeling of the parton shower and hadronization on the measure-

ment. An additional $t\bar{t}$ sample was generated using the same settings as the nominal sample but raising the h_{damp} parameter from $h_{\text{damp}} = m_{\text{top}}$ to $h_{\text{damp}} = \infty$. This sample was used for gauging the effect of the modeling of the p_T spectrum of the $t\bar{t}$ system on the cross-section.

A sample offering a description of the $pp \to t\bar{t}b\bar{b}$ process in terms of LO matrix elements was also used. More specifically a $pp \to t\bar{t} + \leq 3$ partons sample was was generated with MADGRAPH [147] interfaced to PYTHIA 6.427 using the Perugia 2011C tune. For this sample the CT10 PDF set was used in the calculation of the matrix element. MADGRAPH uses a five-flavor scheme for the calculation of the matrix element, although with massive b-quarks. This sample is expected to offer a more accurate description of the kinematics of the additional b quarks in the high-p_T, non-collinear region compared to the POWHEG samples mentioned above.

The effect of the renormalization and factorization scale variation is studied using the aforementioned MADGRAPH+PYTHIA sample. Since this sample is obtained by merging samples with different final state parton multiplicities, the renormalization and factorization scales follow from the MLM matching procedure, as implemented in MADGRAPH [66]. More specifically the final state partons, after the shower, are clustered into jets using the k_T algorithm [148] with a radius parameter $R = 1$. The clustering stops when a $2 \to 2$ process is reconstructed. The factorization scale is then set equal to the k_T scale of the last clustering and the renormalization scale is set to

$$\begin{aligned}\mu &= Q\sqrt{\left(m_i^2 + p_{T,i}^2\right)\left(m_j^2 + p_{T,j}^2\right)} \\ &= Q\left\{\left[\left(\sum_{p\in i} p_i\right)^2 + \left(\sum_{p\in i} p_{x,i}\right)^2 + \left(\sum_{p\in i} p_{y,i}\right)^2\right]\right. \\ &\times \left.\left[\left(\sum_{p\in j} p_j\right)^2 + \left(\sum_{p\in j} p_{x,j}\right)^2 + \left(\sum_{p\in j} p_{y,j}\right)^2\right]\right\}^{1/2}, \end{aligned} \tag{7.7}$$

where i, j are the two clustered jets in the final state. The factor Q is varied by a factor of two ($Q = 2$ in the Q2up sample and $Q = 1/2$ in the Q2down sample). The Perugia 2012 radHi(radLo) tune [143] was used for the Q2down(Q2up) sample in order to harmonize the scales used in the calculation of the matrix elements with the scales used in the parton shower and the simulation of the underlying event.

Table 7.1 contains a list of the $t\bar{t}$ samples used in this analysis. All of these samples were normalized to the inclusive $t\bar{t}$ cross-section calculated at NNLO+NNLL accuracy [149].

The contribution from the $t\bar{t} + W/Z$+jets processes was simulated using MADGRAPH with the CTEQ6L1 PDF set, interfaced to PYTHIA 6.426 using the AUET2B tune.

The $t\bar{t}H$ process was simulated using NLO matrix elements for $pp \to t\bar{t}H$ provided by the HELAC-ONELOOP package [150], interfaced to PYTHIA 8 [82] through POWHEG-BOX [140], also known as the POWHEL approach [151]. The matrix element calculation was performed using the CT10 PDF set and the parton shower used the AU2CT10 tune.

The background from Z+jets events was simulated using LO matrix elements from ALPGEN 2.14 with the CTEQ6L1 PDF set, interfaced to PYTHIA 6.426 and using the Perugia 2011C tune. Samples of different parton multiplicities have been merged with the MLM merging scheme [152], to provide samples of LO+PS accuracy with up to 5 partons (in addition to the Z boson) for the case of Z+LF (light flavor) samples and up to 3 additional partons in the case of the $Zc\bar{c}$ and $Zb\bar{b}$ samples. The samples involving the production of heavy flavor (HF) partons have been found to underestimate the HF content in Z+jets events and a re-weighting procedure, described in Section 10.1 has been devised to correct for it.

The background from di-boson processes was simulated using ALPGEN 2.14 with the CTEQ6L1 PDF set, interfaced to HERWIG 6.520 using the AUET2CTEQ6L1 tune.

The single-top process in the Wt channel was simulated using POWHEG-BOX, version 1, revision 2330, interfaced to PYTHIA 6.426 using the Perugia 2011C tune. The CT10 PDF set was used for the matrix element calculation, while the CTEQ6L1 PDF set was used in the parton shower. The interference with the $t\bar{t}$ process that arises at NLO was removed by the so-called diagram removal scheme [141]. Two additional Wt samples were used to assess the modeling uncertainties. The first of those consisted of the same POWHEG-BOX sample, this time obtained with the diagram subtraction scheme. The second sample was generated with MC@NLO 4.06 [141, 153] with the CT10 PDF set, interfaced to HERWIG 6.520 using the AUET2CT10 tune. In the s and t-channels one can have only one lepton from the $t \to Wb$ decay, therefore in order for such a process to be mis-identified as signal one jet must be mis-identified as a lepton and an additional jet is needed to take the place of the mis-identified jet. Both the s

and t-channel contributions are therefore negligible and are not considered further in the analysis.

Table 7.2 contains a list of the non-$t\bar{t}$ MC samples used in this analysis.

The samples that use HERWIG and PYTHIA for showering and hadronization were interfaced to PHOTOS [154] for modeling of QED final-state radiation and TAUOLA [155] for modeling the decays of τ leptons. The $t\bar{t}H$ sample was interfaced to PHOTOS++ [156]. The samples which employ HERWIG for the simulation of parton showers were interfaced to JIMMY for the simulation of multi-parton interactions [78].

All simulated samples are normalized to their respective theoretical cross-sections, using the latest available theoretical estimates. All samples are generated using a top mass of $m_t = 172.5$ GeV. The Higgs mass for the $t\bar{t}H$ sample is set to $m_H = 125$ GeV.

All the MC samples are simulated taking into account the pile-up conditions in the 2012 data, including both the effects of in-time and out-of-time pile-up. Pile-up is modeled by overlaying simulated hits from events with exactly one inelastic (signal) collision per bunch crossing with hits from non-single diffractive (minimum-bias) events that are produced with PYTHIA 8.160 using the A2M tune [157] and the MSTW2008LO PDF [99]. The number of overlaid minimum-bias events is sampled according to a Poisson distribution with a mean corresponding to the average number of inelastic pp interactions, recorded in the 8 TeV run. The bunch-filling pattern surrounding the signal interaction is used to modulate this number, so that only filled bunch-crossings are simulated. The number of simulated bunch crossings is different for each detector subsystem, taking into account their different sensitivities to out-of-time pile-up.

The generated particles are propagated either through a full simulation of the ATLAS detector [158] using GEANT4 [159] or a fast detector simulation, with parametrized calorimeter showers [160].

We note that in several of the samples listed above, in particular the ones employing NLO matrix elements, different PDF sets are used in the calculation of the matrix element and in the tune, the latter employing a LO PDF set. This is a priori inconsistent, however for all relevant applications this usage offers several advantages without leading to any significant complications. More precisely, the use of different PDF sets in the matrix element calculation and in the tune allows to explore the impact of several PDF sets on the matrix element calculation, eliminating the need for a complete

retuning of the parton showers and MPI. Moreover, the bulk of the MPI and ISR interactions involve low p_T exchanges, which probe small x values of the PDFs. At NLO and higher orders, the splitting functions obtain a dependence $\ln(1/x)$, which diverges as $x \to 0$ [161]. In order to avoid that the gluon PDF becomes too big in the medium to high x region, where the PDFs are fitted to existing data, some PDF groups allow that the gluon PDF becomes negative at low x. For this reason, the use of LO PDFs are preferred over the use of NLO ones for tuning the MPI and (initial state) parton showers. Therefore in calculations employing NLO matrix elements, it is advisable to use two different PDF sets, a NLO one for the matrix element and a LO one for the tune [162].

Sample	Generator	Top decays	Description of $t\bar{t}b\bar{b}$	Flavor scheme	N_{events}	Detector simulation
$t\bar{t}$ ($h_{\text{damp}} = m_{\text{top}}$, nominal)	POWHEG+PYTHIA 6	non all hadronic	PS	5F	50M	GEANT4
$t\bar{t}$ ($h_{\text{damp}} = \infty$)	POWHEG+PYTHIA 6	di-lepton	PS	5F	40M	AFII
$t\bar{t}$ (Powheg+Herwig)	POWHEG+HERWIG	di-lepton	PS	5F	10M	GEANT4
$t\bar{t}+ \leq 3j$ (MADGRAPH+PYTHIA 6)	MADGRAPH+PYTHIA 6	di-lepton	merged LO+PS	5F massive b	5M	AFII
$t\bar{t}+ \leq 3j$ (MADGRAPH+PYTHIA 6 Q2down)	MADGRAPH+PYTHIA 6	di-lepton	merged LO+PS	5F massive b	5M	AFII
$t\bar{t}+ \leq 3j$ (MADGRAPH+PYTHIA 6 Q2up)	MADGRAPH+PYTHIA 6	di-lepton	merged LO+PS	5F massive b	5M	AFII

Table 7.1: Monte Carlo samples used for assessing the $t\bar{t}$ modeling uncertainties. The last column indicates whether the samples are propagated through a full simulation of the ATLAS detector (GEANT4) or a fast simulation using parametrized calorimeter showers (AFII).

Sample	Generator	Decay channel	Number of events	Normalization
Single top (Wt channel - DR)	MC@NLO+HERWIG	inclusive	2M	approx. NNLO [163]
Single top (Wt channel - DR)	POWHEG+PYTHIA 6	di-lepton	1M	approx. NNLO [163]
Single top (Wt channel - DS)	POWHEG+PYTHIA 6	di-lepton	1M	approx. NNLO [163]
ZZ, WZ, WW	ALPGEN+HERWIG	W(incl.),$Z \to ll$	2.46M	NLO [164]
Z+jets	ALPGEN+PYTHIA 6	di-lepton	29M	NNLO [165]
$t\bar{t} + W/Z$+jets	MADGRAPH+PYTHIA 6	non all hadronic	3.2M	NLO [166]
$t\bar{t}H$	POWHEL+PYTHIA 8	di-lepton	1.9M	NLO

Table 7.2: Monte-Carlo samples for non-$t\bar{t}$+jets processes used in the analysis.

Chapter 8

Event selection and definition of the fiducial phase space

The measurement of the $t\bar{t}b\bar{b}$ final state involves the reconstruction and identification of electrons, muons and jets, as well as the identification of b-jets. The following sections describe the reconstruction and selection of the final state objects, as well as the selection requirements imposed in order to isolate the signal events from the ensemble of events selected by the single lepton trigger chain. This chapter also describes the definition of the fiducial phase space, to which the measurement is unfolded.

8.1 Object reconstruction and selection

The final state objects that are used in the measurement are reconstructed and selected as follows.

Electrons: Electrons are required to have $p_T > 25$ GeV and $|\eta|$ <2.47, excluding the transition region between the barrel and the end-cap ($1.37 < |\eta| < 1.52$). Only electrons satisfying the tightest identification criteria are selected. The longitudinal impact parameter of the electron track with respect to the primary vertex is required to be less than 2 mm. The deposited energy in a cone of radius $\Delta R < 0.2$ around the electron (excluding the deposit from the electron itself) is required to be less than 6 GeV and the sum of the transverse momenta of tracks in a cone of radius $\Delta R < 0.3$ around the electron track (excluding the electron track momentum) is required to

be less than 6 GeV. These isolation requirements correspond to a 98% efficiency of reconstructing and identifying true prompt electrons.

Muons: The combined muon candidate tracks are required to have $p_T > 25$ GeV, $|\eta| < 2.5$ and to pass tight identification criteria. Their longitudinal impact parameter with respect to the primary vertex is required to be less than 2 mm. Muons are required to be separated by $\Delta R > 0.4$ from the nearest jet, and to satisfy the so-called mini-isolation requirement $I_\ell < 0.05$, where I_ℓ is the sum of p_T of tracks[1] in a cone of radius $10\ \text{GeV}/p_T^{\text{muon}}$ around the muon, excluding the muon track, divided by the p_T of the muon.

Jets: Jets reconstructed with the anti-k_T algorithm [86] with a radius parameter of $R = 0.4$ are used. The jets' transverse momenta are corrected using the jet-area based method [127] in order to remove the contributions from pile-up interactions and are calibrated with the LCW+JES scheme. Jets are required to have $p_T > 25$ GeV and $|\eta| < 2.5$. To reduce the contribution from pile-up jets, jets with $p_T < 50$ GeV are required to satisfy $|\text{JVF}(\text{jet}, \text{PV}_0)| > 0.5$, where the JVF variable is defined in equation (5.5). Jets within $\Delta R < 0.2$ of a selected electron are not considered.

Electron-jet overlap removal: Since the jet clustering algorithms incorporate the electromagnetic clusters in the clustering procedure, jets that are within $\Delta R < 0.2$ of a reconstructed electron are removed, in order to avoid counting the electron energy deposits twice. If the nearest jet surviving the above cut is within $\Delta R < 0.4$ of a reconstructed electron, the electron is removed, in order to obtain an event sample in which the electrons are cleanly separated from nearby jet activity.

***b*-tagging:** Reconstructed jets are b-tagged using the MV1 algorithm [135, 167] Jets are defined as being b-tagged if the MV1 weight is greater than 0.7892, which corresponds to an inclusive efficiency of 70%. The b-tagging efficiency in simulation is corrected with scale factors derived from measurements in dilepton $t\bar{t}$ events using a combinatorial likelihood approach [168].

[1] The tracks must have $p_T > 1$ GeV, $d_0 < 10$ mm, $z_0 \sin\theta < 10$ mm and a total of at least 4 hits and 0 dead sensors in the SCT and pixel detectors.

8.2 Event selection

Events that fired the single lepton trigger chain are required to have at least 1 primary vertex with at least 5 associated reconstructed tracks. In order to suppress events containing cosmic rays, events with two muons with a transverse impact parameter with respect to the primary vertex $d_0 > 0.5$ mm and separated in azimuth by $\Delta\phi > 3.1$ rad are vetoed.

Since two leptons of opposite charge are expected from the decays of the top and antitop quarks, the events are required to have exactly two leptons of opposite charge reconstructed with the offline algorithms, with at least one of them being within $\Delta R < 0.15$ from the leptons that fired the corresponding triggers. Occasionally muons may radiate photons which carry a substantial amount of the muon's energy[2]. These Bremsstrahlung photons can then split into an e^+e^- pair and leave a large amount of energy deposit in the calorimeter, causing the muon to be reconstructed as both a muon and an electron. In order to suppress this process, events containing an electron and a muon separated by $\Delta\theta < 0.005$ and $\Delta\phi < 0.005$ are vetoed. Events in which the pair of leptons had an invariant mass $M_{ll} < 15$ GeV are vetoed. In order to suppress the background from Z+jets events, in which the Z boson decays into two leptons, events containing same flavor leptons (ee or $\mu\mu$) are vetoed if $|M_{ll} - 91\text{ GeV}| < 10$ GeV. In addition to the above cuts, simulated events had to fulfill the requirement that the di-lepton pair do not come from hadron decays. This cut ensures that only leptons from W decays are selected.

A "pre-selected" sample is defined as the set of events fulfilling the requirements described above and containing at least two reconstructed b-jets. The pre-selected sample is 95% pure in $t\bar{t}$ events and is used as a control region for studying the modeling of the $t\bar{t}$ events. The signal region is defined as the subset of the "pre-selected" sample which contains exactly four reconstructed b-jets.

Table 8.1 contains a summary of the event selection requirements.

[2]This effect is known as catastrophic Bremsstrahlung.

Pre-selection
≥ 1 primary vertex with ≥ 5 associated tracks exactly two oppositely charged leptons with $p_T > 25$ GeV and $\|\eta\| < 2.5$ $M_{ll} > 15$ GeV for all channels and $\|M_{ll} - 91\| > 10$ GeV for $ee, \mu\mu$ channels ≥ 2 b-jets with $p_T > 25$ GeV and $\|\eta\| < 2.5$
Signal region
pass pre-selection exactly four b-jets

Table 8.1: Summary of requirements that define the "pre-selection" and the signal regions.

8.3 Definition of the fiducial phase space

The fiducial phase space is designed to be as close as possible to the phase space of the measurement, so as to minimize extrapolations in phase-space regions which are not experimentally accessible and where, as a result, the validity of the simulation cannot be verified.

Leptons and jets on truth level are defined using particles directly produced in pp interactions with a lifetime greater than 30 ps or from subsequent decays of particles with a shorter lifetime. This lifetime cut corresponds to a decay length of $\ell = 1 \cdot \beta\gamma$ cm in the detector rest frame. Since the first detector layer is only 5 cm away from the interaction point, particles with a lifetime longer than 30 ps, produced even at moderately high energies, have a significant probability of interacting with the detector material before they decay and therefore are allowed to be decayed only by the detector simulation package, which correctly accounts for the particles' interactions with the detector material.

To select the leptons from W-boson decays, all leptons (e, μ, ν_e, ν_μ, ν_τ) are required to not be hadron decay products[3]. Electrons and muons are "dressed" by adding to their four-momentum the four-momenta of photons within a cone of radius $R = 0.1$ around the original lepton's direction. Photons which are produced by the interaction of the primary particles from the hard scattering interaction with the detector material are not used in the dressing procedure. The dressing procedure mimics the fact that electrons clusters have a size of $\eta \times \phi = 0.125 \times 0.125$ in the barrel region and $\eta \times \phi = 0.125 \times 0.175$ in the end-cap region, and therefore collinear photon radiation cannot be resolved in the calorimeter for $\Delta R(e, \gamma) \lesssim 0.1$. While for muons, the object after the emission of photon radiation is what comes closest to what is reconstructed as a muon track, the Bremsstrahlung effects for muons are expected to be much smaller than for electrons[4] therefore muons are dressed so that they are handled on equal footing with electrons. The dressed leptons are required to be within $|\eta| < 2.5$ and have $p_T > 25$ GeV.

Jets are defined using the anti-k_t algorithm with a radius parameter of $R = 0.4$. Following what has been done for the jet calibration procedure, all particles are

[3] Leptons coming from $W \to \tau \to e/\mu$ are also considered in the definition of the fiducial phase space.

[4] The ratio of the radiated powers behaves like $\frac{P_e}{P_\mu} \propto \left(\frac{\gamma_e}{\gamma_\mu}\right)^4 \propto \left(\frac{m_\mu}{m_e}\right)^4 \sim 10^9$.

considered for jet clustering, except for leptons produced from W-boson decays[5]. Photons that are used to dress electrons and muons are also excluded from the jet clustering. Jets are required to be within $|\eta| < 2.5$ and have $p_T > 20$ GeV.

Truth level jets are identified as b-jets (c-jets) if a b (c and no b) hadron with $p_T > 5$ GeV is ghost-matched to the jet. Ghost matching is a procedure to associate particles to jets, based on the notion of the jet catchment area [129]. Isolated anti-k_T jets are circular and therefore a particle can be matched to a jet with a geometrical matching, i.e. $\Delta R(\text{particle}, \text{jet}) < R_{\text{jet}}$, where ΔR is the Euclidean distance in the $\eta - \phi$ plane. The $t\bar{t}b\bar{b}$ cross-section peaks at $\Delta R(b, \bar{b}) \to 0$ as explained in Chapter 9, therefore a high number of close-by jets is expected in the signal region. Geometrical matching does not provide a unique answer for cases with $\Delta R(\text{jet}_1, \text{jet}_2) < R_{\text{jet}}$. Ghost matching consists of scaling a particle's 4-momentum by a small number (10^{-6}), and including it in the jet clustering, which is performed with an infrared and collinear safe algorithm (such as anti-k_T). The 4-momentum of the particle must be made small enough, so that it does not alter the result of the jet clustering. Since the clustering procedure gives a unique answer to which jet a particle is clustered, ghost matching provides more reliable results than the geometric matching[6] for non-isolated jets and is therefore more suitable for final states with close-by jets like $t\bar{t}b\bar{b}$.

Reconstructing correctly the multiplicity of b hadrons clustered in a b-jet is crucial for some of the truth-level studies presented in this note, in particular the study of the b-tagging efficiency as a function of the multiplicity of clustered b-hadrons, presented in Section 9.3. In order to avoid over-counting b/c hadrons that stem from the decay of b/c excited states, only b/c hadrons that don't decay further into b/c hadrons are considered in the ghost matching. Moreover in order to correctly identify c-jets, $b \to c$ transitions have to be excluded, therefore only c hadrons that don't come from the decay of b hadrons are considered for ghost matching.

The invariant mass of the two leptons in the fiducial phase space is required to satisfy $M_{ll} > 15$ GeV. In events with two electrons or two muons a cut on the di-lepton invariant mass is applied $|M_{ll} - 90|$ GeV > 10 GeV, in order to suppress the background from Drell-Yan events.

[5] This implies that neutrinos from hadron decays are included in jets.

[6] This refers in particular to cases where two jets are separated by $\Delta R < 0.4$. In this case two cones with radii $R = 0.4$ centered at the jet axes will overlap and the particles that lie in the overlapping region would not be uniquely assignable to either of the two jets.

Leptons and jets in events with $\min \Delta R(\text{lepton}, \text{jet}) < 0.4$ have a high probability of being mis-identified in the detector. In data, leptons overlapping with jets are handled by the overlap removal procedure that is described in Section 8.1. Performing the same overlap removal for simulated events would be ill-defined, since it would lead, among other, to a violation of four-momentum conservation. Therefore a veto on events containing leptons with $\min \Delta R(\text{lepton}, \text{jet}) < 0.4$ is instead applied in the definition of the fiducial phase space.

The fiducial phase space is defined by the presence of two leptons and exactly 4 b-jets, satisfying the criteria outlined above. Table 8.2 summarizes the requirements used in the definition of the fiducial phase space. The above definitions follow closely what was done in [146].

Fiducial phase space definition
exactly two oppositely charged leptons with $p_T > 25$ GeV and $\lvert\eta\rvert < 2.5$
$M_{ll} > 15$ GeV for all channels and $\lvert M_{ll} - 91\rvert > 10$ GeV for $ee, \mu\mu$ channels
exactly four b-jets with $p_T > 20$ GeV and $\lvert\eta\rvert < 2.5$
no jet-electron or jet-muon pair with $\Delta R < 0.4$

Table 8.2: Summary of requirements used in the definition of the fiducial phase space.

Chapter 9

Studies of potential systematic effects due to the $t\bar{t}b\bar{b}$ event topology

The presence of four b-jets in the $t\bar{t}b\bar{b}$ final state makes the identification of b-jets the key element of this analysis. As can be seen from Figure 2.1, there are two production mechanisms for b-quarks in the $t\bar{t}b\bar{b}$ final state: (i) QCD production via the splitting of a gluon into a $b\bar{b}$ pair and (ii) electroweak production, which proceeds predominantly via the decay of a top quark $t \to Wb$. The different production mechanisms affect both the kinematics of the individual b-quarks and the event topology.

Moreover, with four b-jets in the final state, the cross-section measurement is very sensitive to the knowledge of the b-tagging efficiency. For the dominant contributions to the cross-section (see Figure 2.1) we can schematically write[1]

$$\sigma_{t\bar{t}b\bar{b}} \sim \epsilon^2_{b,\text{top } b-\text{jets}} \cdot \epsilon^2_{b,\text{non}-\text{top } b-\text{jets}}, \tag{9.1}$$

where the efficiency factors ϵ_b are taken from simulation and corrected with scale factors derived from measurements in a sample of $t\bar{t}$ events. Since this sample is dominated by b-quarks from top decays, a mis-modeling of $\epsilon_{b,\text{top } b-\text{jets}}$ would be corrected by the associated scale factors. However for $\epsilon_{b,\text{non}-\text{top } b-\text{jets}}$, no dedicated scale factors exist, therefore a potential mis-modeling of $\epsilon_{b,\text{non}-\text{top } b-\text{jets}}$ could affect the measurement. Similar arguments hold for the difference in the b-tagging efficiency between b-jets with one or more clustered b-hadrons, with $t\bar{t}$ events being dominated

[1] It is known [169] that in $t\bar{t}$ events, it is more likely than average to tag a second b if one b-jet has already been tagged, i.e. the probability for tagging two b-jets is higher than ϵ^2_b, due to both kinematic and instrumental correlations.. The effect is small (<0.5% in inclusive $t\bar{t}$ events) and is neglected here for simplicity.

by jets with one clustered b-hadron and $t\bar{t}b\bar{b}$ events typically containing both. In the following sections we examine the dependence of ϵ_b on the b-jet production mechanism and on the clustered b-hadron multiplicity in order to determine their effect on the measurement.

9.1 Production of b quarks via top decay and via gluon splitting

The two b-quark production mechanisms in $t\bar{t}b\bar{b}$ events (neglecting contributions from electroweak production of $b\bar{b}$ pairs which are negligible [98]) are depicted in Figure 9.1. At leading order, when the tops are produced with no additional radiation, the top

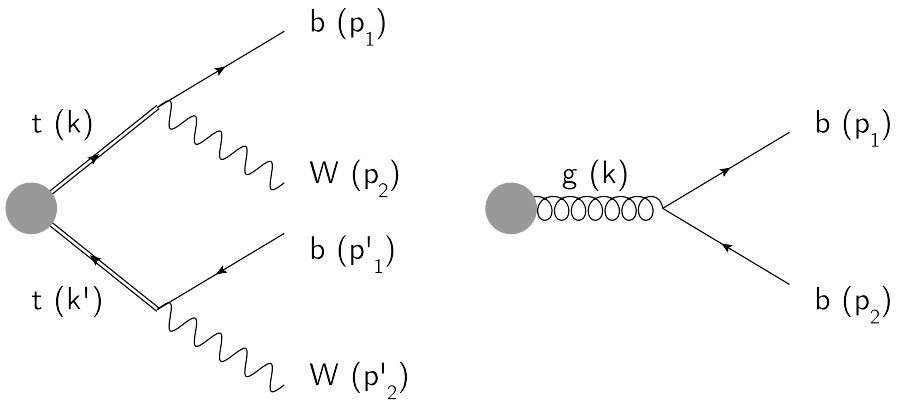

Figure 9.1: The different b-quark production mechanisms in $t\bar{t}b\bar{b}$ events: decay of top quarks (left) and gluon splitting to $b\bar{b}$ pairs (right). The parentheses indicate the 4-momenta of the partons and the blob represents all possible diagram insertions.

and anti-top are back-to-back in order to conserve 4-momentum. Therefore, we expect that in inclusive $t\bar{t}$ events, the b-quarks are mostly produced with large separations. The situation is different for b-quarks produced by gluon splitting. Considering the gluon propagator of the $g \to b\bar{b}$ amplitude in Figure 9.1, we obtain

$$\frac{1}{k_g^2} = \frac{1}{2m_b^2 + 2E_b E_{\bar{b}}(1 - \beta_b \beta_{\bar{b}} \cos\theta)}, \tag{9.2}$$

where $\beta = E/p$ is the Lorentz β factor, θ is the opening angle of the outgoing particles and we have used the fact that $k = (p_1 + p_2)$. We observe that the $g \to b\bar{b}$ amplitude is enhanced when the b-quarks are collinear, i.e. when $\theta \to 0$. We therefore expect that

in $t\bar{t}b\bar{b}$ events, there will be a small separation between non-top b-quarks/jets and a large separation between top b-quarks/jets. The small separation between non-top b-quarks also implies that the fraction of non-top b-jets with more than one clustered b-hadron will be higher than for the top-b-jets. The ΔR distribution between different types of b-jets is shown in Figure 9.2.

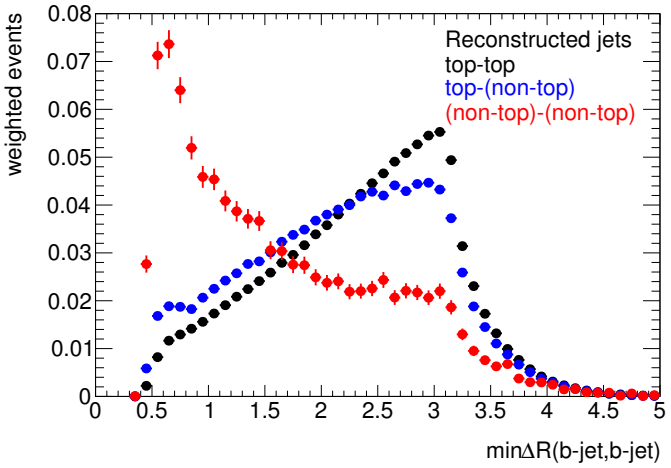

Figure 9.2: Minimum ΔR separation between two top b-jets (black), between a top and a non-top b-jet (blue) and two non-top b-jets (red). The b-jets from the top decay tend to be produced back-to-back, while non-top b-jets tend to be produced collinearly. The (non-top)-(non-top) b-jet distribution displays a cut-off at values equal to the radius parameter of the jet algorithm. The distribution is obtained from events in the pre-selected sample using the Powheg+Pythia sample with $h_{\text{damp}} = \infty$ and is normalized to unity. Other generators display qualitatively the same behavior.

The p_T and η spectra of top and non-top b-jets are shown in Figure 9.3. We observe that the non-top b-jets tend to be significantly softer than the top b-jets. The η spectrum displays small differences, with the top b-jets being produced slightly more centrally than the non-top b-jets. We thus conclude that the bulk of the signal will contain non-top b-jets with a small separation populating the low p_T region of the phase space.

9.2 Differences in b-tagging efficiency between top and non-top b-jets

In order to study the dependence of ϵ_b on the production mechanism of b-jets, simulated b-jets built from stable particles are divided in top b-jets and non-top b-jets. The

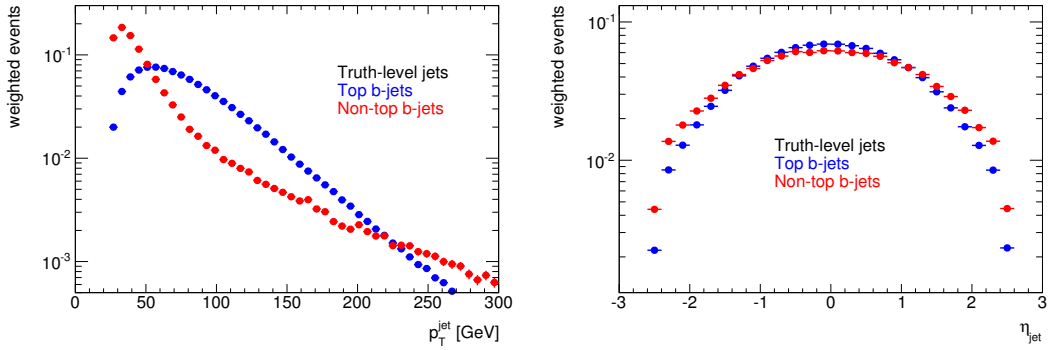

Figure 9.3: p_T (left) and η distribution of top and non-top b-jets at truth level. The non-top b-jets are significantly softer than the top b-jets. The top b-jets are slightly more central than non-top b-jets. The distribution is obtained from events in the pre-selected sample using the Powheg+Pythia sample with $h_{\text{damp}} = \infty$ and is normalized to unity. Other generators display qualitatively the same behavior.

first class consists of jets that contain among the clustered particles a b hadron and a b quark that comes from the decay of a top quark (has a top quark in its ancestors) and the second class consists of jets that contain a b hadron but no b quarks coming from the top decays. Only the b hadrons which don't decay further into b hadrons are considered. Simulated jets reconstructed from calorimeter energy deposits, inherit the type of the closest truth jet, within $\Delta R < 0.4$. If more than one truth jets lie within $\Delta R < 0.4$, the reconstructed jet is matched to the truth jet whose invariant mass is closest to the reconstructed jet's invariant mass. The b-tagging efficiency calculated as

$$\epsilon_b^{\text{top/non-top}} = \frac{\text{number of top/non-top b-jets with MV1} > w_{cut}}{\text{total number of top/non-top b-jets}}, \tag{9.3}$$

is then plotted for both classes of b-jets as a function of p_T, η and jet isolation, as shown in Figures 9.4-9.6. A dependence of ϵ_b on the production mechanism of b-jets should show up as a difference between ϵ_b^{top} and $\epsilon_b^{\text{non-top}}$ in certain kinematic regions. No significant differences are observed in the region $p_T < 50$ GeV, where the bulk of the signal lies (cf. Figure 9.4 and Figure 9.5). For jets with $p_T > 50$ GeV, some differences are observed, particularly in the regions with $|\eta| > 1.2$, where the b-tagging efficiency depends strongly on η (Figure 9.6). Part of the difference in the b-tagging efficiency between top and non-top b-jets is due to the different p_T and η spectra of the top and non-top b-jets. Since only 28% of the events measured in data have a 3rd b-jet with $p_T > 50$ GeV and only 25% of those have a 4th b-jet with $p_T > 50$ GeV, the remaining difference in the b-tagging efficiencies is not expected to affect significantly the outcome of the measurement.

We further observe that the b-tagging efficiency is significantly lower for soft jets with a small ΔR separation (Figure 9.7).

9.3 Differences in b-tagging efficiency between b-jets with one and more than one clustered b-hadron

Collinear $g \to b\bar{b}$ splittings can give rise to jets containing more than 1 b hadrons. The presence of more than 1 b-hadrons in a jet is expected to increase the probability of a jet being tagged by the b-tagging algorithm, since the jet will contain more tracks with high impact parameters and more secondary vertices than a jet with a single b hadron. The presence of b-jets with more than one b-hadron in the sample is in turn expected to increase the overall b-tagging efficiency.

The b-tagging efficiency for jets with one and two b hadrons has been estimated in simulated events using equation (9.3) and is shown in Figure 9.8. It is found that the b-tagging efficiency is up to 13% higher for b-jets containing more than one b hadron. The effect is highly dependent on the jet p_T, η and isolation and in the region that contains the bulk of the signal the differences are smaller. Moreover the fraction of jets containing 2 b hadrons is found to be small. More specifically the nominal simulation sample predicts that only 0.7% of top b-jets and 9.7% of non-top b-jets contain 2 b hadrons in the "pre-selected sample". The overall effect on the b-tagging efficiency is therefore expected to be small. Predictions for the difference in the b-tagging efficiencies are shown in Table 9.1.

Model	Fraction of top b-jets with ≥ 2 B hadrons [%]	Fraction of non-top b-jets with ≥ 2 B hadrons [%]	Difference in ϵ_b [%]
Powheg+Pythia ($h_{\text{damp}} = m_{\text{top}}$)	0.6	5.8	2.4 ± 1.2
Powheg+Pythia ($h_{\text{damp}} = \infty$, AFII)	2.0	7.9	3.9 ± 0.5
Powheg+Pythia ($h_{\text{damp}} = \infty$, GEANT4)	2.7	7.2	4.7 ± 1.2
Powheg+Herwig	0.4	11.5	11.2 ± 0.9
MadGraph+Pythia	0.9	6.7	1.2 ± 2.0
MadGraph+Pythia (Q2down)	1.5	9.1	2.3 ± 1.6
MadGraph+Pythia (Q2up)	2.3	4.3	1.7 ± 2.5

Table 9.1: Fractions of top and non-top b-jets containing at least 2 b hadrons and inclusive differences between the b-tagging efficiencies for b jets with one and with more than one b hadron. The last column is obtained from a sample with $N_{b-\text{jets}} \geq 0$ while the other two correspond to the signal region.

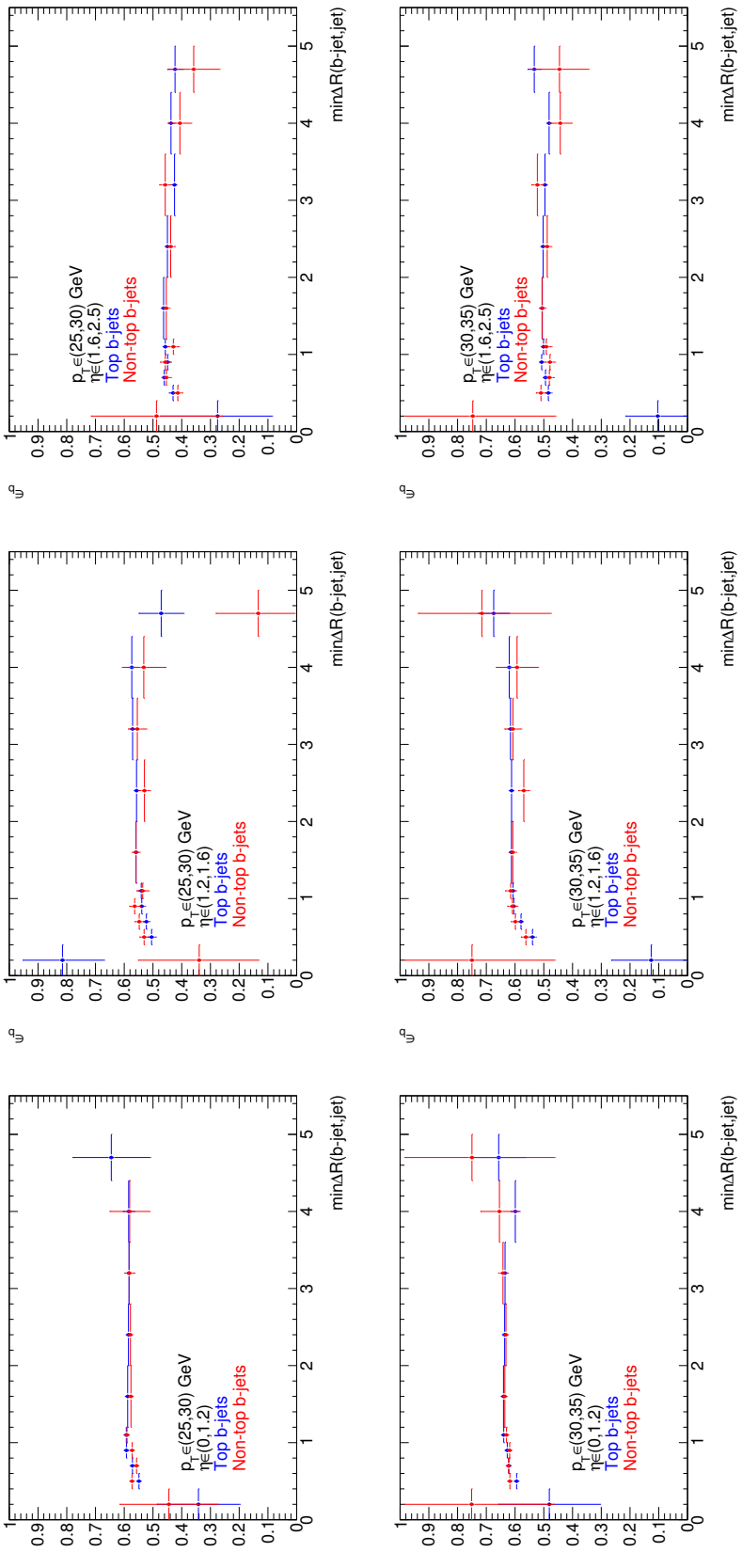

Figure 9.4: b-tagging efficiency ϵ_b in bins of p_T, η and jet isolation for top b-jets (blue) and non-top b-jets (red). The plots correspond to a sample with $N_{b-\text{jets}} \geq 0$. The p_T, η and min ΔR(jet,jet) bins are defined by using the kinematics of the truth jets to which the reconstructed jets match. The plots correspond to the region $25 \leq p_T < 30$ GeV (top line) and $30 \leq p_T < 35$ GeV (bottom line). No significant differences are observed between ϵ_b^{top} and $\epsilon_b^{\text{non-top}}$.

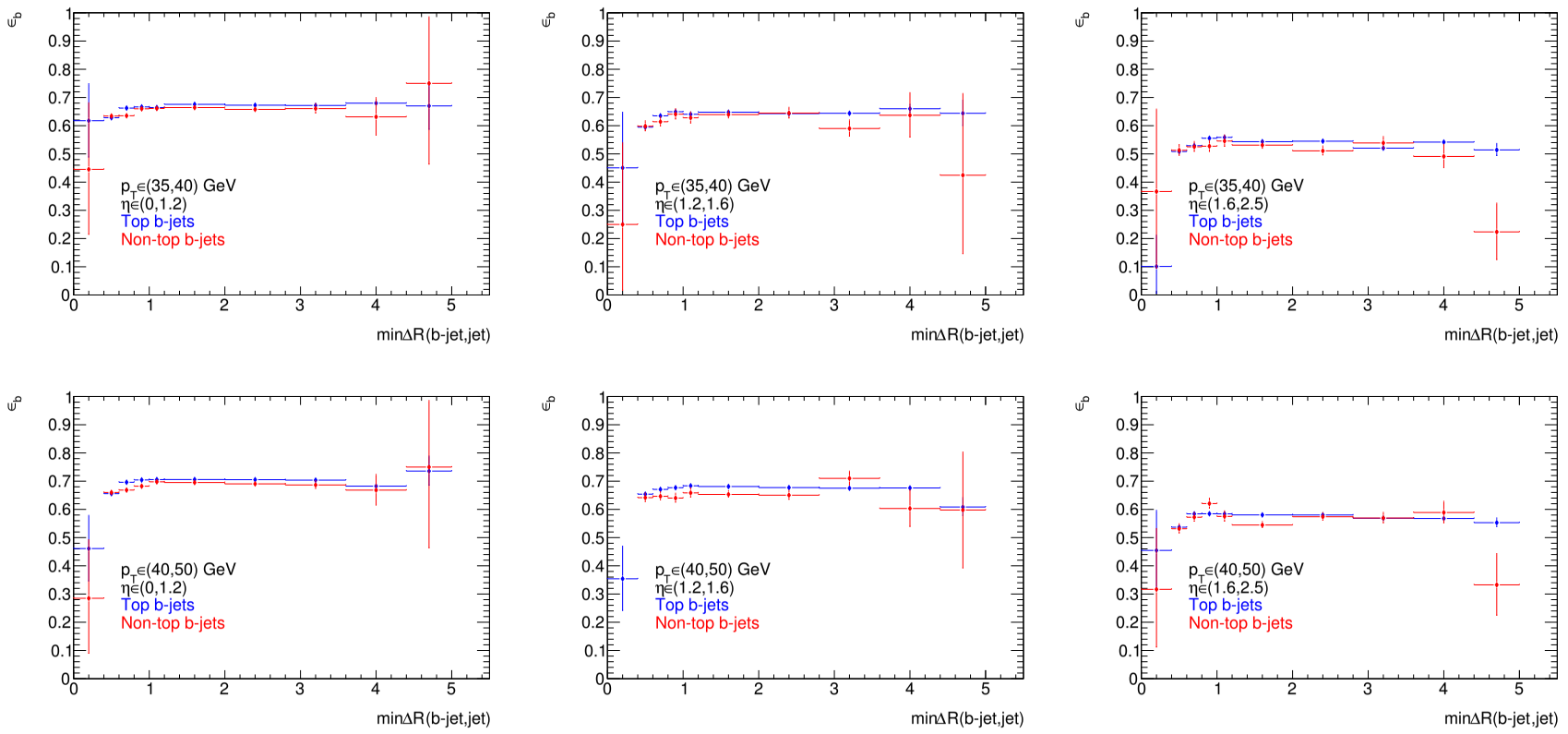

Figure 9.5: b-tagging efficiency ϵ_b in bins of p_T, η and jet isolation for top b-jets (blue) and non-top b-jets (red). The plots correspond to a sample with $N_{b-\text{jets}} \geq 0$. The p_T, η and min ΔR(jet,jet) bins are defined by using the kinematics of the truth jets to which the reconstructed jets match. The plots correspond to the region $35 \leq p_T < 40$ GeV (top line) and $40 \leq p_T < 50$ GeV (bottom line). No significant differences are observed between ϵ_b^{top} and $\epsilon_b^{\text{non-top}}$.

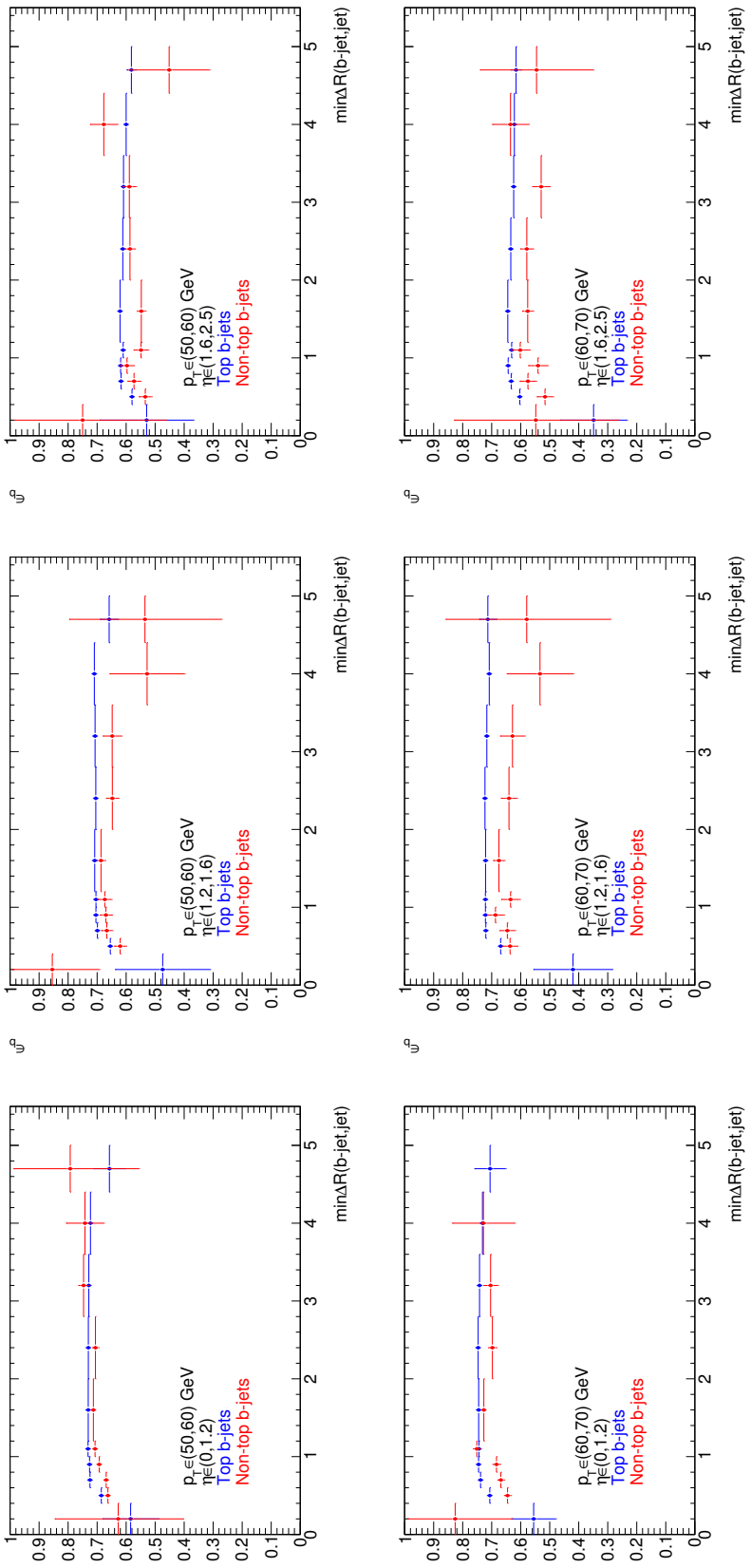

Figure 9.6: b-tagging efficiency ϵ_b in bins of p_T, η and jet isolation for top b-jets (blue) and non-top b-jets (red). The plots correspond to a sample with $N_{b-\text{jets}} \geq 0$. The p_T, η and min ΔR(jet,jet) bins are defined by using the kinematics of the truth jets to which the reconstructed jets match. The plots correspond to the region $50 \leq p_T < 60$ GeV (top line) and $60 \leq p_T < 70$ GeV (bottom line). Significant differences are observed between ϵ_b^{top} and $\epsilon_b^{\text{non-top}}$ particularly for $p_T > 60$ GeV and in the more forward regions. It is worth noticing that in the region with $|\eta| > 1.2$ the b-tagging efficiency highly depends on η (Figure 9.7 b). Moreover, as shown in Figure 9.3, the non-top b-jets are expected to have a significantly harder p_T spectrum than the non-top b-jets. Therefore the observed difference between ϵ_b^{top} and $\epsilon_b^{\text{non-top}}$ is at least partly due to the difference in the top and non-top b-jet kinematics within the bin.

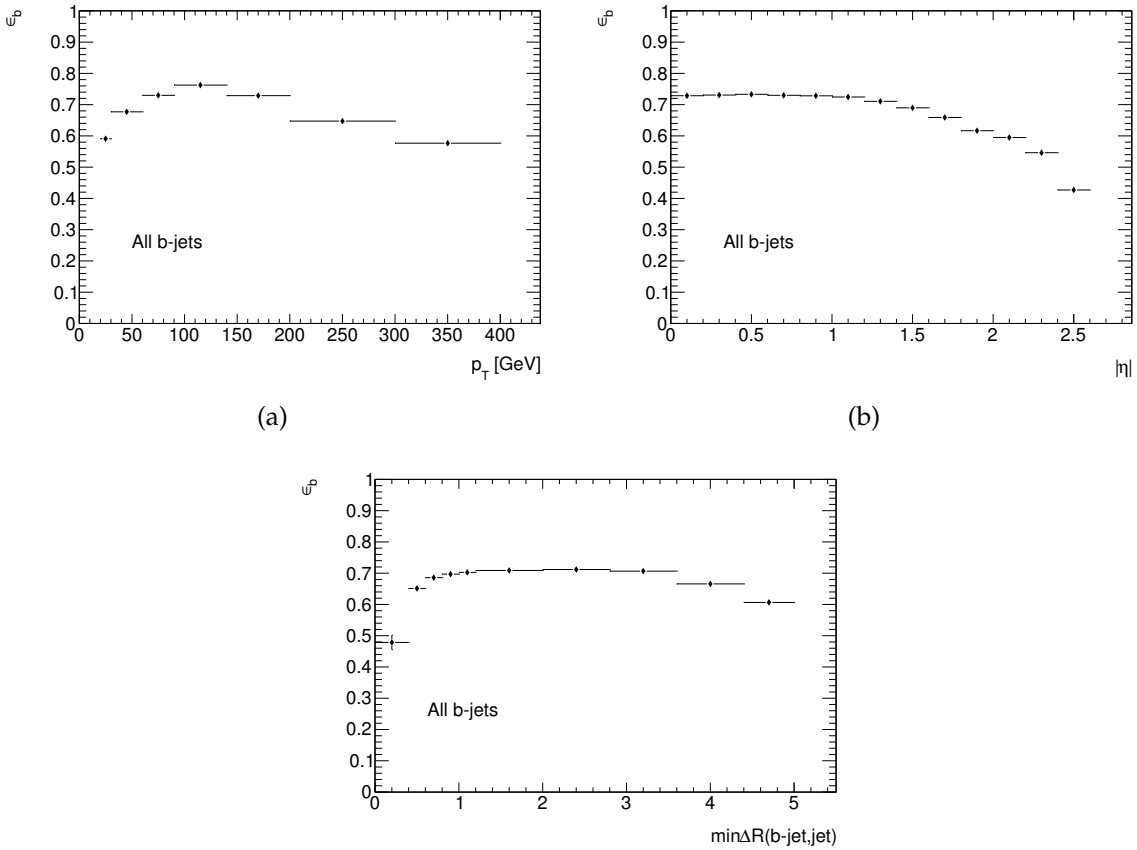

Figure 9.7: b-tagging efficiency ϵ_b as a function of the jet's p_T (a), pseudorapidity (b), and isolation (c). The b-tagging efficiency is determined from events with $N_{b-\text{jets}} \geq 0$.

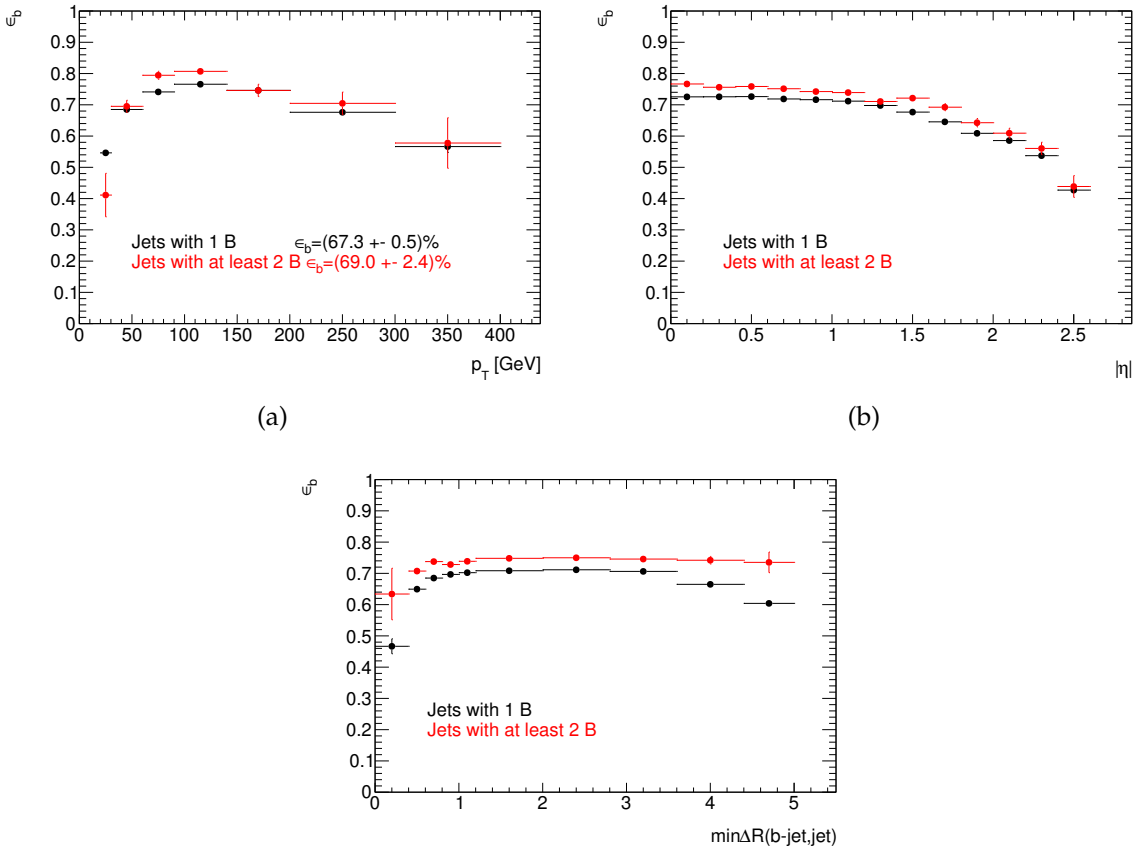

Figure 9.8: b-tagging efficiency for b-jets containing one b hadron (black) and two b hadrons (red) as a function of the jet's p_T (a), pseudorapidity (b), and isolation (c). The plots correspond to a sample with $N_{b-\text{jets}} \geq 0$. The x-axes correspond to the kinematics of the truth jets to which the reconstructed jets match.

Chapter 10

Modeling of the control regions

Since part of the input for the cross-section calculation, such as the fiducial efficiency and the background estimates, is taken from simulation, the quality of the modeling has to be assessed by comparing the simulation with data measured in control regions.

The principal control region used in this analysis is the pre-selection region, which was defined in Table 8.1. As discussed earlier, the pre-selection region is mostly comprised of inclusive $t\bar{t}$ events, therefore constituting a natural starting point for the study of $t\bar{t}b\bar{b}$ events. We note that discrepancies in the kinematic distributions of the leptons and b-jets in the pre-selection region are bound to affect the determination of the fiducial efficiency, thereby also affecting the estimation of the $t\bar{t}b\bar{b}$ cross-section. In this section we present several distributions of the kinematics of the final-state objects, as well as the event topology and discuss the quality of their modeling.

Two control regions enriched in Z+LF and Z+HF jets events were constructed to examine the modeling of the Z+jets background processes, thereby constraining the estimate for the Z+jets contribution in the signal region. Both regions were constructed based on the selection criteria as in Table 8.1, but reversing the Z-mass veto, i.e. retaining only the event in which the invariant mass of the lepton pair satisfies $81 \leq M_{ll} \leq 101$ GeV. The Z+LF jets region (ZLF) was constructed by requesting $N_{b-\text{jets}} = 0$ while the region enriched in Z+HF jets (ZHF) was defined by requesting $N_{b-\text{jets}} \geq 1$. These regions are orthogonal to themselves, as well as to the pre-selected region and the signal region.

10.1 Modeling of the Z+jets control region

The event yields for the ZLF and ZHF control regions are shown in Table 10.1. We observe that both control regions are dominated by Z+jets events as expected, with the Z+LF jets being dominant in the ZLF region and the Z+HF jets being dominant in the ZHF region. While the agreement between data and simulation is within 1% in the ZLF region, a discrepancy of 35% is observed in the ZHF region, suggesting that the simulation underestimates the production of heavy flavor jets in the sample enriched in Z bosons. This observation is in agreement with what has already been observed in the measurements of Z production in association with heavy flavor jets [1] and $t\bar{t}Z$ [170].

The cross-section of the Z+jets samples are corrected with scale factors obtained by solving the following system of equations

$$\begin{pmatrix} N^{Z+\text{LF jets}}_{\text{ZLF region}} & N^{Z+\text{HFjets}}_{\text{ZLF region}} \\ N^{Z+\text{LF jets}}_{\text{ZHF region}} & N^{Z+\text{HFjets}}_{\text{ZHF region}} \end{pmatrix} \begin{pmatrix} \text{SF}_{\text{LF}} \\ \text{SF}_{\text{HF}} \end{pmatrix} = \begin{pmatrix} N^{\text{data}}_{\text{ZLF region}} - N^{\text{other}}_{\text{ZLF region}} \\ N^{\text{data}}_{\text{ZHF region}} - N^{\text{other}}_{\text{ZHF region}} \end{pmatrix}, \quad (10.1)$$

which has the solution $\text{SF}_{\text{LF}} = 0.93$ and $\text{SF}_{\text{LF}} = 1.63$. After re-weighting the event yields are in better agreement between data and simulation in both control regions, as shown in Table 10.1.

The effect of the re-weighting is illustrated in Figure 10.1, which shows the invariant mass of the lepton pair. The re-weighting factors only affect the normalization, without affecting the shape of the distributions, therefore the effects observed in Figure 10.1 are similar for other event and object distributions.

10.2 Modeling of the pre-selection region

The event yields for the pre-selected sample, after the application of the data-to-MC correction factors and the Z+jets re-weighting factors described in the previous section, is given in Table 10.2. We observe that the $e\mu$ channel displays the best agreement between data and simulation, while in the $\mu\mu$ and ee channels an excess of 2.9% and 9% respectively is observed in data. This can be attributed partly to the remaining normalization discrepancy in the Z+jets estimate and partly to the omission of the

Sample	Control region before reweighting		Control region after reweighting	
	ZLF	ZHF	ZLF	ZHF
Data	439827	51486	439827	51486
Simulation	434932	38062	439955	51499
$Z+$ LF jets	378126	10401	351657	9673
$Z+$ HF jets	49990	22486	81483	36652
Other processes	6816	5175	6816	5175
Inclusive $t\bar{t}$	670	3943	670	3943
Dibosons	6084	1020	6084	1020
Single top	50	149	50	149
$t\bar{t}+W/Z$+jets	12	60	12	60
$t\bar{t}H$	0	3	0	3

Table 10.1: Measured and expected number of events in the ZLF and ZHF control regions. The last columns correspond to the yields obtained after re-weighting the Z+jets samples as described in the text.

background from jets which are reconstructed as electrons. The overall discrepancy is at the level of 3% and is covered by the systematic uncertainties.

Sample	ee	$e\mu$	$\mu\mu$	All channels
Data	4538	12127	6863	23528
Simulation	4165	11945	6668	22777
Inclusive $t\bar{t}$	3794	11624	6158	21576
Single top	96	266	149	511
Z+jets	256	7	333	596
$t\bar{t}+W/Z$+jets	12	34	18	63
$t\bar{t}H$	4	11	6	21
Dibosons	3	3	4	10

Table 10.2: Data yields and MC predictions for the number of events in the "pre-selected" sample. The numbers include the Z+jets re-weighting factors (Section 10.1) as well as the data-to-MC correction factors.

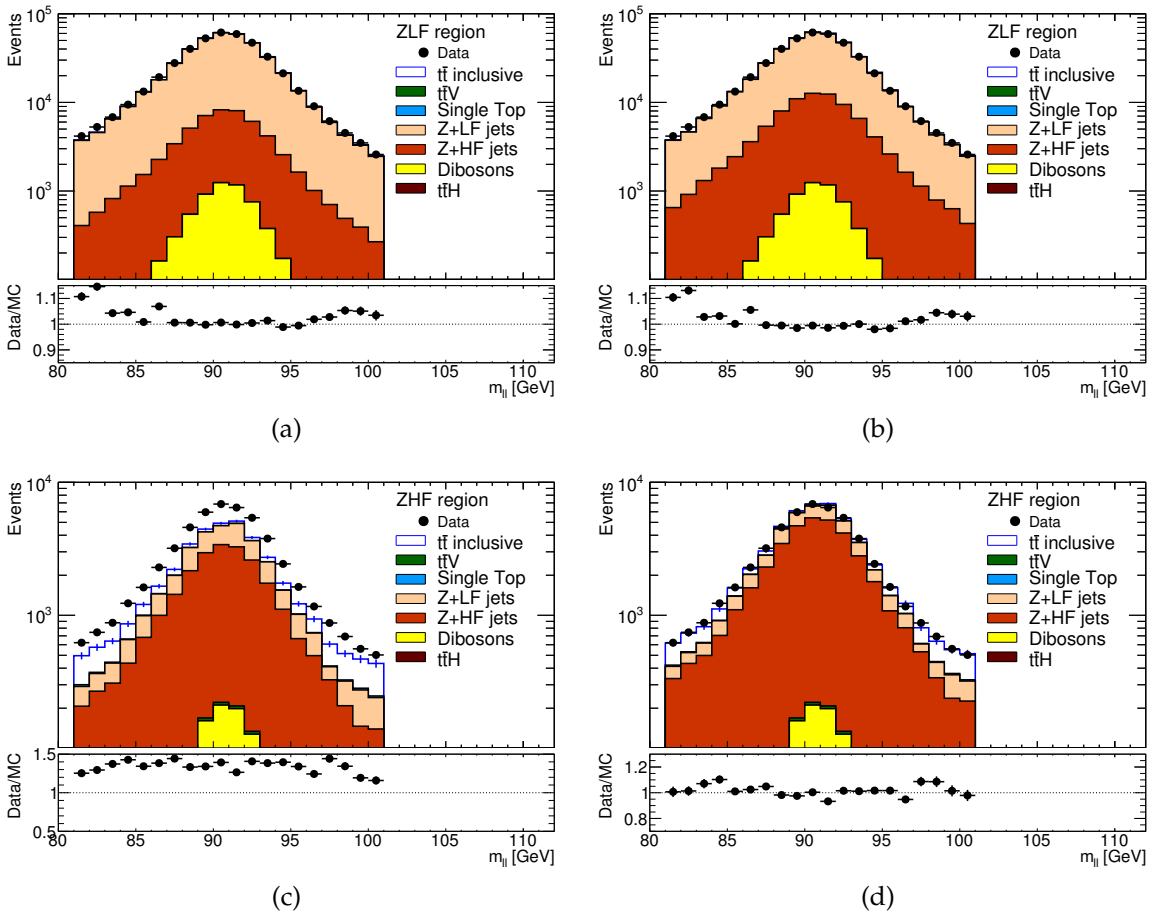

Figure 10.1: The di-lepton invariant mass spectrum for events that lie in the ZLF (top) and ZHF (bottom) control regions, before re-weighting (left) and after re-weighting (right). The distribution peaks at the value of the Z pole mass, indicating that the sample is dominated by events in which a Z boson is produced. The simulation underestimates the Z+HF fraction in the ZHF region, which is observed as a deficit of events in the simulation (left). The reweighting procedure based on equation (10.1) greatly improves the agreement between data and simulation (right).

Figures 10.2-10.7 show event and object level distributions for the preselected $t\bar{t}$ events.

The kinematics of the leptons and the leading jets is well described by the nominal simulation sample as shown in Figures 10.3 and 10.4 respectively. This leads to a good description of the inclusive jet multiplicity (Figure 10.2 a) up to relatively high multiplicities. The b-jet multiplicity on the other hand doesn't depend only on the inclusive jet production rate but also on the rate of $g \to b\bar{b}$ splitting in the parton shower. The nominal simulation sample and all samples that don't contain matrix

elements for the full $t\bar{t}b\bar{b}$ process tend to underestimate the high b-jet multiplicity region (Figure 10.2 b). The MadGraph+Pythia sample which contains matrix elements for $t\bar{t}b\bar{b}$, provides a better description of the high end b-jet multiplicity region (central scale and Q2down samples), however at the expense of a worse modeling of the inclusive jet multiplicities.

Distributions that characterize the event topology, such as the distance between the lepton pair (Figure 10.2 e) or between the two closest jets in the event (Figure 10.3 e). These distributions, are very sensitive to the modeling details, such as the spin correlations between the top decay products, which significantly affect the distance between the two leptons, and the implementation of the parton shower and hadronization models, which can have a marked impact on the distance between the jets.

The b-tagging weights of the two highest p_T b-jets is shown to be described by the simulation within the systematic uncertainties (Figure 10.5 a, b). The b-tagging weights of the 3rd and 4th highest p_T jets are higher in data than in simulation (Figure 10.5 c, d) but still at the limit of the systematic uncertainty. This discrepancy manifests itself in a higher number of b-jets measured in data than predicted by simulation, as seen in Figure 10.2 b.

Some disagreement is observed between data and simulation in the description of the kinematics of the 3rd and 4th highest p_T b-jets, as shown in Figure 10.7, however the low statistics obscure any underlying systematic effects. Most strikingly, the pseudorapidity distribution of the 4th highest p_T b-jet seems to be asymmetric in data, with an excess of events in the region $\eta < 0$. Out of a total of 39 events, 28 of them are observed in the region with $\eta < 0$. The probability to have such a fluctuation, assuming that the pseudorapidity distribution is symmetric is given by

$$P(k \geq 28) = \sum_{k=28}^{39} \frac{39!}{k!(39-k)!} 0.5^k 0.5^{39-k} = 0.47\%, \tag{10.2}$$

corresponding to 2.6 σ. While this probability is small, the fact that no such effect appears neither when a looser b-tagging operating point is chosen (which corresponds to higher statistics) nor in the 3rd b-jet p_T spectrum, suggests that the observed asymmetry is due to a statistical fluctuation.

10.3 Comparisons with different generators

In the previous section it was demonstrated that the nominal simulation sample, in which the additional b-jets are described only by the parton shower, underestimates the rate of production of events with ≥ 3 b-jets. It is instructive to see whether a sample offering a matrix-element description of the additional b-jets (like MADGRAPH) provides a better description of the additional b-jet multiplicity and p_T spectra.

Figure 10.8 shows the measured and simulated jet multiplicity and p_T spectra for the 4 b-tagged jets for events in the pre-selected region. The measured distributions are compared with the nominal sample as well as with the MADGRAPH+PYTHIA 6 sample with three different scale choices. It is observed that the nominal simulation sample provides the best description of the two leading b-tagged jets and of the b-jet multiplicity for events with 2 b-jets, which constitute the bulk of the phase space of inclusive $t\bar{t}$ events.

The MADGRAPH+PYTHIA 6 sample with the central scale underestimates the inclusive $t\bar{t}$ production rate, which shows up as an underestimation of events with 2 b-jets. The χ^2 statistic, defined as $\chi^2 \equiv \sum_i^{N_{\text{bins}}} \frac{(E_i - O_i)^2}{E_i}$, where E_i, O_i are the expected and observed number of events in bin i respectively is shown in Table 10.3 for the nominal and MADGRAPH+PYTHIA 6 samples. The nominal sample is shown to provide the best description of the rate of events with exactly 2 b-jets, however for the more inclusive case with $N_{b-\text{jets}} \geq 2$ the MADGRAPH+PYTHIA 6 samples (central scale and Q2 down) are in better agreement with the data. In the region with additional b-jets ($N_{b-\text{jets}} \geq 3$), all MADGRAPH+PYTHIA 6 samples are in better agreement with the data than the nominal sample, with the Q2 down sample being closest to the observation.

While it is expected that in the MADGRAPH+PYTHIA 6 samples the additional b-jets will be harder than in the nominal sample, thereby leading to a higher cross-section, the low statistics do not allow to draw any definite conclusions concerning the difference in the predicted cross-sections.

Generator	χ^2		
	2 b-jets	$\geq$ 2 b-jets	$\geq$ 3 b-jets
POWHEG+PYTHIA 6	7	41	35
MADGRAPH+PYTHIA 6	87	93	6
MADGRAPH+PYTHIA 6 (Q2 up)	304	319	15
MADGRAPH+PYTHIA 6 (Q2 down)	12	17	5

Table 10.3: χ^2 statistic representing the agreement between data and simulation for events with exactly 2, $\geq$ 2 and $\geq$ 3 b-jets.

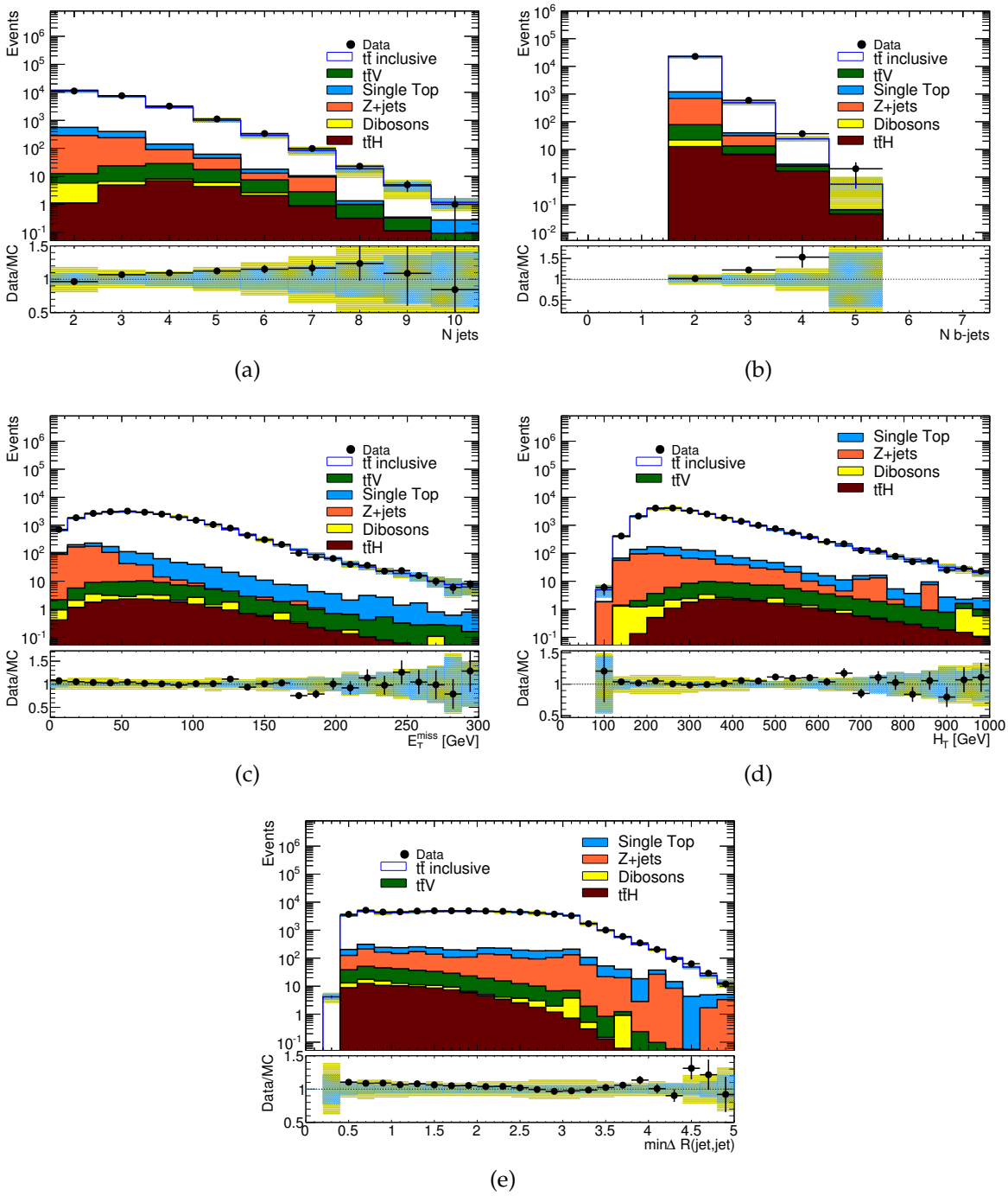

Figure 10.2: Event level distributions for the pre-selected events. Total jet multiplicity (a), b-jet multiplicity (b), missing transverse energy (c), scalar sum of transverse momenta of leptons and jets (d), jet isolation(e). The blue band corresponds to the uncertainty due to detector effects and the yellow band indicates the total systematic uncertainty obtained by adding in quadrature the uncertainty due to detector effects and the modeling uncertainty. The statistical uncertainty of the MC samples is added in quadrature to the total systematic uncertainty. The inclusive $t\bar{t}$ prediction was obtained from the nominal MC sample.

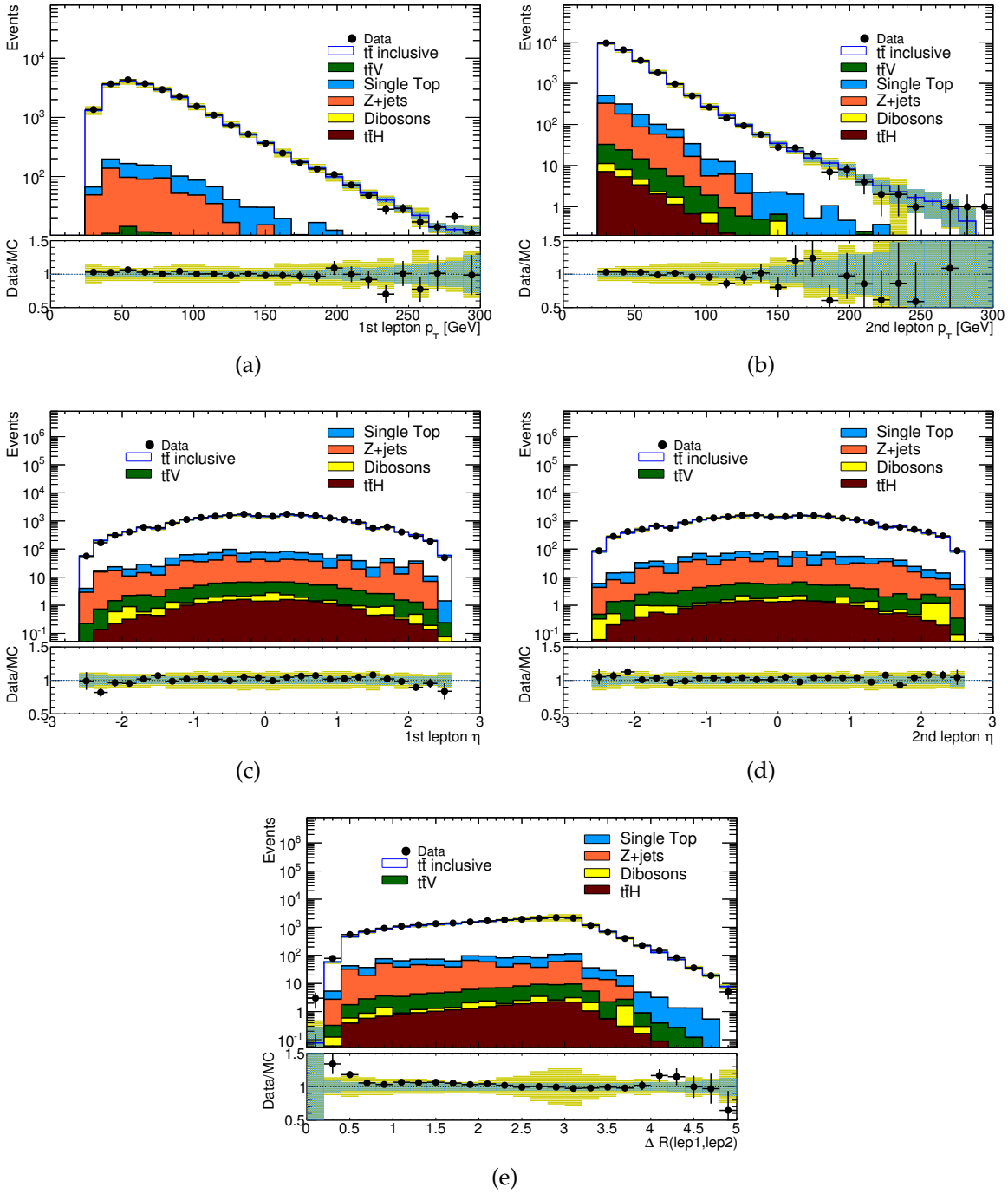

Figure 10.3: Kinematic distributions for leptons in the pre-selected events. Leading lepton p_T (a), Leading lepton η (b), subleading lepton p_T (c) and η (d), ΔR separation between leptons (e). The blue band corresponds to the uncertainty due to detector effects and the yellow band indicates the total systematic uncertainty obtained by adding in quadrature the uncertainty due to detector effects and the modeling uncertainty. The statistical uncertainty of the MC samples is added in quadrature to the total systematic uncertainty. The inclusive $t\bar{t}$ prediction was obtained from the nominal MC sample.

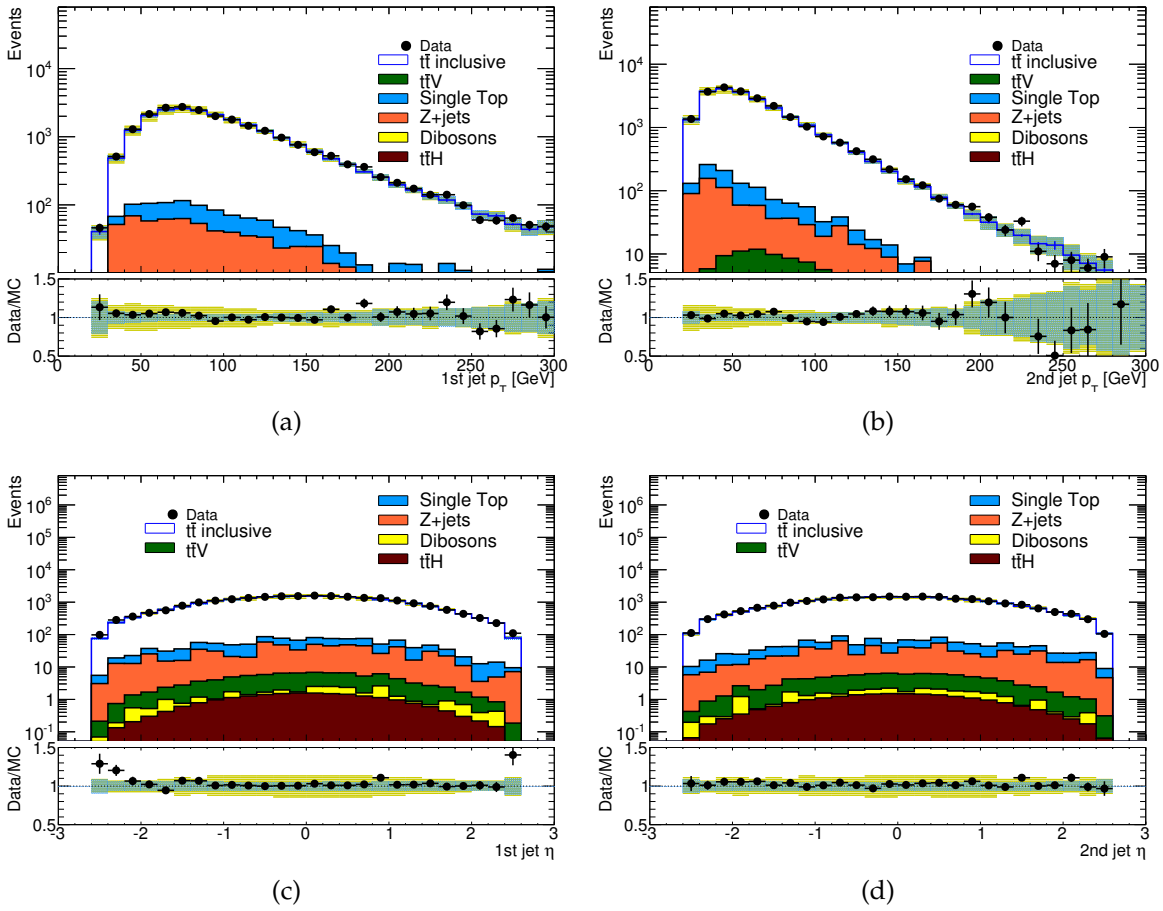

Figure 10.4: Jet properties in the pre-selected events: leading jet p_T (a), η (c) and b-tagging weight (e), sub-leading jet p_T (b), η (d). The blue band corresponds to the uncertainty due to detector effects and the yellow band indicates the total systematic uncertainty obtained by adding in quadrature the uncertainty due to detector effects and the modeling uncertainty. The statistical uncertainty of the MC samples is added in quadrature to the total systematic uncertainty. The inclusive $t\bar{t}$ prediction was obtained from the nominal MC sample.

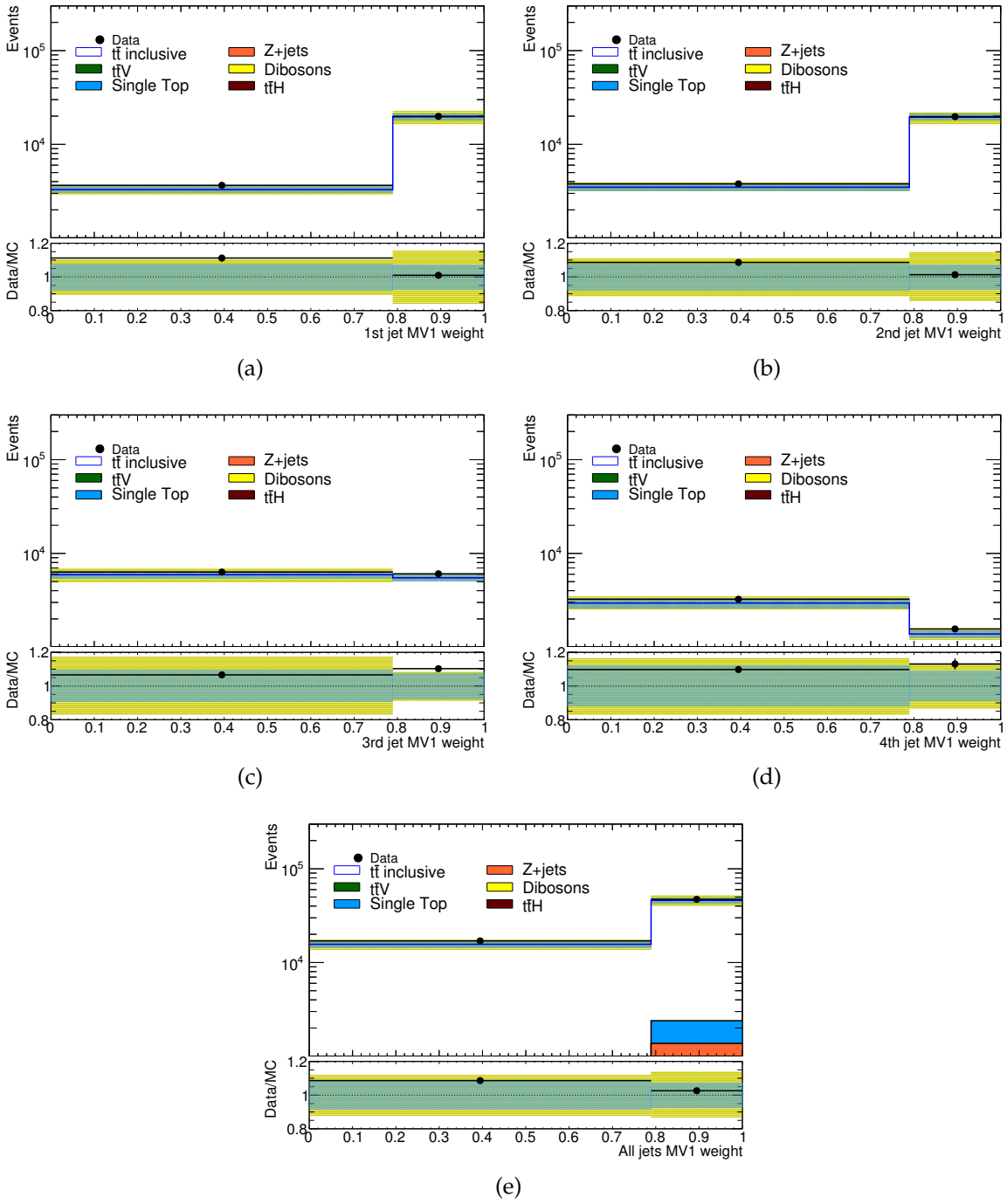

Figure 10.5: b-tagging weight of the first four highest p_T jets (a-d) and of all jets in the event (e). Only two bins are shown, corresponding to the regions in which the b-tagging algorithm is calibrated from in-situ measurements. The bin with MV1>0.7892 corresponds to b-tagged jets. We observe that the two leading jets, which are expected to correspond to the b-jets from the top decay are mostly b-tagged, while the 3rd and 4th b-jets in the inclusive $t\bar{t}$ sample are mostly LF jets. The blue band corresponds to the uncertainty due to detector effects and the yellow band indicates the total systematic uncertainty obtained by adding in quadrature the uncertainty due to detector effects and the modeling uncertainty. The statistical uncertainty of the MC samples is added in quadrature to the total systematic uncertainty. The inclusive $t\bar{t}$ prediction was obtained from the nominal MC sample.

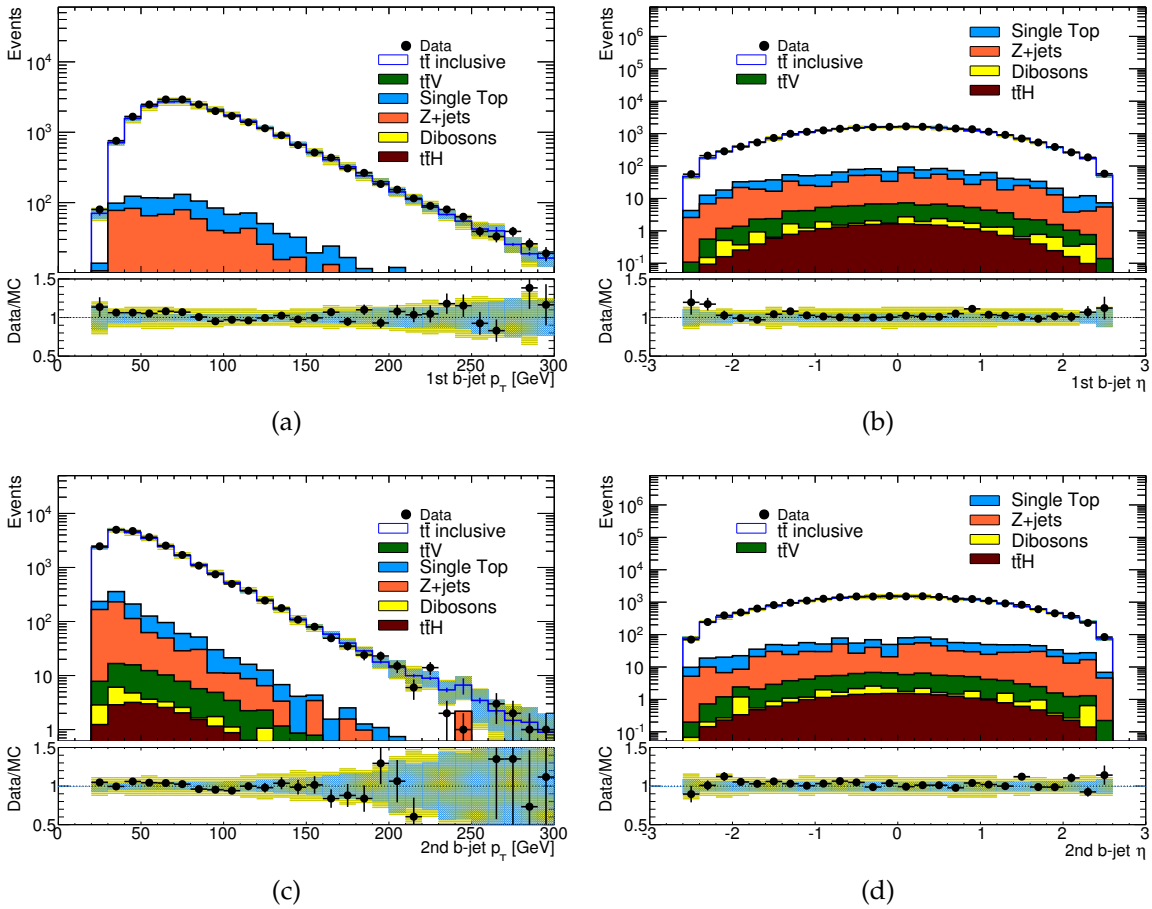

Figure 10.6: Kinematic distributions for two leading b-jets in the combination of channels using the pre-selected events. The blue band corresponds to the uncertainty due to detector effects and the yellow band indicates the total systematic uncertainty obtained by adding in quadrature the uncertainty due to detector effects and the modeling uncertainty. The statistical uncertainty of the MC samples is added in quadrature to the total systematic uncertainty. The inclusive $t\bar{t}$ prediction was obtained from the nominal MC sample.

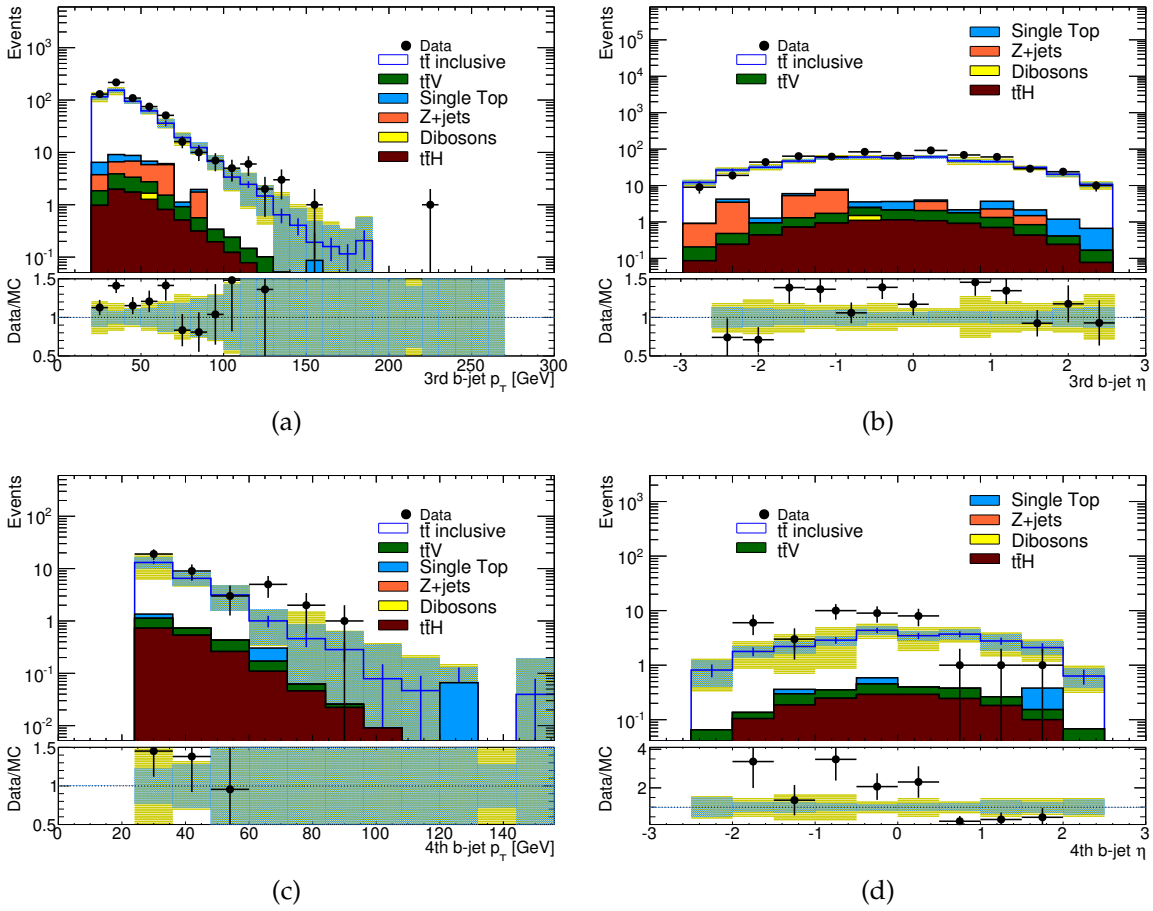

Figure 10.7: Kinematic distributions for the 3rd and 4th highest p_T b-jets in the combination of channels using the pre-selected events. The dominant contribution to these events is expected to be coming from events with a $t\bar{t}b\bar{b}$ partonic final state. The blue band corresponds to the uncertainty due to detector effects and the yellow band indicates the total systematic uncertainty obtained by adding in quadrature the uncertainty due to detector effects and the modeling uncertainty. The statistical uncertainty of the MC samples is added in quadrature to the total systematic uncertainty. The inclusive $t\bar{t}$ prediction was obtained from the nominal MC sample.

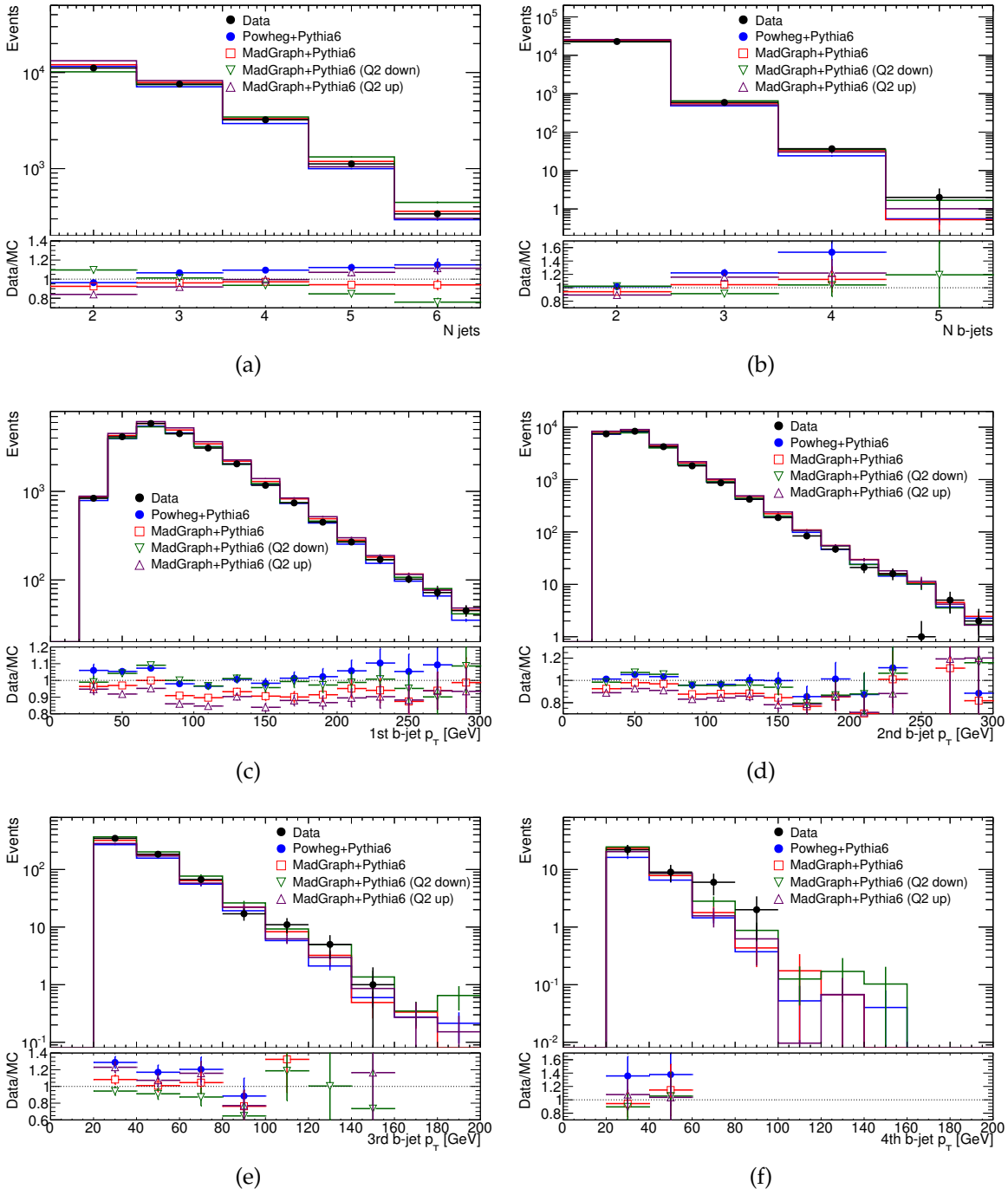

Figure 10.8: Inclusive (a) and b-tagged (b) jet multiplicities and p_T spectra of the 4 b-tagged jets (c-f). The histograms correspond to the sum of signal and background events.

Chapter 11

Backgrounds

This section describes the estimation of the two classes of background processes that contaminate the signal region:

- $t\bar{t}$+jets processes, described in Section 11.1 and
- non-$t\bar{t}$+jets processes, described in Section 11.2.

11.1 Backgrounds from $t\bar{t}$+jets processes

Events from $t\bar{t}$+jets processes constitute the dominant background for the $t\bar{t}b\bar{b}$ measurement. For the fiducial cross-section measurement, all events which are reconstructed in the signal region but don't satisfy the fiducial phase space requirements are considered to be background, as shown schematically in Figure 6.1.

The $t\bar{t}$+jets background can further be split into two categories

1. processes which contain the $t\bar{t}b\bar{b}$ final state at parton level in the inclusive phase space but don't fulfill the fiducial phase space requirements (referred to as "non-fiducial" background) and
2. processes which don't contain $t\bar{t}b\bar{b}$ at parton level (referred to as "mis-tagged" background).

An illustrative example of the two categories of $t\bar{t}$+jets background is shown in Figure 11.1.

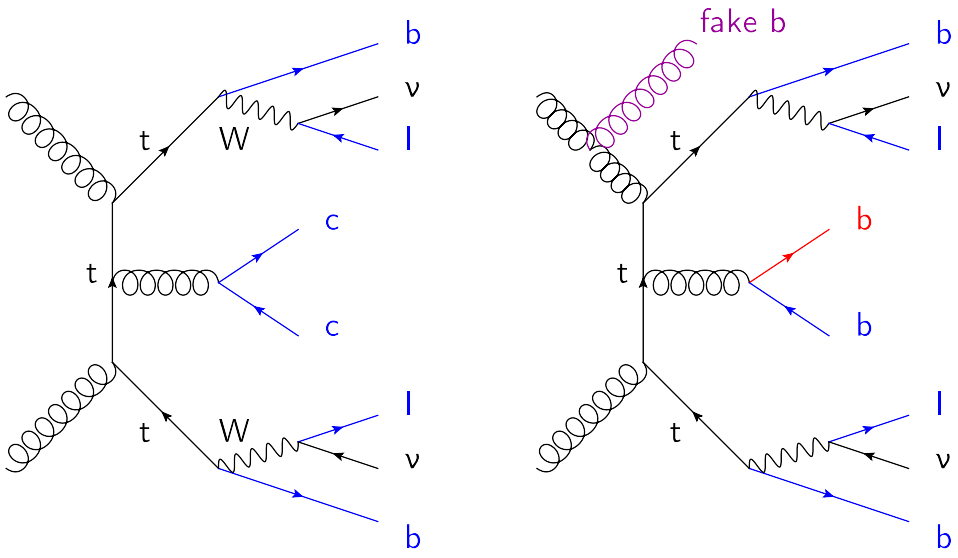

Figure 11.1: Example processes representing the mis-tagged (left) and non-fiducial background (right). The mis-tagged background corresponds to processes that don't contain $t\bar{t}b\bar{b}$ in the partonic final state, while the non-fiducial background contains processes that contain $t\bar{t}b\bar{b}$ in the final state at parton level, but do not satisfy the fiducial phase space cuts. A red (blue) color denotes objects which fail (pass) the fiducial phase space requirements.

The "mis-tagged" component is comprised of processes in which there are two or fewer b-jets in the fiducial volume, and two or more mis-tagged c or LF jets. These processes are denoted by $t\bar{t}c\bar{c}$, $t\bar{t}jj$ and $t\bar{t}cj$ according to the flavor of the jets that are mis-tagged. Since these processes are different from $t\bar{t}b\bar{b}$ at parton level we consider that their contribution to the signal region is independent of the number of observed signal events. Therefore a constant estimate of the number of $t\bar{t}c\bar{c}$, $t\bar{t}jj$ and $t\bar{t}cj$ events is obtained from simulation and subtracted from the number of events in the signal region.

The "non-fiducial" component comprises of events that are expected to contain $t\bar{t}b\bar{b}$ at parton level but lie outside of the fiducial phase-space. This category contains different types of events

- **events with unmatched jets**: these are events which have 4 reconstructed b-jets but one or more of the reconstructed b-jets cannot be matched to a b-jet in the fiducial volume. This can happen when at truth level a jet falls below the p_T threshold, while being reconstructed above the threshold due to detector resolution effects. This effect affects low p_T jets close to the reconstruction threshold. Moreover a single truth jet can occasionally be reconstructed as two jets due to fluctuations in

the calorimeter (Figure 11.2). Lowering the jet p_T threshold in the definition of the fiducial phase space could mitigate these effects, as shown in Figure 11.2. This however would come at the expense of higher modeling uncertainties, which arise due to differences of the simulation models in the description of soft jets.

- **events with an odd number of *b*-jets** ($t\bar{t}bc$, $t\bar{t}bj$): given that the proton has zero bottomness, processes with an odd number of b-quarks can only arise due to CKM suppressed transitions, which are negligibly small. Events with an odd number of b-jets can therefore only arise from processes containing an even number of b-quarks, with two b-quarks merging into a single jet or one b-jet lying outside of the fiducial phase-space. At the same time a c or LF jet must be mis-tagged in order for the event to be reconstructed in the signal region. These events are denoted by $t\bar{t}bc$ or $t\bar{t}bj$).

- **events that fail the lepton cuts**: these are events with exactly four b-jets in the fiducial volume which fail one of the lepton kinematic cuts.

The common characteristic of these processes is the fact that they are all expected to arise from processes containing $t\bar{t}b\bar{b}$ at parton level, therefore their production rate will be proportional to the $t\bar{t}b\bar{b}$ cross-section. For this reason, their contribution to the signal region is scaled with the number of signal events, as indicated by equation (6.5).

Events from the $t\bar{t}H$ and $t\bar{t}Z$ processes that don't satisfy the fiducial phase space requirements are also classified according to the above criteria as mis-tagged or non-fiducial background.

In order to identify the different "mis-tagged" and "non-fiducial" components, the $t\bar{t}$+jets background events are split into the following categories

- events that pass all the fiducial cuts except for the requirement $N_{b-\text{jets}}^{\text{fiducial}} = 4$ and have
  - $N_{b-\text{jets}}^{\text{fiducial}} = 3$ (Figure 11.3 a)
  - $N_{b-\text{jets}}^{\text{fiducial}} = 2$ (Figure 11.3 b)
  - $N_{b-\text{jets}}^{\text{fiducial}} < 2$ or $N_{b-\text{jets}}^{\text{fiducial}} > 4$ (Figure 11.3 c)
- events that fail the fiducial cuts and have
  - $N_{b-\text{jets}}^{\text{fiducial}} \neq 4$ (Figure 11.3 d)

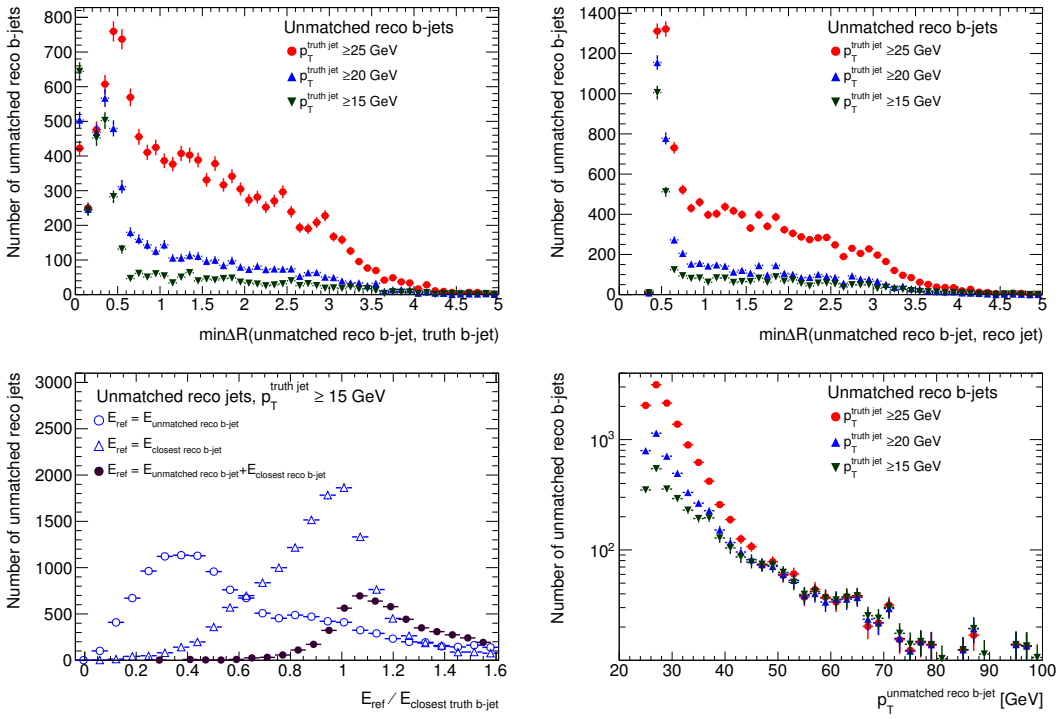

Figure 11.2: Minimum ΔR distance between reconstructed b-jets that don't match to any truth jets and the closest truth jet (top left) or the closest reconstructed jet (top right) for three different truth jet p_T thresholds. As the truth jet p_T is lowered, the number of unmatched jets decreases. This suggests that unmatched jets are mostly due to detector resolution effects. It is also observed that as the truth jet p_T threshold is lowered, unmatched b-jets are only observed in the region geometrically overlapping ($\Delta R \leq 0.8$) with both the closest reconstructed jet (top right) and the closest truth jet (top left). In such cases only one of the two reconstructed jets whose invariant mass is closest to the truth jet's invariant mass is considered to be matched. We observe that the sum of the energies of the two reconstructed jets (the unmatched one and its closest neighbor) peaks around the energy of the closest truth jet (bottom left), with a spread of around 20%, which is the typical energy resolution for low p_T jets (bottom right). This points to the fact that the second effect giving rise to unmatched jets is the splitting of a truth jet into two reconstructed jets in the calorimeter.

– $N_{b-\text{jets}}^{\text{fiducial}} = 4$ (Figure 11.3 e),

as displayed in Figure 11.3. The composition of the different background contributions in terms of the underlying partonic process are shown in Table 11.1. Table 11.2 shows the same contributions, normalized to the the total number of $t\bar{t}$+jets background events in the signal region. It is observed that the dominant background contributions come from non-fiducial events. The dominant contribution from mis-tagged events

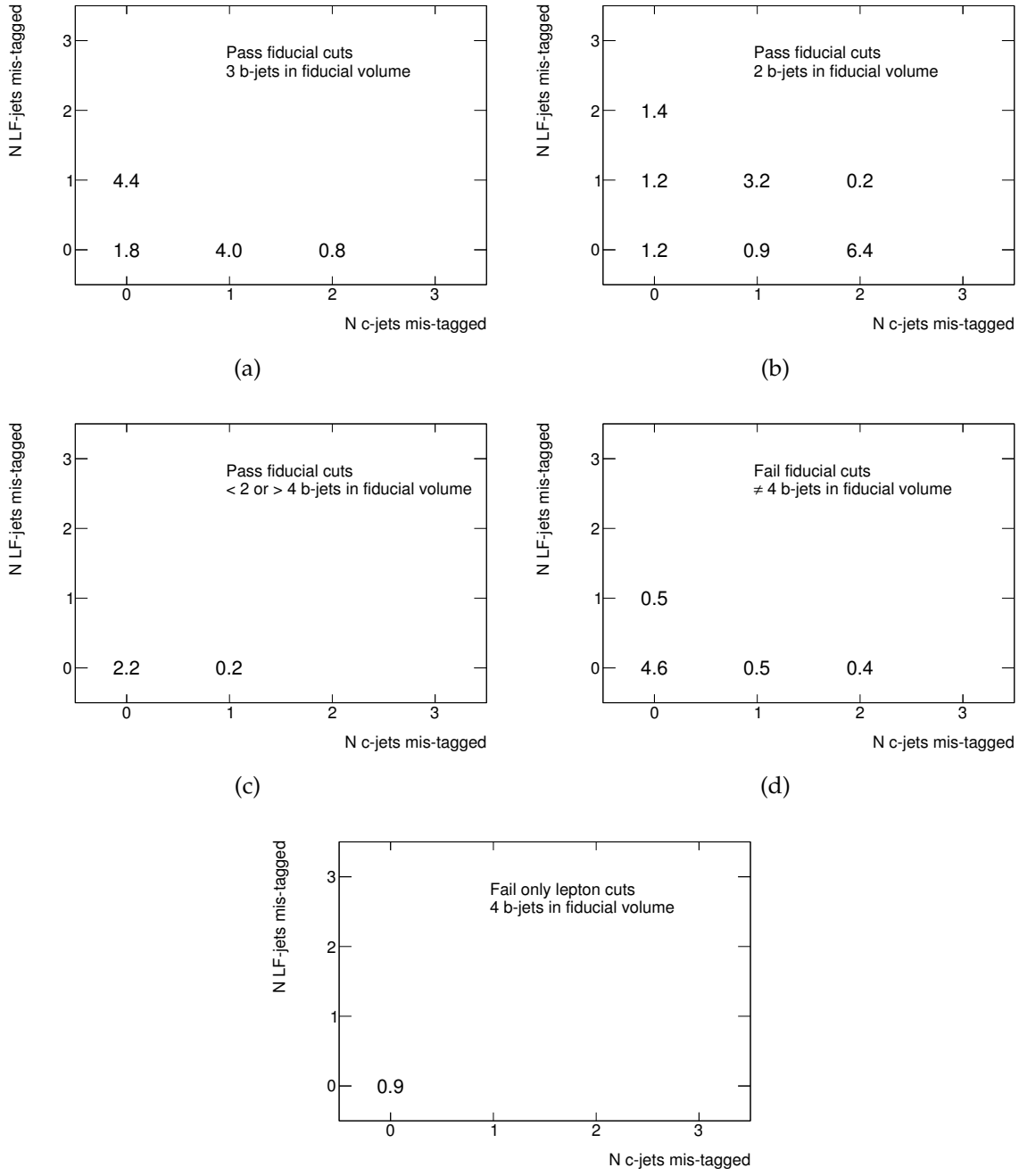

Figure 11.3: Number of mis-tagged c (a) and LF-jets (b) in different background regions. The plots are normalized to the total fraction of $t\bar{t}+$ jets background events. The predictions correspond to the baseline MC sample, i.e. Powheg interfaced to Pythia with $h_{\text{damp}} = m_{\text{top}}$.

corresponds to the $t\bar{t}c\bar{c}$ process. The predictions vary significantly among the different models.

Process	Powheg +Pythia ($h_{\text{damp}} = m_{\text{top}}$)	Powheg +Pythia ($h_{\text{damp}} = \infty$)	MadGraph +Pythia	MadGraph +Pythia (Q2 down)	MadGraph +Pythia (Q2 up)	Powheg +Herwig
Mis-tagged						
$t\bar{t}c\bar{c}$	6.9%	7.6%	8.7%	7.6%	10.5%	5.9%
$t\bar{t}jj$	1.4%	2.5%	1.2%	1.6%	1.2%	3.3%
$t\bar{t}cj$	3.2%	5.4%	3.9%	2.3%	5.7%	3.3%
≥ 3 mis-tagged jets	0.2%	0.4%	0.5%	0.3%	0%	0.2%
Non-fiducial						
$t\bar{t}bj$	4.4%	5.4%	7.8%	5.1%	3.8%	6.8%
$t\bar{t}bc$	4.0%	4.9%	3.6%	7.2%	3.0%	3.8%
fail only lepton cuts	0.9%	1.5%	1.8%	2.2%	1.1%	1.6%
unmatched jets	13.2%	10.7%	11.5%	13.7%	11.4%	11.0%
Total	34.2%	38.4%	39.0%	40.0%	36.7%	35.9%

Table 11.1: Contributions to the $t\bar{t}$+jets background from different processes. The numbers express fractions of the total number of expected signal and background events reconstructed in the signal region. Contributions from $t\bar{t}H$ and $t\bar{t} + W/Z$ processes that may contribute to these backgrounds are not included in this table.

Process	Powheg +Pythia ($h_{\text{damp}} = m_{\text{top}}$)	Powheg +Pythia ($h_{\text{damp}} = \infty$)	MadGraph +Pythia	MadGraph +Pythia (Q2 down)	MadGraph +Pythia (Q2 up)	Powheg +Herwig	$\frac{\text{max} - \text{min}}{2 \cdot \text{nominal}}$
Mis-tagged							
$t\bar{t}c\bar{c}$	20.2%	19.8%	22.3%	19.0%	28.6%	16.4%	30%
$t\bar{t}jj$	4.1%	6.5%	3.1%	4.0%	3.3%	9.2%	74%
$t\bar{t}cj$	9.4%	14.1%	10.0%	5.7%	15.5%	9.2%	52%
≥ 3 mis-tagged jets	0.6%	1.0%	1.3%	0.7%	0%	0.6%	108%
Non-fiducial							
$t\bar{t}bj$	12.9%	14.1%	20.0%	12.8%	10.4%	18.9%	37%
$t\bar{t}bc$	11.7%	12.8%	9.2%	18.0%	8.2%	10.6%	42%
fail only lepton cuts	2.6%	3.9%	4.6%	5.5%	3.0%	4.5%	56%
unmatched jets	38.6%	27.9%	29.5%	34.2%	31.1%	30.6%	14%
Total	100%	100%	100%	100%	100%	100%	-

Table 11.2: Same as Table 11.1, but the individual background components are now normalized to the total number of expected $t\bar{t}$+jets background events in the signal region. The last column shows the modeling variation for the different background components, calculated by taking half of the difference between the extremal predictions for each component, normalized by the nominal prediction, which corresponds to the Powheg+Pythia $h_{\text{damp}} = m_{\text{top}}$ sample.

The estimates for the mis-tagged component of $t\bar{t}$+jets processes and of the signal fraction f_{sig} defined in equation (6.4), are given in Table 11.3. An illustration of the mis-

Model	$N_{t\bar{t}\text{+jets}}^{\text{mis-tagged}}$	f_{sig}
Powheg+Pythia ($h_{damp} = m_{top}$)	2.61 ± 0.37	0.758 ± 0.056
Powheg+Pythia ($h_{damp} = \infty$)	4.04 ± 0.25	0.743 ± 0.026
Powheg+Herwig	3.18 ± 0.46	0.745 ± 0.053
MadGraph+Pythia	4.37 ± 0.84	0.723 ± 0.080
MadGraph+Pythia (Q2up)	5.06 ± 1.15	0.779 ± 0.112
MadGraph+Pythia (Q2down)	3.96 ± 0.67	0.693 ± 0.063

Table 11.3: Expected number of mis-tagged $t\bar{t}$+jets events reconstructed in the signal region, and f_{sig}, the estimated fraction of $t\bar{t}b\bar{b}$ events which are in the fiducial region. The uncertainties are due to the limited MC statistics.

tagged background and of the signal fraction is shown in Figure 11.4 and Figure 11.5 respectively.

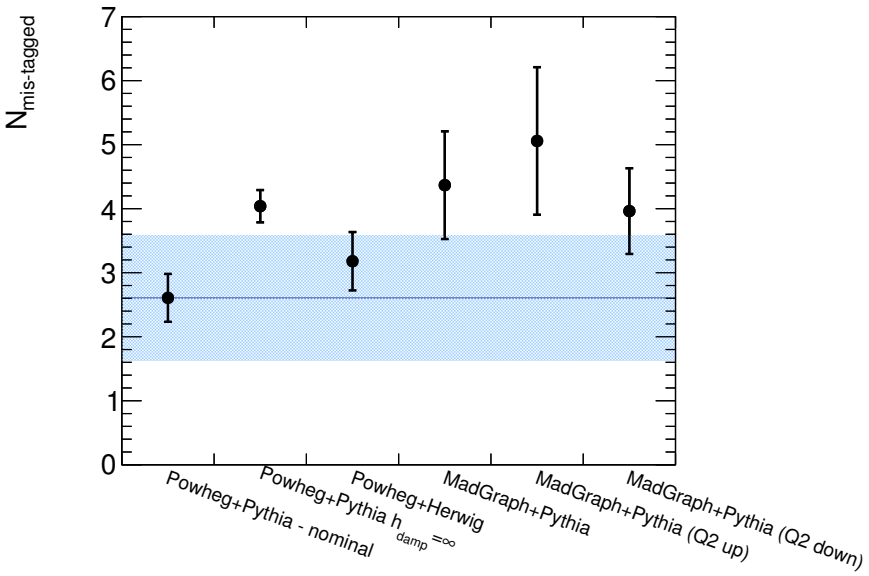

Figure 11.4: Expected number of mis-tagged $t\bar{t}$+jets events in signal region estimated with different models. The dashed line indicates the central value for the estimate of mis-tagged events, which is taken to coïncide with the nominal MC prediction, and the blue band corresponds to the modeling uncertainty. The prediction from POWHEG+PYTHIA with $h_{\text{damp}} = \infty$ is shown for illustrative purposes only and is not used in the calculation of the modeling uncertainty.

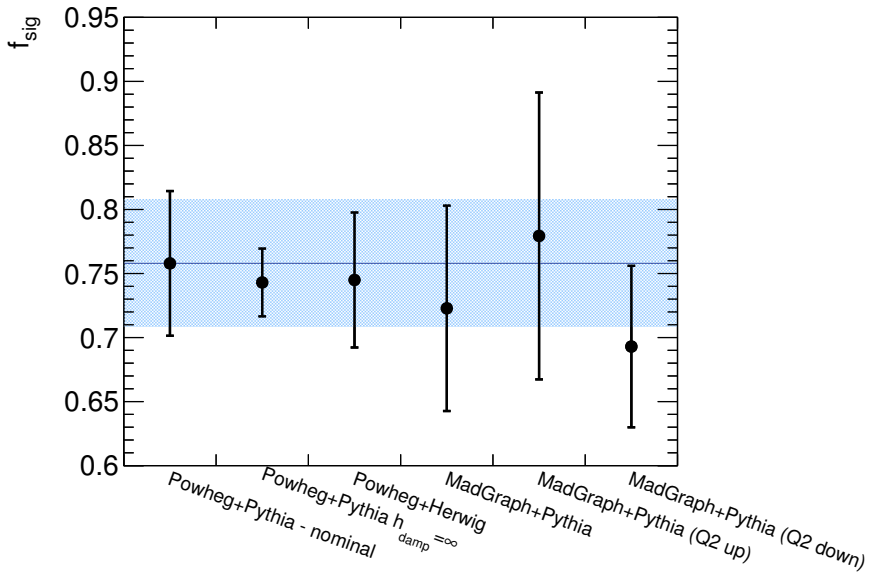

Figure 11.5: Ratio of signal to signal and non-fiducial events in signal region estimated with different models. The dashed line indicates the central value for the estimate of mis-tagged events, which is taken to coïncide with the nominal MC prediction, and the blue band corresponds to the modeling uncertainty. The prediction from POWHEG+PYTHIA with $h_{\text{damp}} = \infty$ is shown for illustrative purposes only and is not used in the calculation of the modeling uncertainty.

11.1.1 Validation of the background estimate

A method to validate the simulation of the backgrounds taken from Monte Carlo is to perform the cross-section measurement in regions with larger or smaller background contributions. This is done by replacing the $N_{b-\text{jets}} = 4$ requirement by $N_{b-\text{jets}} = 3$, using the 80% operating point of the MV1c tagger, and then binning in the MV1c weight of the fourth jet[1]. The results are shown in Figure 11.6. The contribution of the non-$t\bar{t}$+jets and of the mis-tagged $t\bar{t}$+jets background varies from less than 1% to slightly more than 50% of the data. If the cross-section for background processes were mis-modeled, we would expect a trend to emerge in the measured signal cross-sections, as the background contributions become more or less significant. Instead, the four bins show good agreement, and no trend is observed. This gives confidence that the simulation is correctly modeling the cross-sections for background processes.

[1]The MV1c efficiency has been calibrated using dilepton $t\bar{t}$ events, using several bins of b-tagging efficiency, what is technically referred to as "pseudo-continuous" calibration.

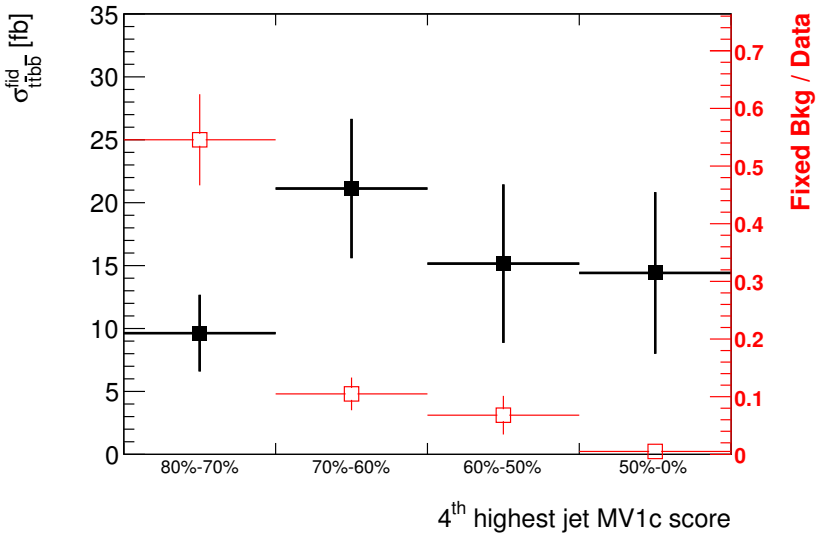

Figure 11.6: In black, measured fiducial cross-section for $t\bar{t}b\bar{b}$, binned in different regions of the fourth-highest MV1c weight. The leftmost bins correspond to a higher b-tagging efficiency (looser MV1c cuts) and to a higher probability for mis-tagging c/LF jets. Only statistical errors are shown. In red, the contribution of the fixed background as a fraction of the data, where fixed background refers to mis-tagged and non-$t\bar{t}$ events. No trend is observed moving from regions of lower to higher background contribution.

11.2 Backgrounds from non-$t\bar{t}$+jets processes

The signal region receives contributions from non-$t\bar{t}$+jet processes, that are mis-identified as signal. The backgrounds considered come from single top, Z+jet, and di-boson processes, as well as from the reducible component of $t\bar{t}H(H \to b\bar{b})$ and $t\bar{t}Z(Z \to b\bar{b})$. Their relative contribution to the total number of expected events is estimated from simulation.

For the di-boson and Z+jets processes, no simulated events pass the full event selection, due to the small statistics of the simulation samples. In order to derive an estimate for their contribution to the signal region the following method is employed. First the efficiency of the di-lepton invariant mass cut

$$\epsilon_{M_{\ell\ell}} = \frac{N_{\text{events after cut}}}{N_{\text{events before cut}}} \tag{11.1}$$

is calculated in the "pre-selection" sample. Then the di-lepton invariant mass cut is removed, in order to increase the statistics of the di-boson and Z+jets samples in the

signal region. The final prediction is obtained by scaling the number of di-boson and Z+jets events that end up in the signal region by $\epsilon_{M_{\ell\ell}}$.

Multi-jet and W+jets processes could also contribute to the signal region through the mis-identification of jets as electrons. These processes would affect mostly the ee final state, where the probability of having a jet faking an electron is twice as high as in the $e\mu$ final state. The ee final state has the lowest contribution to the total cross-section (due to the lowest product of branching ratio and reconstruction efficiency among the di-lepton channels). These backgrounds have been studied and found to be sub-dominant in the context of the inclusive $t\bar{t}$ cross-section measurement [169]. The requirement of a high b-jet multiplicity, is expected to further reduce this background, therefore we consider it to be negligible.

The predictions for the non-$t\bar{t}$+jets backgrounds are given in Table 11.4.

Source	$B/(S+B)$
Z+jets	3.3%
Single top	1.7%
$t\bar{t}+W/Z$+jets	1.4%
$t\bar{t}H$	1.0%
Di-boson	0.016%

Table 11.4: Ratio of background contributions to signal+background. The $t\bar{t}+Z/W$+jets and $t\bar{t}H$ contributions correspond to their reducible components.

Chapter 12

Calculation of the fiducial efficiency

Given a set of signal events N^{fid} that lie in the fiducial volume, only a subset $N^{\text{reco\&fid}} < N^{\text{fid}}$ of those can be reconstructed in the signal region, due to detector inefficiencies in the reconstruction and identification of the final state objects. The relation between N^{fid} and $N^{\text{reco\&fid}}$ is illustrated in Figure 6.1. The number of events reconstructed in the signal region, starting from the set of signal events in the fiducial volume is given by

$$\tilde{N}^{\text{reco\&fid}} = \epsilon_{\text{fid}} \cdot N^{\text{fid}}, \tag{12.1}$$

where ϵ_{fid} is the fiducial efficiency and the tilde in $\tilde{N}^{\text{reco\&fid}}$ indicates that when applying the selection requirements on the reconstructed objects, the events are weighted by the appropriate data-to-MC scale factors. Solving for ϵ_{fid} and taking into account that $\tilde{N}^{\text{reco\&fid}} \subset N^{\text{fid}}$ we obtain

$$\epsilon_{\text{fid}} = \frac{\tilde{N}^{\text{reco\&fid}}}{N^{\text{fid}}}, \tag{12.2}$$

$$\delta\epsilon_{\text{fid}} = \sqrt{\frac{\epsilon_{\text{fid}}(1-\epsilon_{\text{fid}})}{N^{\text{fid}}}}. \tag{12.3}$$

For the case where more than one process contributes to the signal (e.g. $t\bar{t}H(b\bar{b})$, $t\bar{t}Z(b\bar{b})$), the above equations become

$$\epsilon_{\text{fid}} = \frac{\sum_i \frac{\tilde{N}_i^{\text{reco\&fid}}}{N_i^{\text{gen}}}\sigma_i}{\sum_i \frac{N_i^{\text{fid}}}{N_i^{\text{gen}}}\sigma_i}, \tag{12.4}$$

$$\delta\epsilon_{\text{fid}} = \frac{\sqrt{\sum_i \left(\frac{\sigma_i}{N_i^{\text{gen}}}\right)^2 \epsilon_{\text{fid},i}(1-\epsilon_{\text{fid},i})N_i^{\text{gen}}}}{\sum_i \frac{N_i^{\text{fid}}}{N_i^{\text{gen}}}\sigma_i}, \tag{12.5}$$

where N_i^{gen} indicates the total number of generated events in sample i.

Predictions of various models for the fiducial efficiency are given inTable 12.1 and shown in Figure 12.1. The most significant efficiency losses are due to the b-tagging efficiency (we naïvely expect a 70% efficiency for identifying the two leading b-jets and around 60% efficiency for identifying the two additional low-p_T b-jets), the lepton identification (around 70% efficiency for identifying two leptons) and due to the jet reconstruction, which is affected by resolution effects and the JVF cut (around 85% efficiency for reconstructing at least 4 jets).

Differences of up to 40% are observed between the different models and the nominal prediction, which can be ascribed to differences in the predicted kinematics of the final-state objects.

Model	ϵ_{fid} [%]
Powheg+Pythia ($h_{damp} = m_{top}$)	6.34 ± 0.39
Powheg+Pythia ($h_{damp} = \infty$)	5.98 ± 0.17
Powheg+Herwig	6.61 ± 0.53
MadGraph+Pythia	7.05 ± 0.52
MadGraph+Pythia (Q2up)	8.50 ± 0.94
MadGraph+Pythia (Q2down)	5.77 ± 0.44
$t\bar{t}H(b\bar{b})$	8.78 ± 0.24
$t\bar{t}Z(b\bar{b})$	9.02 ± 0.50

Table 12.1: Estimates for the fiducial efficiency. The errors correspond to the uncertainty due to the limited size of the simulation samples.

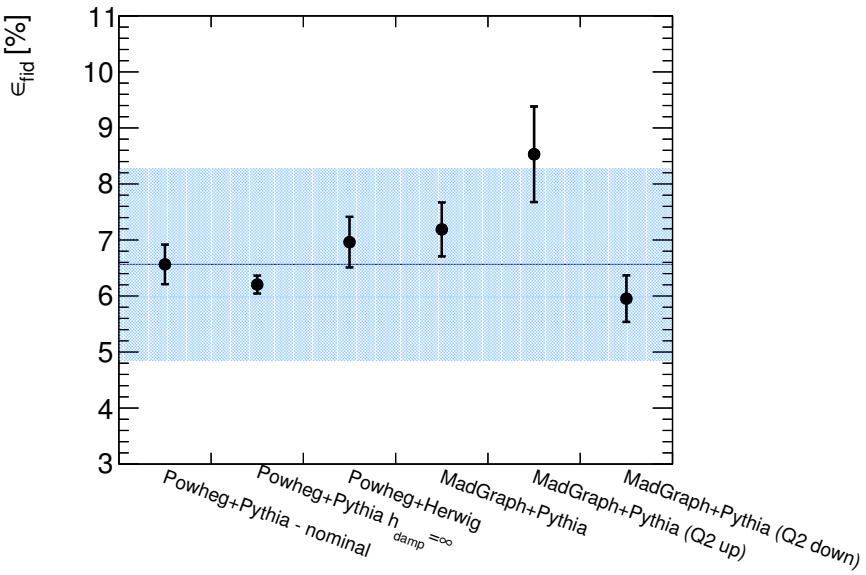

Figure 12.1: Predictions for the fiducial efficiency derived with different models. The blue band corresponds to the modeling uncertainty.

Chapter 13

Measurement uncertainties

The total uncertainty on the fiducial cross-section is given by

$$\delta\sigma^{\text{fid}}_{t\bar{t}b\bar{b}} = \sqrt{\delta\sigma^2_{\text{stat}} + \delta\sigma^2_{\text{sys}} + \delta\sigma^2_{\text{lumi}}}, \tag{13.1}$$

where the three components refer to the statistical, systematic, and luminosity uncertainties. The statistical uncertainty is taken from Poisson statistics considering only the size of the data sample. The systematic uncertainties may be classified as coming from detector performance, $t\bar{t}+$ jets modeling and from the uncertainties on the cross-sections of the non-$t\bar{t}+$jets backgrounds. The evaluation of these uncertainties is described in Sections 13.2, 13.3 and 13.4 respsctively. The uncertainty due to the limited statistics of the simulated samples is accounted for in the systematic uncertainty. The uncertainty on the luminosity measurement is considered separately from the other systematic sources, as described in Section 13.1.

13.1 Uncertainties related to the luminosity measurement

As can be seen from equation (6.5), the measured cross-section depends on the integrated luminosity $\mathcal{L}$. The integrated luminosity of the sample was measured to be 20.3 fb^{-1}, with an uncertainty of $\pm 2.8\%$. The uncertainty is derived, following the same methodology as that detailed in Ref. [171], from a preliminary calibration of the luminosity scale derived from beam-separation scans performed in November 2012.

In equation (6.5), the luminosity appears explicitly in the denominator, but it is also implicit in $N_{t\bar{t}+\text{jets}}^{\text{mis-tagged}}$ and $N_{\text{bg}}^{\text{non-}t\bar{t}+\text{jets}}$, which are scaled to the luminosity of the data sample[1]. e.g.

$$N_{t\bar{t}+\text{jets}}^{\text{mis-tagged}} \rightarrow N_{t\bar{t}+\text{jets}}^{\text{mis-tagged}} \frac{\mathcal{L}\,\sigma_{t\bar{t}}}{N_{t\bar{t}}^{\text{gen}}}, \tag{13.2}$$

where $N_{t\bar{t}}^{\text{gen}}$ is the total number of generated events. The luminosity dependence of the $N_{t\bar{t}+\text{jets}}^{\text{mis-tagged}}$ and $N_{\text{bg}}^{\text{non-}t\bar{t}+\text{jets}}$ terms is cancelled by the denominator and the uncertainty of the cross-section due to the luminosity is given by

$$\delta\sigma_{\text{lumi}} = \frac{N_{\text{data}} \cdot f_{sig}}{\epsilon_{\text{fid}} \cdot \mathcal{L}} \cdot \frac{\delta\mathcal{L}}{\mathcal{L}}. \tag{13.3}$$

13.2 Uncertainties related to the detector performance

As described in the previous chapter, the measurement is based on reconstructed objects, specifically leptons and jets. The identification efficiencies, energy scales and resolutions are derived in simulation and are corrected with scale factors to match the data. The uncertainties on these corrections have to be propagated to the measurement. For scale factors on efficiencies for triggering, reconstructing, or identifying physics objects, the correction is applied by modifying the event weight. For energy scales and resolutions, the correction is applied by smearing or re-scaling the objects' energies. The uncertainties on the data-to-MC correction factors are evaluated by considering $\pm 1\sigma$ variations around their central values. The variations of the different scale factors are performed independently (one at a time) assuming that they are uncorrelated.

For each variation the cross-section is re-calculated according to equation (6.5). This accounts for correlations that exist between the number of background events, f_{sig} and the fiducial efficiency.

The following sources are considered in the calculation of uncertainties:

Lepton-related uncertainties: The uncertainties considered are related to the elec-

[1]The scaling factor appearing in equation (13.2) is obtained by solving the equation $\mathcal{L} = C\mathcal{L}_{\text{MC}} = C\frac{N_{\text{gen}}}{\sigma_{\text{MC}}}$, where $\mathcal{L}, \mathcal{L}_{\text{MC}}$ are the integrated luminosities of the data and MC samples respectively, N_{gen} is the number of generated events and σ_{MC} is the cross-section of the MC sample, incorporating any potential higher-order correction factors and event generation efficiencies.

tron and muon identification efficiencies, their energy scale as well as the resolution of the measurement of the electron energy and muon momentum. The electron and muon trigger efficiencies also form part of the lepton-related uncertainties.

Jet-related uncertainties: The uncertainties considered are related to the jet energy scale and resolution. The uncertainties related to the JVF cut efficiency and to the modeling of the pile-up subtraction are also included here.

***b*-tagging uncertainties**: These include the uncertainties from the b-tagging efficiency as well as the mis-tagging efficiency correction factors.

Table 13.1 contains a list of the uncertainties listed above relative to the $t\bar{t}b\bar{b}$ cross-section. The dominant systematic uncertainty is due to the determination of the b-tagging efficiency ($^{+12.9}_{-11.9}$% on $\sigma_{t\bar{t}b\bar{b}}$). The jet energy scale is the second dominant systematic but is significantly smaller than the b-tagging one, contributing with an uncertainty of $^{+5.5}_{-4.9}$%. The LF and c-jet mis-tagging uncertainties are significantly smaller than the b-tagging uncertainties due to the small contribution of $t\bar{t}$+charm and $t\bar{t}$+LF jets in the signal region. A complete breakdown of the systematic uncertainty sources is given in Appendix B.

Source	Uncertainty [% on $\sigma_{t\bar{t}b\bar{b}}$]
b-tagging	$^{+12.9}_{-11.9}$
Jet	$^{+5.5}_{-4.9}$
LF-jet mis-tagging	$\pm$ 4.3
Electron	2.0
Muon	1.9
c-jet mis-tagging	1.7
Sum	$^{+15.0}_{-14.0}$

Table 13.1: Relative systematic uncertainties (in %) due to the variation of the data-to-MC correction factors on the predicted cross-section. The individual uncertainty components are given in Appendix B.

13.3 Modeling uncertainties

Comparisons between simulation samples can probe different aspects of the event modeling and can thus be used to assess the modeling uncertainties associated with the measurement. Pairwise comparisons between the nominal model and alternative models are designed to target one modeling component at a time, so as to minimize correlations among the different modeling variations.

The following components are considered in the derivation of the modeling uncertainty:

- **Generator uncertainty**: covers differences in the computation of the hard/non-collinear part of the scattering process. It is estimated by comparing the MADGRAPH samples which provide LO matrix elements for $t\bar{t}+ \leq 3$ jets to the POWHEG+PYTHIA 6 sample with $h_{\text{damp}} = \infty$ which provides NLO matrix elements for inclusive $t\bar{t}$ production, both of which being interfaced to the same parton shower. The two samples differ by the perturbative accuracy at which the matrix elements are computed and by the way the matrix elements are matched to the parton shower. More specifically in the POWHEG case, the matching is done with the Powheg method [67, 68], while in the MADGRAPH case the matching is done with the MLM matching [152].

- **Parton shower/hadronization uncertainty**: covers the differences in the simulation of the soft part of the scattering process, including soft/collinear gluon emissions and $g \to q\bar{q}$ splittings that are generated by the showering generators, the difference in the description of multi-parton interactions and also the difference in the modeling of the non-perturbative hadronization transition. It is estimated by comparing the POWHEG inclusive $t\bar{t}$ sample interfaced to PYTHIA 6 and to HERWIG. The two showers differ most notably by the choice of the shower evolution variable (transverse momentum of the splitting for PYTHIA 6, splitting angle for HERWIG), the handling of the low p_T behavior of the $2 \to 2$ scattering for multi-parton interactions and by the description of hadronization. The POWHEG+HERWIG sample is only available with the parameter h_{damp} set to infinity. In order to isolate the effect of the parton shower, the uncertainty is derived by comparing to the POWHEG+PYTHIA 6 sample with the same setting.

- **Scale/ISR/FSR uncertainties**: are expected to estimate the uncertainty due to missing higher order terms in the perturbative expansion. They are estimated

from the MADGRAPH+PYTHIA 6 sample by varying the renormalization and factorization scales (equation (7.7)) by a factor of two. Since the underlying event tune is consistently varied with the choice of scale (i.e. a tune with a higher (lower) α_s value is chosen for the lower (higher) scale choice), this uncertainty also covers the uncertainty related to the production of QCD radiation in the initial and final state.

- **PDF uncertainty** : covers the theoretical and experimental uncertainties related to the PDF used in the matrix element calculation. It is estimated using the MC@NLO inclusive $t\bar{t}$ sample interfaced to HERWIG. The PDF uncertainty is estimated using the cross-sections obtained with the CT10, MSTW2008NLO and NNPDF error PDF sets. The CTEQ and MSTW collaborations use the Hessian method for estimating the PDF uncertainties, whereby the Hessian matrix[2] parametrizes the form of the goodness-of-fit quantity χ^2_{global} around its global minimum. The uncertainty on the cross-section for the MSTW2008NLO case is given by

$$\delta\sigma_{\text{PDF}} = \frac{1}{2}\sqrt{\sum_{i=1}^{20}\left[\sigma^{\text{fid}}_{t\bar{t}b\bar{b}}(\text{PDF}^{+}_{i}) - \sigma^{\text{fid}}_{t\bar{t}b\bar{b}}(\text{PDF}^{-}_{i})\right]^2}, \tag{13.4}$$

while for CT10 an asymmetric error is used:

$$\delta\sigma_{\text{PDF}} = \sqrt{\sum_{i=1}^{26}\left\{\max\left[\sigma^{\text{fid}}_{t\bar{t}b\bar{b}}(\text{PDF}^{+}_{i}) - \sigma^{\text{fid}}_{t\bar{t}b\bar{b}}(\text{PDF}_0), \sigma^{\text{fid}}_{t\bar{t}b\bar{b}}(\text{PDF}^{-}_{i}) - \sigma^{\text{fid}}_{t\bar{t}b\bar{b}}(\text{PDF}_0), 0\right]\right\}^2} \tag{13.5}$$

$$\delta\sigma_{\text{PDF}} = \sqrt{\sum_{i=1}^{26}\left\{\max\left[\sigma^{\text{fid}}_{t\bar{t}b\bar{b}}(\text{PDF}_0) - \sigma^{\text{fid}}_{t\bar{t}b\bar{b}}(\text{PDF}^{+}_{i}), \sigma^{\text{fid}}_{t\bar{t}b\bar{b}}(\text{PDF}_0) - \sigma^{\text{fid}}_{t\bar{t}b\bar{b}}(\text{PDF}^{-}_{i}), 0\right]\right\}^2}. \tag{13.6}$$

The CT10 uncertainties are reduced by a factor of 1.645 in order to convert the 90% CL uncertainties into 68% CL uncertainties. For NNPDF, the uncertainty is

[2]The Hessian matrix is defined by: $H_{ij} = \frac{1}{2}\frac{\partial\chi^2_{\text{global}}}{\partial a_i \partial a_j}\Big|_{\text{min}}$.

taken as

$$\delta\sigma_{\text{PDF}} = \sqrt{\sum_{i=1}^{100} \frac{\sigma^{\text{fid}}_{t\bar{t}b\bar{b}}(\text{PDF}_i)^2}{100} - \left[\sum_{i=1}^{100} \frac{\sigma^{\text{fid}}_{t\bar{t}b\bar{b}}(\text{PDF}_i)}{100}\right]^2}. \tag{13.7}$$

The envelope of the resulting error bands gives the total PDF uncertainty, as seen in Figure 13.1.

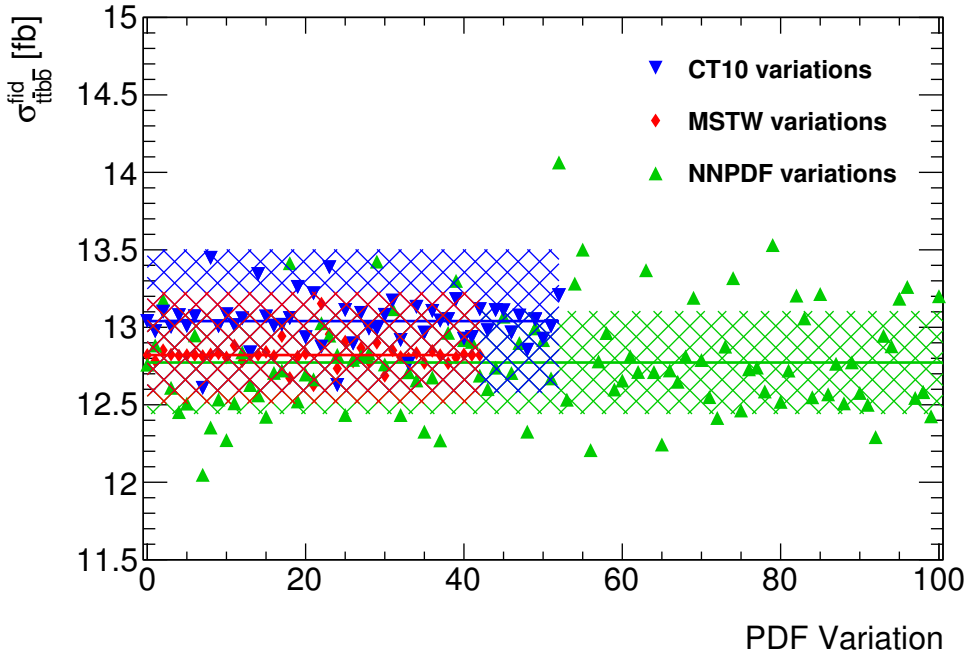

Figure 13.1: Cross-section obtained using different PDF sets with the MC@NLO inclusive sample. The numbers have been scaled to match the nominal measurement. The error bands are calculated as described in the text. The total uncertainty is taken as half the distance from the top of the highest error band to the bottom of the lowest.

The individual variations with respect to the nominal cross-section, with the exception of the scale uncertainty, are added in quadrature to obtain the total modeling uncertainty

$$\delta\sigma^{\text{fid,modeling}}_{t\bar{t}b\bar{b}} = \sqrt{\sum_{\text{var}} \left|\sigma^{\text{fid}}_{t\bar{t}b\bar{b},\text{nominal}} - \sigma^{\text{fid}}_{t\bar{t}b\bar{b},\text{var}}\right|^2}. \tag{13.8}$$

For the scale uncertainty,

$$\delta\sigma_{\text{scale}} = \frac{\sigma^{\text{fid}}_{t\bar{t}b\bar{b}}(\text{MG Q2down}) - \sigma^{\text{fid}}_{t\bar{t}b\bar{b}}(\text{MG Q2up})}{\sigma^{\text{fid}}_{t\bar{t}b\bar{b}}(\text{MG central})} \tag{13.9}$$

is used and added in quadrature to the other modeling uncertainties. The result is displayed graphically in Figure 13.2. Table 13.3 summarizes the effect of the modeling uncertainties on the cross-section together with the rest of the uncertainty sources.

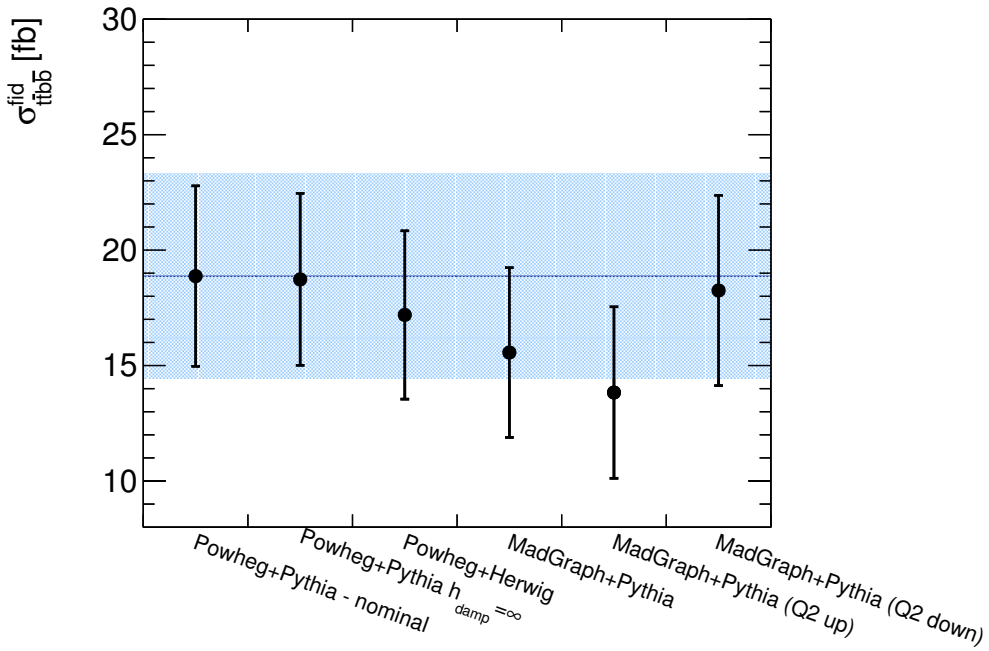

Figure 13.2: Cross-sections obtained with different modeling assumptions as explained in the text. The error bars correspond to the total uncertainty, consisting of the statistical, systematic and luminosity uncertainty, which is derived separately for each prediction. The blue band corresponds to the total modeling uncertainty, obtained by adding in quadrature the variations of the individual modeling components. The prediction from POWHEG+PYTHIA with $h_{\text{damp}} = \infty$ is shown for illustrative purposes only and is not used in the calculation of the modeling uncertainty.

We note that in equation (13.8), $\sigma^{\text{fid}}_{t\bar{t}b\bar{b},\text{var}}$ is calculated from equation (6.5) where both the signal and background components are varied simultaneously according to the modeling variation that is considered. In other words, the effect of the modeling variations is considered to affect the signal and background in a correlated way. A cross-check has been performed, where the effect of each modeling variation was considered to affect the signal and background in an uncorrelated way. Assuming that

the signal and background uncertainties are uncorrelated leads to a total modeling uncertainty of 20.3% on $\sigma_{t\bar{t}b\bar{b}}$, to be compared with 23.8% obtained with the correlated treatment. The reduction of the uncertainty is due to the fact that the modeling variations tend to move the cross-section in the same direction and therefore adding the uncertainties in quadrature (uncorrelated case) leads to a smaller total uncertainty than adding them linearly (correlated case).

13.4 Uncertainties related to the cross-sections of the simulated event samples

The uncertainties on the cross-section for simulated samples other than $t\bar{t}+$ jets have been taken from the latest available theoretical calculations, as indicated in Table 13.2. The number for $t\bar{t}H$ includes the uncertainty on the branching ratio of $H \to b\bar{b}$. For single top, the uncertainty is obtained by adding in quadrature the theoretical uncertainty on the cross-section of the nominal sample, the difference between the MC@NLO and Powheg samples obtained using the diagram removal scheme and the difference between the Powheg samples obtained with the diagram subtraction and diagram removal schemes. The latter gives the dominant contribution to the uncertainty. Additionally, an uncertainty of 50% is assumed on the cross-section for the $t\bar{t}c\bar{c}$ and $t\bar{t}cj$ processes. These are considered to be uncorrelated with the rest of the modeling uncertainties.

For the signal processes $t\bar{t}H$ and $t\bar{t}Z$, the cross-section uncertainties affect the relative weight of these samples compared to the $t\bar{t}$ sample (see equation (12.4)) in the calculation of the fiducial efficiency and signal fraction f_{sig}.

Process	Uncertainty [%]	Uncertainty taken from
Single top	86	-
Di-boson	34	[66]
Z+jets	48	[66]
$t\bar{t} + W/Z$+jets	14	[166]
$t\bar{t}H$	$^{+10}_{-13}$	[145]
$t\bar{t}c\bar{c}$	50	-
$t\bar{t}cj$	50	-

Table 13.2: Relative systematic uncertainties on the cross-section of the background samples.

Source	Uncertainty [%]
Modeling uncertainty	23.8
Generator	16.9
Scale/ISR/FSR	14.2
Showering/hadronization	8.2
PDF	3.3
Data-to-MC correction factors	$^{+15.0}_{-14.0}$
$t\bar{t}c\bar{c}$, $t\bar{t}cj$	1.9
Other cross-sections	1.6
MC statistics	9.6
Total systematic uncertainty	$^{+29.8}_{-29.3}$
Statistical uncertainty	18.4
Luminosity uncertainty	3.2
Total uncertainty	$^{+35.2}_{-34.7}$

Table 13.3: Relative uncertainties (in %) on the measured cross-section.

Chapter 14

Results

This chapter presents the calculation of the $t\bar{t}b\bar{b}$ production cross-section in data and the comparison with different theoretical predictions.

14.1 The measured cross-section

The number of events in the signal region is given in Table 14.1. As was already observed in Section 10.3, the nominal simulation sample underestimates the rate of signal events. Table 14.2 contains the values of the parameters entering into the cross-section calculation (equation (6.5)). The result for the measured cross-section is

$$\sigma^{\text{fid}}_{t\bar{t}b\bar{b}} = 18.9 \pm 3.5\ (\text{stat})^{+5.6}_{-5.5}\ (\text{sys}) \pm 0.6\ (\text{Lumi})\ \text{fb}. \tag{14.1}$$

In order to facilitate comparisons with theoretical calculations, which usually only contain the pure QCD production terms for $t\bar{t}b\bar{b}$, an alternative calculation was also performed wherein the $t\bar{t}H(b\bar{b})$ and $t\bar{t}Z(b\bar{b})$ (both the reducible and irreducible final states) were subtracted from the signal, based on predictions obtained from simulation. In this case, the result is

$$\sigma^{\text{fid, QCD}}_{t\bar{t}b\bar{b}} = 17.8 \pm 3.5\ (\text{stat})^{+5.9}_{-5.7}\ (\text{sys}) \pm 0.6\ (\text{Lumi})\ \text{fb}. \tag{14.2}$$

Data	37
MC Expectation (S+B)	$25.0\ ^{+7.1}_{-4.8}$
Total signal (MC)	$16.0\ ^{+4.2}_{-2.9}$
$t\bar{t}b\bar{b}$ QCD signal	$14.0\ ^{+4.0}_{-2.6}$
$t\bar{t}Z$ signal	$0.56\ ^{+0.13}_{-0.13}$
$t\bar{t}H$ signal	$1.47\ ^{+0.27}_{-0.29}$
Total Background (MC)	$9.0\ ^{+3.6}_{-2.9}$
Non-fiducial (MC)	$5.1\ ^{+3.3}_{-2.9}$
Mis-tagged (MC)	$2.61\ ^{+1.49}_{-1.61}$
$t\bar{t}c\bar{c}$ QCD	$1.44\ ^{+0.82}_{-0.65}$
$t\bar{t}cj$ QCD	$0.67\ ^{+0.61}_{-0.67}$
$t\bar{t}jj$ QCD	$0.30\ ^{+0.32}_{-0.30}$
$t\bar{t}+W/Z$	$0.15\ ^{+0.14}_{-0.14}$
$t\bar{t}H$	$0.02\ ^{+0.03}_{-0.02}$
≥ 3 mis-tagged jets	$0.04\ ^{+0.03}_{-0.03}$
Non $t\bar{t}$+jets (MC)	$1.25\ ^{+1.06}_{-0.94}$
Single top	$0.42\ ^{+0.46}_{-0.42}$
Di-boson	$0.004\ ^{+0.003}_{-0.003}$
Z+jets	$0.82\ ^{+0.96}_{-0.82}$

Table 14.1: Measured number of events with exactly 4 reconstructed b-jets and estimates for the signal and background events. The MC predictions for signal and non-fiducial background are not used in the measurement but are shown for comparison. Uncertainties on the MC predictions include all systematic and statistical sources.

N_{4b}^{data}	37
$\mathcal{L}$	20.3 ± 0.6 fb^{-1}
$N_{t\bar{t}+\text{jets}}^{\text{mis-tagged}}$	2.6 ± 0.4 (stat) $^{+1.4}_{-1.6}$ (sys)
$N_{\text{bg}}^{\text{non-}t\bar{t}+\text{jets}}$	1.2 ± 0.9 (stat) $^{+0.6}_{-0.6}$ (sys)
f_{sig}	0.76 ± 0.06 (stat) $^{+0.06}_{-0.06}$ (sys)
$\epsilon_{\text{fid}}(\%)$	6.6 ± 0.4 (stat) $^{+1.6}_{-0.9}$ (sys)

Table 14.2: Values for each parameter entering into the cross-section calculation. Uncertainties are separated into statistical and systematic effects.

14.2 Comparison with theory

The cross-section for the pure QCD production of $t\bar{t}b\bar{b}$ was compared to a series of theoretical predictions.

The most precise theoretical predictions available to date consist of NLO calculations for $pp \to t\bar{t}b\bar{b}$ interfaced to parton showers. These calculations are available both through the MADGRAPH5_AMC@NLO [88] and the POWHEL framework [94]. Both calculations contain only the pure QCD terms $(\mathcal{O}(\alpha_s^5))$, neglecting the mixed QCD-EW and the pure EW ones as well as their interference.

For the MADGRAPH5_AMC@NLO sample two different functional forms for the renormalization and factorization scale were chosen, in order to probe the sensitivity of the process to the choice of scale. The scales were defined by

$$\mu^2_{\text{BDDP}} = m_{\text{top}} \sqrt{p_T(b) p_T(\bar{b})} \tag{14.3}$$

$$\mu_{\text{H}_\text{T}/4} = \frac{\sum_{i \in \text{ final state}} \sqrt{m_i^2 + p_{T,i}^2}}{4}. \tag{14.4}$$

where μ^2_{BDDP} was first proposed in [93]. A sample of 10 million inclusive $t\bar{t}b\bar{b}$ events was generated using the CT10 4f PDF set and the Monash tune [172]. The parton level sample was interfaced to PYTHIA 8.205 [102], which was used for handling the top decays (retaining only the decays to final states with two leptons[1]), showering and hadronization[2]. The sample was generated with very loose generation cuts on jets,

[1] The decays to all lepton flavors (e, μ, τ) were simulated.

[2] In the matching of AMC@NLO to PYTHIA 8 the counter-terms that correct for the double-counting of the NLO emissions in the shower have been calculated assuming massless split-

i.e. $p_T > 5$ GeV and $|\eta| < 4$, where jets were defined by clustering partons with the anti-k_T algorithm with a radius parameter of $R = 0.4$.

For the POWHEL sample the renormalization and factorization scales were set to

$$\mu_{\mathrm{H_T}/4} = \frac{\sum_{i\in \text{ underlying Born}} \sqrt{m_i^2 + p_{T,i}^2}}{4}, \tag{14.5}$$

where in contrast to equation (14.4), the scale is evaluated using the underlying Born configuration. The sample was generated[3] with massless b-quarks and therefore cuts on $p_T(b) > 2$ GeV and $m_{b\bar{b}} > 2$ GeV had to be applied in order to avoid the divergences associated with gluon splittings into massless quarks.

The MADGRAPH5_AMC@NLO and POWHEL samples are thus expected to differ with respect to the matrix element to parton shower matching scheme (MC@NLO vs Powheg matching) and the choice of the active number of flavors in the calculation (4FS vs 5FS). Small differences are also expected to arise due to the slightly different definition of the scales (using the underlying Born or the real kinematics) and the value of the top quark mass (173.2 GeV in POWHEL vs 172.5 GeV in MADGRAPH5_AMC@NLO). However these are expected to be smaller than the differences from the matching scheme and the flavor number scheme.

The uncertainties associated to the aforementioned predictions are obtained by simultaneously varying the renormalization and factorization scales by a factor of two, using the re-weighting procedure[4] described in [174].

A merged LO+PS prediction was obtained with the MADGRAPH+PYTHIA 6 sample, described in Section 7.2, which was normalized to the NNLO+NNLL inclusive $t\bar{t}$ cross-section [149].

Finally, in order to better gauge how the different descriptions of the $g \to b\bar{b}$ splitting in the parton shower affect the $t\bar{t}b\bar{b}$ cross-section, a LO $pp \to t\bar{t}$ sample was generated with PYTHIA 8.205, normalizing the inclusive cross-section to the NNLO+NNLL result. The effect of the different modeling of $g \to b\bar{b}$ was assessed by varying the wgtq and sgtq parameters, as explained in Section 2.3.

ting kernels for $g \to b\bar{b}$. Therefore in order to ensure that the ME/PS matching is valid, the `TimeShower:weightGluonToQuark` parameter (wgtq) in PYTHIA 8 had to be set to 1, for the MADGRAPH5_AMC@NLO samples. We also chose to set wgtq to 1 for the POWHEL sample, in order to be able to compare the two calculations on a more equal footing.

[3] The parton-level sample was provided by the POWHEL collaboration.

[4] This procedure exploits the new LHEF v3.0 standard adopted in [173].

The fiducial cross-section was estimated using RIVET 2.2.1 [175] and is shown in Table 14.3 for each of the aforementioned models.

Several observations can be made by comparing the predicted cross-sections to the measured one:

1. by comparing the results obtained with the BDDP and $H_T/4$ scales, or equivalently by comparing the upper and lower limits of each prediction, it is evident that the data favor the predictions obtained with soft renormalization/factorization scales,

2. comparing the 4FS (AMC@NLO) with 5FS (POWHEL) predictions, at equivalent values of the renormalization/factorization scales[5], we observe that the 5FS calculation gives a higher cross-section than the 4FS one. We note that the 5FS resums logarithms of the kind $\ln \frac{Q^2}{m_b^2}$ arising from $g \to b\bar{b}$ splitting and is thus expected to give a higher cross-section than the 4FS one. If large logarithms of this kind affect the 4FS calculation, choosing soft renormalization/factorization scales in the calculation would have an equivalent effect on the cross-section as a resummation of these terms, as has been discussed in Section 2.2 and [5]. The difference of the cross-sections between the two flavor schemes is nonetheless significantly smaller than their respective scale uncertainties,

3. concerning the different models for the $g \to b\bar{b}$ splitting, the two extremal predictions, corresponding to the wgtq3 and wgtq5, sgtq=1 models are shown in Table 14.3. The wgtq3 model overestimates the $t\bar{t}b\bar{b}$ cross-section by more than 1σ[6], indicating that this model predicts too high a $g \to b\bar{b}$ rate. This observation is also confirmed by comparisons to the $g \to b\bar{b}$ measurements at LEP and SLC [177]. The variations between the remaining models are significantly smaller than the factor of 2 difference between the extremal ones and are in agreement with the measurement within the uncertainties. The spread between the remaining models could be further constrained by more precise measurements of $\sigma_{t\bar{t}b\bar{b}}$ in the future,

4. the sgtq parameter available in some of the PYTHIA 8 models provides an additional degree of freedom that could be used to tune the $g \to b\bar{b}$ rate to the

[5] Due to the difference in the nominal choice of scales, one has to compare the central value (lower limit) of the AMC@NLO+PYTHIA 8 prediction with $\mu = H_T/4$ with the upper limit (central value) of the POWHEL prediction.

[6] An even higher (more than 2σ) discrepancy was observed in the analyses with three resolved b-jets [176].

available measurements. The combination of the wgtq6 model with sgtq=0.25 was found to agree best with the measurement reported here.

A graphical representation of the different predictions and the measured cross-section is shown in Figure 14.1.

Generator	Scale	m_{top} [GeV]	m_b [GeV]	$\sigma_{t\bar{t}b\bar{b}}^{\text{fid, QCD}}$ [fb]
aMC@NLO+Pythia 8	BDDP	172.5	4.8	$17.5^{+6.6}_{-5.4}$
aMC@NLO+Pythia 8	$H_T/4$	172.5	4.8	$11.7^{+4.3}_{-3.5}$
Powhel+Pythia 8	$H_T/2$	173.2	0	$8.9^{+4.3}_{-1.8}$
MadGraph+Pythia 6	equation (7.7)	172.5	4.8	$12.8^{+3.9}_{-2.7}$
Pythia 8 (wgtq3)	$\sqrt{m_T(t)m_T(\bar{t})}$	172.5	4.8	29.0
Pythia 8 (wgtq5, sgtq=1)	$\sqrt{m_T(t)m_T(\bar{t})}$	172.5	4.8	12.6
Pythia 8 (wgtq6, sgtq=0.25)	$\sqrt{m_T(t)m_T(\bar{t})}$	172.5	4.8	15.7
Powheg+Pythia 6	$\sqrt{p_T^2(t)+m^2(t)}$	172.5	0	10.9
Measurement	$17.8^{+6.9}_{-6.7}$ fb			

Table 14.3: Comparison of the predictions for $\sigma_{t\bar{t}b\bar{b}}^{\text{fid, QCD}}$ obtained with a series of different models with the measured cross-section.

We note that processes beyond the Standard Model (BSM) which lead to the production of a $t\bar{t}b\bar{b}$ final state could affect the measurement. A characteristic example is the production of a charged Higgs ($H^{\pm}$) in association with a top quark, which occurs in models with an extended Higgs sector, such as the 2 Higgs Doublet Models [178] or the Minimal Supersymmetric Standard Model [179]. An inspection of the Feynman diagrams for the process $pp \to \bar{t}bH^+$ (Figure 14.2) reveals that such processes are indistinguishable from the QCD production of $t\bar{t}b\bar{b}$ and could thus contribute to the signal region. The distinctive characteristic of such processes is the resonant shape in the invariant mass spectrum of the 4 b-jets in the final state, which is absent in the case of the QCD production of $t\bar{t}b\bar{b}$. In inclusive measurements, like the one reported here, it is impossible to differentiate between the two processes and therefore the existence of such BSM processes would be manifested as an excess of the observed cross-section compared to the SM expectation. More differential measurements exploiting variables that can discriminate between the SM and BSM production of $t\bar{t}b\bar{b}$ are therefore necessary and dedicated searches are under way in both ATLAS [180] and CMS [181] collaborations.

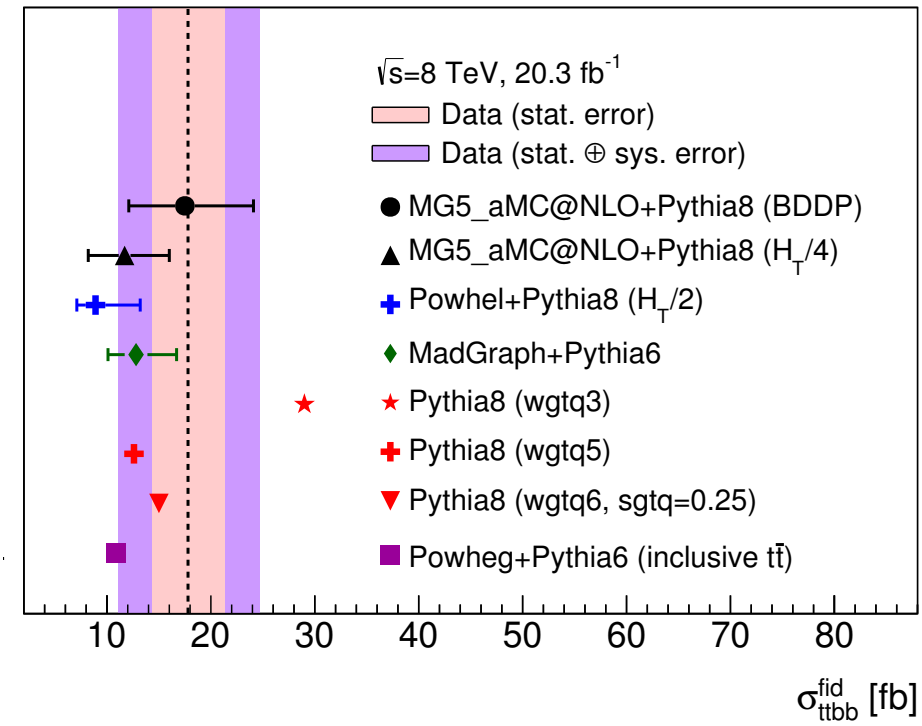

Figure 14.1: Comparison of the fiducial $t\bar{t}b\bar{b}$ cross-section, with theoretical predictions obtained with the most accurate $t\bar{t}b\bar{b}$ theory predictions available to date. The colored bands indicate the statistical and total uncertainties of the measurement, as described in the legend. The data prefer a softer scale choice (BDDP instead of $H_T/4$). The difference between the 4FS (AMC@NLO) and 5FS (POWHEL) predictions seems to be significantly smaller than the associated scale uncertainties. In the PYTHIA 8 predictions where the additional b-jets come only from the parton shower, the different models for the description of $g \to b\bar{b}$ splitting have a significant impact on the $t\bar{t}b\bar{b}$ cross-section, with the extremal predictions differing by more than a factor of 2. The wgtq3 model seems to overestimate the $g \to b\bar{b}$ rate.

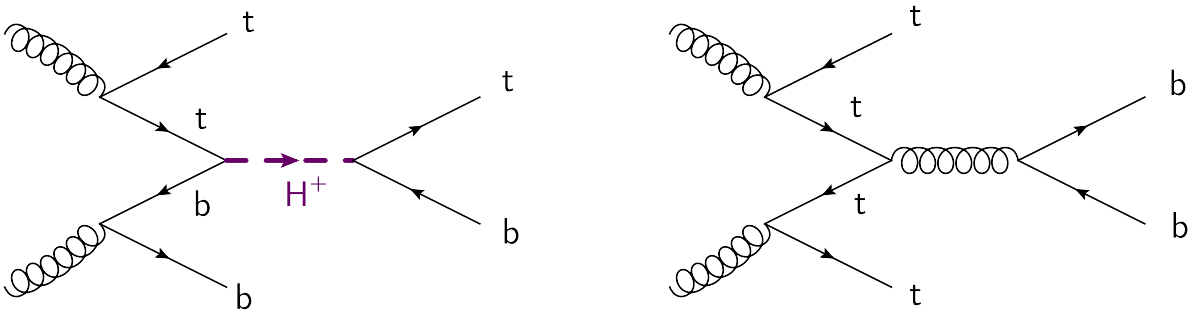

Figure 14.2: The production of a charged Higgs H^+ in association with a top quark (left) leads to a final state with a $t\bar{t}$ and a $b\bar{b}$ pair, which is indistinguishable from the QCD production of $t\bar{t}b\bar{b}$ (right). In contrast to the QCD production of $t\bar{t}b\bar{b}$, the process with the charged Higgs would produce a distinctive resonant shape in the invariant mass of the 4 b-jets in the final state. In an inclusive measurement, such as the one reported here, the existence of such BSM processes would be manifested as an enhancement of the $t\bar{t}b\bar{b}$ cross-section compared to the SM expectation.

Chapter 15

Conclusions and outlook

This thesis presented the measurement of the $t\bar{t}b\bar{b}$ production cross-section. The fiducial cross-section for the production of a $t\bar{t}b\bar{b}$ final state irrespective of the production mechanism has been found to be

$$\sigma^{\text{fid}}_{t\bar{t}b\bar{b}} = 18.9 \pm 3.5\ (\text{stat})^{+5.6}_{-5.5}\ (\text{sys}) \pm 0.6\ (\text{Lumi})\ \text{fb}. \tag{15.1}$$

Subtracting the contributions of the $t\bar{t}H(b\bar{b})$ and $t\bar{t}Z(b\bar{b})$ final states, based on the respective theory estimates, we obtain

$$\sigma^{\text{fid,QCD}}_{t\bar{t}b\bar{b}} = 17.8 \pm 3.5\ (\text{stat})^{+5.9}_{-5.7}\ (\text{sys}) \pm 0.6\ (\text{Lumi})\ \text{fb}. \tag{15.2}$$

The measured cross-section has been compared with a series of theoretical predictions utilizing the latest developments in NLO+PS matching techniques as well as with models that offer different descriptions of the $g \to b\bar{b}$ splitting kernels. The most extreme PYTHIA 8 model is shown to be in tension with the measurement, overestimating the $t\bar{t}b\bar{b}$ cross-section by more than 1σ. While the accuracy of the measurement is not as high as to exclude any of the remaining models, it does reveal certain systematic trends among the theoretical predictions. Most notably, the data is shown to favor the calculations performed with renormalization and factorization scales which are softer than the typical scales used in similar calculations involving multi-particle final states. The spread between the theoretical predictions indicates that future, more precise measurements could differentiate between those models. A measurement of the $t\bar{t}b\bar{b}$ production could therefore provide supplementary constrains for the modeling of $g \to b\bar{b}$ in the parton shower generators.

The dominant uncertainties affecting the measurement come from the modeling of the $t\bar{t}b\bar{b}$ final state, statistics and b-tagging. The upcoming Run 2 of the LHC with an increased center-of-mass energy will provide the opportunity to collect more data, thereby helping to reduce the statistical uncertainty of the measurement. For $\sqrt{s} = 13$ TeV, the $t\bar{t}b\bar{b}$ cross-section is expected to increase by a factor of 5 compared to $\sqrt{s} = 8$ TeV [89] and with an integrated luminosity of 100 fb^{-1} expected to be collected during Run 2, the statistical uncertainty of the measurement would decrease by a factor of 5. The statistics could also be increased by lowering the p_T threshold of the leptons. Preliminary studies indicated a gain of more than 25% in statistics when the sub-leading lepton p_T threshold was lowered from 25 to 15 GeV. Extending the phase space towards the softer region comes at the expense of higher systematic uncertainties, therefore detailed studies would be needed to verify whether lowering the p_T thresholds would reduce the total uncertainty of the measurement.

A possible way to reduce the systematic uncertainties, once a $t\bar{t}b\bar{b}$ sample with large statistics is available, would be to increase the jet p_T threshold. This is expected to reduce both the detector related systematic uncertainties (e.g. jet energy scale) as well as the modeling ones, since the modeling of hard jets is better controlled than the modeling of soft jets, which involves substantially different phenomenological models of soft QCD. This avenue was already exploited by the CMS collaboration in [182].

Including more measurement regions, enriched in c and LF jets, is substantial in order to constrain the background contributions from the $t\bar{t}$+charm and $t\bar{t}$+LF processes, which are not well known theoretically and could also help in reducing the total uncertainty by constraining some of the systematic uncertainties from in-situ measurements. This has been exploited by the ATLAS collaboration in [176]. A more sophisticated measurement method, e.g. based on multivariate discriminants, could also help to enhance the signal-to-background ratio thereby also reducing the total uncertainty of the measurement. Such techniques have been used by the CMS collaboration in [182, 183]. Employing the latest available theoretical predictions for $t\bar{t}b\bar{b}$, based on NLO calculations could potentially help to reduce the modeling uncertainties.

Measurements performed in different phase space regions have also been performed, both in the ATLAS as well as the CMS collaborations [176, 182, 183]. Results have been obtained both in the lepton plus jets channel, as well as the di-lepton one with either 3 or 4 resolved b-jets in the final state, as well as for the cross-section ratio $\sigma_{t\bar{t}b\bar{b}}/\sigma_{t\bar{t}jj}$. While the lepton plus jets channel offers higher statistics, due to the

increased branching ratio, it suffers from larger backgrounds, particularly from events where one of the W bosons decays into a c-quark. While measuring the phase space region with 4 resolved b-jets is closer to the region that is probed by the $t\bar{t}H$ measurements, the region with 3 resolved b-jets provides complementary information on the rate of collinear $g \to b\bar{b}$ splittings, which result in b-jets with 2 clustered b-hadrons and on the soft end of the spectrum. This information is important not only for constraining the total $t\bar{t}b\bar{b}$ rate for the $t\bar{t}H$ measurements but also for testing the QCD calculations at high energy scales and putting constraints on Monte-Carlo generators.

Finally, it has to be emphasized that inclusive measurements of the $t\bar{t}b\bar{b}$ production only offer a limited amount of information (a single number) with which one can interpret the agreement between data and theory and identify the sources of any potential discrepancies. Differential measurements of the $t\bar{t}b\bar{b}$ production (e.g. as a function of the jet multiplicity or as a function of the b-jet p_T), which will become possible only with higher statistics, are thus of prime importance for a conclusive interpretation of the results.

Appendix A

Pile-up jet identification and suppression

One of the main challenges for the $\sqrt{s} = 8$ TeV analyses was the large number of inelastic pp collisions in each bunch crossing. The mean number of inelastic interactions $\langle\mu\rangle$ is defined as follows

$$\langle\mu\rangle = \frac{L\,\sigma_{\text{inel}}}{N_{\text{bunch}}\,f_{\text{LHC}}}, \tag{A.1}$$

where L is the instantaneous luminosity, σ_{inel} is the inelastic pp cross-section, N_{bunch} is the number of proton bunches and f_{LHC} is the bunch revolution frequency. During the $\sqrt{s} = 8$ TeV run, events with a maximum of approximately 40 interactions were recorded, with an average of $\langle\mu\rangle \approx 21$, as shown in Figure A.1.

The presence of additional interactions in the same bunch crossing, referred to as in-time pile-up, produces additional signal in the ATLAS sub-detectors. In sub-detectors whose read-out time is longer than the bunch spacing (such as the LAr calorimeter), signal modulation can also occur from signals in surrounding bunch crossings, an effect known as out-of-time pile-up. Pile-up interactions have a detrimental effect on the reconstruction of physics objects, particularly jets, leading to a net increase of particle and jet multiplicities, the modification of the jet structure and jet kinematics an overall resolution degradation.

Different techniques exist to mitigate the effect of pile-up on the jet kinematics and suppress pile-up jets, as described in Section 5.2. While these techniques have been demonstrated to perform well for the 2012 pile-up conditions, the increase of the instantaneous luminosity in the upcoming LHC runs calls for a deeper understanding

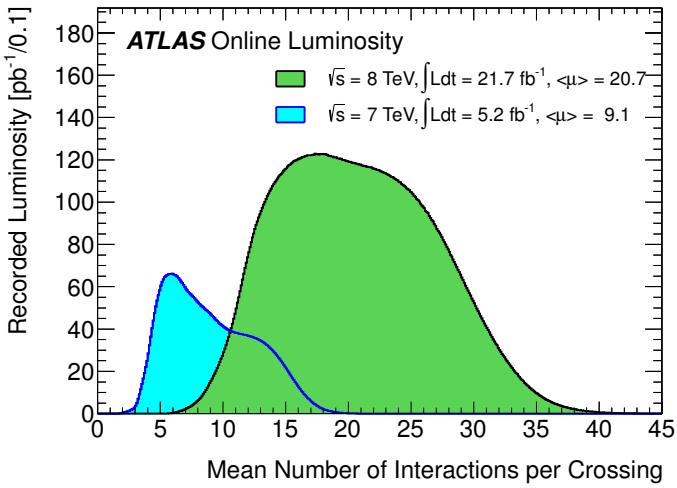

Figure A.1: Mean number of inelastic pp interactions in the 2011 and 2012 datasets.

of the characteristics of pile-up jets. Moreover, the pile-up suppression techniques developed so far rely on tracking information, which is not available for $|\eta| > 2.5$. In this appendix we examine how pile-up jets could be defined in Monte-Carlo, investigate their characteristic properties and propose a novel way to suppress pile-up jets using only calorimeter information.

A.1 Classification schemes

As shown in Figure A.2, jets reconstructed in events with pile-up (PU) interactions will typically contain particles from both the hard-scattering (HS) interaction as well as from PU interactions. The HS interaction is defined as the interaction which leads to the primary vertex with the highest $\sum_{\text{track}} p_{T,\text{track}}^2$. In order to separate PU from HS jets, a well defined classification scheme is needed. The main characteristics that such a scheme must possess are

- independence of pile-up, i.e. the scheme must return the same number of HS jets independently of the amount of PU interactions in the event
- a high efficiency in finding the HS jets in an event.

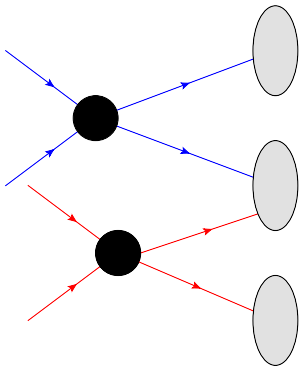

Figure A.2: A cartoon depicting two interactions, a hard-scattering interaction (blue) and a pile-up interaction (red). The outgoing particles from the different interactions are clustered into jets (grey blobs), which may contain particles from both the HS as well as from PU interactions.

Several classification schemes can be developed using the following starting point

$$\begin{aligned} \sum_{\text{HS} \in \text{ jet}} \mathcal{O}_{\text{HS}} > \sum_{\text{PU} \in \text{ jet}} \mathcal{O}_{\text{PU}} \Rightarrow \text{jet is HS} \\ \sum_{\text{HS} \in \text{ jet}} \mathcal{O}_{\text{HS}} < \sum_{\text{PU} \in \text{ jet}} \mathcal{O}_{\text{PU}} \Rightarrow \text{jet is PU,} \end{aligned} \tag{A.2}$$

where the sums run over the HS and PU particles that are clustered in a given jet and $\mathcal{O}_{\text{HS}(PU)}$ refers to a characteristic observable built from those particles, such as the particle multiplicity N, energy E, transverse momentum p_T etc. The classification schemes obtained are respectively called N-scheme, E-scheme, p_T-scheme and so on.

The main criterion for assessing the performance of the aforementioned classification schemes is their stability under different amounts of pile-up. This can be quantified by comparing the number of HS jets predicted by each scheme for different pile-up conditions.

This was accomplished by generating[1] semi-leptonic $t\bar{t}$ events using the MC@NLO generator interfaced to HERWIG and JIMMY using the CT10 PDF set. The effect of in and out-of-time pile-up was modeled by overlaying GEANT4 digitized hits from events with exactly one $t\bar{t}$ event with hits from minimum-bias events generated with PYTHIA 8.160 using the A2M tune and the MSTW2008LO PDF. The number of overlaid minimum-bias events was sampled from a Poisson distribution with mean values of

[1]Monte-Carlo samples were kindly provided by Gabriel Facini.

$\langle\mu\rangle = 20$ and $\langle\mu\rangle = 40$. The jets were reconstructed from stable particles excluding muons and neutrinos and were required to have $p_T > 15$ GeV and $|\eta| < 2.5$.

In semi-leptonic $t\bar{t}$ events with no pile-up interactions, two LF jets are expected from the hadronically decaying top. Additional radiation in the initial and final states can increase this number, with the acceptance cuts in p_T and η smearing the truth jet multiplicity spectrum. These effects result in a distribution peaked at $N = 3$, as shown in Figure A.3.

The multiplicity distributions of truth HS LF jets obtained in the N and E-schemes are shown in Figure A.3. In the N-scheme, the HS jets have an abundance of HS particles, while PU jets have an abundance of PU particles. As expected, when the amount of pile-up increases, more PU particles get clustered in the jets and the amount of HS jets decreases. For high pile-up almost no HS jets are found, which indicates that the N-scheme behaves poorly. In the E-scheme on the other hand, HS jets are defined as the jets in which most of the energy is carried by HS particles. The predicted HS jet multiplicity in this scheme is stable up to $\langle\mu\rangle = 20$ but becomes sensitive to pile-up for higher values of $\langle\mu\rangle$. This scheme would thus be suitable for the 7 and 8 TeV runs but not for the upcoming 13 TeV one. Other schemes based on p_T, p_T^2 etc have a comparable performance to the E-scheme.

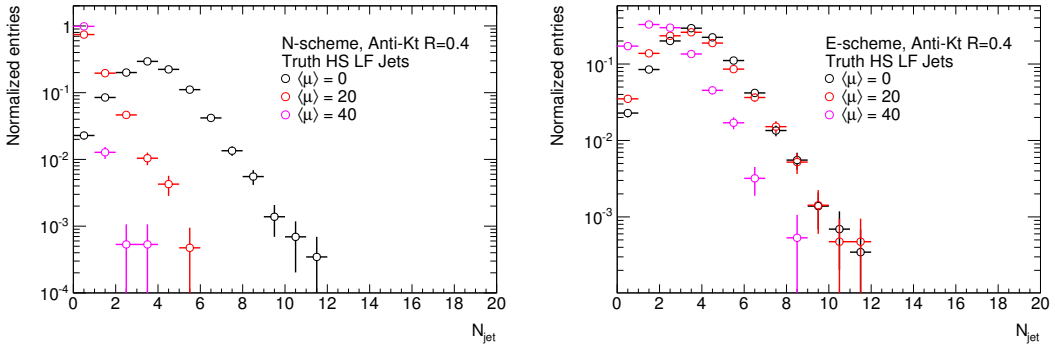

Figure A.3: Truth jet multiplicity for HS LF jets in $t\bar{t}$ events obtained with the N-scheme (left) and the E-scheme (right) for three different pile-up scenarios. We observe that the N-scheme is very sensitive to the amount of pile-up and therefore not a suitable classification scheme. The E-scheme is able to reproduce the correct jet multiplicity for medium amounts of pile-up ($\langle\mu\rangle$=20), but its performance deteriorates in high pile-up environments ($\langle\mu\rangle$=40).

The classification scheme with the highest stability against pile-up is the so-called CRSS scheme, introduced in [184]. The CRSS scheme is based on two independent jet clusterings. In the first clustering only HS particles are used to build "hard jets". In

the second clustering all particles in the event (HS and PU) are clustered building "full jets". The common constituents between hard and full jets are identified and the ratio

$$C_{p_T} \equiv \frac{p_T^{\text{common}}}{p_T^{\text{hard jet}}} = \frac{\sqrt{\sum_{\text{common}}(p_{x,\text{common}}^2 + p_{y,\text{common}}^2)}}{p_T^{\text{hard jet}}} \tag{A.3}$$

is calculated for each pair of hard and full jets. If $C_{p_T} > 0.5$ then the full jet is considered to be a HS jet. It is evident that in this way only one full jet can be matched to a given hard jet and this scheme provides an unambiguous classification even in very dense environments with overlapping jets. Since the identification of HS jets is based only in the HS constituents, the CRSS scheme is very robust against pile-up and has a very high HS jet identification efficiency, as shown in Figure A.4.

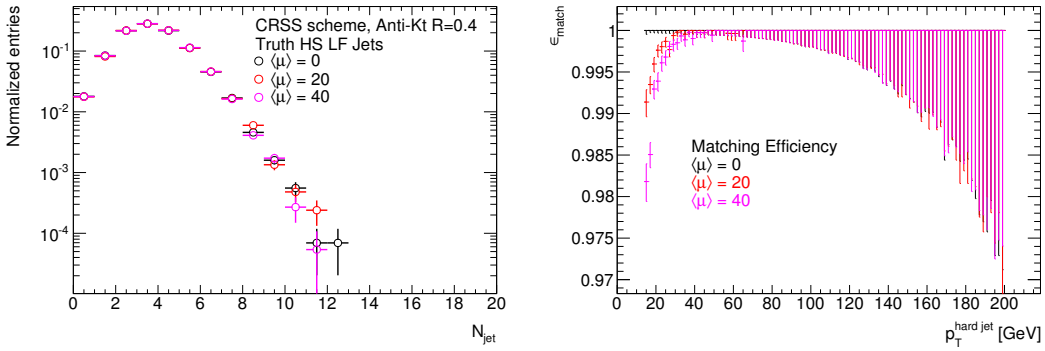

Figure A.4: Truth jet multiplicity for HS LF jets in $t\bar{t}$ events obtained (left) and efficiency for finding a given HS jet (right) in the CRSS scheme. We observe that the CRSS scheme has a very high efficiency for identifying the HS jets and it is very robust against pile-up.

The investigation of the above jet classification schemes, has revealed the fact that the 2012 pile-up conditions were at the border were different classification schemes could be used based on discriminants built from simple kinematic variables, as in equation (A.2). For the upcoming 13 TeV run, with a projected pile-up of $\langle\mu\rangle \approx 40$, the CRSS scheme seems to be the only viable option for correctly classifying HS and pile-up jets in Monte-Carlo.

A.2 Properties of pile-up jets

With the help of the CRSS scheme, we can now unambiguously distinguish HS jets from PU jets in Monte-Carlo. The next question that we want to address is if we can use this information in order to identify and suppress pile-up jets in data. Since the CRSS scheme is based on the use of Monte-Carlo information, it is not directly applicable in data. Nevertheless one can make use of this scheme in order to distinguish HS jets from PU jets in Monte-Carlo and identify systematic differences in their properties, which would in turn be directly observable in data.

The first discriminating characteristic that we found is the transverse momentum of the HS and PU constituents, shown in Figure A.5. We observe that HS jets tend to contain hard particles from the HS interaction and soft particles from the PU interaction with a significant p_T spread between the two. On the other hand PU jets contain soft HS and PU particles of roughly the same p_T. This has a profound impact on the substructure of the jets. As shown in Figure A.6, the HS jets have a discernible high-density core consisting of hard particles from the HS interaction, while PU jets have a uniform surface density of particles, with no distinguishable substructure.

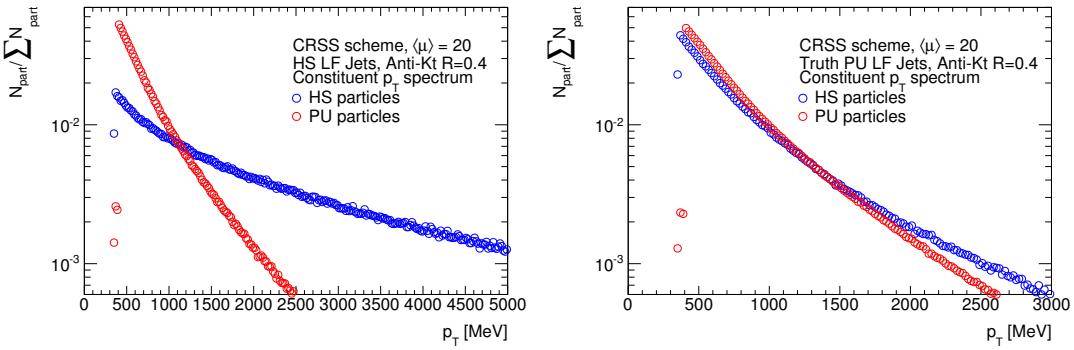

Figure A.5: Transverse momentum of HS particles (blue) and PU particles (red) clustered in HS jets (left) and PU jets (right). It is evident that HS jets contain two distinct collections of particles; hard particles from the HS interaction and soft particles from the PU interaction. On the other hand, PU jets contain soft HS and PU particles with a small p_T spread between the two. The plots are normalized to the total number of jet constituents.

This characteristic structure of PU jets may strike as being in contradiction with what one expects from the development of a QCD parton cascade. More precisely, color coherence forces successive parton branchings to self-collimate [49], thereby leading to jets with a higher particle density in the core. We have found that if one

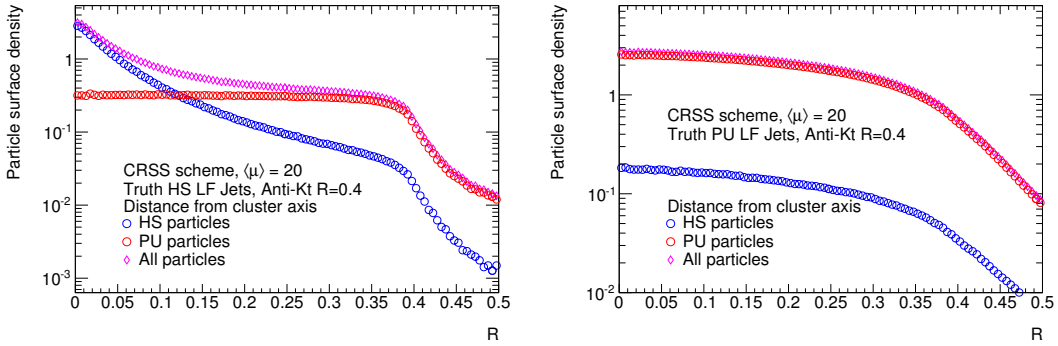

Figure A.6: Surface density of HS particles (blue) and PU particles (red) clustered in HS jets (left) and PU jets (right). The total surface density of clustered particles is shown in magenta. We observe that HS jets have a clear high-density core, while PU jets appear more like a uniform collection of particles with no distinguishable core.

considers a single PU interaction removing the HS interaction, the resulting jets display the characteristic high-density core expected from the coherent parton branching formalism. However in a high pile-up environment, the PU jets are comprised of a collection of particles of approximately equal momenta (Figure A.5). The resulting jet's momentum, which is given by the sum of the constituents' momenta, will therefore be roughly equidistant from the constituents' momenta giving rise to a jet with a uniform surface density.

A.3 Suppression of pile-up jets using only calorimeter information

Having established that significant differences exist between HS and PU jets the salient question becomes whether these differences can be exploited to construct discriminants that can be used for PU jet suppression. The simplest discriminant that can be constructed is the fraction of energy deposited in a cone of certain radius R around the jet axis, e.g. for $R = 0.15$ one defines

$$E_{\text{cone15}} \equiv \left(\sum_{\substack{i \in \text{ jet} \\ \Delta R(i,\text{jet}) < 0.15}} E_i \right) \cdot E_{\text{jet}}^{-1}. \tag{A.4}$$

As shown in Figure A.7, for HS jets most of the jet's energy is deposited within a cone of $R = 0.15$ around the jet axis, while for PU jets this fraction is almost always less than 40%. Placing a cut at $E_{\text{cone15}} = 0.4$ we obtain a rejection of 95% for PU jets with an efficiency of 82% for selecting HS jets. Other discriminants can be constructed by exploiting the fact that high-energy particles in HS jets are clustered near the jet axis, therefore one can introduce a weighted sum in equation (A.4), using functions of the particles' distance from the jet axis as a weight. One such example, using

$$E_{\text{cone15}}^{\text{weighted}} \equiv \sum_{\substack{i \in \text{ jet} \\ \Delta R(i,\text{jet}) < 0.15}} \frac{R_i \cdot E_i}{E_{\text{jet}}} \tag{A.5}$$

is illustrated in Figure A.7. Placing a cut at $E_{\text{cone15}}^{\text{weighted}} = 5$, we obtain a 92% rejection

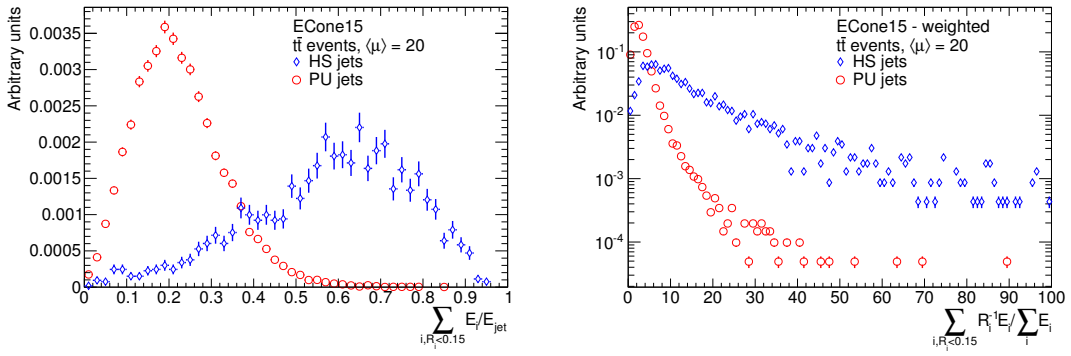

Figure A.7: Discriminants that can be used to separate HS from PU jets based purely on calorimetric information. The plot on the left shows the fraction of the jet's energy deposited within a cone of radius $R = 0.15$ from the jet axis for HS jets (blue) and PU jets (red). The plot on the right shows the sum of the energy of the jet constituents within the same cone, weighted by the inverse of the particle's distance from the jet axis.

against PU jets and a 82% efficiency for selecting HS jets, which is comparable with the E_{cone15} method.

In conclusion we note that while jet substructure might prove to be a valuable tool to identify and suppress pile-up jets, especially in the forward regions, there are several aspects of jet reconstruction in the detector that may change the above picture and therefore warrant a closer examination. More precisely, while the above studies were performed with jets not corrected for pile-up contamination, it is known that the jet-area based pile-up subtraction method alters the jet shapes. The above study should therefore be repeated after the PU contamination has been subtracted from the

jets. Moreover the granularity in the forward region of the detector might worsen the performance of the discriminants that we proposed. It is therefore necessary to repeat these studies taking into account the characteristics of the detector in the forward region.

Appendix B

Breakdown of systematic uncertainties

Source	Uncertainty on $\sigma_{t\bar{t}b\bar{b}}$ [%]
jeff	-0.02
jer	1.73
BJesUnc down	2.47
BJesUnc up	-1.57
EtaIntercalibrationModel down	1.46
EtaIntercalibrationModel up	-1.78
EtaIntercalibrationStatMethod down	0.63
EtaIntercalibrationStatMethod up	-0.17
JesEffectiveDet1 down	0.98
JesEffectiveDet1 up	-0.37
JesEffectiveDet2 down	-0.03
JesEffectiveDet2 up	-0.07
JesEffectiveDet3 down	-0.27
JesEffectiveDet3 up	-0.05
JesEffectiveMix1 down	-0.01
JesEffectiveMix1 up	-0.05
JesEffectiveMix2 down	-0.24
JesEffectiveMix2 up	-0.01
JesEffectiveModel1 down	2.08
JesEffectiveModel1 up	-3.42
JesEffectiveModel2 down	-0.02
JesEffectiveModel2 up	0.39
JesEffectiveModel3 down	-0.24
JesEffectiveModel3 up	-0.39
JesEffectiveModel4 down	-0.05
JesEffectiveModel4 up	-0.05
JesEffectiveStat1 down	1.00
JesEffectiveStat1 up	-0.40
JesEffectiveStat2 down	-0.33
JesEffectiveStat2 up	-0.28
JesEffectiveStat3 down	-0.27
JesEffectiveStat3 up	0.02
Pileup OffsetMu down	-0.01
Pileup OffsetMu up	-0.04
Pileup OffsetNPV down	1.08
Pileup OffsetNPV up	-0.59
Pileup Pt down	-0.04
Pileup Pt up	-0.03
Pileup Rho down	1.79
Pileup Rho up	-1.23
SinglePart down	-0.01
SinglePart up	-0.02
eer down	-0.60
eer up	-0.58
ees down	0.27
ees up	-0.60
el idSF down	1.94
el idSF up	-1.92
el recSF down	0.21
el recSF up	-0.25
el trigSF down	0.06
el trigSF up	-0.09
flavor comp down	0.60
flavor comp up	-0.80
flavor response down	0.27
flavor response up	-0.49
jvf down	-1.30
jvf up	2.66
mu idSF down	0.55
mu idSF up	-0.58
mu recSF down	0.45
mu recSF up	-0.48
mu trigSF down	0.18
mu trigSF up	-0.21
muid down	-1.00
muid up	-1.08
mums down	-1.64
mums up	-0.97
musc down	-1.07
musc up	-1.87
btag0 down	1.86
btag0 up	0.72
btag1 down	-0.04
btag1 up	0.13
btag2 down	4.94
btag2 up	-4.61
btag3 down	-1.74
btag3 up	1.88
btag4 down	-8.60
btag4 up	9.58
btag5 down	6.65
btag5 up	-6.12
mistag0 down	-0.02
mistag0 up	-0.01
mistag1 down	-0.01
mistag1 up	-0.02
mistag2 down	-0.01
mistag2 up	-0.03
mistag3 down	0.01
mistag3 up	-0.05
mistag4 down	-0.11
mistag4 up	0.08
mistag5 down	-0.13
mistag5 up	0.10
mistag6 down	0.16
mistag6 up	-0.20
mistag7 down	-0.03
mistag7 up	-0.01
mistag8 down	0.42
mistag8 up	-0.45
mistag9 down	0.43
mistag9 up	-0.47
mistag10 down	-1.11
mistag10 up	1.07
mistag11 down	-4.32
mistag11 up	4.16
ctautag0 down	0.76
ctautag0 up	0.77
ctautag1 down	0.58
ctautag1 up	-0.58
ctautag2 down	0.37
ctautag2 up	-0.38
ctautag3 down	-1.41
ctautag3 up	1.38
Total	21

Table B.1: Relative uncertainties (in %) on the cross-section obtained using the Powheg+Pythia AFII sample.

Source	Uncertainty on ϵ_{fid} [%]
jeff	0.01
jer	-5.70
BJesUnc down	-1.50
BJesUnc up	1.52
EtaIntercalibrationModel down	-0.91
EtaIntercalibrationModel up	1.70
EtaIntercalibrationStatMethod down	-0.46
EtaIntercalibrationStatMethod up	-0.04
JesEffectiveDet1 down	-0.94
JesEffectiveDet1 up	-0.04
JesEffectiveDet2 down	0.04
JesEffectiveDet2 up	0.09
JesEffectiveDet3 down	0.06
JesEffectiveDet3 up	0.06
JesEffectiveMix1 down	0.02
JesEffectiveMix1 up	0.06
JesEffectiveMix2 down	0.03
JesEffectiveMix2 up	-0.42
JesEffectiveModel1 down	-1.34
JesEffectiveModel1 up	2.20
JesEffectiveModel2 down	-0.42
JesEffectiveModel2 up	-0.44
JesEffectiveModel3 down	0.02
JesEffectiveModel3 up	0.10
JesEffectiveModel4 down	0.06
JesEffectiveModel4 up	0.06
JesEffectiveStat1 down	-0.96
JesEffectiveStat1 up	-0.00
JesEffectiveStat2 down	0.02
JesEffectiveStat2 up	0.07
JesEffectiveStat3 down	0.06
JesEffectiveStat3 up	-0.46
Pileup OffsetMu down	0.02
Pileup OffsetMu up	0.04
Pileup OffsetNPV down	-0.62
Pileup OffsetNPV up	-0.45
Pileup Pt down	0.04
Pileup Pt up	0.03
Pileup Rho down	-1.45
Pileup Rho up	0.31
SinglePart down	0.02
SinglePart up	0.02
eer down	0.50
eer up	0.47
ees down	-0.19
ees up	0.48
el idSF down	-1.78
el idSF up	1.82
el recSF down	-0.21
el recSF up	0.23
el trigSF down	-0.06
el trigSF up	0.08
flavor comp down	-0.41
flavor comp up	-0.49
flavor response down	-0.41
flavor response up	-0.01

Source	Uncertainty on ϵ_{fid} [%]
jvf down	0.08
jvf up	0.39
mu idSF down	-0.49
mu idSF up	0.52
mu recSF down	-0.41
mu recSF up	0.43
mu trigSF down	-0.16
mu trigSF up	0.17
muid down	-0.05
muid up	0.01
mums down	0.49
mums up	0.49
musc down	0.01
musc up	0.49
btag0 down	-1.47
btag0 up	-0.41
btag1 down	0.01
btag1 up	-0.11
btag2 down	-5.02
btag2 up	5.14
btag3 down	1.80
btag3 up	-1.88
btag4 down	9.33
btag4 up	-8.73
btag5 down	-6.16
btag5 up	6.40
mistag0 down	0.01
mistag0 up	0.01
mistag1 down	0.01
mistag1 up	0.01
mistag2 down	-0.01
mistag2 up	0.03
mistag3 down	0.01
mistag3 up	0.01
mistag4 down	0.01
mistag4 up	0.01
mistag5 down	0.02
mistag5 up	-0.01
mistag6 down	-0.07
mistag6 up	0.08
mistag7 down	0.02
mistag7 up	-0.00
mistag8 down	-0.16
mistag8 up	0.17
mistag9 down	0.06
mistag9 up	-0.04
mistag10 down	0.14
mistag10 up	-0.12
mistag11 down	0.75
mistag11 up	-0.73
ctautag0 down	0.00
ctautag0 up	-0.04
ctautag1 down	-0.08
ctautag1 up	0.04
ctautag2 down	-0.02
ctautag2 up	-0.02
ctautag3 down	0.13
ctautag3 up	-0.17

Table B.2: Relative uncertainties (in %) on the fiducial efficiency obtained using the Powheg+Pythia AFII sample.

Source	Uncertainty on $N_{t\bar{t}+\text{jets}}^{\text{mis-tagged}}$ [%]
jeff	-0.06
jer	8.70
BJesUnc down	-0.47
BJesUnc up	-0.00
EtaIntercalibrationModel down	-0.12
EtaIntercalibrationModel up	3.78
EtaIntercalibrationStatMethod down	-0.05
EtaIntercalibrationStatMethod up	3.82
JesEffectiveDet1 down	-0.01
JesEffectiveDet1 up	3.72
JesEffectiveDet2 down	-0.00
JesEffectiveDet2 up	-0.05
JesEffectiveDet3 down	-0.00
JesEffectiveDet3 up	-0.05
JesEffectiveMix1 down	-0.03
JesEffectiveMix1 up	0.00
JesEffectiveMix2 down	-0.03
JesEffectiveMix2 up	3.84
JesEffectiveModel1 down	-1.67
JesEffectiveModel1 up	3.41
JesEffectiveModel2 down	3.84
JesEffectiveModel2 up	-0.01
JesEffectiveModel3 down	-0.05
JesEffectiveModel3 up	3.90
JesEffectiveModel4 down	-0.00
JesEffectiveModel4 up	-0.05
JesEffectiveStat1 down	-0.01
JesEffectiveStat1 up	3.83
JesEffectiveStat2 down	3.84
JesEffectiveStat2 up	0.00
JesEffectiveStat3 down	0.00
JesEffectiveStat3 up	3.75
Pileup OffsetMu down	-0.04
Pileup OffsetMu up	-0.07
Pileup OffsetNPV down	2.69
Pileup OffsetNPV up	-0.26
Pileup Pt down	-0.10
Pileup Pt up	-0.00
Pileup Rho down	-1.35
Pileup Rho up	3.72
SinglePart down	-0.03
SinglePart up	-0.00
eer down	-0.06
eer up	-0.06
ees down	-0.12
ees up	-1.73
el idSF down	-2.58
el idSF up	2.48
el recSF down	-0.37
el recSF up	0.24
el trigSF down	-0.15
el trigSF up	0.02
flavor comp down	-1.34
flavor comp up	3.26
flavor response down	-0.78
flavor response up	3.77
jvf down	2.71
jvf up	6.74
mu idSF down	-0.52
mu idSF up	0.39
mu recSF down	-0.44
mu recSF up	0.32
mu trigSF down	-0.24
mu trigSF up	0.11
muid down	-0.19
muid up	-0.19
mums down	-0.19
mums up	-0.20
musc down	-0.06
musc up	-0.06
btag0 down	-3.83
btag0 up	-4.26
btag1 down	-0.39
btag1 up	0.23
btag2 down	-2.73
btag2 up	2.62
btag3 down	1.24
btag3 up	-1.38
btag4 down	4.07
btag4 up	-4.15
btag5 down	-4.42
btag5 up	4.34
mistag0 down	-0.01
mistag0 up	-0.11
mistag1 down	-0.04
mistag1 up	-0.09
mistag2 down	-0.11
mistag2 up	-0.02
mistag3 down	-0.23
mistag3 up	0.10
mistag4 down	0.34
mistag4 up	-0.47
mistag5 down	0.17
mistag5 up	-0.30
mistag6 down	-0.33
mistag6 up	0.20
mistag7 down	0.08
mistag7 up	-0.21
mistag8 down	-0.16
mistag8 up	0.04
mistag9 down	-1.50
mistag9 up	1.33
mistag10 down	1.47
mistag10 up	-1.63
mistag11 down	8.37
mistag11 up	-7.99
ctautag0 down	-3.56
ctautag0 up	-3.67
ctautag1 down	-4.91
ctautag1 up	5.04
ctautag2 down	-3.19
ctautag2 up	3.27
ctautag3 down	9.26
ctautag3 up	-8.81

Table B.3: Relative uncertainties (in %) on the number of "mis-tag" events $N_{t\bar{t}+\text{jets}}^{\text{mis-tagged}}$ obtained using the Powheg+Pythia AFII sample.

Source	Uncertainty on f_{sig} [%]
jeff	-0.01
jer	-3.41
BJesUnc down	0.89
BJesUnc up	-0.08
EtaIntercalibrationModel down	0.53
EtaIntercalibrationModel up	0.18
EtaIntercalibrationStatMethod down	0.16
EtaIntercalibrationStatMethod up	0.08
JesEffectiveDet1 down	0.03
JesEffectiveDet1 up	-0.13
JesEffectiveDet2 down	0.00
JesEffectiveDet2 up	0.01
JesEffectiveDet3 down	-0.21
JesEffectiveDet3 up	0.00
JesEffectiveMix1 down	-0.00
JesEffectiveMix1 up	0.01
JesEffectiveMix2 down	-0.22
JesEffectiveMix2 up	-0.13
JesEffectiveModel1 down	0.58
JesEffectiveModel1 up	-1.03
JesEffectiveModel2 down	-0.15
JesEffectiveModel2 up	-0.05
JesEffectiveModel3 down	-0.22
JesEffectiveModel3 up	0.01
JesEffectiveModel4 down	0.01
JesEffectiveModel4 up	0.01
JesEffectiveStat1 down	0.02
JesEffectiveStat1 up	-0.10
JesEffectiveStat2 down	-0.01
JesEffectiveStat2 up	-0.21
JesEffectiveStat3 down	-0.21
JesEffectiveStat3 up	-0.15
Pileup OffsetMu down	0.01
Pileup OffsetMu up	-0.01
Pileup OffsetNPV down	0.67
Pileup OffsetNPV up	-1.06
Pileup Pt down	-0.00
Pileup Pt up	0.00
Pileup Rho down	0.21
Pileup Rho up	-0.63
SinglePart down	-0.00
SinglePart up	-0.00
eer down	-0.11
eer up	-0.11
ees down	0.07
ees up	-0.26
el idSF down	-0.10
el idSF up	0.07
el recSF down	-0.03
el recSF up	0.01
el trigSF down	-0.01
el trigSF up	-0.01
flavor comp down	0.09
flavor comp up	-1.03
flavor response down	-0.20
flavor response up	-0.20
jvf down	-1.02
jvf up	3.60
mu idSF down	0.00
mu idSF up	-0.03
mu recSF down	-0.01
mu recSF up	-0.02
mu trigSF down	-0.00
mu trigSF up	-0.02
muid down	-1.07
muid up	-1.09
mums down	-1.17
mums up	-0.50
musc down	-1.07
musc up	-1.40
btag0 down	0.06
btag0 up	-0.03
btag1 down	-0.07
btag1 up	0.05
btag2 down	-0.61
btag2 up	0.57
btag3 down	0.18
btag3 up	-0.21
btag4 down	0.35
btag4 up	-0.41
btag5 down	-0.37
btag5 up	0.34
mistag0 down	-0.02
mistag0 up	-0.01
mistag1 down	-0.00
mistag1 up	-0.02
mistag2 down	-0.03
mistag2 up	0.00
mistag3 down	0.00
mistag3 up	-0.03
mistag4 down	-0.07
mistag4 up	0.05
mistag5 down	-0.09
mistag5 up	0.07
mistag6 down	0.07
mistag6 up	-0.10
mistag7 down	0.00
mistag7 up	-0.03
mistag8 down	0.25
mistag8 up	-0.28
mistag9 down	0.37
mistag9 up	-0.40
mistag10 down	-0.86
mistag10 up	0.82
mistag11 down	-2.97
mistag11 up	2.76
ctautag0 down	0.48
ctautag0 up	0.45
ctautag1 down	0.11
ctautag1 up	-0.15
ctautag2 down	0.10
ctautag2 up	-0.14
ctautag3 down	-0.56
ctautag3 up	0.52

Table B.4: Relative uncertainties (in %) on the signal fraction parameter f_{sig} obtained using the Powheg+Pythia AFII sample.

Bibliography

[1] ATLAS Collaboration, "Measurement of differential production cross-sections for a Z boson in association with b-jets in 7 TeV proton-proton collisions with the ATLAS detector," *JHEP*, vol. 1410, p. 141, 2014, arXiv:1407.3643.

[2] ATLAS Collaboration, "Measurement of the cross-section for W boson production in association with b-jets in pp collisions at $\sqrt{s}$ = 7 TeV with the ATLAS detector," *JHEP*, vol. 1306, p. 084, 2013, arXiv:1302.2929.

[3] CMS Collaboration, "Measurement of the production cross sections for a Z boson and one or more b jets in pp collisions at $\sqrt{s}$ = 7 TeV," *JHEP*, vol. 1406, p. 120, 2014, arXiv:1402.1521.

[4] CMS Collaboration, "Measurement of the production cross section for a W boson and two b jets in pp collisions at $\sqrt{s}$=7 TeV," *Phys.Lett.*, vol. B735, pp. 204–225, 2014, arXiv:1312.6608.

[5] F. Maltoni, G. Ridolfi, and M. Ubiali, "b-initiated processes at the LHC: a reappraisal," *JHEP*, vol. 1207, p. 022, 2012, arXiv:1203.6393.

[6] G. Luisoni, C. Oleari, and F. Tramontano, "Wbbj production at NLO with POWHEG+MiNLO," 2015, arXiv:1502.01213.

[7] S. Bansal, P. Bartalini, B. Blok, D. Ciangottini, M. Diehl, *et al.*, "Progress in Double Parton Scattering Studies," 2014, arXiv:1410.6664.

[8] K. A. Assamagan and N. Gollub, "The ATLAS discovery potential for a heavy charged Higgs boson in $gg \to tbH^{\pm}$ with $H^{\pm} \to tb$," *Eur.Phys.J.*, vol. C39S2, pp. 25–40, 2005, arXiv:hep-ph/0406013.

[9] ATLAS Collaboration, "Search for strong production of supersymmetric particles in final states with missing transverse momentum and at least three b-jets at $\sqrt{s}$= 8 TeV proton-proton collisions with the ATLAS detector," *JHEP*, vol. 1410,

p. 24, 2014, arXiv:1407.0600.

[10] DELPHI Collaboration, "Measurement of the multiplicity of gluons splitting to bottom quark pairs in hadronic Z0 decays," *Phys.Lett.*, vol. B405, pp. 202–214, 1997.

[11] ALEPH Collaboration, "A Measurement of the gluon splitting rate into b anti-b pairs in hadronic Z decays," *Phys.Lett.*, vol. B434, pp. 437–450, 1998.

[12] SLD Collaboration, "Measurement of the probability for gluon splitting into b anti-b in Z0 decays," 1999, arXiv:hep-ex/9908028.

[13] DELPHI Collaboration, "Measurement of the rate of b anti-b b anti-b events in hadronic Z decays and the extraction of the gluon splitting into b anti-b," *Phys.Lett.*, vol. B462, pp. 425–439, 1999.

[14] OPAL Collaboration, "Production rates of b anti-b quark pairs from gluons and b anti-b b anti-b events in hadronic Z0 decays," *Eur.Phys.J.*, vol. C18, pp. 447–460, 2001, arXiv:hep-ex/0010029.

[15] J. Iliopoulos, "Progress in Gauge Theories," pp. III.89–116, 1974.

[16] P. W. Higgs, "Broken symmetries, massless particles and gauge fields," *Phys.Lett.*, vol. 12, pp. 132–133, 1964.

[17] F. Englert and R. Brout, "Broken Symmetry and the Mass of Gauge Vector Mesons," *Phys.Rev.Lett.*, vol. 13, pp. 321–323, 1964.

[18] P. W. Higgs, "Broken Symmetries and the Masses of Gauge Bosons," *Phys.Rev.Lett.*, vol. 13, pp. 508–509, 1964.

[19] G. Guralnik, C. Hagen, and T. Kibble, "Global Conservation Laws and Massless Particles," *Phys.Rev.Lett.*, vol. 13, pp. 585–587, 1964.

[20] P. W. Higgs, "Spontaneous Symmetry Breakdown without Massless Bosons," *Phys.Rev.*, vol. 145, pp. 1156–1163, 1966.

[21] L. D. Landau, "Theory of phase transformations I," *Phys.Z.Sowjetunion*, vol. 11, p. 26, 1937.

[22] L. D. Landau, "Theory of phase transformations II," *Phys.Z.Sowjetunion*, vol. 11, p. 545, 1937.

[23] S. Glashow, "Partial Symmetries of Weak Interactions," *Nucl.Phys.*, vol. 22, pp. 579–588, 1961.

[24] A. Salam, "Renormalizability of gauge theories," *Phys.Rev.*, vol. 127, pp. 331–334, 1962.

[25] S. Weinberg, "A Model of Leptons," *Phys.Rev.Lett.*, vol. 19, pp. 1264–1266, 1967.

[26] F. Hasert, H. Faissner, W. Krenz, J. Von Krogh, D. Lanske, *et al.*, "Search for Elastic ν_μ Electron Scattering," *Phys.Lett.*, vol. B46, pp. 121–124, 1973.

[27] F. Hasert *et al.*, "Observation of Neutrino Like Interactions Without Muon Or Electron in the Gargamelle Neutrino Experiment," *Phys.Lett.*, vol. B46, pp. 138–140, 1973.

[28] UA1 Collaboration, "Experimental Observation of Isolated Large Transverse Energy Electrons with Associated Missing Energy at s**(1/2) = 540-GeV," *Phys.Lett.*, vol. B122, pp. 103–116, 1983.

[29] UA1 Collaboration, "Experimental Observation of Lepton Pairs of Invariant Mass Around 95-GeV/c^2 at the CERN SPS Collider," *Phys.Lett.*, vol. B126, pp. 398–410, 1983.

[30] UA2 Collaboration, "Observation of Single Isolated Electrons of High Transverse Momentum in Events with Missing Transverse Energy at the CERN anti-p p Collider," *Phys.Lett.*, vol. B122, pp. 476–485, 1983.

[31] UA2 Collaboration, "Evidence for Z0 —> e+ e- at the CERN anti-p p Collider," *Phys.Lett.*, vol. B129, pp. 130–140, 1983.

[32] ATLAS Collaboration, "Observation of a new particle in the search for the Standard Model Higgs boson with the ATLAS detector at the LHC," *Phys.Lett.*, vol. B716, pp. 1–29, 2012, arXiv:1207.7214.

[33] CMS Collaboration, "Observation of a new boson at a mass of 125 GeV with the CMS experiment at the LHC," *Phys.Lett.*, vol. B716, pp. 30–61, 2012, arXiv:1207.7235.

[34] M. Gell-Mann, "A Schematic Model of Baryons and Mesons," *Phys.Lett.*, vol. 8, pp. 214–215, 1964.

[35] G. Zweig, "An SU(3) model for strong interaction symmetry and its breaking.

Version 1," 1964.

[36] M. Han and Y. Nambu, "Three Triplet Model with Double SU(3) Symmetry," *Phys.Rev.*, vol. 139, pp. B1006–B1010, 1965.

[37] D. J. Gross and F. Wilczek, "Ultraviolet Behavior of Nonabelian Gauge Theories," *Phys.Rev.Lett.*, vol. 30, pp. 1343–1346, 1973.

[38] H. D. Politzer, "Reliable Perturbative Results for Strong Interactions?," *Phys.Rev.Lett.*, vol. 30, pp. 1346–1349, 1973.

[39] J. Bjorken, "Asymptotic Sum Rules at Infinite Momentum," *Phys.Rev.*, vol. 179, pp. 1547–1553, 1969.

[40] J. I. Friedman and H. W. Kendall, "Deep inelastic electron scattering," *Ann.Rev.Nucl.Part.Sci.*, vol. 22, pp. 203–254, 1972.

[41] J. Augustin, A. Boyarski, M. Breidenbach, F. Bulos, J. Dakin, *et al.*, "Total Cross-Section for Hadron Production by electron-Positron Annihilation Between 2.4-GeV and 5.0-GeV Center-Of-Mass Energy," *Phys.Rev.Lett.*, vol. 34, p. 764, 1975.

[42] TASSO Collaboration, "Evidence for Planar Events in e+ e- Annihilation at High-Energies," *Phys.Lett.*, vol. B86, p. 243, 1979.

[43] C.-N. Yang and R. L. Mills, "Conservation of Isotopic Spin and Isotopic Gauge Invariance," *Phys.Rev.*, vol. 96, pp. 191–195, 1954.

[44] P. A. Dirac, "The Quantum theory of electron," *Proc.Roy.Soc.Lond.*, vol. A117, pp. 610–624, 1928.

[45] P. Dirac, "A Theory of Electrons and Protons," *Proc.Roy.Soc.Lond.*, vol. A126, p. 360, 1930.

[46] R. Brock *et al.*, "Handbook of perturbative QCD: Version 1.0," *Rev.Mod.Phys.*, vol. 67, pp. 157–248, 1995.

[47] P. A. Dirac, "Quantum theory of emission and absorption of radiation," *Proc.Roy.Soc.Lond.*, vol. A114, p. 243, 1927.

[48] E. Fermi, *Nuclear Physics*. University of Chicago Press, 1950.

[49] R. Ellis, W. Stirling, and B. Webber, *QCD and collider physics*. Cambridge University Press, 1996.

[50] K. Olive *et al.*, "Review of Particle Physics," *Chin.Phys.*, vol. C38, p. 090001, 2014.

[51] R. P. Feynman, "Very high-energy collisions of hadrons," *Phys.Rev.Lett.*, vol. 23, pp. 1415–1417, 1969.

[52] J. Bjorken and E. A. Paschos, "Inelastic Electron Proton and gamma Proton Scattering, and the Structure of the Nucleon," *Phys.Rev.*, vol. 185, pp. 1975–1982, 1969.

[53] S. Drell and T.-M. Yan, "Partons and their Applications at High-Energies," *Annals Phys.*, vol. 66, p. 578, 1971.

[54] A. Bodek, M. Breidenbach, D. Dubin, J. Elias, J. I. Friedman, *et al.*, "Observed Deviations from Scaling of the Proton Electromagnetic Structure Functions," *Phys.Lett.*, vol. B52, p. 249, 1974.

[55] J. C. Collins and D. E. Soper, "The Theorems of Perturbative QCD," *Ann.Rev.Nucl.Part.Sci.*, vol. 37, pp. 383–409, 1987.

[56] V. Gribov and L. Lipatov, "Deep inelastic e p scattering in perturbation theory," *Sov.J.Nucl.Phys.*, vol. 15, pp. 438–450, 1972.

[57] L. Lipatov, "The parton model and perturbation theory," *Sov.J.Nucl.Phys.*, vol. 20, pp. 94–102, 1975.

[58] G. Altarelli and G. Parisi, "Asymptotic Freedom in Parton Language," *Nucl.Phys.*, vol. B126, p. 298, 1977.

[59] Y. L. Dokshitzer, "Calculation of the Structure Functions for Deep Inelastic Scattering and e+ e- Annihilation by Perturbation Theory in Quantum Chromodynamics.," *Sov.Phys.JETP*, vol. 46, pp. 641–653, 1977.

[60] F. Bloch and A. Nordsieck, "Note on the Radiation Field of the electron," *Phys.Rev.*, vol. 52, pp. 54–59, 1937.

[61] T. Kinoshita, "Mass singularities of Feynman amplitudes," *J.Math.Phys.*, vol. 3, pp. 650–677, 1962.

[62] T. Lee and M. Nauenberg, "Degenerate Systems and Mass Singularities," *Phys.Rev.*, vol. 133, pp. B1549–B1562, 1964.

[63] S. Catani, F. Krauss, R. Kuhn, and B. Webber, "QCD matrix elements + parton showers," *JHEP*, vol. 0111, p. 063, 2001, arXiv:hep-ph/0109231.

[64] L. Lönnblad, "Correcting the color dipole cascade model with fixed order matrix elements," *JHEP*, vol. 0205, p. 046, 2002, arXiv:hep-ph/0112284.

[65] M. L. Mangano, M. Moretti, F. Piccinini, and M. Treccani, "Matching matrix elements and shower evolution for top-quark production in hadronic collisions," *JHEP*, vol. 0701, p. 013, 2007, arXiv:hep-ph/0611129.

[66] J. Alwall, S. Höche, F. Krauss, N. Lavesson, L. Lönnblad, *et al.*, "Comparative study of various algorithms for the merging of parton showers and matrix elements in hadronic collisions," *Eur.Phys.J.*, vol. C53, pp. 473–500, 2008, arXiv:0706.2569.

[67] S. Frixione, P. Nason, and C. Oleari, "Matching NLO QCD computations with Parton Shower simulations: the POWHEG method," *JHEP*, vol. 0711, p. 070, 2007, 0709.2092.

[68] P. Nason, "A New method for combining NLO QCD with shower Monte Carlo algorithms," *JHEP*, vol. 0411, p. 040, 2004, hep-ph/0409146.

[69] H. Elvang and Y.-t. Huang, "Scattering Amplitudes," 2013, arXiv:1308.1697.

[70] T. Gleisberg and S. Höche, "Comix, a new matrix element generator," *JHEP*, vol. 0812, p. 039, 2008, arXiv:0808.3674.

[71] F. Caravaglios and M. Moretti, "An algorithm to compute Born scattering amplitudes without Feynman graphs," *Phys.Lett.*, vol. B358, pp. 332–338, 1995, arXiv:hep-ph/9507237.

[72] T. Gleisberg, S. Höche, F. Krauss, M. Schonherr, S. Schumann, *et al.*, "Event generation with SHERPA 1.1," *JHEP*, vol. 0902, p. 007, 2009, arXiv:0811.4622.

[73] T. Sjöstrand and M. van Zijl, "A Multiple Interaction Model for the Event Structure in Hadron Collisions," *Phys.Rev.*, vol. D36, p. 2019, 1987.

[74] AFS Collaboration, "Double Parton Scattering in pp Collisions at $\sqrt{s} = 63$-GeV," *Z.Phys.*, vol. C34, p. 163, 1987.

[75] UA5 Collaboration, "Charged Particle Correlations in $\bar{P}P$ Collisions at c.m. Energies of 200-GeV, 546-GeV and 900-GeV," *Z.Phys.*, vol. C37, pp. 191–213, 1988.

[76] E735 Collaboration, "Charged particle multiplicity correlations in $p\bar{p}$ collisions

at $\sqrt{s}$ = 0.3-TeV to 1.8-TeV," *Phys.Lett.*, vol. B353, pp. 155–160, 1995.

[77] R. Corke and T. Sjöstrand, "Multiparton Interactions and Rescattering," *JHEP*, vol. 1001, p. 035, 2010, arXiv:0911.1909.

[78] J. M. Butterworth, J. R. Forshaw, and M. H. Seymour, "Multiparton interactions in photoproduction at HERA," *Z. Phys. C*, vol. 72, pp. 637–646, 1996, 9601371.

[79] B. Webber, "A QCD Model for Jet Fragmentation Including Soft Gluon Interference," *Nucl.Phys.*, vol. B238, p. 492, 1984.

[80] B. Andersson, G. Gustafson, G. Ingelman, and T. Sjöstrand, "Parton Fragmentation and String Dynamics," *Phys.Rept.*, vol. 97, pp. 31–145, 1983.

[81] T. Sjöstrand, S. Mrenna, and P. Z. Skands, "PYTHIA 6.4 physics and manual," *JHEP*, vol. 0605, p. 026, 2006, 0603175.

[82] T. Sjöstrand, S. Mrenna, and P. Z. Skands, "A Brief Introduction to PYTHIA 8.1," *Comput. Phys. Commun.*, vol. 178, pp. 852–867, 2008, 0710.3820.

[83] G. Corcella *et al.*, "HERWIG 6.5 release note," 2002, 0210213.

[84] M. Bähr *et al.*, "Herwig++ physics and manual," *Eur. Phys. J.*, vol. C 58, pp. 639–707, 2008, 0803.0883.

[85] G. P. Salam, "Towards Jetography," *Eur.Phys.J.*, vol. C67, pp. 637–686, 2010, arXiv:0906.1833.

[86] M. Cacciari, G. P. Salam, and G. Soyez, "The anti-k_t jet clustering algorithm," *JHEP*, vol. 04, p. 063, 2008, 0802.1189.

[87] M. Dasgupta, L. Magnea, and G. P. Salam, "Non-perturbative QCD effects in jets at hadron colliders," *JHEP*, vol. 0802, p. 055, 2008, arXiv:0712.3014.

[88] J. Alwall, R. Frederix, S. Frixione, V. Hirschi, F. Maltoni, *et al.*, "The automated computation of tree-level and next-to-leading order differential cross sections, and their matching to parton shower simulations," *JHEP*, vol. 1407, p. 079, 2014, arXiv:1405.0301.

[89] G. Bevilacqua and M. Worek, "On the ratio of ttbb and ttjj cross sections at the CERN Large Hadron Collider," 2014, arXiv:1403.2046.

[90] G. Bevilacqua, M. Czakon, C. Papadopoulos, R. Pittau, and M. Worek, "Assault

on the NLO Wishlist: $pp \to t\bar{t}b\bar{b}$," *JHEP*, vol. 0909, p. 109, 2009, arXiv:0907.4723.

[91] S. Frixione, P. Nason, and G. Ridolfi, "A Positive-weight next-to-leading-order Monte Carlo for heavy flavour hadroproduction," *JHEP*, vol. 0709, p. 126, 2007, arXiv:0707.3088.

[92] A. Bredenstein, A. Denner, S. Dittmaier, and S. Pozzorini, "NLO QCD corrections to $pp \to t\bar{t}b\bar{b}$ + X at the LHC," *Phys.Rev.Lett.*, vol. 103, p. 012002, 2009, arXiv:0905.0110.

[93] A. Bredenstein, A. Denner, S. Dittmaier, and S. Pozzorini, "NLO QCD Corrections to Top Anti-Top Bottom Anti-Bottom Production at the LHC: 2. full hadronic results," *JHEP*, vol. 1003, p. 021, 2010, arXiv:1001.4006.

[94] A. Kardos and Z. Trócsányi, "Hadroproduction of t anti-t pair with a b anti-b pair with PowHel," 2013, arXiv:1303.6291.

[95] F. Cascioli, P. Maierhoefer, N. Moretti, S. Pozzorini, and F. Siegert, "NLO matching for ttbb production with massive b-quarks," 2013, arXiv:1309.5912.

[96] S. Höche, F. Krauss, P. Maierhoefer, S. Pozzorini, M. Schonherr, *et al.*, "Next-to-leading order QCD predictions for top-quark pair production with up to two jets merged with a parton shower," 2014, arXiv:1402.6293.

[97] R. Frederix, S. Frixione, F. Maltoni, and T. Stelzer, "Automation of next-to-leading order computations in QCD: The FKS subtraction," *JHEP*, vol. 0910, p. 003, 2009, arXiv:0908.4272.

[98] A. Denner, R. Feger, and A. Scharf, "Irreducible background and interference effects for Higgs-boson production in association with a top-quark pair," 2014, arXiv:1412.5290.

[99] A. Martin, W. Stirling, R. Thorne, and G. Watt, "Parton distributions for the LHC," *Eur. Phys. J.*, vol. C63, pp. 189–285, 2009, arXiv:0901.0002.

[100] E. Norrbin and T. Sjöstrand, "QCD radiation off heavy particles," *Nucl.Phys.*, vol. B603, pp. 297–342, 2001, arXiv:hep-ph/0010012.

[101] S. Catani, S. Dittmaier, M. H. Seymour, and Z. Trócsányi, "The Dipole formalism for next-to-leading order QCD calculations with massive partons," *Nucl.Phys.*, vol. B627, pp. 189–265, 2002, arXiv:hep-ph/0201036.

[102] T. SjŽstrand, S. Ask, J. R. Christiansen, R. Corke, N. Desai, P. Ilten, S. Mrenna, S. Prestel, C. O. Rasmussen, and P. Z. Skands, "An Introduction to PYTHIA 8.2," *Comput. Phys. Commun.*, vol. 191, pp. 159–177, 2015, arXiv:1410.3012.

[103] L. Evans and P. Bryant, "LHC Machine," *JINST*, vol. 3, p. S08001, 2008.

[104] ATLAS Collaboration, "Measurements of underlying-event properties using neutral and charged particles in pp collisions at 900 GeV and 7 TeV with the ATLAS detector at the LHC," *Eur.Phys.J.*, vol. C71, p. 1636, 2011, arXiv:1103.1816.

[105] H. Schulz and P. Skands, "Energy Scaling of Minimum-Bias Tunes," *Eur.Phys.J.*, vol. C71, p. 1644, 2011, arXiv:1103.3649.

[106] ATLAS Collaboration, "Improved luminosity determination in pp collisions at $\sqrt{s}$ = 7 TeV using the ATLAS detector at the LHC," *Eur.Phys.J.*, vol. C73, p. 2518, 2013, arXiv:1302.4393.

[107] S. van der Meer, "Calibration of the effective beam height in the ISR," no. CERN-ISR-PO-68-31. ISR-PO-68-31, 1968.

[108] C. Rubbia, "Measurement of the luminosity of p$\overline{p}$ collider with a (generalized) Van der Meer Method," Nov 1977.

[109] ATLAS Collaboration, "Luminosity Determination Using the ATLAS Detector," Tech. Rep. ATLAS-CONF-2010-060, CERN, Geneva, Jul 2010.

[110] P. Jenni, M. Nordberg, M. Nessi, and K. Jon-And, *ATLAS Forward Detectors for Measurement of Elastic Scattering and Luminosity*, . Technical Design Report, Geneva: CERN, 2008.

[111] ATLAS Collaboration, "The ATLAS experiment at the CERN Large Hadron Collider," *JINST*, vol. 3, p. S08003, 2008.

[112] CMS Collaboration, "The CMS experiment at the CERN LHC," *JINST*, vol. 3, p. S08004, 2008.

[113] ALICE Collaboration, "The ALICE experiment at the CERN LHC," *JINST*, vol. 3, p. S08002, 2008.

[114] LHCb Collaboration, "The LHCb Detector at the LHC," *JINST*, vol. 3, p. S08005, 2008.

[115] LHCf Collaboration, "The LHCf detector at the CERN Large Hadron Collider,"

JINST, vol. 3, p. S08006, 2008.

[116] TOTEM Collaboration, "The TOTEM experiment at the CERN Large Hadron Collider," *JINST*, vol. 3, p. S08007, 2008.

[117] MoEDAL Collaboration, "Technical Design Report of the MoEDAL Experiment," Jun 2009.

[118] TOTEM Collaboration, *Total cross section: elastic scattering and diffraction dissociation at the LHC, .* Letter of Intent, Geneva: CERN, 1997.

[119] ATLAS Collaboration, "Charged-particle multiplicities in pp interactions measured with the ATLAS detector at the LHC," *New J.Phys.*, vol. 13, p. 053033, 2011, arXiv:1012.5104.

[120] M. Shochet, L. Tompkins, V. Cavaliere, P. Giannetti, A. Annovi, and G. Volpi, "Fast TracKer (FTK) Technical Design Report," Jun 2013. ATLAS Fast Tracker Technical Design Report.

[121] ATLAS Collaboration, "Improved electron reconstruction in ATLAS using the Gaussian Sum Filter-based model for bremsstrahlung," 2012.

[122] ATLAS Collaboration, "Electron reconstruction and identification efficiency measurements with the ATLAS detector using the 2011 LHC proton-proton collision data," *Eur.Phys.J.*, vol. C74, p. 2941, 2014, arXiv:1404.2240.

[123] ATLAS Collaboration, "Electron efficiency measurements with the ATLAS detector using the 2012 LHC proton-proton collision data," Jun 2014, ATLAS-CONF-2014-032.

[124] ATLAS Collaboration, "Electron and photon energy calibration with the ATLAS detector using LHC Run 1 data," *Eur.Phys.J.*, vol. C74, no. 10, p. 3071, 2014, arXiv:1407.5063.

[125] ATLAS Collaboration, "Measurement of the muon reconstruction performance of the ATLAS detector using 2011 and 2012 LHC proton-proton collision data," *Eur.Phys.J.*, vol. C74, no. 11, p. 3130, 2014, arXiv:1407.3935.

[126] W. Lampl *et al.*, "Calorimeter clustering algorithms: description and performance," April 2008.

[127] ATLAS Collaboration, "Pile-up subtraction and suppression for jets in ATLAS,"

Aug 2013, ATLAS-CONF-2013-083.

[128] M. Cacciari and G. P. Salam, "Pileup subtraction using jet areas," *Phys. Lett.*, vol. B659, pp. 119–126, 2008, 0707.1378.

[129] M. Cacciari, G. P. Salam, and G. Soyez, "The Catchment Area of Jets," *JHEP*, vol. 0804, p. 005, 2008, arXiv:0802.1188.

[130] ATLAS Collaboration, "Jet energy measurement with the ATLAS detector in proton-proton collisions at $\sqrt{s} = 7$ TeV," *Eur.Phys.J.*, vol. C73, no. 3, p. 2304, 2013, arXiv:1112.6426.

[131] ATLAS Collaboration, "Jet energy resolution in proton-proton collisions at $\sqrt{s} =$ 7 TeV recorded in 2010 with the ATLAS detector," *Eur.Phys.J.*, vol. C73, no. 3, p. 2306, 2013, arXiv:1210.6210.

[132] ATLAS Collaboration, "Performance of the ATLAS Secondary Vertex b-tagging Algorithm in 7 TeV Collision Data," Jul 2010, ATLAS-CONF-2010-042.

[133] ATLAS Collaboration, "Performance of Impact Parameter-Based b-tagging Algorithms with the ATLAS Detector using Proton-Proton Collisions at Ãs = 7 TeV," Oct 2010, ATLAS-CONF-2010-091.

[134] G. Piacquadio and C. Weiser, "A new inclusive secondary vertex algorithm for b-jet tagging in ATLAS," *J.Phys.Conf.Ser.*, vol. 119, p. 032032, 2008.

[135] ATLAS Collaboration, "Commissioning of the ATLAS high-performance b-tagging algorithms in the 7 TeV collision data," Jul 2011, ATLAS-CONF-2011-102.

[136] ATLAS Collaboration, "Calibration of the performance of *b*-tagging for *c* and light-flavour jets in the 2012 ATLAS data," Jul 2014, ATLAS-CONF-2014-046.

[137] ATLAS Collaboration, "Calibration of *b*-tagging using dileptonic top pair events in a combinatorial likelihood approach with the ATLAS experiment," Feb 2014, ATLAS-CONF-2014-004.

[138] M. Wielers, R. Mantifel, A. Tricoli, and P. Bell, "Single Electron Trigger Performance Plots," Jun 2012.

[139] ATLAS Collaboration, "Performance of the ATLAS muon trigger in pp collisions at $\sqrt{s} = 8$ TeV," *Eur.Phys.J.*, vol. C75, no. 3, p. 120, 2015, arXiv:1408.3179.

[140] S. Alioli, P. Nason, C. Oleari, and E. Re, "A general framework for implementing NLO calculations in shower Monte Carlo programs: the POWHEG BOX," *JHEP*, vol. 1006, p. 043, 2010, 1002.2581.

[141] S. Frixione, E. Laenen, P. Motylinski, B. R. Webber, and C. D. White, "Single-top hadroproduction in association with a W boson," *JHEP*, vol. 0807, p. 029, 2008, arXiv:0805.3067.

[142] H.-L. Lai, M. Guzzi, J. Huston, Z. Li, P. M. Nadolsky, *et al.*, "New parton distributions for collider physics," *Phys. Rev.*, vol. D82, p. 074024, 2010, 1007.2241.

[143] P. Z. Skands, "Tuning Monte Carlo Generators: The Perugia Tunes," *Phys.Rev.*, vol. D82, p. 074018, 2010, arXiv:1005.3457.

[144] P. M. Nadolsky *et al.*, "Implications of CTEQ global analysis for collider observables," *Phys. Rev.*, vol. D 78, p. 013004, 2008, 0802.0007.

[145] S. Dittmaier, S. Dittmaier, C. Mariotti, G. Passarino, R. Tanaka, *et al.*, "Handbook of LHC Higgs Cross Sections: 2. Differential Distributions," 2012, arXiv:1201.3084.

[146] ATLAS Collaboration, "Measurement of the $t\bar{t}$ production cross-section as a function of jet multiplicity and jet transverse momentum in 7 TeV proton-proton collisions with the ATLAS detector," 2014, arXiv:1407.0891.

[147] J. Alwall, P. Demin, S. de Visscher, R. Frederix, M. Herquet, *et al.*, "MadGraph/MadEvent v4: The New Web Generation," *JHEP*, vol. 0709, p. 028, 2007, arXiv:0706.2334.

[148] S. D. Ellis and D. E. Soper, "Successive combination jet algorithm for hadron collisions," *Phys. Rev.*, vol. D48, p. 3160, 1993, arXiv:hep-ph/9305266.

[149] M. Czakon, P. Fiedler, and A. Mitov, "Total Top-Quark Pair-Production Cross Section at Hadron Colliders Through $O(?\frac{4}{S})$," *Phys.Rev.Lett.*, vol. 110, p. 252004, 2013, arXiv:1303.6254.

[150] A. van Hameren, C. Papadopoulos, and R. Pittau, "Automated one-loop calculations: A Proof of concept," *JHEP*, vol. 0909, p. 106, 2009, arXiv:0903.4665.

[151] M. Garzelli, A. Kardos, C. Papadopoulos, and Z. Trócsányi, "Standard Model Higgs boson production in association with a top anti-top pair at NLO with parton showering," *Europhys.Lett.*, vol. 96, p. 11001, 2011, arXiv:1108.0387.

[152] M. L. Mangano, M. Moretti, F. Piccinini, R. Pittau, and A. D. Polosa, "ALPGEN, a generator for hard multiparton processes in hadronic collisions," *JHEP*, vol. 07, p. 001, 2003, 0206293.

[153] S. Frixione and B. R. Webber, "Matching NLO QCD computations and parton shower simulations," *JHEP*, vol. 0206, p. 029, 2002, arXiv:hep-ph/0204244.

[154] P. Golonka and Z. Was, "PHOTOS Monte Carlo: A Precision tool for QED corrections in Z and W decays," *Eur. Phys. J.*, vol. C45, pp. 97–107, 2006, hep-ph/0506026.

[155] S. Jadach, Z. Was, R. Decker, and J. H. Kuhn, "The tau decay library TAUOLA: Version 2.4," *Comput.Phys.Commun.*, vol. 76, pp. 361–380, 1993.

[156] N. Davidson, T. Przedzinski, and Z. Was, "PHOTOS Interface in C++: Technical and Physics Documentation," 2010, arXiv:1011.0937.

[157] ATLAS Collaboration, "Summary of ATLAS pythia 8 tunes," August 2012, ATL-PHYS-PUB-2012-003.

[158] ATLAS Collaboration, "The ATLAS simulation infrastructure," *Eur. Phys. J.*, vol. C 70, pp. 823–874, 2010, 1005.4568.

[159] S. Agostinelli *et al.*, "GEANT4: A simulation toolkit," *Nucl. Instrum. Meth.*, vol. A 506, pp. 250–303, 2003.

[160] E. Richter-Was, D. Froidevaux, and L. Poggioli, "ATLFAST 2.0 a fast simulation package for ATLAS," Nov 1998.

[161] A. De Roeck and R. Thorne, "Structure Functions," *Prog.Part.Nucl.Phys.*, vol. 66, pp. 727–781, 2011, arXiv:1103.0555.

[162] T. Sjöstrand, "Why mb/ue physics prefer lo pdfs," 2013.

[163] N. Kidonakis, "Next-to-next-to-leading-order collinear and soft gluon corrections for t-channel single top quark production," *Phys. Rev.*, vol. D83, p. 091503, 2011, arXiv:1103.2792.

[164] J. M. Campbell, R. K. Ellis, and C. Williams, "Vector boson pair production at the LHC," *JHEP*, vol. 07, p. 018, 2011, arXiv:1105.0020.

[165] K. Melnikov and F. Petriello, "Electroweak gauge boson production at hadron colliders through O(alpha(s)^2)," *Phys. Rev.*, vol. D74, p. 114017, 2006, arXiv:hep-

ph/0609070.

[166] M. Garzelli, A. Kardos, C. Papadopoulos, and Z. Trócsányi, "t $\bar{t}$ W^{+-} and t $\bar{t}$ Z Hadroproduction at NLO accuracy in QCD with Parton Shower and Hadronization effects," *JHEP*, vol. 1211, p. 056, 2012, arXiv:1208.2665.

[167] ATLAS Collaboration, "Measurement of the b-tag Efficiency in a Sample of Jets Containing Muons with 5 fb^{-}1 of Data from the ATLAS Detector," Mar 2012, ATLAS-CONF-2012-043.

[168] J. Jovicevic, G. Piacquadio, F. Filthaut, T. Scanlon, and M. zur Nedden, "Calibration of *b*-tagging of the LCW+JES jets using di-leptonic top pair events and a combinatorial likelihood approach," Jan 2014, ATL-COM-PHYS-2014-038.

[169] ATLAS Collaboration, "Measurement of the $t\bar{t}$ production cross-section using $e\mu$ events with b -tagged jets in pp collisions at $\sqrt{s} = 7$ and 8 TeV with the ATLAS detector," *Eur.Phys.J.*, vol. C74, no. 10, p. 3109, 2014, arXiv:1406.5375.

[170] ATLAS Collaboration, "Evidence for the associated production of a vector boson (W, Z) and top quark pair in the dilepton and trilepton channels in pp collision data at $\sqrt{s} = 8$ TeV collected by the ATLAS detector at the LHC," Jul 2014.

[171] ATLAS Collaboration, "Measurement of the inclusive jet cross section in pp collisions at $\sqrt{s}$=2.76 TeV and comparison to the inclusive jet cross section at $\sqrt{s}$=7 TeV using the ATLAS detector," *Eur.Phys.J.*, vol. C73, p. 2509, 2013, arXiv:1304.4739.

[172] P. Skands, S. Carrazza, and J. Rojo, "Tuning PYTHIA 8.1: the Monash 2013 Tune," *Eur.Phys.J.*, vol. C74, no. 8, p. 3024, 2014, arXiv:1404.5630.

[173] J. Butterworth, G. Dissertori, S. Dittmaier, D. de Florian, N. Glover, *et al.*, "Les Houches 2013: Physics at TeV Colliders: Standard Model Working Group Report," 2014, arXiv:1405.1067.

[174] R. Frederix, S. Frixione, V. Hirschi, F. Maltoni, R. Pittau, *et al.*, "Four-lepton production at hadron colliders: aMC@NLO predictions with theoretical uncertainties," *JHEP*, vol. 1202, p. 099, 2012, arXiv:1110.4738.

[175] A. Buckley, J. Butterworth, L. Lönnblad, D. Grellscheid, H. Hoeth, *et al.*, "Rivet user manual," *Comput.Phys.Commun.*, vol. 184, pp. 2803–2819, 2013, arXiv:1003.0694.

[176] ATLAS Collaboration, "Measurements of the fiducial cross section for $t\bar{t}$ production with one or two additional b-jets using the ATLAS detector at sqrts=8 TeV," Apr 2015.

[177] F. Jiménez, "Charm and bottom production at particle colliders," 2012, LU TP 14-15.

[178] T. D. Lee, "A Theory of Spontaneous T Violation," *Phys. Rev.*, vol. D8, pp. 1226–1239, 1973.

[179] S. Dimopoulos and H. Georgi, "Softly Broken Supersymmetry and SU(5)," *Nucl. Phys.*, vol. B193, p. 150, 1981.

[180] L. Barak, M. zur Nedden, A. Ferrari, A. Juste, S. Khanov, A. Knue, A. Madsen, K. Nagata, G. Navarro, A. Nikiforov, P. Onyisi, D. Pelikan, S. Raddum, F. Rizatdinova, C. Sandoval, K. Sato, J. Schaarschmidt, D. Sidorov, J. Yu, H. Y. Cohen, E. Etzion, P. O. J. Gradin, and M. Pitt, "Search for heavy charged Higgs bosons in the $H^{\pm} \to tb$ decay channel with pp collision data recorded at $\sqrt{s} = 8$ TeV with the ATLAS detector," Dec 2013.

[181] CMS Collaboration, "Search for a heavy charged Higgs boson in proton-proton collisions at sqrts=8 TeV with the CMS detector," 2014.

[182] "Measurement of the ttbb cross section and the ratio ttbb/ttjj in the lepton+jets final state at 8 TeV with CMS detector," no. CMS-PAS-TOP-13-016, 1900.

[183] CMS Collaboration, "Measurement of the cross section ratio ttbb/ttjj in pp Collisions at 8 TeV," 2013, CMS-PAS-TOP-13-010.

[184] M. Cacciari, J. Rojo, G. P. Salam, and G. Soyez, "Jet Reconstruction in Heavy Ion Collisions," *Eur.Phys.J.*, vol. C71, p. 1539, 2011, arXiv:1010.1759.

Acknowledgements

In the contemporary hep-ex world with collaborations counting members in the thousands, writing a thesis is certainly not a one-man show. Had it not been for the dedication of the many people who worked before me to design, build, operate, calibrate and understand the myriad facets of the ATLAS detector, this thesis would not have been possible. My gratitude and admiration extends to all of them.

A special mention is necessary for the people that played a prominent role in my career as a PhD candidate. First and foremost I would like to thank my supervisor Judith Katzy, for never failing to provide me with interesting and challenging tasks, making sure that I always followed through, teaching me to be goal-oriented and for the many hours that she spent meticulously checking this manuscript and all the previous ones that resulted from my work as a PhD.

My sincere thanks to Klaus Mönig, who acted as my second supervisor and provided mentoring at various stages of this work, for his invaluable comments on the thesis and for inviting me to present my research to the HU research seminars; interacting with the DESY Zeuthen and HU ATLAS groups has been a truly inspiring experience.

Many thanks to Thomas Lohse and Christian Schwanenberger, who accepted the burdensome task of refereeing the thesis, as well as to Heiko Lacker and Peter Uwer who kindly accepted to be part of my defense committee.

I gratefully acknowledge the support that I received from the MCnet network, that allowed me to spend three months working with the Lund theory group. Thanks to all of the Lund theory group for providing such a stimulating environment and particularly to my supervisor Torbjörn Sjöstrand, for being an unparalleled teacher. I hope one day I will understand how he could instill in me the desire to always surpass myself without ever being demanding.

I owe a big thanks to the people with whom I have worked most closely at DESY: Karl-Johan Grahn and Alexander Grohsjean for the innumerable discussions and for help especially during the beginning of my PhD and Nedaa Asbah and John Keller for the very fruitful and enjoyable collaboration on the $t\bar{t}b\bar{b}$ analysis, on which this thesis is based and especially for providing Figures 11.6 and 13.1.

Thanks to my fellow $t\bar{t}b\bar{b}$ analyzers, especially Julian Glatzer, Jie Yu and Matthias Danninger for the many hours that we spent together discussing about all the intricacies of the analysis. Alison Lister, Richard Hawkings and Will Bell should be mentioned here not only for being my collaborators in the analysis but also for their professional support and advice, for which I am truly indebted.

During my involvement in the top analyses, I have benefited enormously from discussions with Jike Wang, Stefan Guindon, Valerio Dao, Andrea Knue, Gaetano Barone and of course my DESY ground-floor top neighbors Cécile Deterre, Jay Howarth and Roger Naranjo, who were always willing to offer advice and technical support whenever needed.

I am grateful to Ewelina Lobodzinska and Sebastian Pieć for their collaboration in the development of my very first analysis at DESY, which later turned into my first publication. For that I also owe a big thanks to my collaborators in the pile-up suppression analysis: John Backus Mayes, Lene Bryngemark, Craig Sawyer and Ariel Schwartzman. Thanks to Gabriel Facini who kindly provided crucial input when it was needed. Pavel Starovoitov deserves a special mention, not only as my collaborator in the jet analysis but also for always being willing to share his expertise on jet physics and his insights in general.

I would also like to thank Stefano Frixione and Rikkert Frederix who provided invaluable support and feedback from the theoretical side of the analysis and Maria Vittoria Garzelli, for helping with the POWHEL predictions and for being willing to spend a non-negligible amount of her time discussing the results. From my theory friends, I could not forget to mention Andrew Papanastasiou and Stefan Prestel, who had to endure my mind-numbing "theory-time" trips to the 3rd floor. Many thanks for our discussions and for teaching me a great deal!

I am also grateful to the people who made working at DESY an enjoyable experience and especially to Martin, Nils, Benjamin, Marco, Phil and Richard for the enriching discussions at the juniors' meeting. An enormous thanks to David South who made sure that we always had the necessary computing resources at our disposal. A big thanks is due to Mike Medinnis and Sabine Krohn, as well as to Bernd Krempl from the DESY International Office, for their support with administrative matters and not only.

Last but not least, the permanent resident in my theses acknowledgments: Nikos Rompotis, for being a true experimentalist who I can look up to.

Finally, большое спасибо Лене за всё and thanks to my family for putting up with me and for continuing to love me even though I didn't become a plumber.

This thesis is dedicated to the memory of my uncle; the reason that I am where I am.